Measurement and Characterization of Liquid Transfer between Two Solid Surfaces

by

Huanchen Chen

A thesis submitted in partial fulfillment of the requirements for the degree of

Doctor of Philosophy

Department of Mechanical Engineering
University of Alberta

Abstract

Drop transfer from one solid surface to another through stretching liquid bridges between them is important for many industrial applications. Due to the different dominate forces, three possible regimes exist: Quasi-static Regime, where the transfer process is only dominated by surface forces; Dynamic Regime, where inertia and viscous forces are the dominate forces; and Transition Regime, where all three types of forces are important. In this dissertation, the transfer processes in all of the three different regimes are studied.

For liquid transfer in Quasi-static Regime, the effects of contact angle hysteresis (*CAH*) are typically ignored in the literature. In this dissertation, with both the experimental measurements and simulation results from an analytical model, the importance of surface *CAH* in the transfer process is shown. Systematic studies on the role of advancing contact angle (θ_a), receding contact angle (θ_r) and *CAH* in determining the transfer ratio (α), maximum adhesion force (F_{max}) and pull-off force (F_{pf}) are performed. The transfer ratio is found to be governed by contact line pinning at the end of the stretching stage caused by *CAH*, which is controlled by θ_r of the surfaces. An empirical equation which is able to predict the transfer ratio by only knowing θ_r of the two surfaces is provided.

The value of F_{max} is found to be strongly influenced by the contact line pinning in early stretching stage. For symmetric liquid bridge between two identical surfaces, F_{max} may be determined only by θ_a, only by θ_r, or by both θ_a and θ_r, depending on the magnitude of the contact angles. For asymmetric bridges, F_{max} is found to be affected by the length of the contact line pinning period on the two surfaces. For F_{pf}, it is found that when one of the surfaces has a θ_r larger than 90°, F_{pf} decreases with the increase of θ_r on either surface. For the cases where θ_r of both surfaces are smaller than 90°, significantly smaller F_{pf} is seen when contact line pinning occurs on both surfaces, as compared to F_{pf} when contact line pinning occurs only on one of the surfaces.

For the liquid transfer in Transition and Dynamic Regimes, based on the value of Reynolds number (*Re*), the transfer process can have two different scenarios: one with negligible inertia effects ($Re<<1$) and the other with significant inertia effects ($Re>1$). For the liquid transfer with negligible inertia effects, the viscosity of the liquid is shown to act as a velocity shift such that, given the surface contact angle and the minimum separation between the two surfaces at which stretching begins, the transfer ratio is only a function of the Capillary number (*Ca*). Specifically, α converges from one plateau value to 0.5 with the increasing of *Ca*. The low-*Ca* plateau is the value in the Quasi-static Regime, whereas the high- *Ca* plateau of 0.5 is caused by the symmetric breakage shape of liquid bridge. Based on the observations, an empirical function $\alpha=F(Ca)$ was proposed and validated with experimental results. With this equation, by only knowing transfer ratio at two different stretching speeds in the Transition Regime, the transfer ratio under any value of stretching speed can be estimated. When the inertia effects become important (large *Re*), satellite drops appear when the liquid bridge breaks. Different from the transfer cases with negligible inertia effects, asymmetric shape of liquid bridge at the breakage is observed. Due to both the satellite drop and asymmetric breakage shape, α does not converge to 0.5 as it is observed in the system with negligible inertia effects.

Acknowledgements

Frist of all, I would like to sincerely thank my two supervisors, Dr. Alidad Amirfazli and Dr. Tian Tang for their strong support and great effort in guidance during the development of this thesis. I feel so lucky to have the opportunity conducting research with them. The training I got under them supervision will be a lifelong asset for me.

Special thanks are given to my friends in Mechanical Department of University of Alberta for their help and support during my research. They are Guoping Fang, Andrew J. B. Milne, Farshid Chini, Alberto Baldelli, Mina Karimi, Sara Madani, Maninderjit Singh and Maryam Mohseni. I would also thank Deepak Mandal, Chitiiran Krishna Moorthy from York University, and Antonio Criscione from Technical University Darmstadt for their help during my last two years study in York University.

I also gratefully acknowledge the financial support from Xerox Foundation.

Finally, I must acknowledge my parents. Without their support, love, and understanding, I could never have accomplished any of these works.

Preface

Chapter 2 of this thesis has been published as H. Chen, T. Tang and A. Amirfazli, "Fabrication of Polymeric Surfaces with Similar Contact Angle but Dissimilar Contact Angle Hysteresis", Colloids and Surfaces A: Physicochemical and Engineering Aspects, 408, 17-21 (2012).

Chapter 3 of this thesis has been published as H. Chen, A. Amirfazli and T. Tang, "Modeling Liquid Bridge between Surfaces with Contact Angle Hysteresis", Langmuir, 29, 3310-3319 (2013).

Chapter 4 of this thesis has been published as H. Chen, T. Tang and A. Amirfazli, "Mechanism of Liquid Transfer between Two Surfaces and the Role of Contact Angles", Soft Matter, 10, 2503-2507 (2014).

Chapter 5 of this thesis has been accepted to be published as H. Chen, T. Tang and A. Amirfazli, "Effect of Contact Angle Hysteresis on Breakage of a Liquid Bridge", Eur. Phys. J. Special Topics, 224, 277–288, (2015).

Chapter 6 of this thesis has been submitted to Soft Matter as H. Chen, T. Tang, H. Zhao, K-Y Law, and A. Amirfazli “Transfer (it) by Pinning (it): How Contact Angle Hysteresis Governs Liquid Transfer”.

Chapter 7 of this thesis has been submitted to Physics of Fluids as H. Chen, T. Tang and A. Amirfazli, "Effects of Surface Contact Angle on Fast Liquid Transfer ".

Chapter 8 of this thesis has been submitted to Langmuir as H. Chen, T. Tang and A. Amirfazli, " Fast Liquid Transfer between Surfaces: Breakup of Stretching Liquid Bridges ".

Contents

List of Tables

List of Figures

List of Abbreviations

θ_a	Advancing Contact Angle
θ_r	Receding Contact Angle
SCA	Surface Contact Angle
CA	Contact Angle
CAH	Contact Angle Hysteresis
PMMA	Poly(methyl methacrylate)
PEMA	Poly(ethyl methacrylate).
PS	Polystyrene
OTS	Octadecyltrichlorosilane
PP	Polypropylene
VOF	Volume of Fluid
RMS	Root Mean Square Roughness

Chapter 1.

1. Introduction

1.1 Background

Liquid drop transfer from one surface to another through elongating liquid bridges formed between the two surfaces is widely seen in our daily lives. For example, in offset printing, the ink is transferred between rollers through stretching ink bridges formed between them [1-4]. Similar transfer process can also be seen in many other industrial applications, e.g. packaging, drop deposition, and micro-gripping [5-7]. Recently, several studies were performed to utilize such contact transfer process to print micro-scale electrical circuits and semiconductors [8, 9]. Besides in the industry, such liquid transfer process can also be seen in nature [10, 11]. For example, vertebrates with incomplete cheeks (like cat) rely on their dorsal side of the tongue tip to form liquid bridge to move water into the mouth [10].

Given the importance of such transfer process, a number of previous studies were done to understand it. Since offset printing involves the widest application of such contact transfer, past work in the literature were typically designed to represent the process of ink transfer in the offset printing. The schematic of the offset printing mechanism is shown in Figure 1a, where ink is transferred from one roller to another by stretching the ink bridge in between. Since the size of the rollers (radius on the order of 0.1 m) is normally much larger than the size of the ink drop (radius on the order of 10-100 μm) [4], the rollers are normally treated as two flat surfaces and the procedure is simplified to what is shown in Figure 1b. Firstly, a liquid drop is placed on the donor surface. Then another surface (acceptor) is brought toward the liquid drop. Once the acceptor surface contacts the liquid drop, a liquid bridge is formed between the surfaces. The acceptor surface stops approaching the donor surface when the separation between them (H) reaches a certain minimum distance (H_{min}). After a short pause, the acceptor surface is retreated with a certain speed (U) until the liquid bridge breaks. Part of the liquid will be transferred from the donor surface to the acceptor surface. The transfer ratio (α), which is defined as the volume of the liquid transferred to the acceptor surface over the total volume of the liquid, is of particular interest because total transfer (α =1) is desired to ensure the printing quality. Besides the transfer ratio, the adhesion force between the liquid bridge and surfaces is also important, especially in the study of wet adhesion [12-16]. In particular, the largest value of the adhesion force during the stretching stage describes the strength of the wet adhesion systems.

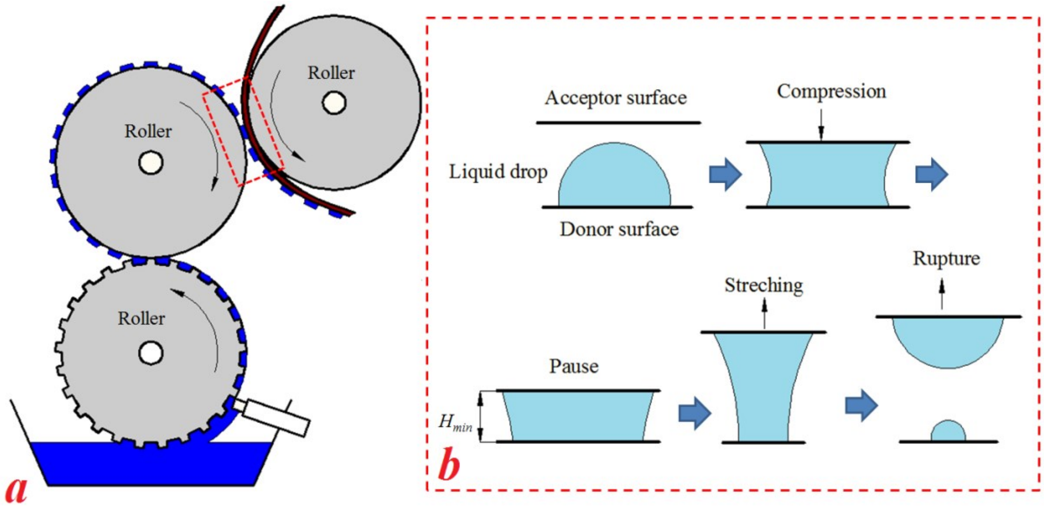

Figure 1.1: (a) Schematic of the offset printing mechanism. (b) Typical experimental procedure for liquid transfer.

As shown in Figure 1b, the liquid transfer is a complex process, and involves a number of physical parameter: stretching speed (U); liquid properties e.g. surface tension (γ), density (ρ), viscosity (μ), volume (V); surface contact angle (SCA), including advancing contact angle (θ_a), receding contact angle (θ_r), and contact angle hysteresis (CAH); and other parameters that can affect the liquid geometry, such as H_{min}. Many previous studies were performed to understand the effects of these parameters. In the next section of this chapter, a brief literature review of studies on liquid transfer is provided.

1.2 Literature review

Pioneering studies on liquid transfer were performed by Chadov and Yakhnin [17, 18]. In their work, experiments were carried out for several different liquids transferred under different stretching speeds. The transfer ratio of glycerol/water mixture transferred from Teflon surface to a zinc surface in [18] is re-plotted as function of *U* (mm/s) in Figure 2. It can be seen that when *U* is smaller than ~1 mm/s, the transfer ratio is a constant value. When *U* is larger than ~100 mm/s, the transfer ratio stays at 0.5. For ***U*** between 1 mm/s and 100 mm/s, the transfer ratio converges to 0.5 with the increase of ***U***.

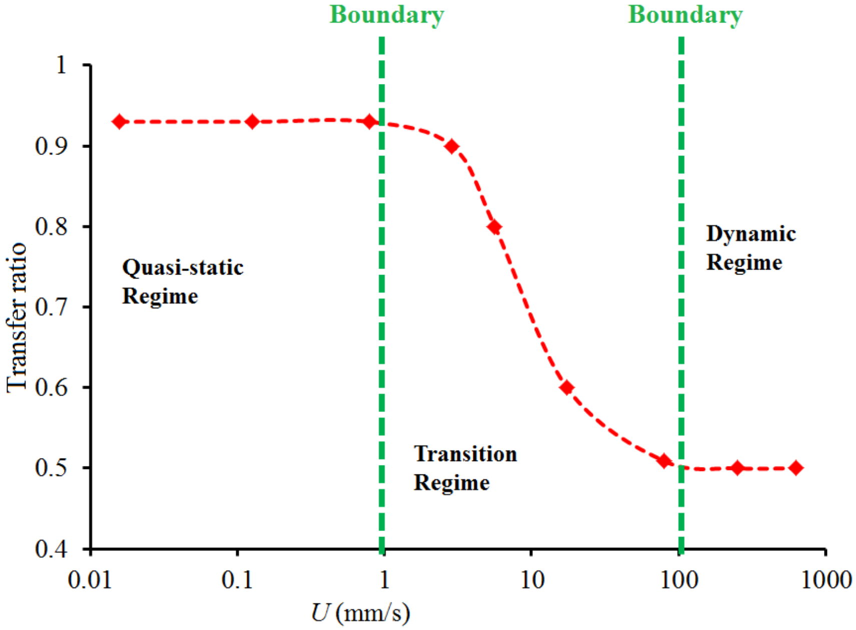

Figure 1.2: Transfer ratio as function of *U* for water/glycerol mixture (30% water and 70% glycerol) transferred from a Teflon surface to a zinc surface (replotted from [18]).

Based on such observations, three regimes for liquid transfer were defined in [17, 18] for the first time: Quasi-static Regime, where the process is only dominated by surface forces; Dynamic Regime, where viscous and inertial forces dominate; and Transition Regime, where surface, viscous and inertial forces all play roles. The transfer ratio shows a completely different dependence on *U* in the three regimes: it is constant in the Quasi-static Regime, varies with *U* and converges to 0.5 in the Transition Regime, and stays at 0.5 in the Dynamic Regime Although the two pioneer studies provided good phenomenon descriptions and the basic concepts to characterize the process of liquid transfer, it is neither comprehensive nor systematic. The boundaries between these regimes, i.e., velocities separating the regimes, were not investigated; as well the detailed roles of surface, viscous and inertial forces in each of the regimes were not further explored. Following these two works, a number of studies were performed to advance the understanding of liquid transfer process in the different regimes. In the following, reviews about the literature in different regimes are provided.

1.2.1 Quasi-static Regime

For liquid transfer in the Quasi-static regime, the process is only governed by surface forces which are determined by liquid surface tension (γ) and the profile of the liquid bridge. The profile can be affected by several physical parameters: *SCA*, volume of the liquid (V), and H. Therefore, most studies on Quasi-static transfer have focused on understanding the effects of each parameter on the liquid bridge profile. Based on the constraints applied on the liquid bridge during the transfer process, the liquid bridge can be classified as an "r" bridge or a "θ" bridge [19]. For the "r" bridge, the contact radii on the two solid surfaces are assumed to be pinned during the entire transfer process (Figure 3a). For the "θ" bridge, no constraint is applied on the contact radius, however the contact angles between the liquid bridge and the surfaces are assumed to be constant (Figure 3b).

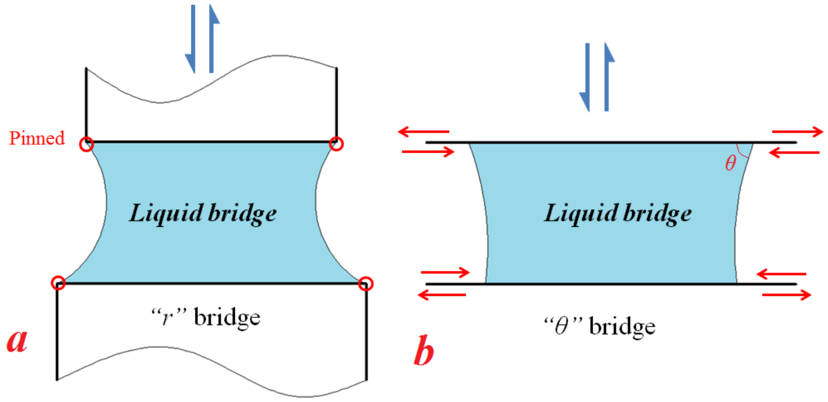

Figure 1.3: Schematic drawings of the two types of liquid bridge during Quasi-static transfer: (a) "r" bridge, and (b) "θ" bridge.

Previous studies were performed to investigate the governing parameters for both "*r"* and "θ" bridges in Quasi-static Regime [20-28]. One of the most representative studies was done by Qian and Gao [22] who built a theoretical model based on the Young-Laplace equation [29] to simulate the profile of a liquid bridge during stretching. In this model, given the liquid surface tension, volume and *H*, the profile of liquid bridge was calculated with boundary conditions on the two surfaces. For "*r"* bridge, since the contact lines on the two surfaces were always pinned, the values of contact radii were used as boundary conditions. For "θ" bridge, instead of using the contact radii, the contact angles between the liquid and the two surfaces served as boundary conditions. This model works well to capture the process of liquid transfer with the "*r"* bridge constraint. Several other studies based on this model were performed to further study "*r"* bridges [23, 25], where the effects of contact radius, liquid volume and surface tension on the profile of the liquid bridge and the adhesion force were discussed. For the "θ" bridge, the model by Qian and Gao assumed a constant value for the contact angle between the liquid and each surface. According to Young's equation [30], ideally, only one unique equilibrium contact angle exists between a liquid and a surface. However, in practice, due to surface roughness and heterogeneity, when a surface is wetted by a liquid, the contact angle is not a unique value but can vary within a range [31, 32]. The upper limit of this range is called the advancing contact angle (θ_a) which is the value of the contact angle when the contact line starts to expand (shown in Figure 4a). The lower limit is named as the receding contact angle (θ_r) which is the value when the contact line starts to shrink (shown in Figure 4b). *CAH* is the difference between θ_a and θ_r, and the contact angle can be any value between θ_a and θ_r when the contact line is pinned. This effect of *CAH* was not addressed in Qian and Gao's model. During the process of liquid transfer, the liquid bridge will be first compressed and then stretched. The contact line can expand, shrink, or remain pinned during the process; hence the contact angles at the surfaces are not necessarily constant but can change between their advancing and receding values. Therefore, the effects of surface *CAH* cannot be neglected for the study of the transfer process.

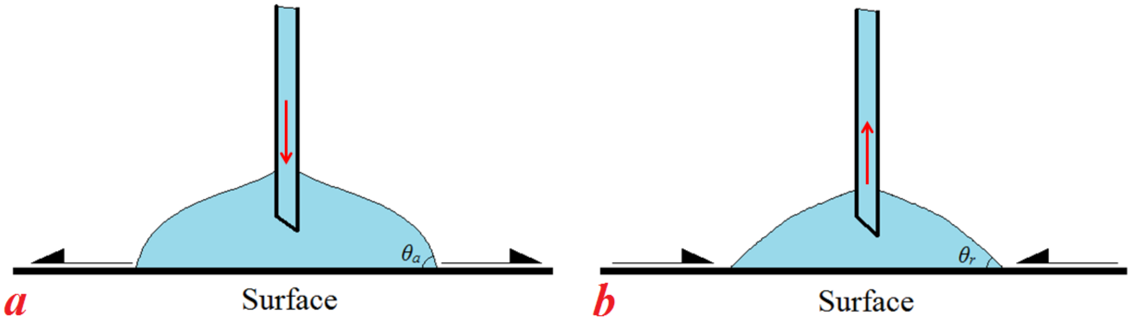

Figure 1.4: Schematic drawings for advancing contact angle (a) and receding contact angle (b).

Only very few studies attempted to address the effect of the *CAH* during liquid transfer. Souza *et al.* [33, 34] performed both experimental and numerical studies to investigate the effect of *CAH* on the adhesion force between liquid bridge and surfaces. They observed in the experiments that during the compression stage, the contact angle between the liquid and surface stayed at θ_a while in the stretching stage, the contact angle stayed at θ_r. Based on such experimental observations, a Surface Evolver model was built to calculate the adhesion force in the compression and stretching stages. However, this study assumed a single value for the contact angle during either the compression stage or the stretching stage. It did not capture how the contact angle changed from θ_a to θ_r at the beginning of the stretching stage, nor did it address how the profile of the liquid bridge and the adhesion force changed with the change in contact angle. Also, this study only focused on the effects of *CAH* on the adhesion force, while no information on transfer ratio was provided. In a separate study, Samuel *et al.* [35] performed an experimental study of liquid transfer from different donor surfaces to a hydrophilic platinum ring with a fix diameter. In this study the effects of *CAH* of the donor surface on both the adhesion force and transfer ratio were discussed. However, the experimental method used was not able to represent the transfer process in most of the applications. Firstly, by using a platinum ring as the acceptor surface, the contact radius on the acceptor surface was always fixed. In addition, compared with the normal liquid bridges in the applications (e.g. printing), which only have one liquid/air interface, the liquid bridge in this study has one more liquid/air interface enclosed by the ring. Therefore, the results obtained from this study may not be applicable to real applications.

Based on the discussion above, it is clear that for the liquid transfer in the Quasi-static Regime, the effects of *CAH* on the behavior of transfer process, e.g. profile of the liquid bridge, adhesion force, and transfer ratio, need to be addressed to improve the understanding of liquid transfer.

1.2.2 Transition and Dynamic Regime

In most of the applications, the liquid bridge is stretched with a relatively fast speed; hence the viscous and inertia effects are not negligible. Based on the definition of the three regimes, when the effects of either viscous or inertia forces become much larger than the effects of surface forces, the transfer process falls in the Dynamic Regime. For liquid transfer in the Transition Regimes, surface, inertia and viscous forces all play roles. Typically, the three forces (surface, inertia and viscous) in the transfer systems are typically qualitatively described by three dimensionless numbers: Capillary number ($Ca = U\mu/\gamma$, ratio of viscous to surface forces), Weber number ($We = \rho U^2 V^{1/3}/\gamma$, ratio of inertial to surface forces), and Reynolds number ($Re = \rho U V^{1/3}/\mu$, ratio of viscous force to the inertial forces). Based on the expression of the three dimensionless numbers, the viscous forces can be affected by the liquid viscosity μ and stretching speed U, while the inertial forces can be affected by liquid density ρ, volume V and U. Besides these four governing parameters, γ and *SCA* which influence the surface forces also need to be considered in the study of transfer in the Transition Regime. The physical parameters which can affect the transfer process in the Transition and Dynamic Regime are summarized in Table 1.

Table 1.1: Relevant physical parameters for the surface, viscous, and inertial forces in the Transition and Dynamic Regimes of liquid transfer.

Physical parameter	**Transition Regime**	**Dynamic Regime**
γ	Related to surface forces	Negligible
SCA	Related to surface forces	Negligible
μ	Related to viscous forces	Related to viscous forces
ρ	Related to inertial forces	Related to inertial forces
V	Related to inertial forces	Related to inertial forces
U	Related to both viscous & inertial forces	Related to both viscous & inertial forces

To understand the liquid transfer in Transition and Dynamic Regimes, based on a water jet model, Zhang *et al.* [36] built a one-dimensional (1-D) approximate model to numerically simulate the profile of a liquid bridge with two pinned contact radii. This model neglected the axial speed, which was extended by Yildirim and Basaran [37] to a two-dimensional (2-D) model. In both models, axisymmetric Navier–Stokes and continuity equations were solved with appropriate boundary conditions. The effects of the liquid viscosity, stretching speed, H_{min}, and values of contact radii were well discussed. However, in both studies, the contact radii on the two surfaces were assumed to be pinned which is not the situation in most of the applications. Several other studies about liquid transfer with the inertia and viscous effects can also be found [38-41]. However, all of these studies focused on understanding the role of the viscosity and inertial forces. The effects of *SCA* were not discussed in a clear or systematic way. Although, based on the definition of the three regimes, *SCA* does not affect the process in the Dynamic Regime, its effects cannot be neglected in the Transition Regime, which can further affect the boundaries that separate the regimes.

The importance of *SCA* in fast liquid transfer was noted in two recent studies [42, 43]. In most practical situations, e.g. offset printing, small volume (radius on the order of 1 μm) of viscous liquid is typically used, which corresponds to small inertia effects. Therefore, in both of these two studies, the inertia forces are neglected and only the surface and viscous forces are considered. Huang *et al.* [42] used the volume of fluid (VOF) method to study the process of fast liquid transfer with *Re* of the system in the range of 0.0008-0.04. It was shown that the value of the transfer ratio could be significantly affected by γ, U, SCA and μ of the system. However, how exactly these parameters affect the surface or viscous forces were not thoroughly discussed in this study. Another study performed by Dodds *et al.* [43] investigated the effects of viscous and surface forces during fast transfer using a finite element model. In this model, the effects of the inertia forces were again neglected, and the liquid transfer process was characterized by Ca. Their simulation results show that the transfer ratio converged to 0.5 when Ca increased from 0.01 to 1, which agreed with the observations made in [17, 18]. In both [42, 43], the contact angles between liquid and surfaces were simply assumed as constant values. As explained in Section 1.2.1, in practice, the contact angle is not a constant, and the effects of CAH need to be considered. Furthermore, different from the liquid transfer in the Quasi-static Regime where the contact angle is constant when the contact line is advancing (θ_a) or receding (θ_r), for fast liquid transfer the value of the contact angle were found to have a complex dependence on the speed of the contact line [44].

Although the inertia effects in majority of the applications are small, in some situations, liquid transfer with considerable large inertia effects also exists. For example, during cat lapping, the water bridge is retreated by its tongue with a very quick speed, which can be up to ～720mm/s. Given the small viscosity of water and fast retreat speed, the value of Re can be quite large (>500). To investigate the inertia effects during fast liquid transfer, Dodds *et al.* [45] performed a numerical study of liquid transfer from one surface (SCA: 70^o) to another (SCA: 90^o) with the same Ca (0.1) but different Re (from 0 to 100). Their results showed that when the inertia effects become important (Re >1), satellite drops at the bridge breakage could be observed. And the transfer ratio was found to increase from 0.08 to approximately 0.5 when Re increased from 0.1 to 100. Park *et al.* [46], simulated the process of water transfer between two surfaces with different U (10 mm/s to 250 mm/s). It was found that when U became sufficiently large (U >200mm, Re >222), instead of converging to 0.5, the transfer ratio could decrease with the increase of U. Therefore the observations made that transfer ratio always converges to 0.5 at high speed may not be valid when Re becomes large. Unfortunately, no further discussion was provided in this study on what caused α not to converge to 0.5.

Based on the discussions above, it is clear that the work in literature has been disjointed as many parameters were considered in isolation. The three regimes were studied in isolation; hence the interactions between them were not understood. The range of parameters studied was also normally narrow in each of the studies. Therefore, a comprehensive and systematic study on the liquid transfer process is needed. Particularly, the following four knowledge gaps need to be filled to improve the understanding of liquid transfer.

1. The effects of *SCA* on the liquid transfer in the three regimes as well as the boundaries separating the three regimes are still unclear.
2. What are roles of the physical parameters listed in Table 1 in determining the transfer ratio when properly considering the *SCA*?
3. Based on the effects of physical parameters on the transfer ratio, is it possible to predict the value of transfer ratio with only knowing the specification of the transfer system?
4. How does the liquid bridge behave when the inertia effects are important?

1.3 Goals of the Thesis

In this thesis, both experiments and simulations are performed to understand the transfer process in all three regimes. Considering the state of present knowledge gaps in the brief literature review above, the goals of this thesis are to:

1. Address the effects of *CAH* and identify the governing parameters for the transfer ratio and maximum adhesion force during the Quasi-static transfer process.
2. Understand the effects of *SCA* and *CAH* in the Transition Regime.
3. Identify the boundaries between the three regimes.
4. Investigate the governing parameters for transfer ratio in the Transition and Dynamic Regimes.
5. Based on the understanding of physical parameters affecting the transfer ratio, predict the transfer ratio with only knowing the parameters of the transfer system.

It should be pointed out that this thesis only focuses on the investigation of Newtonian fluid transfer between two solid surfaces. When a non-Newtonian fluid is involved, the liquid viscosity will not be a constant value but depending on the strain rate within the fluid during the transfer process. Therefore, the behaviour of liquid transfer can be more complex in the Transition and Dynamic regimes.

1.4. Outline of This Thesis

One important novelty of the thesis is to consider the effects of *CAH* on the liquid transfer process. Therefore, before starting the study of the liquid transfer, it is necessary to have the ability to fabricate surfaces which have similar advancing or receding contact angle but dissimilar *CAH*. Only with such surfaces, the effects of θ_a, θ_a and *CAH* on the liquid transfer can be addressed. In Chapter 2, the methods to fabricate such polymeric surfaces are introduced. Most of polymeric surfaces used in this thesis were fabricated with these methods.

Liquid transfer in the Quasi-static Regime is studied in Chapters 3-6. In Chapter 3, a theoretical model which can predict the behavior of the liquid bridge during Quasi-static compression and stretching under the influence of *CAH* was developed. With both experimental observations and simulation results (obtained from the theoretical model developed in Chapter 3), the mechanism governing liquid transfer in Quasi-static Regime is discussed in Chapter 4; the effects of *CAH* on the breakage of liquid bridge are discussion in Chapter 5; and in Chapter 6, a comprehensive and systematic study was performed to understand the governing parameters for the transfer ratio and maximum adhesion force. Liquid transfers in the Transition and Dynamic Regimes are discussed in Chapters 7 and 8. A numerical model based on VOF method was developed to help understand the experimental observations of liquid transfer in Transition and Dynamic Regimes. Chapter 7 focuses on discussing the effects of *SCA* and *CAH* on the transfer ratio in Transition Regime as well as on the boundaries between the regimes. In Chapter 8, the effect of the other physical parameters (i.e. γ, μ and H_{min}) on the transfer process in the Transition and Dynamic Regimes are discussed. Results of liquid transfer with large *Re* are also given in Chapter 8. An overall conclusion of this dissertation and future perspectives in the study of liquid transfer are given in Chapter 9.

Bibliography

(1.1) J. A. Lee, J. P. Rothstein, M. Pasquali, *J. Non-Newtonian Fluid Mech.* **199**, 1-11(2013).

(1.2) W. X. Huang, S. H. Lee, H. J. Sung, T. M. Lee, D. S. Kim, *Int. J. Heat Fluid Flow* **29**, 1436-1446 (2008).

(1.3) A. A. Darhuber, S. M. Troian, *J. Appl. Phys.* **90**, 3602-3609 (2001).

(1.4) H. W. Kang, H. J. Sung, T.M. Lee, D.S. Kim, C.J. Kim, *J. Micromech. Microeng.* **19**, 015025 (2009).

(1.5) S. Deladi, N. R. Tas, J. W. Berenschot, G. J. M. Krijnen, M. J. de Boer, J. H. de Boer, M. Peter, M. C. Elwenspoek, Appl. Phys. Lett. **85**, 5361–5363(2004).

(1.6) S. Kumar, *Annu. Rev. Fluid Mech.* **47**, 67-94 (2015).

(1.7) P. Lambert, A. Chau, A. Delchambre, S. Regnier, *Langmuir*, **24 (7)**, 3157-3163 (2008）.

(1.8) M. Pudas, J. Hagberg, S. Leppavuori, *J. Eur. Ceram. Soc.* **24**, 2943-2950 (2004).

(1.9) P. Kopola, T. Aernouts, S. Guillerez, H. Jin, M. Tuomikoski, A. Maaninen, J. Hast, *Solar Energy Mat. Solar Cells* **94**, 1673-1680 (2010).

(1.10) M. Prakash, D. Quere, J. W. M. Bush, *Science* **320**, 931-934 (2008).

(1.11) P. M. Reis, S. Jung, J. M. Aristoff, R. Stocker, *Science*, **330**, 1231 (2010).

(1.12) S. Gorb, *Proc. Roy. Soc. Lond. B* **265**, 747–52 (1998).

(1.13) B. N. J. Persson, *J. Phys.: Condens. Matter* **19**, 376110 (2007).

(1.14) T. Eisner, D. J. Aneshansley, *Proc. Natl. Acad. Sci.* **97**, 6568–6573 (2000).

(1.15) A. F. G. Dixon, P. C. Croghan, R. P. Gowing, *J. Expl. Biol.* **152**, 243–253 (1990).

(1.16) W. Federle, M. Riehle, A. S. G. Curtis, R. J. Full, *Integr. Comp. Biol.* **42**, 1100–1106 (2002).

(1.17) A. V. Chadov, E. D. Yakhnin, *Kolloidn. Zh.* **41**, 817 (1979).

(1.18) E. D. Yakhnin, A. V. Chadov, *Kolloidn. Zh.* **45**, 1183 (1983**)**.

(1.19) M. A. Fortes, *J. Colloid Interface Sci.* **88**, 338-352 (1982).

(1.20) A. A. Darhuber, S. M. Troian, *J. Appl. Phys.* **90**, 3602-3609 (2001).

(1.21) S. J. Hong, T. H. Chou, S. H. Chan, Y. J. Sheng, H. K. Tsao, *Langmuir* 28, 5606−5613 (2012).

(1.22) J. Qian, H. Gao, *Acta Biomaterialia* **2**, 51–58 (2006).

(1.23) E. Cheung, M. Sitti, *J. Adhesion Sci. Tech.* **22**, 569-589 (2008).

(1.24) B. N. J. Persson, *J. Phys.: Condens. Matter*. **19**, 376110 (2007).

(1.25) B. Qian, K. S. Breuer, *J. Fluid Mech.* **666**, 554-572 (2011).

(1.26) G. Lian, C. Thornton, M. J. Adams *J. Colloid Interface Sci.***161**, 138-147 (1993).

(1.27) S. Gorb, *Proc. Roy. Soc. Lond. B* **265**, 747-52 (1998).

(1.28) B. Qian, M. Loureiro, D. Gagnon, A. Tripathi, K. S. Breuer, *Phys. Rev. Lett.* **102 (16)**, 164502 (2009).

(1.29) T. Young, Philos. Trans. R. Soc. London **95**, 65−87 (1805).

(1.30) Adamson AW. Physical chemistry of surfaces. New York, NY: John Wiley & Sons Inc; 1976

(1.31) C. N. C. Lam, R. Wu, D. Li, M. L. Hair, A. W. Neumann, *Adv. Colloid Interface Sci.*, 96, 169-191(2002).

(1.32) H. Tavana, in *Applied Surface Thermodynamics*, 2nd ed.; A.W. Neumann, R. David, Y. Zuo, Ed.; Surfactant Sci. Series; CRC: Boca Raton, USA, 2010; vol. 151, 315-316.

(1.33) E. J. D. Souza, L. Gao , T. J. McCarthy, E. Arzt, A. J. Crosby, *Langmuir*, **24 (4)**, 1391-1396 (2008).

(1.34) E. J. De Souza, M. Brinkmann, C. Mohrdieck, E. Arzt, *Langmuir* **24 (16)**, 8813-8820 (2008).

(1.35) B. Samuel, H. Zhao, K-Y Law, *J. Phys. Chem. C* **115**, 14852-14861(2011).

(1.36) X. Zhang, R. S. Padgett, A. Basaran, *J. Fluid Mech.* **329**, 207-245(1996).

(1.37) O. E. Yildirim, O. A. Basaran, *Chem. Eng. Sci*. **56**, 211–233 (2001).

(1.38) J. Meseguer, A. Sanz, *J. Fluid Mech.* **153**, 83-101 (1985).

(1.39) P. Doshi, R. Suryo, O. E. Yildirim, G. H. McKinley, O. A. Basaran, *J. Non-Newtonian Fluid Mech.* **113**, 1–27 (2003).

(1.40) H. S. Huynh, J. P. Guan, T. Vuong, T. W. Ng, *Langmuir* **29 (37)**, 11615–11622 (2013).

(1.41) Y. C. Liao, E. I. Franses, O. A. Basaran, *Phys. Fluids* **18**, 022101 (2006).

(1.42) W.X. Huang, S.H. Lee, H.J. Sung, T. M. Lee, D. S. Kim, *Int. J. Heat Fluid Flow* **29**, 1436–1446 (2008)

(1.43) S. Dodds, M. Carvalho, S. Kumar, *Phy. Fluids* **21**, 092103 (2009).

(1.44) S. E. Bai, J. S. Shim, C. H. Lee, C. H. Bai, K. Y. Shin, *Jpn. J. Appl. Phy.* **53**, 05HC05 (2014).

(1.45) S. Dodds, M. Carvalho, S. Kumar, *Phy. Fluids* **23**, 092101 (2011).

(1.46) Park, S-S; Jeon, Y.; Cho, M.; Bai, C.; Lee, D.; Shim, J.; The FEM based liquid transfer model in gravure offset printing using phase field method. *Microsyst Technol* **2012**, 18, 2027–2034.

Chapter 2

2. Fabrication of Polymeric Surfaces with Similar Contact Angle but Dissimilar Contact Angle Hysteresis

2.1. Introduction

Contact angle is an important parameter in surface science. Ideally, the value of contact angle between a liquid and a solid is unique. However, a range of contact angles can be obtained in everyday systems. Contact angle hysteresis (*CAH*) is the difference between the values of upper limit and lower limit for the contact angles seen for a system [1]. Contact angle, *CAH* and its physical interpretation are widely used in industrial and scientific research, e.g. in printing industry, Micro-electro-mechanical systems (MEMS) packaging, self-cleaning surfaces and microcapillary flow. To systematically understand the role of contact angle and *CAH* in any of the above areas, a series of surfaces with different wettability are generally needed.

Usually, researchers can obtain surfaces with different wettability by using different materials. Semenov *et al.* [2] constructed four surfaces (polished epoxy surface, Corning glass 7740, PMMA, and polyethylene terephthalate) with different *CAH* to allow a systematic study of the effect of *CAH* on the evaporation of sessile water drops. In the work of Sakai *et al.* [3], on the relationship between sliding acceleration of water drops and dynamic contact angles, octadecyltrimethoxysilane and heptadecafluorodecyltrimethoxysilane surfaces coated on silicon wafer and Polytetrafluoroethylene plate which had different wettabilities were used.

Normally, surfaces with similar advancing or receding contact angle but dissimilar *CAH* can be obtained by fabricating the surfaces with the same material but different roughness. To study the effect of *CAH* on drop coalescence and mixing, Nilsson and Rothstein [4] fabricated three different Teflon surfaces by sanding them using different grit sand paper, which resulted in surfaces with the same advancing contact angle of 150°, but various *CAH* (3°,15° and 30°).

The methods used to date, as discussed above, usually do not lend themselves to fabricate a series of surfaces with certain wettability characteristics. In many situations, surfaces with an intended contact angle value and *CAH* are needed. By just changing the material, it is difficult to find a polymer which has the values of both contact angle and *CAH* similar to the intended values. Sand paper cannot work for all types of polymers, especially for thin polymer films.

This study introduces several options that can be used to fabricate surfaces with different advancing and receding contact angles with distilled water, especially for fabricating surfaces with similar advancing or receding contact angle, but different *CAH*. Furthermore, the idea of this study can be applied to fabricate surfaces that have different contact angles and *CAH* with other liquids, such as ethanol, oil, etc. Firstly, the note introduces the materials and three different methods of surface fabrication. Secondly, the effects of fabrication methods and parameters for each method on the wettability of fabricated surfaces are discussed. Finally, an example of fabricating a series of surfaces with similar contact angles with water but different *CAH* is given.

2.2. Experimental

2.2.1 Materials and Methods

Four typical polymers: Poly (methyl methacrylate) (PMMA, Aldrich Mw=120,000 Mn=55,000), Polystyrene (Aldrich: Mw=97,400, Mn=97,000), Polypropylene (Aldrich: Mw=250,000, Mn=62,500) and Teflon AF (DuPont Teflon AF 601s2-100-6) were used in this study. Spin coating, spray coating, and heat press were used for surface fabrication. Brief descriptions of each of these methods are given below.

Spin coating is a method which is widely used to apply a uniform thin film onto a flat substrate. Previous researches show that by increasing the spinning rate, lengthening the spinning time, or diluting the concentration of the solution, the thickness of coated polymer film can decrease [5-7]. Spray coating is another surface fabrication method which coats a substrate with a liquid spray of polymeric solution [8]. Compared with spin coating, the surfaces obtained from spray coating usually have larger roughness. The roughness of a sprayed surface can be affected by air pressure, and the distance between the substrate and the spray nozzle [9]. Heat pressing a thermoplastic polymer between two clean plates is another method to produce surfaces. The pressure and temperature employed during the process must be sufficient to cause the polymer to conform to the plate, but not too high to cause changes in polymer chemistry [10]. Surfaces made by heat pressing usually have the same microstructure as that of the plate.

For spin coating and spray coating in this work, each polymer was coated on a plain microscope slide (20mm (W) ×25mm (L)). All of the microscope slides were cleaned by acetone in a sonicator, dried after being rinsed with distilled water several times. The polymer solutions were prepared by dissolving the polymer powder in toluene (Fisher Scientific, 99.9%). All of the solutions were sonicated for 30 mins, in order to completely dissolve the polymer powder. The prepared solutions were contained in a sealed glass bottle to minimize the evaporation of toluene. All the spin coating and spray coating experiments were done at 20°C, at relative humidity of 38% under atmospheric pressure conditions. Sessile drop method [10] with wetting rate 0.8±0.12 mm/min was used to measure the dynamic contact angle between distilled water and the fabricated polymer surfaces. Processing the images taken during the contact angle measurement allows the determination of the contact angle with a precision of about 2°. Surface roughness measurements were conducted using Atomic Force Microscope MFP-3D (Asylum Research) in order to explain the reason for the fabricated surfaces to have different *CAH*.

2.2.2 Factors affecting wettability of surfaces

Besides material property, wettability of a surface can be significantly affected by two other parameters, surface roughness and heterogeneity. In this study, for surfaces made of a single polymeric material, affecting the wettability by presence of possible heterogeneity as a result of molecular group orientation will be less effective than exploiting roughness to affect wettability. Therefore, for single polymeric surfaces, roughness was used as the main parameter to affect the wettability of the surfaces. Usually, the higher the roughness, the higher will be the *CAH* [11], but in certain cases, higher roughness can lead to a lowering of *CAH*, and a marked increase in the advancing contact angle [12, 13], for instance, on superhydrophobic surfaces. With different fabrication methods, the roughness of the obtained surfaces can be quite different from one another, which can result in different surface wettability.

For spin coating, the polymer solution on the substrate is rotated at a very high speed, and the fluid is spread by centrifugal force. Therefore, surface obtained from spin coating usually have a small surface roughness. For spray coating, polymer solution is sprayed onto the substrate. Different from the spin coating, there is no centrifugal force acting on the fluid to spread it. Therefore, compared with spin coating, sprayed surface can have a larger roughness. Although the wettability of spray coated surfaces is very sensitive to the spraying parameters, by using the same spraying parameters, the surfaces can be quite reproducible. For heat press, normally, the obtained surfaces have the same microstructure of the plates which results in similar surface roughness to that of the plate. So the roughness of heat pressed surface can be affected by using different heat press plates. Within each method, characteristics of the fabricated surfaces can still be varied by changing the parameters of these fabrication methods. For spin coating, concentration of the solution, solvent type, spinning rate and spinning time are important parameters which can be used to adjust the roughness of the surfaces, and hence its wettability. For heat pressed surfaces, during the process of separating the polymer surface from the plate, the microstructure of the polymer surface can be altered which can result in different roughness values between the heat pressed surfaces and the plate. Techniques can be used to minimize such alternation to surface texture during separation, which can lead to a smaller roughness for the fabricated surface and consequently a smaller *CAH* (discussed later).

For surfaces made of more than one polymer, besides surface roughness, surface heterogeneity can be used to change the surface wettability, and it can be affected by the ratio of the polymers being blended, the type of the solvent used, and the solubility of the polymer constitutes in the solvent [14, 15]. For instance, surfaces with different wettability can be obtained by using different ratios of PMMA and polystyrene in the mixed solutions.

Normally, in order to fabricate a polymeric surface with a certain value of contact angle and *CAH*, three steps have to be taken: Firstly, an appropriate material which has a similar intrinsic contact angle to the intended contact angle value has to be chosen. The second step is deciding on surface fabrication method according to the intended wettability and material property. After choosing the material and fabrication method, the final step is determining the parameters for the selected method.

2.3. Practical application and discussion

By following the three steps above, a series of surfaces with similar dynamic advancing or receding contact angle but different *CAH* can be fabricated. To demonstrate this point, Table 2.1 shows 6 groups of polymeric surfaces to be fabricated, varying from being hydrophobic to being hydrophilic. Each group contains two surfaces which has either similar dynamic advancing contact angle (θ_a) or similar dynamic receding contact angle (θ_r) but different *CAH*.

Table 2.1: Contact angle and *CAH* of intended polymer surfaces.

Surface No.	Intended contact angle (degree)	intended *CAH* (degree)	Surface No.	intended contact angle (degree)	Intended *CAH* (degree)
A1	θ_a:120 θ_r:108	12	A2	θ_a:130 θ_r:108	22
B1	θ_a:110 θ_r:90	20	B2	θ_a:120 θ_r:90	30
C1	θ_a:90 θ_r:75	15	C2	θ_a:90 θ_r:60	30
D1	θ_a:70 θ_r:55	15	D2	θ_a:70 θ_r:45	25
E1	θ_a:78 θ_r:55	23	E2	θ_a:78 θ_r:65	13

To produce the surfaces in Table 2.1, after the selection of appropriate polymer with closest intrinsic contact angle to the intended value, the fabrication method that is likely to give the desired *CAH* was determined and the process parameters for the selected fabrication method was changed systematically to obtain the desired results. Table 2.2, shows the details of the selected polymers, fabrication methods, and the parameters chosen for each of the fabrication methods.

Table 2.2: Technical details of fabricating each surface given in Table 1.1.

Surfaces No.	Method	Material and fabrication details
A1	Spin coat	A1: Solution: Teflon AF diluted with FC-75 (3M) in the ratio of 1:5 Spin coater speed: 2500 RPM Spin time: 60s
A2	Spray Coat[1]	Solution: Teflon AF diluted with FC-75 (3M) in the ratio of 1:5 Pressure: 300 KPa Distance between surface and spray nozzle:100mm, sprayed 4 - 5 times
B1	Heat press	Material: Polypropylene Plate: Two Microscope slices (plain) Temperature: 179°C Time: 2 mins. Pressure: 645 Pa After heat press, surface placed into 20 °C distilled water immediately
B2	Heat press	Material: Polypropylene Plate : Two Microscope slices (plain) Temperature: 179°C Time: 2 mins. Pressure: 645 Pa After heat press, cool down naturally
C1	Spin coat	Solution: 1wt% solution of Polystyrene in toluene Spin coater speed: 3000 RPM Spin time: 60s
C2	Heat press	Material: Polystyrene Plate: Two slices of Surface A1 (Teflon AF surface) Temperature: 179°C Time: 2 mins. Pressure: 645 Pa After heat press, surface placed into 20 °C distilled water immediately. Cleaned by FC-75 again, after detached from the plate.
D1	Spin coat	Solution: 1wt% solution of PMMA in toluene Spin coater speed: 2000 RPM Spin time: 60s
D2	Spin coat	Solution: 0.2wt% solution of PMMA in toluene Spin coater speed: 3000 RPM Spin time: 60s
E1	Spin coat	Solution: 1wt% PMMA and Polystyrene mixed in toluene solution , ratio of PMMA: Polystyrene = 15:1 Spin coater speed: 2500 RPM Spin time: 60s
E2	Spin coat	Solution: 1wt% PMMA and Polystyrene mixed in toluene solution , ratio of PMMA: Polystyrene = 6:1 Spin coater speed: 2500 RPM Spin time: 60s

[1] AZTEK-Airbrush A320 with nozzle of 9306C (size: 0.5 mm) was used.

In order to test the repeatability of the methods, for each surface three samples were fabricated. On each sample, measurements for contact angle were conducted at three different locations. The value of contact angle is almost constant during the advancing stage of the contact line [1]; therefore, an average value of the contact angle at this stage can be obtained and used as the advancing contact angle. Each of the advancing contact angles shown in Table 2.3 are the average value of the 9 measurements. Different from the advancing contact angle, the value of receding contact angles continued to decrease as the contact line receded (time-dependent receding contact angle [1]); hence a mean receding contact angle could not be determined. In this report, the data of the receding contact angles in Table 2.3 were obtained by averaging the contact angle values of the 9 measurements during the first 5 seconds after the contact line started receding.

Comparing the data in Tables 2.1 and 2.3, it can be seen that the contact angle and *CAH* obtained are close to the intended values. For each group, the surface with a larger roughness has a larger *CAH*, consistent with literature [11].

As indicated before, surfaces obtained from spin coating usually have a very small surface roughness (RMS roughness for Surfaces A1: 0.9nm, C1: 0.4nm, D1:0.4nm, and D2: 0.7nm). Therefore, compared with spray coating (RMS roughness for A2: 432.6nm, *CAH* =22.7°) and heat press (RMS roughness for C2: 8.6nm, *CAH* =28.1°), surfaces obtained by spin coating (A1: *CAH* =9.9°, C1: *CAH* =13.8°) have a smaller *CAH*. Note that the heterogeneity is not a significant factor as single component polymer solutions were used.

For surfaces D1 and D2, although both of them are made of PMMA by spin coating, they have different surface roughness and *CAH*. The differences in generating the two surfaces are that D1 was constructed using slower spinning rate and higher solution concentration. According to literature [4, 5], polymer film of D2 is expected to be thinner than D1, which can lead to that the polymer film of D2 may not completely cover the asperities of the substrate, since the substrates of surfaces D1 and D2 are not perfect smooth. Another possible reason for the difference between D1 and D2 is that during spinning, the solvent evaporates much slower in valley areas (e.g. due to RMS roughness of substrate: 0.46nm) than at other locations, which can result in difference in concentration of solution, hence a difference in surface tension. Therefore, the resultant Marangoni flow [17, 18] may give rise to a larger roughness for the fabricated surface. Because the solution concentration of D2 is much lower than D1, the effects of Marangoni flow on surface D2 might be more pronounced than D1. Either or both of these can result in surface D2 having a larger roughness and CAH, compared with those of D1.

Heat pressed surfaces, B1 (RMS roughness: 8.9nm) and C2 (RMS roughness: 8.6nm) have a much smaller roughness than B2 (RMS roughness: 34.7nm). This can be explained by the fact that for both B1 and C2, precautions were taken to minimize the damage to the surface microstructure during the separation (see Table 2.2). For C2, a spin coated Teflon AF surface was used as the plate. Although the glass transition temperature for the Teflon AF is 160°C which is 19°C lower than the heat press temperature, 179°C is still much lower than its melting point which is about 300°C. Therefore, the Teflon AF plate should not introduce any additional conformational changes to of the heat pressed surface. In addition, the test surface was cleaned by FC-75 again after it was detached from the plate to clean any residual Teflon on the surface. For B1, putting the surface into cold distilled water immediately after heat press can not only help separate the surface from the plate, but also can minimize the surface defect caused by the large value of thermal expansion coefficient of polypropylene. Although both surface B1 and B2 were made of polypropylene, the difference in roughness results in different *CAH* (B1: *CAH* =21.1°, B2: *CAH* = 29.1°).

Both of the two heterogeneous surfaces in group E were spin coated (identical settings) with PMMA and polystyrene mixed solution, but at different ratio of PMMA to polystyrene. AFM images of both surfaces are shown in Figure 2.1. The scan areas were 20×20 μm. The RMS roughness was 1.2nm and 2.9nm for surfaces E1 and E2, respectively. As in typical spin coating of such polymer blends, it is clear that the polymers have separated into domains with different heights, each domain being rich in a particular polymer type. As suggested in the literature, e.g., [14, 15] the size, pattern and distribution of the phase separated polymers and consequently surface roughness and heterogeneity will be influenced by the ratio of the polymers in the blend, spin speed, choice of solvent, etc. It is interesting to note that for surfaces fabricated from a single polymer, it was expected as discussed earlier, that surface roughness will be different (confirmed by AFM imaging, but not shown for brevity; see Appendix A); but as can be seen in Figure 2.1, when polymer blends are used, not only surface heterogeneity is seen, but also surface topography is changing. As seen in Figure 2.1, for surface E1, (PMMA: Polystyrene is 15:1) the polymer domains are small, and distributed nearly uniformly over the surface, leading to a low amplitude high frequency roughness pattern. In case of surface E2, where the ratio of PMMA: polystyrene is decreased to 6:1, the domains have grown larger in size (compared to E1); also the surface roughness amplitude is increased compared to E1 (see Table 2.3). Such changes in surface topography and composition have resulted in different *CAH* (i.e. the wettability of E2 is closer to pure polystyrene surface, since the ratio of PMMA: polystyrene in E2 is lower than that in E1) and open the door for the manipulation of surface wettability as shown in this work to achieve the desired values.

Table 2.3: Contact angles and *CAH* for fabricated surfaces. See Table 2.1 for intended value for the wattebility measures.

Surface No.	Contact angle (degree)	*CAH* (degree)	RMS Roughness (nm)	Surface No.	Contact angle (degree)	*CAH* (degree)	RMS Roughness (nm)
A1	θ_a:122.6±0.75	9.9	0.9	A2	θ_a:128.9±1.11	22.7	432.6
	θ_r:112.7±0.85				θ_R:106.2±0.90		
B1	θ_a:110.6±0.93	21.1	8.9	B2	θ_a:119.9±1.55	29.1	34.7
	θ_r: 89.5±0.76				θ_r:90.8±1.00		
C1	θ_a:89.1±0.56	13.8	0.4	C2	θ_a:89.0±0.82	28.1	8.6
	θ_r:75.3±0.80				θ_r:60.9±1.66		
D1	θ_a:68.8±0.72	13.6	0.4	D2	θ_a:73.5±0.78	24.6	0.7
	θ_r:55.6±0.64				θ_r:48.9±0.66		
E1	θ_a:76.1±0.54	20.4	1.2	E2	θ_a:80.1±0.58	15.6	2.9
	θ_r:55.7±0.64				θ_r:64.5±0.72		

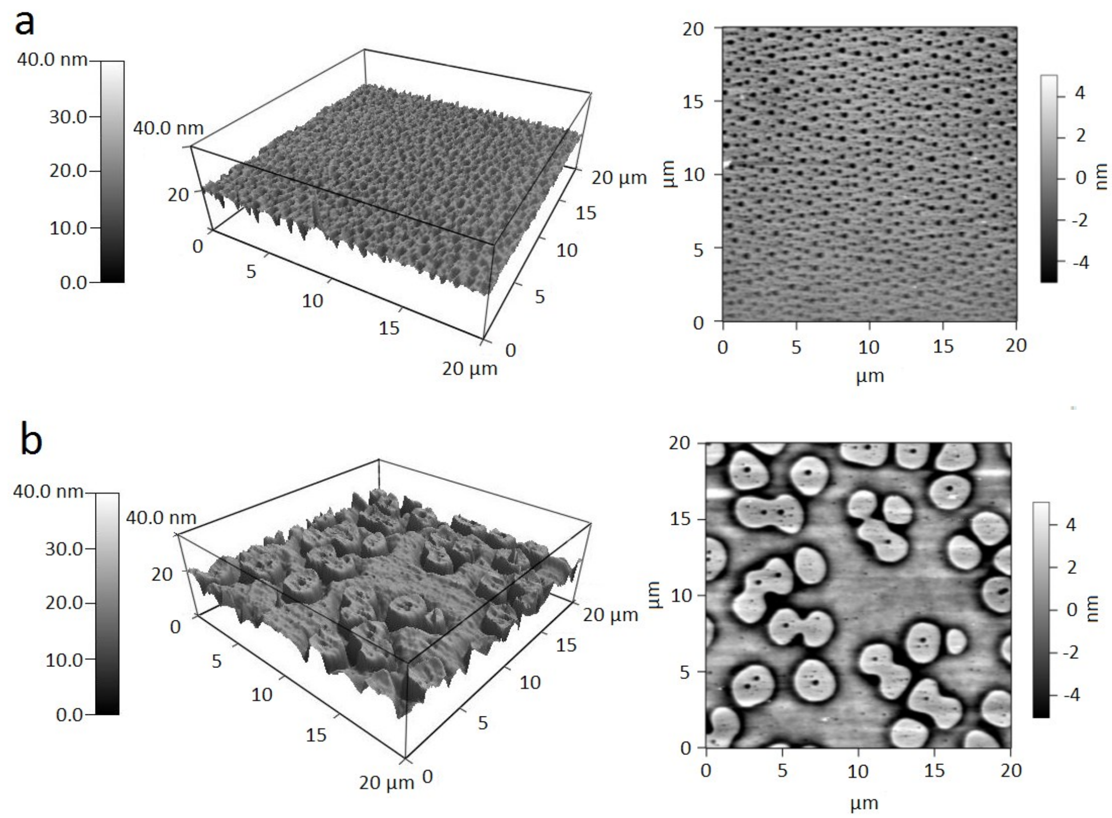

Figure 2.1: (a) 3D (left) and 2D (right) AFM images of surface E1. (b) 3D (left) and 2D (right) AFM images of surface E2.

2.4. Conclusions

This technical note provides options other than using different materials for constructing polymeric surfaces with different wettability. The relationship between surface roughness and surface fabrication methods were discussed. Roughness differences among the surfaces obtained from spin coating, spray coating and heat press can be used to guide the fabrication of surfaces made of a particular material but having different *CAH* (up to 13° difference was found in this work). Chemical heterogeneity is another factor that can affect the wettability of surfaces made of more than one polymer. For surfaces made of mixed solution of PMMA and polystyrene, the ratio of PMMA: polystyrene was used to affect the surface wettability, and the results were explained by changes in pattern and size of the heterogeneous domains on the surface.

Bibliography

(2.1) C.N.C. Lam, R. Wu, D. Li, M.L. Hair, A.W. Neumann, *Adv. Colloid Interface Sci.* **2002**, 96, 169-191.

(2.2) S. Semenov, V.M. Starov, R.G. Rubio, H. Agogo, M.G. Velarde, *Colloids Surface. A* **2011**, 391, 135-144.

(2.3) M. Sakai, J. Song, N. Yoshida, S. Suzuki, Y. Kameshima, A. Nakajima, M. Sakai, *Surface Sci.* **2006**, 600, 204-208.

(2.4) M.A. Nilsson and J.P. Rothstein, *J. Colloid Interface Sci.* **2011**, 363, 646-654.

(2.5) J.D. Le Roux and D.R. Paul, *J. Membrane Sci.* **1992**, 74, 233-252.

(2.6) P.C. Sukanek, Dependence of film thickness on speed in spin coating. *J. Electrochem Soc.* **1991**, 138, 1712-1719.

(2.7) D.W. Schubert and T. Dunkel, *Mat. Res. Innovat.* **2003**, 7, 314-321.

(2.8) D. Barona, A. Amirfazli, *Lab Chip*, **2011**, 11, 936-940.

(2.9) G. Perfetti, T. Alphazan, P. van Hee, W.J. Wildeboer, G.M.H. Meesters, *Eur. J. Pharm. Sci.* **2011**, 43, 262-272.

(2.10) H. Tavana, Contact Angle Measurements: General Procedures and Approaches, in: A.W. Neumann, D. Y. Kwok, R. David, Y. Zuo (Eds.), Applied Surface Thermodynamics, 2nd, CRC, Boca Raton, USA, 2010, PP. 315-316.

(2.11) G. Zografi, B. A. Johnson, *Int. J. Pharm.* 1984, 22, 159-176.

(2.12) R. H. Dettre, R. E. Johnson Jr, *Adv. Chem. Ser.* **1964**, 43, 112-144.

(2.13) W. Li, A. Amirfazli, *Adv. Colloid Interface Sci.* **2007**, 132, 51-68.

(2.14) S. Walheim, M. Böltau, J. Mlynek, G. Krausch, U. Steiner, *Marcromolecules* **1997**, 30, 4995-5003.

(2.15) S. Y. Heriot, R. A. L. Jone, *Nat. Mater.* **2005**, 4, 782-786.

(2.16) R. P. Kusy, M. J. Katz, *J. Mater. Sci.* **1976**, 11, 1475-1486.

(2.17) A.D. Nikolov, D.T. Wasan, A. Chengara, K. Koczo, G.A. Policello, I. Kolossvary, *Adv. Colloid Interface Sci.* **2002**, 96, 325-338.

(2.18) B. S. Dunn, E. J. A. Pope, H. K. Schmidt, M. Yamane, *Proc. SPIE* **2000**, 3943, 280-284.

Chapter 3

3. Modeling Liquid Bridge between Surfaces with Contact Angle Hysteresis

3.1. Introduction

Compressing and stretching liquid bridges between two solid surfaces is a process commonly observed in many industrial areas, such as printing industry (ink transfer) and packaging industry (dispensing of glue) [1-4]. In nature, shorebirds trap and prey by compressing and stretching the liquid bridges inside their breaks [5]. Similar liquid bridges can also be observed in wet adhesion of insects such as beetles and blowflies [6-9]. When these insects attach to solid surfaces, micro liquid bridges are formed with secretory fluid between their attachment pads and the surfaces. These liquid bridges give rise to capillary forces that contribute to the adhesion of the insects to the surfaces [6-9]. Systematic studies of liquid bridge, such as the behaviors of a liquid bridge when it is compressed and stretched, and the adhesion force generated by the liquid bridge, are needed to better understand these phenomena.

A number of works have been done on the behavior of liquid bridges between two surfaces. Chadov and Yakhnin [10, 11] performed the pioneering studies on the transfer of a liquid drop from one surface to another. They suggested three possible regimes according to the dominant forces in the transfer process: quasi-static regime where surface forces dominate; dynamic regime where viscous forces dominate; and transition regime where both surface and viscous forces play important roles. They also established a simple theoretical model and used a dimensionless analysis to predict the liquid transfer ratio based on the surfaces' contact angles. However, this research focused on addressing liquid transfer between two surfaces each with a single given contact angle. Neither the adhesion force acting on the solid surfaces nor the effect of contact angle hysteresis (*CAH*) on the adhesion force and transfer ratio were systematic considered. Another study on the liquid bridge was done by Fortes [12], where a theoretical model was established to obtain the profiles of axisymmetric liquid bridges between two identical parallel plates. In this study, according to different boundary conditions, liquid bridges were classified as "*θ*" bridge (the plates were infinite and the contact angle θ were specified at the liquid-plate boundaries) and "*r*" bridge (the plates were circular and of radius *r*, and the liquid-plate contact lines were pinned at the edge of the plates), and the profiles of liquid bridges in both cases were obtained at given separation between the plates. Qian and Gao [13] built a theoretical model to simulate the stretching of a liquid bridge between a fibril with a given radius and a substrate. Because of the finite size of the fibril, the contact line on the fibril is pinned ("*r* bridge") at its circumference when the separation is small. When the separation is large, the contact radius becomes smaller than the fibril radius and the liquid meets both solid surfaces at the corresponding contact angles ("*θ* bridge"). This study investigated how the liquid volume and surface contact angles alter the stress–separation behavior of the liquid bridge. Based on Qian and Gao's model, a new model was developed by Cheung and Sitti [14] which combines surface tension and dynamic viscous forces to predict the adhesion strength between surfaces that have micro patterned arrays of cylindrical pillars. In this research, the static adhesion force due to the liquid bridge under each pillar was obtained using the results from [13]. The relations between the adhesion strength and the pillar's diameter, edge to edge spacing, preload and contact time were discussed. In the work of Qian and Breuer [1] both theoretical analysis and experimental work was done to obtain the profiles of the liquid bridge with pinned contact line at one surface and fixed contact angle at the other surface during the bridge evolution. In their study, some potential effects of *CAH* on the behavior of liquid bridge were mentioned, but a systematic study was lacking. Hong *et al.* [15] studied the behavior of droplet between an acrylic glass surface and a superhydrophobic surface both experimentally and theoretically. They found that due to the *CAH* of the acrylic glass surface, the wetting behavior of the droplet can be divided into two regimes depending on the gap thickness at the end of the compression process, the contact line withdrawal regime and the contact line pinning regime. However, neither the effect of wettability of the other surface nor the adhesion force acting on the surfaces was systematically studied in this research.

As stated above, previous studies have typically neglected the effect of *CAH* which is a very important parameter in surface science and can influence the behavior of a liquid bridge during its compression and stretching. Ideally, according to the Young's equation, for a surface wetted by a liquid, only one stable contact angle exists between the liquid and the surface. However, in practice instead, a range of contact angles can be found which has been attributed to roughness or heterogeneity of the solid surface [16-19] or change of solid-liquid interfacial energy upon wetting [20]. *CAH* is the difference between the values of upper limit and lower limit for the contact angles seen for a system. The upper bound of this range is called the advancing contact angle (θ_a) which is the value of the contact angle when the contact line starts to expand. The lower bound is named as the receding contact angle (θ_r) which is the value when the contact line starts to shrink/recede [18, 19]. When a liquid bridge is being compressed or stretched between two surfaces, the contact line can expand, shrink, or remain pinned during the process. This indicates that the values of the contact angles at the surfaces are not necessarily constant but can change between their advancing and receding values. Therefore, it is of interest to study how *CAH* affects the profile change of the liquid bridge and the generated adhesion force.

This study models the quasi-static compressing and stretching of a liquid bridge formed between two solid surfaces that have *CAH*. Both symmetric and asymmetric liquid bridges were analyzed and the effects of *CAH* on the liquid bridge profile, the adhesion force and the energy cost during a loading cycle are discussed. In the following, the theoretical model and numerical method to solve the developed boundary value problem are presented first. Afterwards, the findings based on the new model are demonstrated. Potential implications of the findings in practical applications are then discussed. Conclusions are given in the last section.

3.2. Model Development

3.2.1 Formulation

Figure 3.1 shows the schematic of an axisymmetric liquid bridge in equilibrium formed between two solid surfaces. Here R_1 and R_2 are the two contact radii on the surfaces; H is the separation between the two surfaces. θ_1 and θ_2 are the upper and lower contact angles, respectively. A quasi-static process is considered where the liquid bridge is first compressed and then stretched by adjusting the separation H. Such a process is shown in Figure 3.2. The compression stage (loading) is shown in Figure 3.2a-b, where H_0 is used to denote the initial separation at the beginning of the compression stage. The separation at which the compression is stopped, is denoted as H_{min} (Figure 3.2c). The upper surface is then retreated (unloading) and the liquid bridge is stretched until the separation returns to its initial value. In the following, we develop a system of ordinary differential equations and boundary conditions from which the equilibrium shape of the liquid bridge can be numerically obtained at any given H during the process. Different from the previous models, both contact lines in the upper and lower surfaces are allowed to move when the associated contact angles reach their advancing or receding values. When the contact angles are between their advancing and receding values, the contact lines are pinned while θ_1 and θ_2 adjust to accommodate the changes in H. Through this model, we can demonstrate how *CAH* contributes to the behavior of liquid bridge during the loading-unloading cycle and to the adhesion force between the two surfaces that arises from the presence of the liquid.

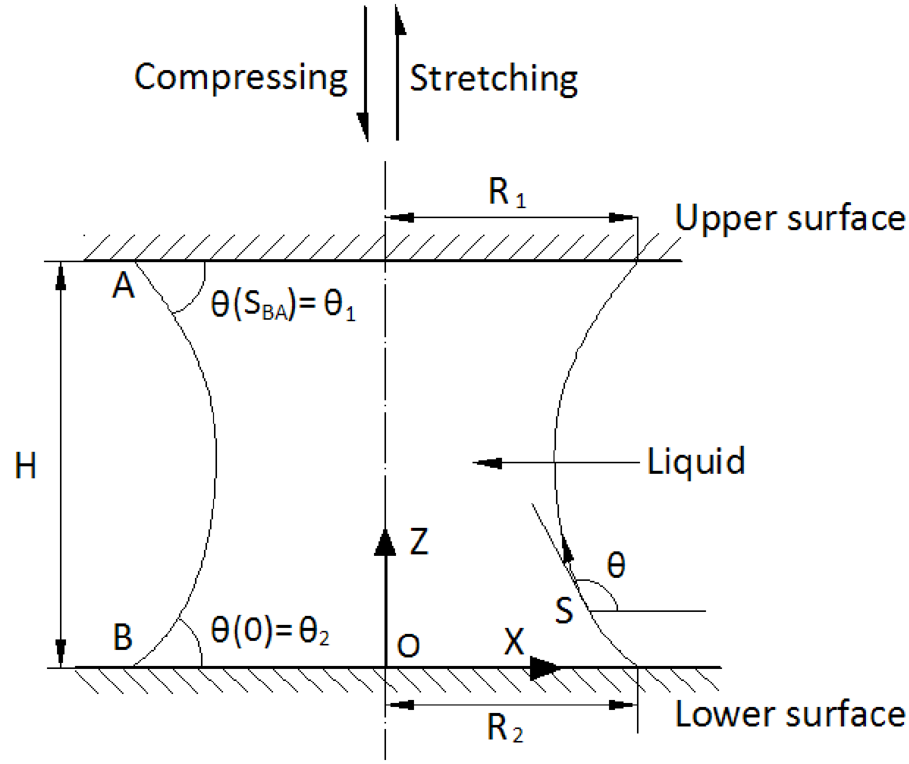

Figure 3.1: Geometry and coordinate system of a liquid bridge in equilibrium between two solid surfaces. 0

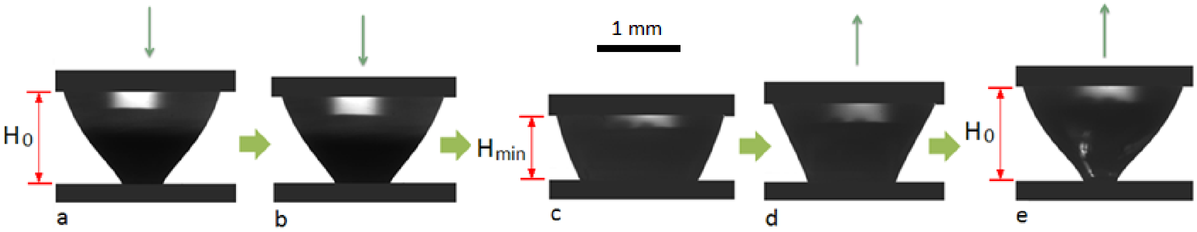

Figure 3.2: Process of quasi-statically compressing and stretching a liquid bridge between two surfaces. (a) and (b): Compressing; (c): Minimum separation; (d) and (e) : Stretching. H_0=1.16mm, H_{min}=0.80mm.

In deriving the equations governing the shape of the liquid bridge, the following assumptions are made. Firstly, both the upper and lower surfaces are assumed to be flat and homogeneous, and each surface has a unique advancing contact angle θ_a and receding contact angle θ_r. Secondly, only small liquid drops with a volume on the order of microliters are considered. Such liquid drops have small Bond numbers (Bo) and therefore the effect of gravity is negligible [14, 21]. Finally, it is assumed that there is no evaporation during the loading-unloading cycle and that the liquid being compressed and stretched is incompressible. The result of this assumption is that the volume of the liquid remains constant during the process. The equilibrium profile of the liquid bridge can be described by the following system of ordinary differential equations

$$\frac{dX}{dS} = cos\theta \qquad (3\text{-}1)$$

$$\frac{dZ}{dS} = sin\theta \qquad (3\text{-}2)$$

$$\frac{d\theta}{dS} = \frac{\Delta P}{\gamma} - \frac{sin\theta}{X} \qquad (3\text{-}3)$$

Equations (3-1) and (3-2) are simple geometric relations while equation (3-3) is obtained from the Young-Laplace equation [22, 23]. As shown in Figure 3.1, X and Z are the coordinates of the axisymmetric liquid bridge, S is the arc length measured from the contact point of the liquid with the lower surface, and θ is the angle between the local tangent of the liquid surface and the horizontal axis; ΔP is the Laplace pressure, which is the pressure difference between the inside and outside of the liquid; γ is the surface tension of the liquid. Since the liquid is in equilibrium and the effect of gravity is negligible, ΔP is constant within the liquid bridge, i.e., it is independent of S.

Equations (3-1)-(3-3) are three first order ordinary differential equations that require three boundary conditions. However, it should be noted that ΔP is not known a priori and is part of the solution. In addition, given the separation, H, the length of the curve S_{BA} is also an unknown that needs to be found as a part of the solution. Therefore, five boundary conditions are needed to solve the boundary value problem. Three of these boundary conditions are given by

$$Z(0)=0 \qquad (3\text{-}4)$$

$$Z(S_{BA})=H \qquad (3\text{-}5)$$

$$\int_0^H \pi X^2 dZ = V \qquad (3\text{-}6)$$

Here, V is the volume of the liquid, being constant for all H. Because in our model the effect of *CAH* is considered, the contact angle between the liquid and the two surfaces are not constant during the loading process. Therefore, the remaining two boundary conditions are given in terms of either contact angle or contact radius on each surface. Specifically, one additional boundary condition on the lower surface is given either by

$$R(0)=R_2 \qquad (3\text{-}7)$$

or by

$$\theta(0)=\theta_2 \qquad (3\text{-}8)$$

Similarly, another boundary condition on the upper surface is given either by

$$R(S_{BA})=R_1 \qquad (3\text{-}9)$$

or by

$$\theta(S_{BA})=\theta_1 \qquad (3\text{-}10)$$

On each surface, when the contact angle is between its advancing and receding values, the contact line is pinned (as it is observed in experiments, see the Results and Discussion Section of this chapter), allowing the contact radius to be taken as the boundary condition. When the contact radius starts to change, the contact angle should be either of its advancing or receding values, which is used as the boundary condition. Therefore, four possible situations exist: Case 1. Both the upper and lower contact lines are pinned (equations (3-9) and (3-7)); Case 2. Upper contact line is pinned and lower contact angle remains constant (equations (3-9) and (3-8)); Case 3. Upper contact angle remains constant and lower contact line is pinned (equations (3-10) and (3-7)); Case 4. Both upper and lower contact angles are constant (equations (3-10) and (3-8)). During the loading process, at each H, which case will be used to solve the liquid bridge profile is determined by checking the contact angles at both surfaces. Solving the governing differential equations (3-1)-(3-3) along with the five boundary conditions (equations (3-4)-(3-6) and two additional boundary conditions as specified above) completely determines the functions *X(S)* and *Z(S)*, which specifies the shape of the liquid bridge.

Once the profile of the liquid bridge is obtained, the adhesion/capillary force can be calculated based on the contact radius, Laplace pressure, and contact angle. The total vertical adhesion (or capillary) force (denoted as F) acting on each surface has two components [13]. One is from the surface tension force acting at the contact line. The other is caused by the Laplace pressure. The magnitude of F is given by [13]:

$$F = 2\pi\gamma R_1 \sin\theta_1 - \pi R_1^2 \Delta P \qquad (3\text{-}11)$$

Here, a positive F means the surfaces are attracted by the liquid bridge, while negative F suggests repulsion. During the loading process, the work done by the vertical adhesion/capillary force F can be obtained from the following equation:

$$W=\int F dH \qquad (3\text{-}12)$$

3.2.2 Numerical method

Figure 3.3(a) shows the procedure of obtaining the liquid bridge profiles during a loading process where the separation H is gradually changed. To start, H, θ_1, and θ_2 are set to their initial values. The contact angle at each surface is compared with its advancing and receding values to determine which of the four cases identified in the Formulation Section should be chosen to solve the boundary value problem at the initial $H = H_0$. With H, V, and all boundary conditions specified, equations (3-1)-(3-3) can be solved using the shooting method (details given later) and the profile of the liquid bridge at $H = H_0$ can be obtained along with the two unknowns ΔP and S_{BA}. Next, a small change is introduced in H (increment in the stretching stage and decrement in the compression stage). Meanwhile, the contact angles of the liquid profile obtained in the previous step is checked to determine whether the contact line will advance, recede, or remain pinned in the next step. This determines the boundary conditions to be used in the next step and the liquid bridge profile is solved again (i.e. equations (3-1)-(3-3)) at the new separation. The procedure is repeated until H reaches its minimum value H_{min} (during compression or loading) or its initial value H_0 (during stretching or unloading). Because whether the contact line will advance, recede, or remain pinned at a given H is determined from the solution in the previous step (at a slightly different H), after the liquid profile is obtained at the present H, the solution is checked for self-consistency. Thus, the resulting contact angles and contact radii at both surfaces are checked to be consistent with the boundary conditions used to solve the boundary value problem. For example, if the receding contact angle at the upper surface was used to calculate the profile of the liquid bridge, the resulting contact radius at the upper surface should not be larger than its value in the previous numerical step. If this is not satisfied after solving the boundary value problem, then it implies that at the upper surface the contact line has the tendency to move outward and the contact angle has the tendency to increase. The boundary condition on the upper surface is then changed to constant radius (equation (3-9)) allowing the contact angle to increase and the boundary value problem is solved again.

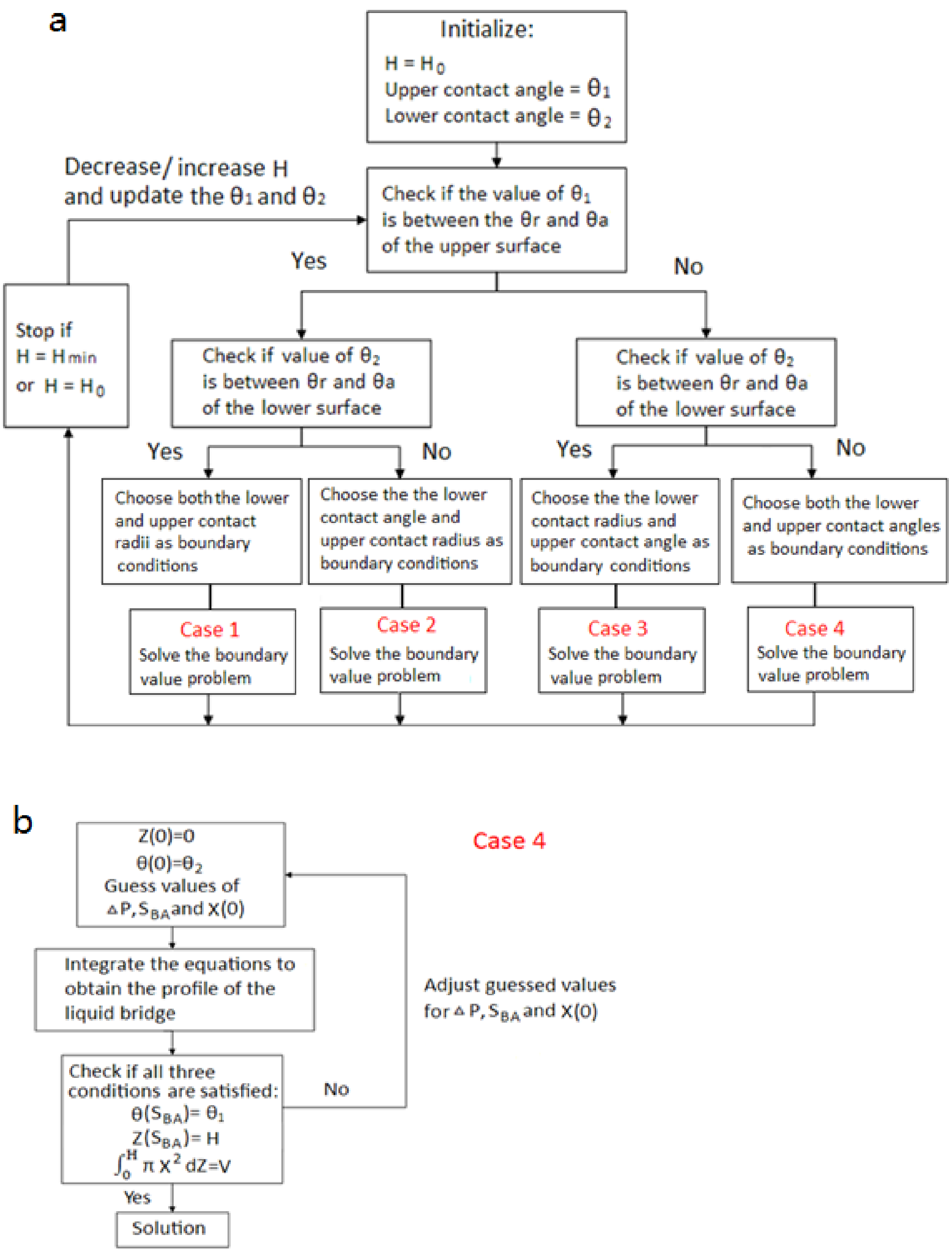

Figure 3.3: (a) Flow chart of how to determine the liquid profile during a process where H is gradually changed. (b) Example of Case 4, where shooting method is used to solve a given boundary value problem. The approach to solve for Cases 1, 2 and 3 are similar to Case 4.

When a specific boundary value problem is prescribed (one of the four cases), the shooting method is used to numerically obtain the liquid profile in terms of $X(S)$, $Z(S)$ and $\theta(S)$. Figure 3.3 (b) shows the numerical scheme using Case 4 as an example. In this case, the five boundary conditions are $Z(0)=0$, $Z(S_{BA})=H$, $\int_0^H \pi X^2 dZ = V$, $\theta(0)=\theta_2$, and $\theta(S_{BA})=\theta_1$. To be able to integrate equations (3-1) to (3-3), the boundary value problem is converted to an initial value problem by making guesses for $X(0)$, S_{BA}, and ΔP. Along with $Z(0)=0$ and $\theta(0)=\theta_2$, equations (3-1)-(3-3) can be integrated to obtain $X(S)$, $Z(S)$, and $\theta(S)$. The other three conditions $Z(S_{BA})=H$, $\int_0^H \pi X^2 dZ = V$, and $\theta(S_{BA})=\theta_1$ are then checked with the obtained solution to see if they are satisfied with the guessed values of $X(0)$, S_{BA}, and ΔP. If not, $X(0)$, S_{BA}, and ΔP are adjusted and the equations are solved again to find the liquid profile so that $Z(S_{BA})$, $\int_0^H \pi X^2 dZ$, and $\theta(S_{BA})$ are closer to their target values. The iteration continues until given convergence criteria ($|Z(S_{BA}) - H| < 10^{-6}$mm, $\left|\int_0^H \pi X^2 \, dZ \; - V\right| < 10^{-6}$μL, and $|\theta(S_{BA}) - \theta_1| < 10^{-6}$) are satisfied.

3.3 Results and Discussion

In the Appendix B, through a normalization of the boundary value problems, it can be shown that when the effect of gravity can be neglected (*Bo* smaller than 1), all lengths that describe the shape of the liquid bridge scale with $\sqrt[3]{V}$. In the following, a particular liquid volume V=2 μl was used for all calculations, but all the characteristics discussed below apply to other liquid volumes as well. In addition, all calculations were performed for water with a surface tension of 72mN/m.

3.3.1 Model Verification

Before performing a systematic numerical study with the current model, the results generated from it were compared with experimental data to test its validity. In particular, we carried out an experiment where a 2 μl water drop (surface tension γ = 72mN/m) was placed between two surfaces (upper surface: PMMA, θ_r=59.4°, θ_a=74.9°; lower surface: spin coated Teflon AF, θ_r=107.5°, θ_a=121°; details of preparation can be found in Chen et al. [24]) to form a liquid bridge. In order to satisfy the quasi-static condition, the water bridge was compressed and stretched with a very low speed (0.001mm/s). H_0 and H_{min} were, respectively, 1.16mm and 0.65mm in the experiment. Simulation using the developed model was performed using the same initial separation, contact radii, and contact angles (measured from the images taken in the experiments). Figure 3.4 shows the comparison between model prediction and experimental data on the values of the contact angle and contact radius on the PMMA surface during the process. It can be seen that the simulation results (lines) match the experimental results (symbols) very well. During the experiment test, approximately 6-8% of the liquid was evaporated into the air. This is the reason that the values of the contact radius from our model were slightly larger than the experimental results at the end of the stretching stage in Figure 3.4. The liquid bridge was formed at point A. At this point the contact angle on the PMMA surface was between its advancing and receding values, which resulted in the contact radius being pinned at the beginning of the compression stage. After the contact angle reached θ_a (point B), it remained constant while the contact line began to expand until H reached the minimum separation H_{min} (point C). In the stretching stage where H increased from point C, similar to the compression stage, the contact line did not move inwards until the contact angle reached θ_r (point D).

Afterwards, the contact radius started to shrink with contact angle being fixed at θ_r until H=0.98mm (point E). This radius is the minimum contact radius (denoted as R_{min} hereafter) that was obtained in the process. After point E, instead of remaining at θ_r, the contact angle started to increase till H returned to its initial value. It should be noted that the contact radius and contact angle changes on the PMMA surface were also affected by the Teflon AF surface (lower surface). Specifically, between points B and C in the compression stage, there exists a point (point 1, see Figure 3.4) at which the contact angle on the Teflon AF surface reached its advancing value and this resulted in a kink in the contact radius curve for the PMMA surface. Again in the stretching stage (between points C and D), when the contact angle on the Teflon AF surface reached its receding value a kink (point 2, see Figure 3.4) was found in the contact angle curve for the PMMA surface. Similar comparisons were done for several different H_0 and H_{min} values and good agreement was found in all cases.

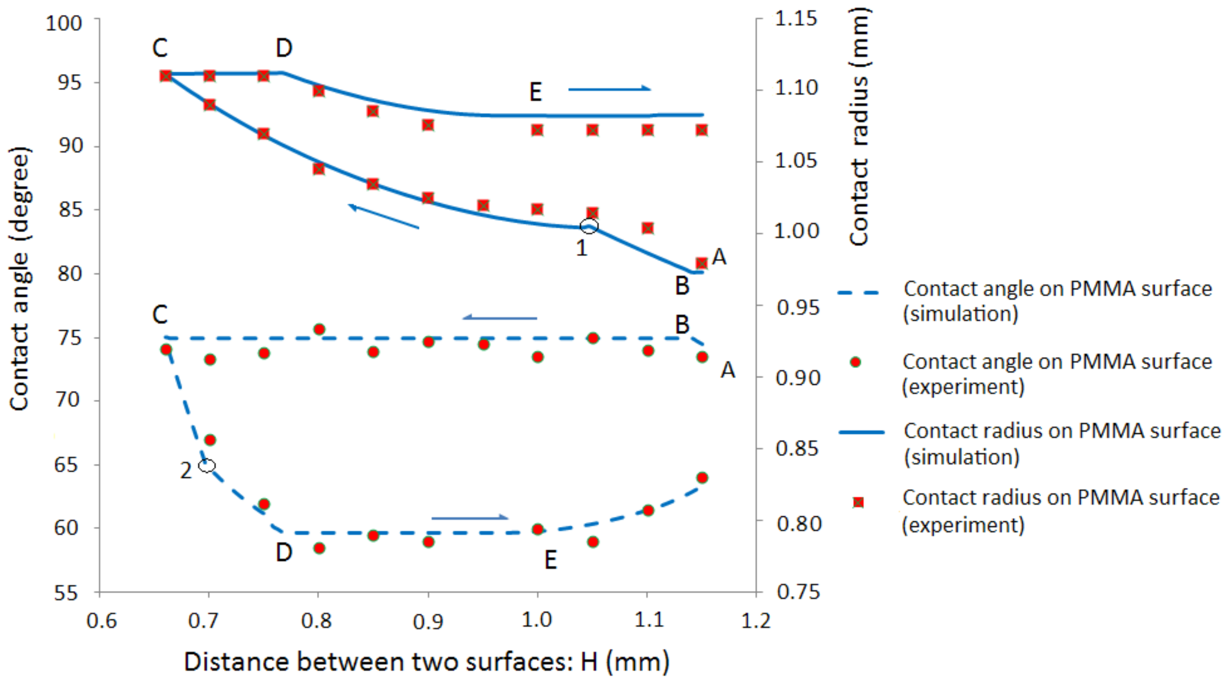

Figure 3.4: Comparison between experimental and simulation results for the contact angle and contact radius of a liquid bridge. The results shown are for PMMA surface (the lower surface was Teflon AF). The liquid was water. The liquid bridge was formed at point A.

In addition to validating the model against experiments, we also made comparison between our results and those available in the literature. Since previous models did not consider *CAH*, precautions were taken before doing the comparison. For the comparisons made with the cases that have a pinned contact line, we assigned a very large *CAH* which effectively led to a fixed contact radius. For the cases that allowed the contact lines to move at fixed contact angles, a very small *CAH* was set in our calculation. The results showed good agreement between our results and literatures [1], which provides additional evidence for the validity of our model (For more information, see Figures B.2 and B.3 in Appendix B).

With the validated model, we now examine the behaviors of the liquid bridge under the effect of *CAH*. First, a symmetric liquid bridge formed between two identical solid surfaces will be discussed. Then, the situation involving an asymmetric liquid bridge between two different surfaces will be addressed.

3.3.2 Liquid bridge between two identical surfaces

3.3.2.1 Overall behavior of liquid bridge

To facilitate the discussion, the average wetting angle (θ_{avg}), defined as the average value of the advancing and receding contact angles, will be used and it serves as a proxy for the equilibrium surface contact angle. Since the two solid surfaces are identical, the contact angle and contact radius at the two surfaces are the same at all *H*. Figure 3.5(a) shows the values of contact angle and contact radius versus *H* for a liquid bridge between three pairs of identical surfaces (Surface A: θ_r=θ_a=60^o, *CAH*=0^o; surface B: θ_r=50^o, θ_a=70^o, *CAH*=20^o; surface C: θ_r=40^o, θ_a=80^o, *CAH*=40^o.) which have the same θ_{avg} but different *CAH*. Without the *CAH*, for both the contact angle and contact radius curves, the compression and stretching curves coincide. However, with *CAH*, the values of contact angle and contact radius are different between the compression stage and the stretching stage at the same H, and the difference increases with the increase of *CAH*. The difference implies that the liquid bridge can possess two different equilibrium profiles at the same *H*, one in the compression stage and the other in the stretching stage. This is demonstrated in Figure 3.5(b) where both snapshots are the liquid bridge profile between two surfaces C at H=0.9mm, C1 during compression and C2 during stretching. The liquid bridge at C1 has the contact angle of 80^o which is the value of the advancing contact angle, while the liquid bridge at C2 has the contact angle of 40^o which is the value of the receding contact angle. The different liquid bridge profiles can lead to the difference in the adhesion force acting on the surface during compression and stretching, as well as energy cost during a loading-unloading cycle (discussed later).

One interesting observation made from Figure 3.5(a) is that at the end of the stretching stage, after the contact radius decreases to a certain value, the contact line stops shrinking and becomes pinned while the contact angle starts to gradually increase from the receding contact angle. This phenomenon can always be observed for liquid bridge between two identical hydrophilic surfaces (average contact angle smaller than 90^o), and it conforms with the observation of Qian *et al.*[1] that "for liquid bridge with intermediate limiting wetting angles when the bridge elongates to a certain height contact line will stop moving while the contact angle grows above the receding angle." The constant contact radius at the final stage of the stretching process is referred to as R_{min} in this study. For a liquid bridge between surfaces with *CAH*, this R_{min} is a critical factor which can affect the contact angle and contact radius curves in the compression and stretching, as demonstrated in the section below.

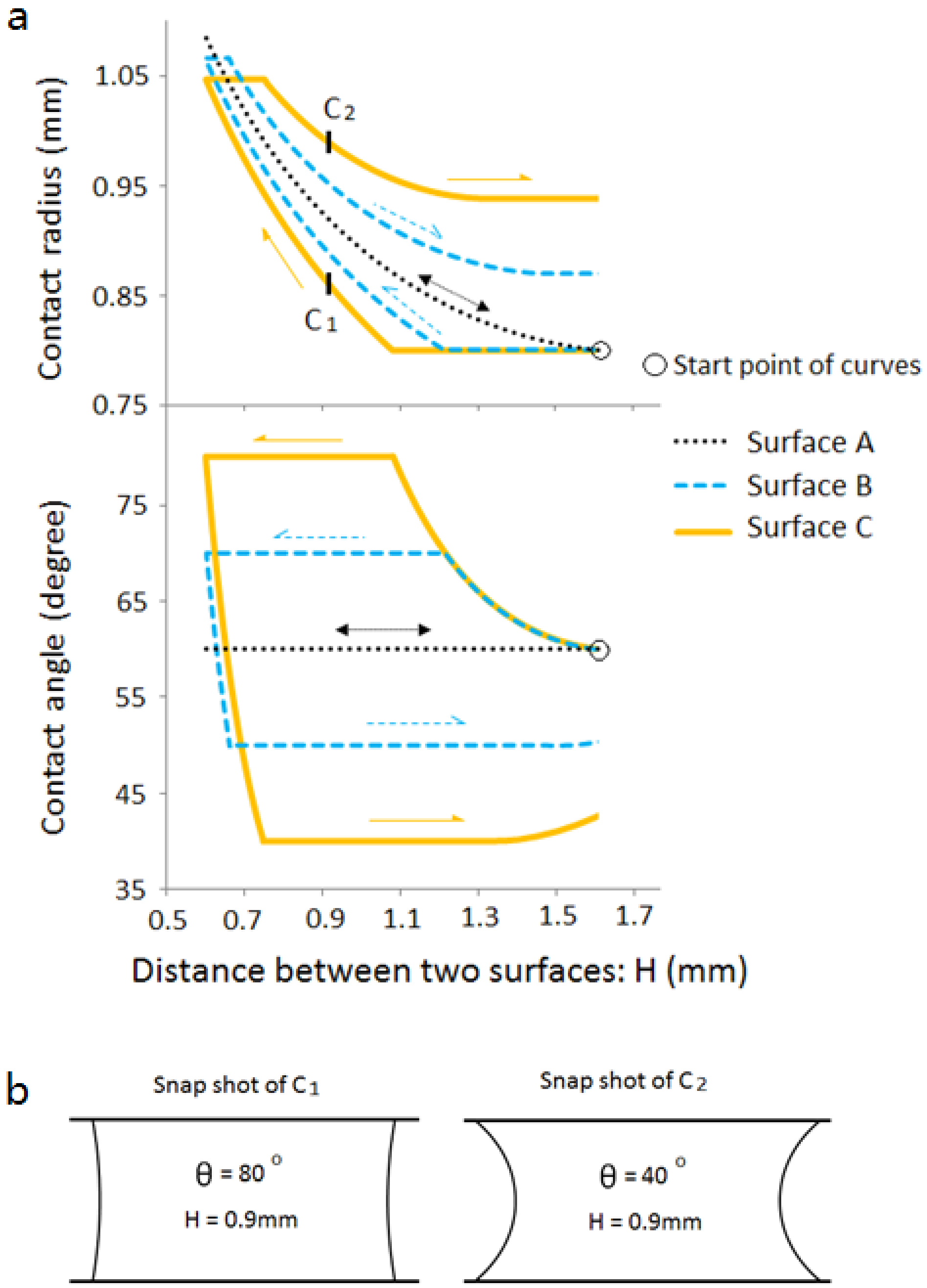

Figure 3.5: (a) Evolution of contact angle and contact radius with surface separation during symmetric compressing and stretching of a water drop between three pairs of identical surfaces. Surface A: $\theta_r=\theta_a=60^o$, $CAH=0^o$; surface B: $\theta_r=50^o$, $\theta_a=70^o$, $CAH=20^o$, surface C: $\theta_r=40^o$, $\theta_a=80^o$, $CAH=40^o$. (b) Snapshots of liquid bridge between two surfaces C. C1: during compression stage, $H=0.9$mm; C2: during stretching stage, $H=0.9$mm.

3.3.2.2 Effect of the minimum separation distance

For a liquid bridge between two surfaces without *CAH*, only one profile of the liquid bridge can be found at a specific *H*, and the compression and stretching of the liquid bridge is a reversible process. Therefore, the minimum separation H_{min} between the two surfaces cannot affect the behavior of the liquid bridge.

However, with *CAH*, it was found that the behavior of liquid bridge can be influenced by the value of H_{min}. This is demonstrated in Figure 3.6 for liquid bridges between two surfaces B (θ_r=50^o, θ_a=70^o, *CAH*=20^o) but with different H_{min}. The solid line, dashed line, dash-dotted line and dotted line have H_{min} of 0.5mm, 0.7mm, 0.97mm, and 1.1 mm, respectively. For the compression stage, all of the four curves coincide before reaching H_{min}. For the stretching stage, the solid line, dashed line and dash-dotted line also overlap with one another after the contact angle decreases to the receding contact angle. However, for the dotted line, in the stretching stage, the contact angle cannot decrease to its receding value (50^o), which leads to the contact radius being pinned during the entire stretching stage. The factor that determines whether a particular H_{min} can give rise to such phenomenon is the minimum contact radius R_{min} defined earlier. During the stretching stage, after the contact angle reduces to its receding value but before the contact radius decreases to R_{min}, the contact line will continue to move. Once the contact radius shrinks to R_{min}, the movement of the contact line stops and instead the contact angle begins to increase. Therefore, if in the compression stage, the value of H_{min} is such that at H_{min} the contact radius is still smaller than R_{min}, then when the liquid bridge is stretched, the contact angle will always be larger than the receding contact angle and the contact line will be pinned at all time. R_{min} can be influenced by both the volume of the liquid and the contact angles of the two surfaces. For example, R_{min} for the liquid bridge between two surfaces B with V=2 µl is 0.87mm. Shown in Figure 3.6, the contact radius will reach 0.87mm when the liquid bridge is compressed to an H value below 0.97mm. Different from the other three cases, the dotted line is the only case where the contact radius is larger than R_{min} at H_{min}, which leads to the contact line not moving during the entire stretching process.

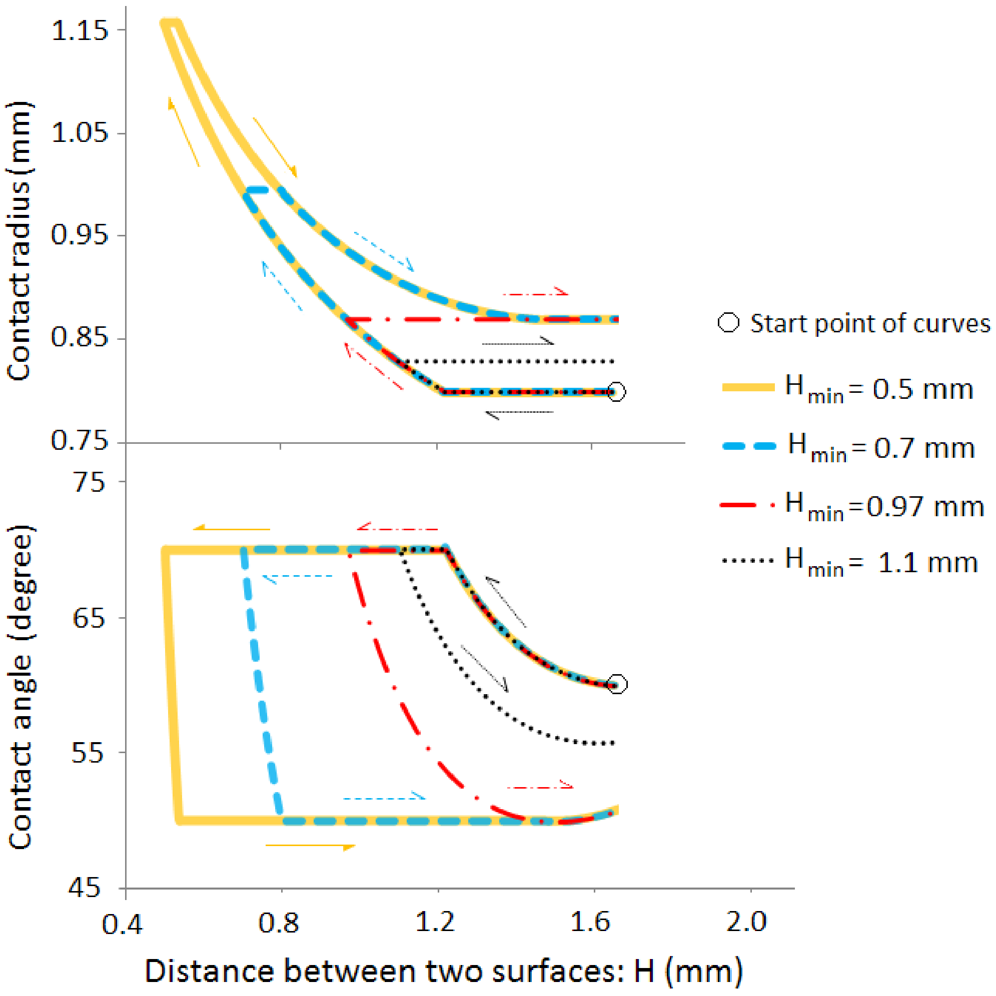

Figure 3.6: Evolution of contact angle and contact radius with surface separation during symmetric water compressing and stretching between two surfaces B (θ_r=50°, θ_a=70°, CAH=20°). The different curves are for different minimum separation H_{min}.

3.3.2.3 Adhesion/capillary force and energy cost due to *CAH*

Figure 3.7 shows the total adhesion/capillary force (*F*) generated by a 2μl liquid bridge between three pairs of identical hydrophilic surfaces (A, B and C as specified earlier) during a compression-stretching loading cycle. As seen in Figure 3.7, when a liquid bridge is formed between two hydrophilic surfaces, *F* generated by the liquid bridge always attracts the two surfaces, and it demonstrates complex non-monotonic relation with the separation *H*. Due to *CAH*, the liquid bridge has different shapes in the compression and stretching stages. As a result, the values of *F* are different at the same separation in the compression and stretching stages. With the same *H*, the contact radius in the stretching stage is larger than contact radius in compression stage; as well the Laplace pressure ΔP in the stretching stage is smaller than in the compression stage. Therefore, according to equation (11), *F* in the compression stage is smaller for all *H*. The peaks in these curves correspond to the maximum vertical adhesion force (F_{max}) during the loading cycle, and it can be influenced by *CAH*. For liquid bridge between hydrophilic surfaces without *CAH*, F_{max} is always found at H_{min}. However, with *CAH*, the maximum adhesion force instead of occurring at H_{min}, is seen at the stretching stage when the contact angle changes from the advancing to the receding value.

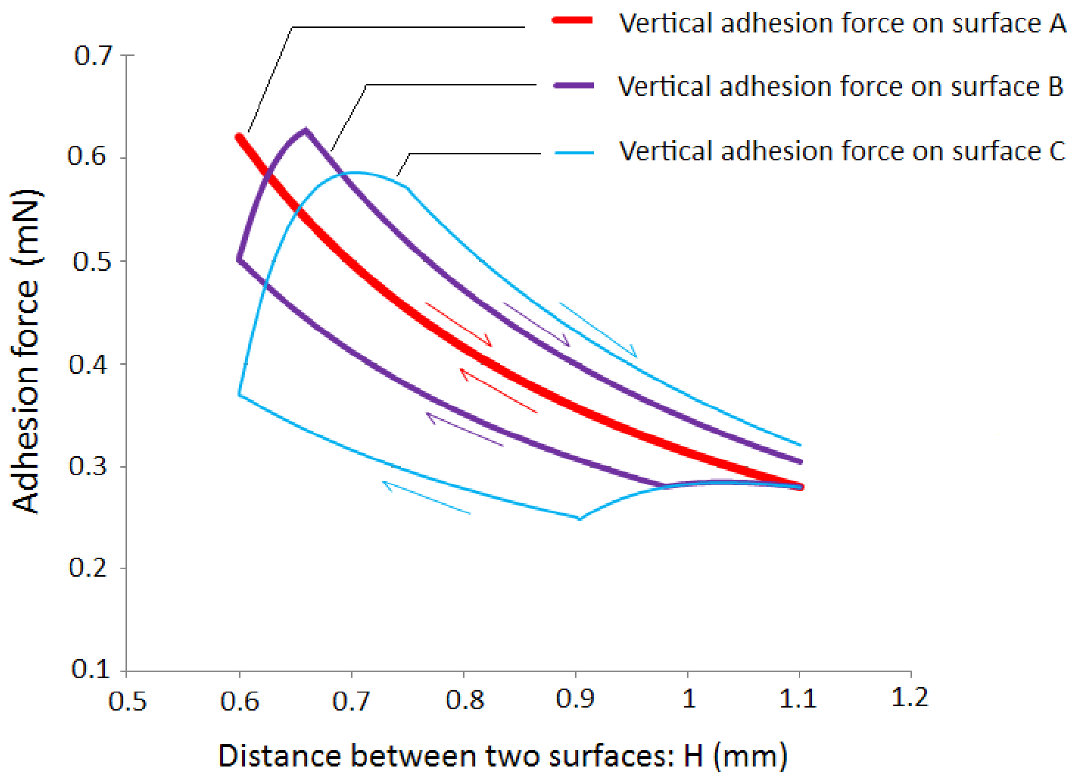

Figure 3.7: Vertical adhesion/capillary force versus surface separation for symmetric compressing and stretching of a water bridge between three pairs of identical surfaces. Surface A: $\theta_r=\theta_a=60^o$, $CAH=0^o$; surface B: $\theta_r=50^o$, $\theta_a=70^o$, $CAH=20^o$; surface C: $\theta_r=40^o$, $\theta_a=80^o$, $CAH=40^o$.

The effect of CAH on the magnitude of F_{max} is summarized in Figure 3.8, where F_{max} is plotted as a function of θ_{avg} during a compressing-stretching cycle between two identical surfaces. The solid line corresponds to two identical surfaces without CAH, and the four dash lines represent the cases involving two identical surfaces with different values of CAH. In this plot, H_{min} is fixed at 0.6mm, and all the processes start and end at H_0=1.1mm. At the start point, the contact angles at both surfaces are assigned to be θ_{avg}. As the solid line shows, F_{max} decreases when the surfaces become more hydrophobic (lower surface energy). F_{max} on surfaces with θ_{avg} of 90^o is only 25% of F_{max} on surfaces with θ_{avg} of 30^o. Such difference becomes smaller as CAH increases. For example, for surfaces with 40^o CAH, F_{max} on surfaces with $\theta_{avg} = 90^o$ is 55% of F_{max} on surface with θ_{avg} = 30°. Another interesting observation made from Figure 3.8 is that for small and intermediate θ_{avg} (in this case smaller than 55°), increasing *CAH* decreases F_{max}. However, for large θ_{avg} (in this case above 70°), F_{max} increases as *CAH* becomes greater. To explain this observation, we note that when θ_{avg} is large, increasing *CAH* allows the receding contact angle to decrease, and the principal radii of curvature at F_{max} to decrease. From the Young-Laplace equation, the magnitude of the Laplace pressure at F_{max} increases, hence leading to increase in F_{max}. When θ_{avg} is small, increasing *CAH* also decreases the receding contact angle. However because the receding contact angle is now very small, the constant volume constraint requires F_{max} to occur at a much larger separation distance *H* compared with the case without *CAH*. As the result, the principal radii of curvature at F_{max} are larger compared with the case of no *CAH*, and the magnitude of Laplace pressure is smaller. Therefore, F_{max} decreases as *CAH* increases.

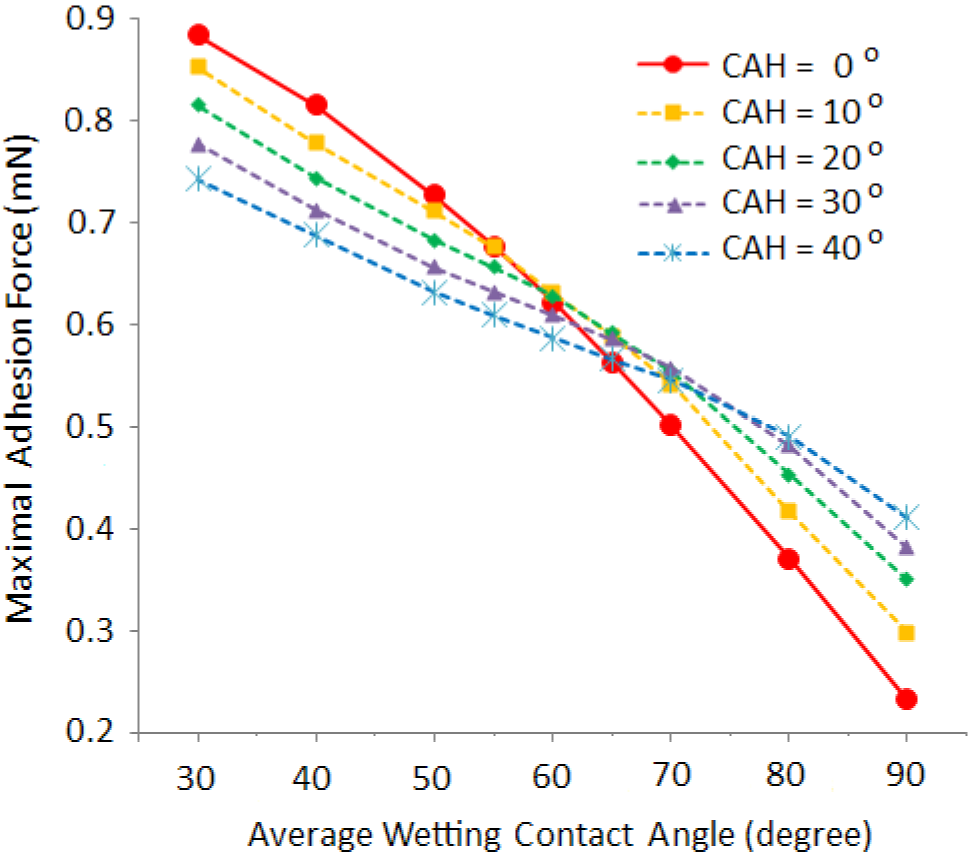

Figure 3.8: Maximum adhesion/capillary force as a function of the average wetting angle during the liquid compressing and stretching. H_{min} is fixed at 0.6mm, and all the processes both start and end at H_0=1.1mm. Lines are to guide the eyes.

The work done on the system during a quasi-static loading of the liquid bridge is the area under the curve relating the adhesion force and the surface separation. Positive work is done during stretching while negative work is done during compression. The net work or energy consumed during a compression-stretching cycle can then be calculated by evaluating the area enclosed by the force-separation curve for the loading cycle. Figure 3.9 shows, as functions of θ_{avg} and for different CAH, the work W_s done on the system during stretching and the negative of the work W_c done on the system (or the work done by the system) during compression. The energy cost during the loading cycle ($\Delta W = W_s - W_c$) is also shown in Figure 3.9. As the plot shows, both W_c and W_s decrease with the increase of θ_{avg}. However, the difference between W_s and W_c (ΔW) increases with the increase of θ_{avg}. Considering CAH, for liquid bridge between surfaces with the same θ_{avg}, W_c decreases monotonically with the increase of CAH. However, similar to F_{max}, W_s decreases with CAH when θ_{avg} is small (see the zoom-in picture in Figure 3.9) but increases with CAH when θ_{avg} is large (above 50^o). ΔW also increases with the increase of CAH for the surfaces with the same θ_{avg}. The ratios of ΔW of surfaces with different CAH are not significantly affected by θ_{avg}. For example, for θ_{avg} between 30^o and 90^o, $\Delta W_{CAH=10}/\Delta W_{CAH=40} = 0.316 \pm 0.0135$, and $\Delta W_{CAH=30}/\Delta W_{CAH=40} = 0.816 \pm 0.0118$.

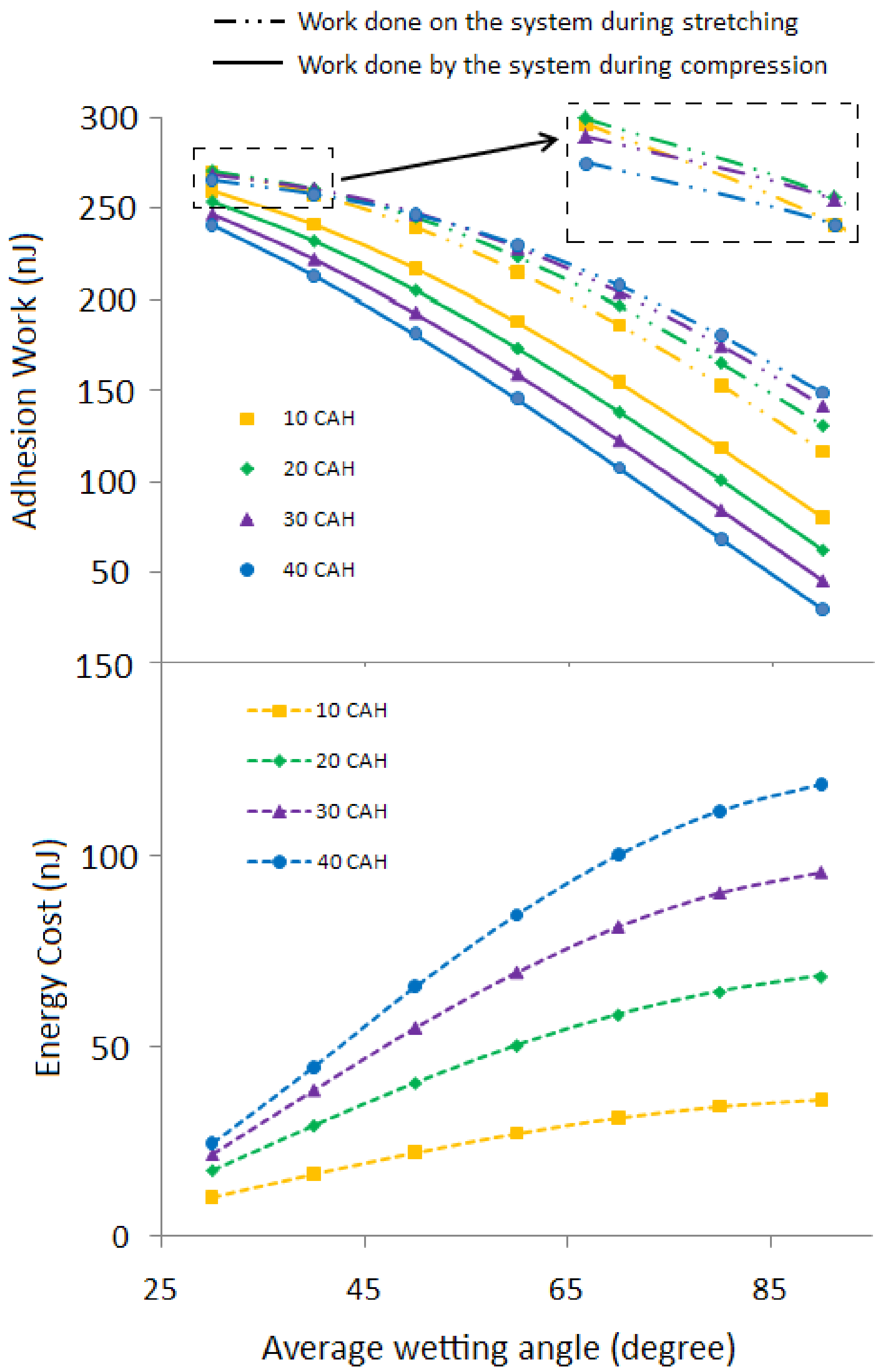

Figure 3.9: Adhesion work and energy cost for liquid bridge compressing and stretching as a function of the average wetting angle. H_{min} is fixed at 0.6mm, and all the processes both start and end at H_0=1.1mm. Lines are to guide the eyes.

3.3.3 Liquid bridge between two different surfaces

For a liquid bridge between two different surfaces, similar features about energy cost and adhesion force can be observed as those between two identical surfaces. Due to *CAH*, the liquid bridge can also possess two different equilibrium profiles at the same H during the loading-unloading cycle. R_{min} also exists in the stretching stage and this can lead to H_{min} influencing the variation of the contact angles and contact radii during the stretching stage.

By comparing Figures 3.4 (two different surfaces) and 3.5 (two identical surfaces), several different features can be found in the behavior of a liquid bridge between two different surfaces. During the compression or stretching, the contact angles on different surfaces do not reach their advancing or receding values at the same time. As a result, kinks (like points 1 and 2 in Figure 3.5) can be found in the contact radius-separation and contact angle- separation curves. For a liquid bridge between two identical surfaces, R_{min} is observed on both surfaces. However, when two surfaces have a large difference in their θ_{avg}, R_{min} usually can only be observed at the surface which is more hydrophilic. For example, in the case of a liquid bridge between PMMA and Teflon AF surfaces, R_{min} is only observed on the PMMA surface (the data of contact radius and contact angle on the Teflon AF surfaces are shown in the Appendix B).

Figure 3.10 shows the energy cost associated with both symmetric and asymmetric liquid bridges with different θ_{avg}. The asymmetric liquid bridge in this plot is formed between two surfaces: one being the same as the surfaces in the symmetric case and the other with $CAH=0^{o}$ and having a constant contact angle equal to θ_{avg} in the symmetric case. H_{min} is fixed at 0.6mm, and all the processes both start and end at H_0 =1.1mm. It can be seen that the asymmetric curves have similar trend as the symmetric curves, namely that the energy cost increases with the increases of θ_{avg} and *CAH*. Because in the asymmetric case, one of the surfaces had no *CAH*, the associated energy cost in a loading cycle is only a fraction of the energy cost in the symmetric case. This fraction depends on *CAH* but is less sensitive to θ_{avg}. For example, for the 10^{o} *CAH* curves, the energy cost of the asymmetric liquid bridge is approximately 50% of the symmetric liquid bridge for all θ_{avg}, and for the 40^{o} *CAH* curves, the dotted line is approximately 32% of the dashed line; and this percentage decreases with the increase of *CAH*.

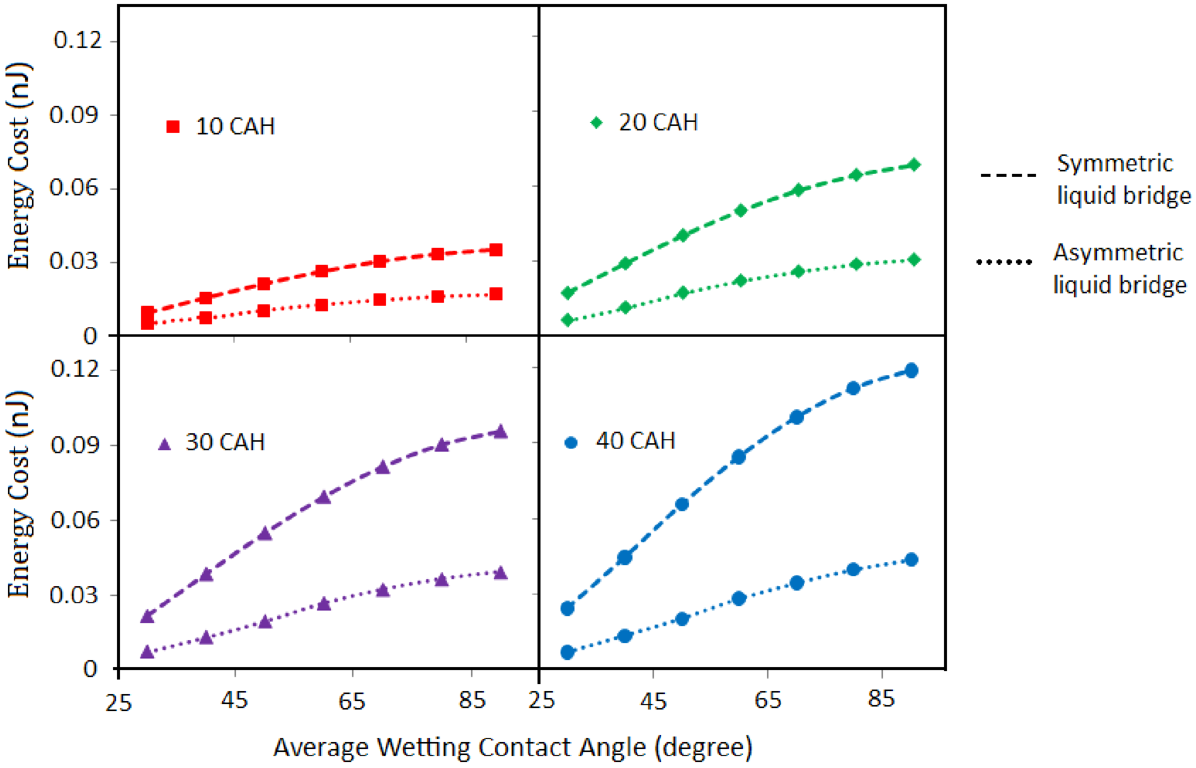

Figure 3.10: Energy cost for both symmetric and asymmetric liquid bridges as a function of the average wetting angle. Lines are to guide the eyes.

3.3.4 Behavior of liquid bridge during multiple compressing and stretching cycles

As shown in Figure 3.5, the final liquid bridge profile is different from the initial one after one loading and unloading cycle. It would be of interest to demonstrate the behavior of the liquid bridge for the next cycle as well. The behaviors of a 2 µl water bridge between surfaces D and E (surface D: θ_r=60^o, θ_a=80^o; surface E: θ_r=40^o, θ_a=60^o.) during three cycles of compressing and stretching are shown in Figure 3.11. It can be seen that the behaviors of liquid bridge in the second cycle are different from the first cycle in the compressing stage. These differences are caused by the different initial contact angle values between the first and second cycles. The initial contact angle values in the first cycle are θ_{avg} of the two surfaces (70^o for surface D, and 50^o for surface E), while the initial contact angle values in the second cycle are θ_r of the two surfaces (60^o for surface D, and 40^o for surface E). Therefore, before the contact angles on both surfaces increase to θ_a in the compressing stage, the values of contact angle and contact radius are different between the first and second cycles at the same *H*. After the second cycle the contact angles on both surfaces return to θ_r, and the behavior of the liquid bridge will not change with further increase of cycles.

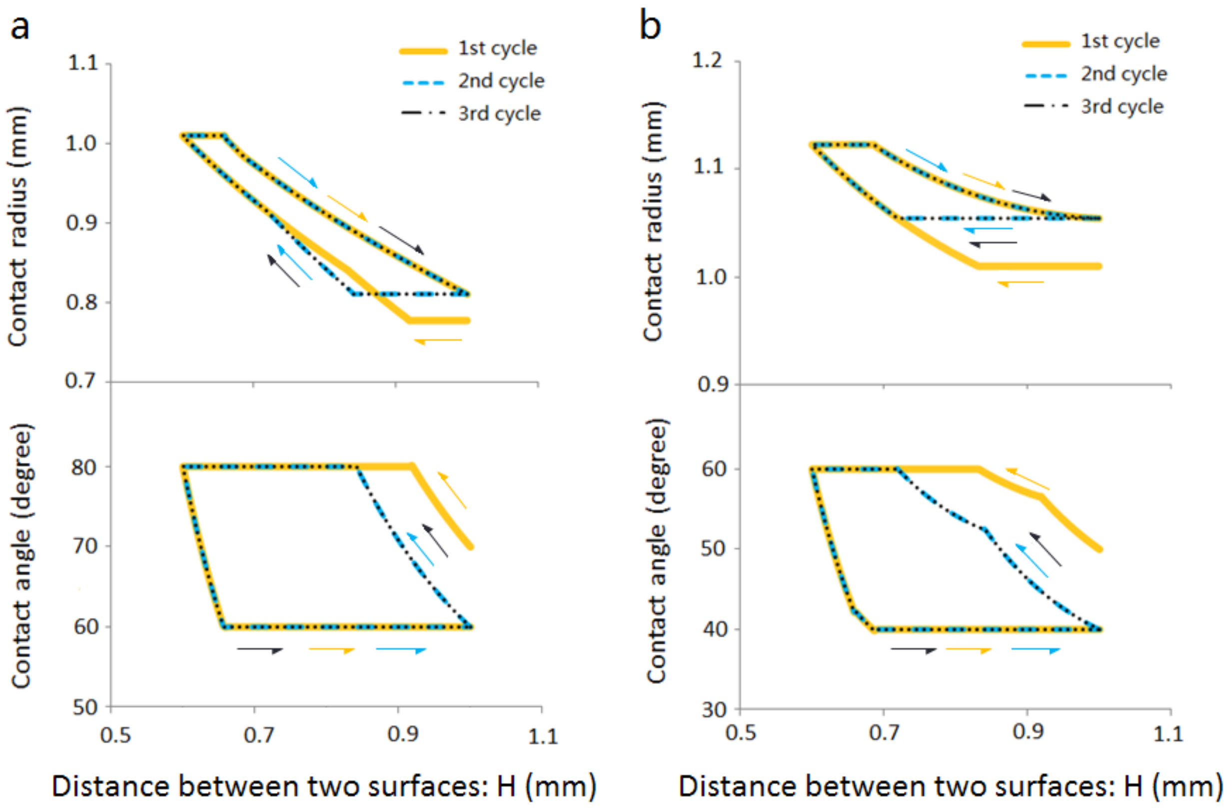

Figure 3.11: Evolution of contact radius and contact angle for a 2 μl water bridge during three cycles of symmetric compressing and stretching between two different surfaces (upper surface with $\theta_r = 60^o$, $\theta_a = 80^o$ and lower surface with $\theta_r = 40^o$, $\theta_a = 60^o$); $H_0 = 1.0$mm, $H_{min} = 0.6$. (a) Contact radius and angle on the upper surface. (b) Contact radius and angle on the lower surface.

3.4 Implications

3.4.1 Wet adhesion

The results from this work can be useful to wet adhesion systems. Compared with dry adhesion which is dominated by the van der Waals interactions, one of the advantages of wet adhesion is that it can usually take effect at larger scales [13, 25]. Dry adhesion become effective only when the two surfaces come into close contact, while due to the formation of liquid bridges, wet adhesion can be important for a large range of separations between the two surfaces. As shown in Figure 3.6, due to *CAH*, there exists a minimum contact radius R_{min} near the end of the stretching stage, and because of this, H_{min} can influence the process of compressing and stretching the liquid bridge. In particular, from Figure 3.6, it can be seen that the contact radius curve of H_{min} =1.1mm is different from the other three lines in the stretching stage. We also observed that during the stretching stage, the liquid bridge with H_{min}=1.1mm ruptures at a larger separation than the other three cases (data not shown); hence the effective range of interaction can affected by the H_{min}. Different from the contact angle or *CAH*, H_{min} is a factor independent of the surfaces' property. This suggests that for wet adhesion system, instead of changing the surfaces, H_{min} can be used to control the interaction range.

For a system consisting of a single liquid bridge, the maximum wet adhesion strength is dependent on F_{max}, which occurs during the stretching stage. As Figure 3.8 shows, for large wetting angles, F_{max} will increase as *CAH* becomes greater. However, for small wetting angles, F_{max} will decrease with the increase of *CAH*. Therefore, in wet adhesion systems involving a single liquid bridge, for surfaces with small contact angles, a small *CAH* can helps to achieve larger wet adhesion strength. For surfaces with large contact angles, the way of increasing the wet adhesion strength is to increase *CAH*. This conclusion is confirmed by the plot of adhesion energy. As shown in Figure 3.9, with a small θ_{avg}, the amount of work that needs to be done to separate the two surfaces decreases with the increase of *CAH*. When θ_{avg} becomes large, larger *CAH* can result in a larger W_s. For a liquid bridge during multiple loading and unloading cycles, as Figure 3.11 shows the behavior of liquid bridge in the stretching stage is not affected by the number of loading and unloading cycles. F_{max} of a wet adhesion system is always observed in the stretching stage. Therefore, the maximum strength of a wet adhesion system is not affected by cyclic loading, a significant advantage over typical dry adhesion systems where the adhesion strength reduces with number of loading cycles

3.4.2 Printing

The finding of the effects of CAH on F_{max} and W_s are also useful for ink transfer in the printing industry. In the printing industry, it is desirable to have a large amount of ink to be transferred from the substrate to the target surface at a small cost of energy. Smaller W_s and F_{max} are associated with easier transfer from one surface to another. For surfaces with small θ_{avg}, a larger CAH can be used to improve the ink transfer ratio, while for the surfaces with larger θ_{avg}, a smaller CAH is more beneficial.

Another interesting finding is that for liquid bridge between two surfaces having very different θ_{avg} value, R_{min} usually can only be observed on the more hydrophilic surface. This can be connected with the study of liquid transfer between two surfaces. The appearance of R_{min} suggests that at the end of the stretching stage, instead of receding, the contact radius will have a tendency to expand. If R_{min} is observed on both two surfaces, the contact radii on both surfaces would tend to expand, which has an adverse effect on liquid transfer. Therefore, in the quasi-static regime, in order to get a full liquid transfer, the two surfaces need to have very different θ_{avg} value.

3.5 Conclusions

A theoretical model was developed to describe a liquid bridge, between two solid surfaces that have contact angle hysteresis (*CAH*), undergoing quasi-static compressing and stretching. Different from the previous models, both contact lines in the upper and lower surfaces were allowed to move when the contact angles reach their advancing or receding values. When the contact angles are between their advancing and receding values, the contact lines are pinned while the contact angles adjust to accommodate the changes in separation. Through this model, it is found that with *CAH*, the liquid bridge can have two different equilibrium profiles at a given separation, one in the compression stage and the other in the stretching stage. This results in the adhesion force being different in the compression and stretching stages, and energy being consumed in the loading cycle. The minimum separation H_{min} between the two solid surfaces is a factor that can affect the behavior of liquid bridge during this process. By changing H_{min}, the effective interaction range of wet adhesion can be increased. The maximum adhesion force decreases for surfaces of higher hydrophobicity. This force also demonstrates interesting dependence on *CAH*. For liquid bridge between surfaces that have small contact angles, increasing *CAH* can decrease the maximum adhesion force. However, for liquid bridge between surfaces that have large contact angles, increasing *CAH* increases the maximum adhesion force.

Bibliography

(3.1) B. Qian, K. S. Breuer, *J. Fluid Mech.* **2011**, 666, 554--572.

(3.2) A. A. Darhuber, S. M. Troian, *J. Appl. Phys.* **2001**, 90, 3602--3609.

(3.3) H. W. Kang, H. J. Sung, T. M. Lee, D. S. Kim, C. J. Kim, *J. Micromech. Microeng.* **2009**, 19, 015025.

(3.4) D. Bonn, J. Eggers, J. Indekeu, J. Meunier, E. Rolley, *Rev. Mod. Phys.* **2009**, 81, 739--805.

(3.5) M. Prakash, D. Quere, J. W. M. Bush, *Science* **2008**, 320, 931--934.

(3.6) S. Gorb, *Proc. Roy. Soc. Lond. B* **1998**, 265, 747--52.

(3.7) T. Eisner, D. J. Aneshansley, *Proc. Natl. Acad. Sci.* **2000**, 97, 6568--6573.

(3.8) A. F. G. Dixon, P. C. Croghan, R. P. Gowing, *J. Expl. Biol.* **1990**, 152, 243--253.

(3.9) W. Federle, M. Riehle, A.S.G. Curtis, R.J. Full, *Integr. Comp. Biol.* **2002**, 42, 1100--1106.

(3.10) A. V. Chadov, E. D. Yakhnin, *Kolloidn. Zh.* **1979**, 41, 817.

(3.11) E. D. Yakhnin, A. V. Chadov, *Kolloidn. Zh.* **1983**, 45, 1183.

(3.12) M. A. Fortes, *J. Colloid Interface Sci.* **1982**, 88, 338--352.

(3.13) J. Qian, H. Gao, *Acta Biomaterialia* **2006**, 2, 51--58.

(3.14) E. Cheung, M. Sitti, *J. Adhesion Sci. Tech.* **2008**, 22, 569--589.

(3.15) S. J. Hong, T. H. Chou, S. H. Chan, Y. J. Sheng, H. K. Tsao, *Langmuir* **2012**, 28, 5606--5613.

(3.16) C. N. C. Lam, R. Wu, D. Li, M. L. Hair, A. W. Neumann, *Adv. Colloid Interface Sci.* **2002**, 96, 169--191.

(3.17) H. Tavana in *Applied Surface Thermodynamics*, 2nd ed.; A.W. Neumann, R. David, Y. Zuo, Ed.; Surfactant Sci. Series; CRC: Boca Raton, USA, 2010; 151, pp 315--316.

(3.18) E. Pierce, F. J. Carmona, A. Amirfazli, *Colloids Surfaces A* **2008**, 323, 73--82.

(3.19) E. L. Decker, B. Frank, Y. Suo, S. Garoff, S. *Colloids and Surfaces A* **1999**, 156, 177--189.

(3.20) T. H. Chou, S. J. Hong, S. H. Chan, Y. J. Sheng, H. K. Tsao, *Langmuir* **2012**, 28, 5158--5166.

(3.21) S. M. I. Saad, Z. Policova, A. W. Neumann, *Colloids Surfaces A* **2011**, 384, 442--452.

(3.22) V. S. Ajaev, G. M. Homsy, Annu. *Rev. Fluid Mech.* **2006**, 38, 277--307.

(3.23) A. W. Adamson, *Physical chemistry of surfaces*; Wiley: New York, 1997; pp 6--8.

(3.24) H. Chen, T. Tang, A. Amirfazli, *Colloids Surfaces A* **2012**, 408, 17--21.

(3.25) B. N. J. Persson, *J. Phys.: Condens. Matter*. **2007**, 19, 376110.

Chapter 4

4. Mechanism of Liquid Transfer between Two Surfaces and the Role of Contact Angles

4.1 Introduction

Liquid transfer between two solid surfaces is observed in a variety of applications, e.g. printing, packaging and micromachined fountain-pen technique [1-8]. In nature, vertebrates with incomplete cheeks must rely on their tongue to move water into the mouth. When cat laps, liquid adhering to the dorsal side of the tongue tip is drawn upward, forming a liquid bridge [9]. The value of the transfer ratio (volume of the liquid transferred onto acceptor surface over the total liquid volume) is important in such cases. Particularly in offset printing, a small amount of ink remaining on the donor surface can result in image quality defects. Considering the importance of the liquid transfer, a simple question can be asked, what factors control the liquid transfer ratio?

Two possible regimes exist for liquid transfer: 1) quasi-static regime in which transfer is dominated by surface forces; 2) dynamic regime where viscous and inertial force cannot be neglected [10, 11]. Transfer ratio in the quasi-static regime has been believed to be controlled by the contact angles (*CA*s) of the two surfaces [10-12]; e.g. for liquid transfer between two surfaces with similar *CA*s, the transfer ratio should be close to 50%. However, the definitions of the *CA*s in these studies are very vague. Aside from idealized surfaces, the *CA* between a liquid and a solid surface is not a unique value. A range of *CA*s exists due to roughness or heterogeneity of the solid surface; such phenomenon is called contact angle hysteresis (*CAH*). The advancing *CA* (θ_a) and receding *CA* (θ_r) are the upper and lower bounds of this range, respectively, and CAH is the difference between them [13]. Due to *CAH*, the *CA* during liquid transfer may not be constant and can be any value between θ_a and θ_r. Therefore, it is necessary to provide a clear understanding on the roles of θ_a, θ_r and *CAH* in determining the transfer ratio. Another traditional thought on the transfer ratio is that it is correlated with the adhesion force between the liquid and solid surfaces [14]; such correlation is thought to be especially important with the pull-off force (F_{pf}), the value of adhesion force just before the liquid bridge breaks. However, no systematic study was performed yet to prove this idea. Through a systematic experimental study accompanied by numerical simulations, this chapter aims at addressing the following questions for quasi-static liquid transfer: how does the transfer ratio depend on the *CA*s and *CAH* of the two surfaces? Are the transfer ratio and the adhesion force correlated? Answer to these questions will help us understand the governing mechanisms for quasi-static liquid transfer.

4.2 Method

Eleven different surfaces were used in this study, which were fabricated from the following materials: silicon, Poly (methyl methacrylate) (PMMA), Polystyrene (PS), Poly (ethyl methacrylate) (PEMA), Teflon AF and Octadecyltrichlorosilane (OTS). Several surface fabrication methods such as spin coating and heat press were used; for details see [15]. One surface, named PMMA (1), was used as the acceptor, which has $\theta_a = 72.6^o$ and $\theta_r = 60.3^o$. The other ten surfaces (shown in Table 4.1) served as donors and have a range of different θ_a and θ_r values (and consequently *CAH*). Detailed information on the surface fabrication and *CA* measurements is provided in the Appendix C.

Each liquid transfer was achieved by first compressing and then stretching a liquid bridge between two surfaces at a very low speed (see Figure 4.1). A 2µL distilled water drop was placed on the donor surface (Figure 4.1a). The acceptor surface was then moved down slowly till a liquid bridge was formed (Figure 4.1b). The separation between the two surfaces at this point is denoted as H_0 (initial separation). The liquid bridge was further compressed till the surface separation decreased to $H_{min} = 0.56$mm (Figure 4.1c). Then it was slowly stretched (Figure 4.1d). When the liquid bridge broke (Figure 4.1e), part of the liquid can be transferred to the acceptor surface. This experimental protocol deemed to represent the process seen in many applications. The acceptor surface was connected to a motion control system (ILS100CC and XPS-C6 from Newport) which provided 5µm/s movement during the whole process. Two perpendicular cameras (DR1-D1312 (IE)-200-G2-8 from Photon Focus and A312f from Basler) were used to capture the image of the liquid bridge. The vertical adhesion force between the liquid and the surfaces was measured by a force cell (F329 from Novatech) with a resolution of 0.005mN placed beneath the donor surface. Experiment for each pair of surfaces was repeated 3 times, and average values of the transfer ratio and adhesion force were calculated. Ambient temperature was controlled at 18±0.9°C. After the transfer, 8.1±1.32% vol. of the water was evaporated, the effect of evaporation considered negligible as good agreement between theoretical prediction and experiments were found (see below and Ref. 17). In our experiments, very small Capillary Number $Ca = \mu U/\gamma \sim O(10^{-7})$ and Weber Number $We = \rho U^2 R/\gamma \sim O(10^{-9})$, were found; U is velocity of the acceptor surface; R is the characteristic length, taken to be the contact radius on the donor surface when the liquid bridge forms; and γ, μ, ρ are respectively the surface tension, viscosity and density of the liquid. This indicates that the transfer was in the quasi-static regime. The effect of the gravity was also small, since the Bond Number was found to be $Bo = g\rho R^2/\gamma \sim O(10^{-2})$, where g is gravitational acceleration.

Table 4.1: Wetting properties of donor surfaces.

Case No.	Donor Surface	θ_a (degree)	θ_r (degree)
1	Silicon	55.1±0.67	45.7±1.23
2	PMMA(2)	71.9±0.70	52.7±1.54
3	PMMA(3)	72.8±0.93	57.9±0.86
4	Blend (1)	73.0±0.82	59.7±0.97
5	Blend (2)	79.4±0.73	63.9±0.94
6	PS (1)	88.6±1.43	66.0±1.27
7	PEMA	77.6±0.79	68.2±0.94
8	PS (2)	91.8±1.30	75.3±0.87
9	OTS	111.1±1.33	98.2±0.89
10	Teflon AF	126.4±1.30	116.4±0.93

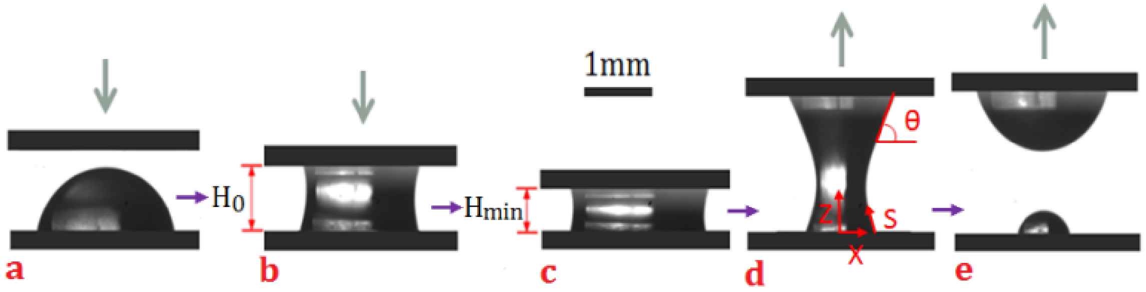

Figure 4.1. Process of quasi-static liquid transfer. (a): liquid drop is placed; (b): liquid bridge forms; (c): liquid bridge is compressed to minimum separation; (d): liquid bridge is stretched; (e): liquid bridge breaks.

To help understand the experimental results, we also employed a numerical model to predict the behavior of the liquid bridge under quasi-static loading. Neglecting gravity, the equilibrium profile of the liquid bridge can be described by the following system of differential equations[16-18]

$$\frac{dX}{dS} = cos\theta \qquad (4\text{-}1)$$

$$\frac{dZ}{dS} = sin\theta \qquad (4\text{-}2)$$

$$\frac{d\theta}{dS} = \frac{\Delta P}{\gamma} - \frac{sin\theta}{X} \qquad (4\text{-}3)$$

where as shown in Figure 4.1d, X and Z are the coordinates of the axisymmetric liquid bridge; S is the arc length; and θ is the angle between the local tangent of the liquid surface and horizontal axis. Laplace pressure, ΔP, is the pressure difference between the inside and outside of the liquid. Given H, and assuming the volume of the liquid is conserved, the shape of the liquid bridge can be obtained by solving equations (4-1)-(4-3) with boundary conditions (BCs) that specify either contact radius or *CA* on the two surfaces. In particular, on each surface, when the *CA* reaches θ_a or θ_r, *CA* will be specify as BC and the contact radius will be solved. When the *CA* is between θ_r and θ_a, the contact radius will be fixed as BC, while the *CA* will be solved. This form of implementing the BC facilitates a realistic modeling of the liquid bridge states [17]. By varying H in small steps, the evolution of the liquid bridge under quasi-static loading can be tracked. When the liquid bridge breaks, it becomes unstable and this tracking process is terminated. This model was shown to be able to correctly predict the behavior of the liquid bridge during a quasi-static compressing/stretching cycle in experiments [17].

After the profile of the bridge is obtained at each *H*, the adhesion force (*F*) between the liquid and the surfaces can be calculated. Due to equilibrium, the forces on the donor and acceptor surfaces have the same magnitude. In this thesis, *F* is evaluated on the donor surface, which is given by [16]:

$$F = 2\pi\gamma R_D \sin\theta_D - \pi R_D^2 \Delta P \qquad (4\text{-}4)$$

where R_D and θ_D are respectively the contact radius and *CA* on the donor surface. Clearly, *F* has two components: one ($2\pi\gamma R_D \sin\theta_D$) originates from the surface tension force acting at the contact line; the other ($-\pi R_D^2 \Delta P$) is caused by ΔP. Because this model is based on equilibrium whereas the liquid bridge experiences a dynamic event when it breaks, F_{pf} is defined as the adhesion force between the liquid bridge and the surfaces one step before the tracking process is terminated.

4.3 Results and Discussion

The experimental transfer ratios of all systems are plotted in Figure 4.2 against $\Delta\theta_r$, which is θ_r of the donor surface minus θ_r of the acceptor surface. It can be seen that the transfer ratio strongly depends on $\Delta\theta_r$. It tends to zero when $\Delta\theta_r$ is very negative, and to one (100% transfer) when $\Delta\theta_r$ is large. For intermediate $\Delta\theta_r$ value, the transfer ratio increases monotonically with $\Delta\theta_r$. On the other hand, θ_a of the donor surface does not play a significant role in determining the transfer ratio. For instance, the donor surfaces of cases 2, 3, and 4 have similar θ_a values (71.9^{o}, 72.8^{o} and 73.0^{o}), but their transfer ratios are very different. In addition, θ_a of these donor surfaces are very close to θ_a of the acceptor surface, but their transfer ratios are not near 50% as traditionally thought. Therefore, the traditional belief that the transfer ratio is controlled by the *CA* of the two surfaces should be clarified in that the controlling *CA* is θ_r, not θ_a.

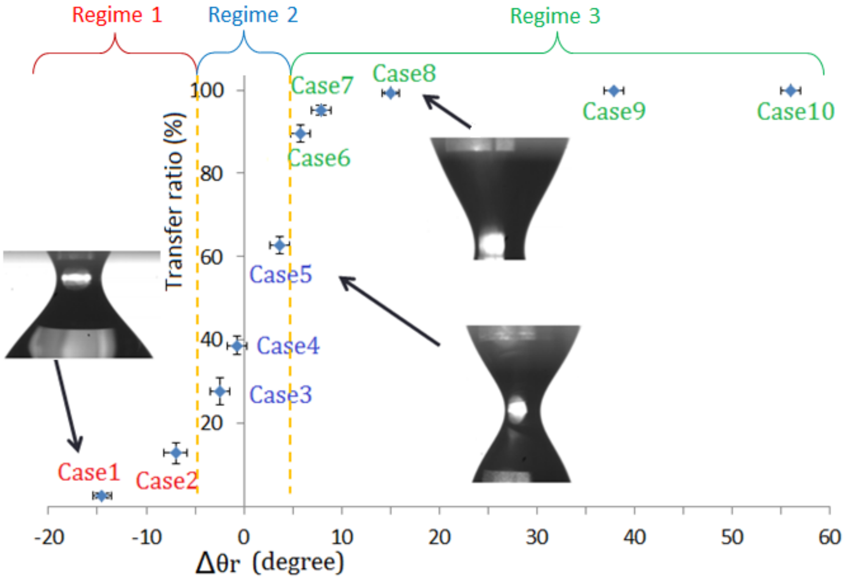

Figure 4.2: Relation between $\Delta\theta_r$ and transfer ratio. Cases in Regimes 1, 2, and 3 respectively have contact line pinned only on the donor surface, on both acceptor and donor surfaces and only on the acceptor surface. Dash lines are the boundary between regimes (same for the rest figures).

Both simulation and experimental results of F_{pf} are given in Figure 4.3, which shows very good agreement. No clear relation between the transfer ratio and F_{pf} can be found. For example, the transfer ratios of cases 8, 9 and 10 are almost the same, but F_{pf} of these cases are very different. The transfer ratios of cases 3, 4 and 5 vary from 27.9% to 62.7%, but F_{pf} of these cases are very similar. Therefore, in contrary to the traditional thoughts, the transfer ratio is determined by $\Delta\theta_r$, but not F_{pf}. In order to understand how $\Delta\theta_r$ affects the transfer ratio, and what causes the lack of correlation between transfer ratio and F_{pf}, we examined the detailed liquid transfer process below, through model studies and experimental analysis.

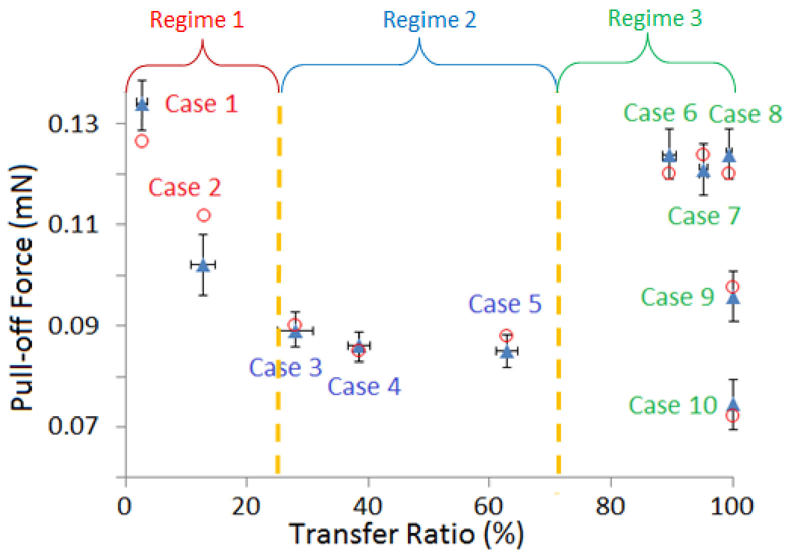

Figure 4.3: Experimental (▲) and simulation results (○) of F_{pf} versus transfer ratio.

Figure 4.4a shows the contact angles and radii on both surfaces during the liquid transfer in a representative case. Both experimental and simulation results are provided. Liquid bridge was formed at point A. As H decreased, the CAs on both surfaces increased to their advancing values and remained constant as H decreased to H_{min}. When the stretching stage started, the CAs first decreased to their receding values. For the donor surface, its CA remained at θ_r and its contact radius continued to decrease for the rest of the stretching process. However, for the acceptor surface, an interesting observation was made. As H increased, the CA first stayed at its receding value while the contact radius kept decreasing, but near the end of the process (after point C1) the contact radius stopped decreasing and became pinned at a certain value (hereafter referred to as R_{min}). Meanwhile the CA started to increase, showing a trend of expanding the contact line. This can be clearly seen from Figure 4.4b. As the stretching proceeded from C1 to C2, the contact radius on the acceptor (top) surface did not change ($R_{C1} = R_{C2}$), while significant shrinkage of the contact area on the donor (lower) surface was seen. This contact line pinning was not only observed experimentally, but also predicted by the numerical model, indicating that such a pinning is necessary to maintain the equilibrium of the liquid bridge.

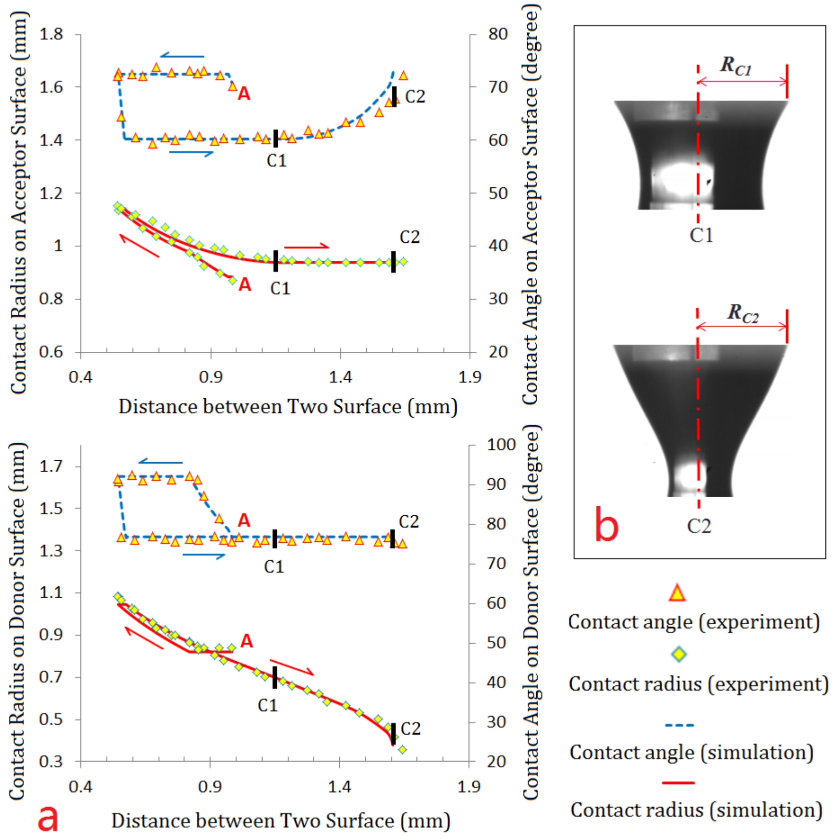

Figure 4.4: (a) Behavior of liquid transfer in case 8 from PS (2) to PMMA(1) surface. (b) Snap shots of the liquid bridge at C1 and C2. Diamond and triangle symbols should be read from left and right axes, respectively.

For all ten cases studied here, contact line pinning was found to occur but its characteristic depended on $\Delta\theta_r$. For the cases with small $\Delta\theta_r$ ($< -5^{\circ}$), θ_r of the donor surface is much smaller than that of the acceptor surface, corresponding to stronger adhesion between the liquid and the donor surface. As a result, near the end of the stretching process R_{min} was observed on the donor surface while the contact radius on the acceptor surface kept decreasing. For the cases with very large $\Delta\theta_r$ ($> 5^{\circ}$), θ_r of the acceptor surface is much smaller and the liquid tends to be attracted more to the acceptor surface. Therefore, R_{min} was only observed on the acceptor surface. When the two surfaces have similar θ_r ($-5^{\circ} < \Delta\theta_r < 5^{\circ}$), R_{min} can be observed on both surfaces.

Having understood the occurrence of R_{min} on different surfaces, the observed strong dependence of transfer ratio on $\Delta\theta_r$ can now be explained, and the ten cases studied here can be divided into 3 regimes as shown in Figure 4. 2 and 4.3. Regime 1 includes cases 1 and 2. R_{min} was observed only on the donor surface, and the contact radius on the acceptor surfaces shrank quickly at the end of the transfer process (see inserted image in Figure 4.2). As a result, the liquid bridge broke near the acceptor surface and most liquid remained on the donor surface. Therefore, the transfer ratio in this regime was close to zero. For cases 3, 4 and 5 located in Regime 2, R_{min} was found on both surfaces and the greatest shrinkage ("necking") occurred in the middle of the liquid bridge (see inserted image in Figure 4.2). Liquid bridge broke at the middle and a medium value of transfer ratio was obtained. For the cases in Regime 3 (cases 6, 7, 8, 9 and 10), contact radius was only pinned on the acceptor surfaces and contact radius on the donor surface shrank quickly (see inserted image in Figure 4.2). Therefore, the liquid bridge broke near the donor surface and the transfer ratio for these cases was very large.

Unlike the transfer ratio, which is determined by the location in the liquid bridge where breakage occurs and hence is directly influenced by the contact line pinning, F_{pf} has a more complex dependence on the shape of liquid bridge. As shown in EQ(4-4), the total adhesion force consists of the surface tension term and the Laplace pressure term. It depends not only on the contact radius and *CA* on the surface, but also the curvature of the liquid bridge $d\theta/dS$ through ΔP (see EQ(3)). Using the numerical model, the two components of F_{pf} (evaluated on the donor surface) are plotted in Figure 4.5, and they exhibit completely different dependence on $\Delta\theta_r$. The surface tension component decreases when $\Delta\theta_r$ increases, while the Laplace pressure term shows an overall increasing trend. The sum of the two components, demonstrates much smaller variations with $\Delta\theta_r$ compared with each component. The relative insensitivity of F_{pf} to $\Delta\theta_r$ is therefore, caused by the mutual compensation of the Laplace pressure term and the surface tension term. For liquid transfer in the quasi-static regime, since the effect of viscous and inertia forces is negligible, the shape of the liquid bridge plays a crucial role in determining the adhesion force and where the breakage might occur. For example, if one examines the images of cases 1 and 8 near breakage in Figure 4.2, the geometry of the liquid bridge near the donor surface of case 1 is similar to that near the acceptor surface of case 8; as well the geometry near the acceptor surface of case 1 is similar to that near the donor surface of case 8. This explains why F_{pf} of cases 1 and 8 are almost identical, even though the evolutions of the adhesion force prior to contact line pinning are very different for the two cases (detailed information is provided in Appendix C). However, because contact line pinning occurs on the donor surface in case 1 but on the acceptor surface in case 8, the transfer ratio in the two cases are drastically different: close to zero in case

1 while close to one in case 8. Therefore, we believe contact line pinning is the key mechanism that governs quasi-static liquid transfer between surfaces with *CAH*, and there is little correlation between the transfer ratio and F_{pf}.

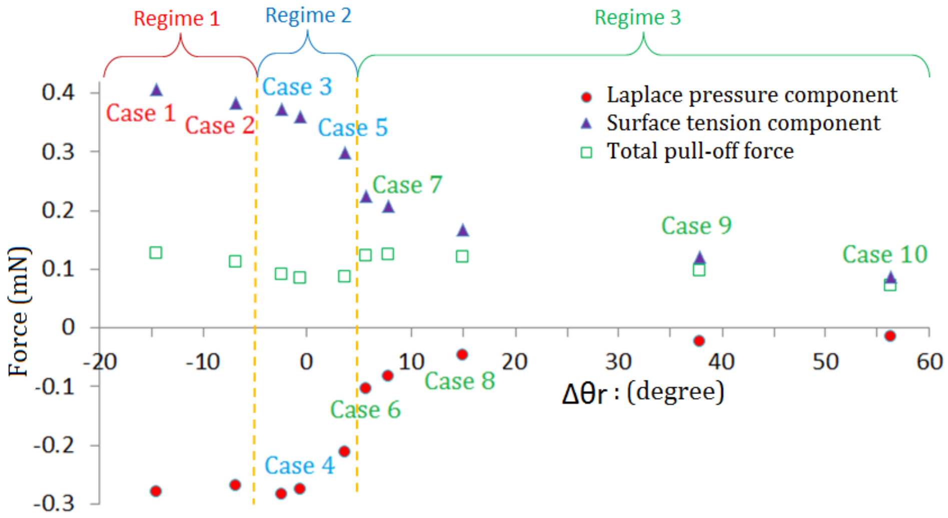

Figure 4.5: Total F_{pf} and its two components: surface tension component and Laplace pressure component.

Although a particular liquid volume (2μL) was used in this study, the numerical model shows that the phenomenon of contact line pinning is not affected by the volume of the liquid [17]. In addition, as long as the initial compression is large enough so that the contact radii on the two surfaces expand beyond R_{min} before stretching, the transfer ratio and pull-off force are insensitive to the value of H_{min}. The findings in this chapter suggest that in applications where liquid bridges are seen, θ_r is much more important than θ_a in controlling the transfer ratio. Furthermore, the transfer ratio not only depends on the absolute values of θ_r, but also $\Delta\theta_r$. It has been argued in the literature that the transfer ratio can never be exactly equal to unity (clear transfer) unless the donor surface has a θ_r larger than 90^o [14]. This is intuitively understandable by looking at the shape of the liquid bridge during the transfer. When θ_r of the donor surface is smaller than 90^o, the neck of the liquid bridge, which is where the liquid bridge is likely to break, can never be on the donor surface. On the other hand, our study showed that even if θ_r of the donor surface is less than 90^o, a very large transfer ratio can still be obtained if $\Delta\theta_r$ is sufficiently large (e.g. in Regime 3). For example, θ_r of the donor surface in case 8 is only 75.3^o, but the transfer ratio in this case is ~99%. This is because in this regime, contact radius on the acceptor surface is pinned at the end of the transfer process, while the contact radius on the donor surface shrinks quickly. Therefore, to achieve a large transfer ratio, it is not always necessary to use a very hydrophobic donor surface. It can also be obtained by using a pair of surfaces with large $\Delta\theta_r$.

4.4 Conclusions

In summary, R_{min} was observed at the end of the transfer process, due to *CAH*. Depending on $\Delta\theta_r$, R_{min} can occur only on the donor surface, only on the acceptor surface, or on both surfaces. These distinct behaviors determine the magnitude of the transfer ratio. In fact, the transfer ratio is strongly dependent on $\Delta\theta_r$, while F_{pf} is quite insensitive to $\Delta\theta_r$ as well as to the transfer ratio. Therefore, different from the usual belief that transfer ratio is controlled by adhesion force, contact line pinning is the governing factor for quasi-static liquid transfer between surfaces with *CAH*. Our results also show that it is possible to obtain a large transfer ratio using a pair of surfaces with large $\Delta\theta_r$.

Bibliography

(4.1) A. F. G. Dixon, P. C. Croghan, R. P. Gowing, *J. Expl. Biol.* **1990**, 152, 243--253.

(4.2) S. Gorb, *Proc. Roy. Soc. Lond. B* **1998**, 265, 747--752.

(4.3) T. Eisner, D. J. Aneshansley, *Proc. Natl. Acad. Sci.* **2000**, 97, 6568--6573.

(4.4) W. Federle, M. Riehle, A. S. G. Curtis, *Integr. Comp. Biol.* **2002**, 42, 1100--1106.

(4.5) D. Bonn, J. Eggers, J. Indekeu, J. Meunier, E. Rolley, *Rev. Mod. Phys.* **2009**, 81, 739--805.

(4.6) B. Qian, M. Loureiro, D. Gagnon, A. Tripathi, and K. S. Breuer, *Phy. Rev. Lett.* **2009**, 102 (16), 164502.

(4.7) H. W. Kang, H. J. Sung, T. M. Lee, D. S. Kim, C. J. Kim, J. Micromech. Microeng. **2009**, 19, 015025.

(4.8) W. X. Huang, S.H. Lee, H. J. Sung, T.M. Lee, D. S. Kim, *Int. J. Heat Fluid Flow*, **2008**, 29, 1436--1446.

(4.9) M. R. Pedro, J. Sunghwan, M. A. Jeffrey, S. Roman, *Science*, **2010**, 330, 1231--1234.

(4.10) A. V. Chadov, E. D Yakhnin, Kolloidn. Zh. **1979**, 41, 817.

(4.11) E. D. Yakhnin, A. V. Chadov, Kolloidn. Zh. **1983**, 45, 1183.

(4.12) A. A. Darhuber, S. M. Troian, *J. Appl. Phys.* **2001**, 90, 3602--3609.

(4.13) C. N. C. Lam, R. Wu, D. Li M. L. Hair, A. W. Neumann, *Adv. Colloid Interface Sci.* **2002**, 96, 169--191.

(4.14) S. Benedict, Z. Hong, K. Y. Law, *J. Phys. Chem. C* **2011**, 115, 14852--14861.

(4.15) H. Chen, T. Tang and A. Amirfazli, *Colloid Surface A*, **2012**, 408, 17--21.

(4.16) J. Qian, H. Gao, *Acta Biomaterialia* **2006**, 2, 51--58.

(4.17) H. Chen, A. Amirfazli and T. Tang, *Langmuir*, **2013**, 29, 3310--3319.

(4.18) B. Qian, K. S. Breuer, *J. Fluid Mech.* **2011**, 666, 554--572.

Chapter 5

5. Effect of Contact Angle Hysteresis on Breakage of a Liquid Bridge

5.1 Introduction

Wetting phenomena which is commonly seen in nature and various industrial applications is also of significant interest to academic researchers. The wettability of a surface is usually described by the contact angle, measured within the liquid at the three phase (solid, vapor, and liquid) contact line [1]. In an ideal situation, the contact angle between a specific liquid and a solid surface is a unique value according to the Young's equation [2]. However, due to the roughness and heterogeneity of surfaces, in reality the contact angle does not exhibit a unique value. A range of values can be found between advancing contact angle, θ_a (maximum value of contact angle when liquid advances over a surface); and receding contact angle, θ_r (minimum value of contact angle when liquid recedes over a surface) [3, 4]. When the contact line is pinned on the surface, the contact angle can have any value between θ_a and θ_r. The contact angle hysteresis (*CAH*) is the difference between θ_a and θ_r.

A numbers of previous works have shown that *CAH* plays a very important role in various types of wetting or dewetting processes, especially the stickiness of surfaces which were shown to be significantly affected by *CAH* [5-11]. For example, *CAH* was shown to be one of the governing parameters determining the motion of a drop on a tilted surface [7-8]; *CAH* can also significantly influence the drop shedding process [9-11]. However, there are very few studies about the effect of *CAH* on processes involving a liquid bridge, e.g. liquid transfer between two solid surfaces, electronic printing by dispensing a liquid (ink) on polymeric surfaces, wet adhesion systems (of sort seen in nature), etc. In many of these processes a liquid bridge is first formed by an approaching surface to another one where liquid is present (e.g. a sessile drop), see Figure 5.1;

the liquid bridge then may be compressed, but the final stage usually involves separation of two surfaces and breakage of the liquid bridge (e.g. as seen in off-set printing). When the liquid bridge breaks the volume of the drop is divided between the lower and upper surfaces. In the limiting situation where no liquid from the lower surface is transferred to the upper surface (see Figure 5.1), it is said that the transfer ratio is zero. The transfer ratio has a value of one, if all of the liquid from the lower surface is transferred to the upper surface when liquid bridge breaks.

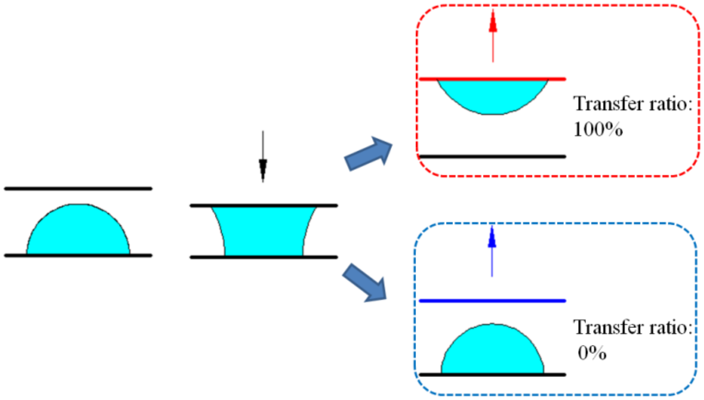

Figure 5.1: Process of liquid drop transfer. Two limiting situations with 100% and 0% transfer ratios are shown.

In this study a typical process of quasi-static compression and stretching of a liquid bridge between two surfaces will be considered. A number of works have been done to understand this process [12-16]. In most of the previous literature, the value of contact angle was simply assumed as a constant (value of equilibrium contact angle, or receding contact angle) during the whole process [14-16]. Such assumption also implicitly means that the contact line continuously recedes to shrink the contact area between one or both surfaces delimiting the liquid bridge, i.e. contact line will not be pinned. However, in various recent studies it was observed that the contact angles of the upper and/or lower surfaces with the liquid bridge during compression and stretching is not constant, i.e. θ_a in most of compressing stage, and θ_r in most of stretching stage [17-19]. Contact line pinning can be observed when the contact angle changes between θ_a and θ_r.

Two recent studies [20, 21] showed that the transfer ratio for quasi-static liquid transfer is strongly depended on the difference between the receding contact angles of the two surfaces. In fact, the key mechanism [21] which governs the transfer ratio is the pinning of contact line (caused by *CAH*) before the pull-off (final breakage) of the liquid bridge. It was found that the contact angle did not always stay at the receding value, but could increase at the end of the stretching stage, due to contact line pinning. Therefore, it was argued [21], the presumption that the receding contact angle will be always observed when liquid bridge breaks is not warranted. Pinning of the contact line will not only change the contact angle and hence the associate surface tension force, but also the shape of the liquid bridge leading to a change in the Laplace pressure (ΔP). Since both surface tension force and Laplace pressure determine the force experienced by the liquid bridge at either of the two delimiting surfaces (see Figure 5.2), it is important and necessary to consider the effect of *CAH* on the adhesion force when liquid bridge breaks (or pull-off force).

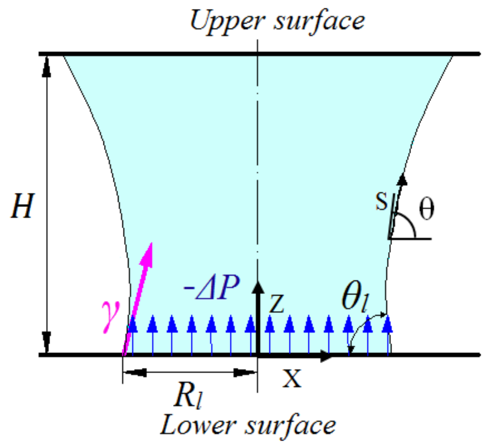

Figure 5.2: Schematic of a liquid bridge between two solid surfaces. R_l and θ_l are the contact radius and contact angle on the lower surface. H is the distance between the two surfaces, and γ is the surface tension of liquid.

In this chapter I present a systematic study about how the pinning of contact line at the end of the stretching stage influences the value of pull-off force (F_{pf}). Different from [21] which studied the mechanism of quasi-static liquid transfer (e.g. the role of pinned contact line), this work is focused on investigating the effect of *CAH* on the pull-off force and address questions such as: how does F_{pf} change with the contact angles and *CAH* of the surfaces? How does such change correlate with the surface separation and geometry of the liquid bridge when it breaks, and how may one make use of the results and modulate F_{pf} via *CAH*? These questions were addressed by firstly, demonstrating the importance of *CAH* in the stretching stage by comparing the process of stretching a liquid bridge with *CAH* and without *CAH*. Secondly, it will be shown how pinning of contact line at the end of stretching stage influences the value of pull-off force.

5.2 Methods

The focus of this study is on a liquid bridge formed between two surfaces that are much larger than the contact area between the liquid bridge and either of the surfaces. Liquid bridge formed between ten different lower surfaces (for wettability data see Table 5.1) and one Poly(methyl methacrylate) upper surface (PMMA(1), θ_a: 72.6^o θ_r: 60.3 ^{o}) were studied experimentally for a 2 µl water drop which has the surface tension and density of 72.8 mN/m and 9.98 g/ml respectively at 20 ^{o}C. With such a small liquid drop, the value of Bond Number ($Bo = \frac{\rho g R^2}{\gamma}$, where *R* is a characteristic length, taken to be the average of the contact radii on the acceptor and donor surfaces) is on the order of 10^{-2}, which indicates that gravity is negligible for the systems we studied. The surfaces were fabricated as described in [22]. In each experiment, the upper surface was stretched at a low speed of 0.005 mm/s to ensure the quasi-static condition (the experimental setup used was similar to one in our earlier study described in [21]). The pull-off forces were recorded by a force cell (resolution of 0.005 mN) attached to the lower surface. All experiments were performed under well controlled ambient conditions (pressure, temperature and relative humidity).

In addition to the experiments, a theoretical model developed earlier by us was used to simulate the quasi-static stretching of a liquid bridge between two surfaces with *CAH*. As shown in Figure 5.2, neglecting the effect of gravity, the equilibrium profile of the liquid bridge can be described by the following equations [17, 23]

$$\frac{dX}{dS} = cos\theta \qquad (5\text{-}1)$$

$$\frac{dZ}{dS} = sin\theta \qquad (5\text{-}2)$$

$$\frac{d\theta}{dS} = \frac{\Delta P}{\gamma} - \frac{sin\theta}{X} \qquad (5\text{-}3)$$

where X and Z are the coordinates of the axisymmetric liquid bridge, S is the arc length measured from the contact point of the liquid with the lower surface, and θ is the angle between the local tangent of the liquid surface and the horizontal axis. Given the surface separation H and assuming the volume of the liquid is conserved, the shape of the liquid bridge can be obtained by solving Eq. (5-1)-(5-3) with boundary conditions that specify either contact radius or contact angle on each of the two surfaces. The shooting method was used to find the solution in an iterative manner [17]. Once the profile of the liquid bridge is obtained, the adhesion force can be calculated based on ΔP, contact angle and contact radius on either upper or lower surface. Taking the lower surface for example, the magnitude of adhesion force can be calculated as:

$$F = 2\gamma\pi R_l \sin\theta_l - \pi R_l^2 \Delta P \qquad (5\text{-}4)$$

The vertical adhesion force consists of two terms, the first due to surface tension force and the second due to Laplace pressure. With this model, the geometry of the liquid bridge during the stretching process was monitored; hence the contact angle, contact radius as well as the adhesion force on both surfaces can be obtained. This theoretical model is based on the assumption of equilibrium. When H becomes larger than a certain value (the separation where liquid bridge breaks, denoted as H_{max}), the liquid bridge becomes unstable, and no convergence solutions can be found from the model. The pull-off force F_p evaluated from the model is based on the last equilibrium solution, obtained at $H \approx H_{max}$.

Table 5.1: Wetting properties of the lower surfaces with water. Sessile drop method was used in the measurement of contact angle. For each surfaces, measurements for contact angle were conducted at three different locations. The shown data are the average value and standard deviation of the three measurements.

Name of surface	θ_a (degree)	θ_r (degree)
Silicon	55.1±0.67	45.7±1.23
PMMA(2)	71.9±0.70	52.7±1.54
PMMA(3)	72.8±0.93	57.9±0.86
Polystyrene & PMMA Blend (1)	73.0±0.82	59.7±0.97
Polystyrene & PMMA Blend (2)	79.4±0.73	63.9±0.94
Polystyrene (1)	88.6±1.43	66.0±1.27
Poly (ethyl methacrylate)	77.6±0.79	68.2±0.94
Polystyrene (2)	91.8±1.30	75.3±0.87
Octadecyltrichlorosilane Treated	111.1±1.33	98.2±0.89
Teflon AF	126.4±1.30	116.4±0.93

5.3 Results and discussion

The first system simulated (denoted as Case 1) is a liquid bridge between a lower surface (θ_a: 90 ^{o}, θ_r: 70 ^{o}) and an upper surface (θ_a: 80^o, θ_r: 60 ^{o}). The initial separation (H_{min}) between the two surfaces was set to be 0.5 mm, and the initial contact angle was set to be the receding contact angle for each of the surfaces. In order to demonstrate the importance of *CAH*, another simulation of stretching the liquid bridge was done, but this time without *CAH* consideration (Case 2). In Case 2, the contact angle of the upper and lower surfaces was set as 60 ^{o} and 70 ^{o}, respectively, which are the values of the receding contact angles in Case 1 (this was done to represent what has been mainly proposed in the literature during the stretching phase, as discussed earlier).

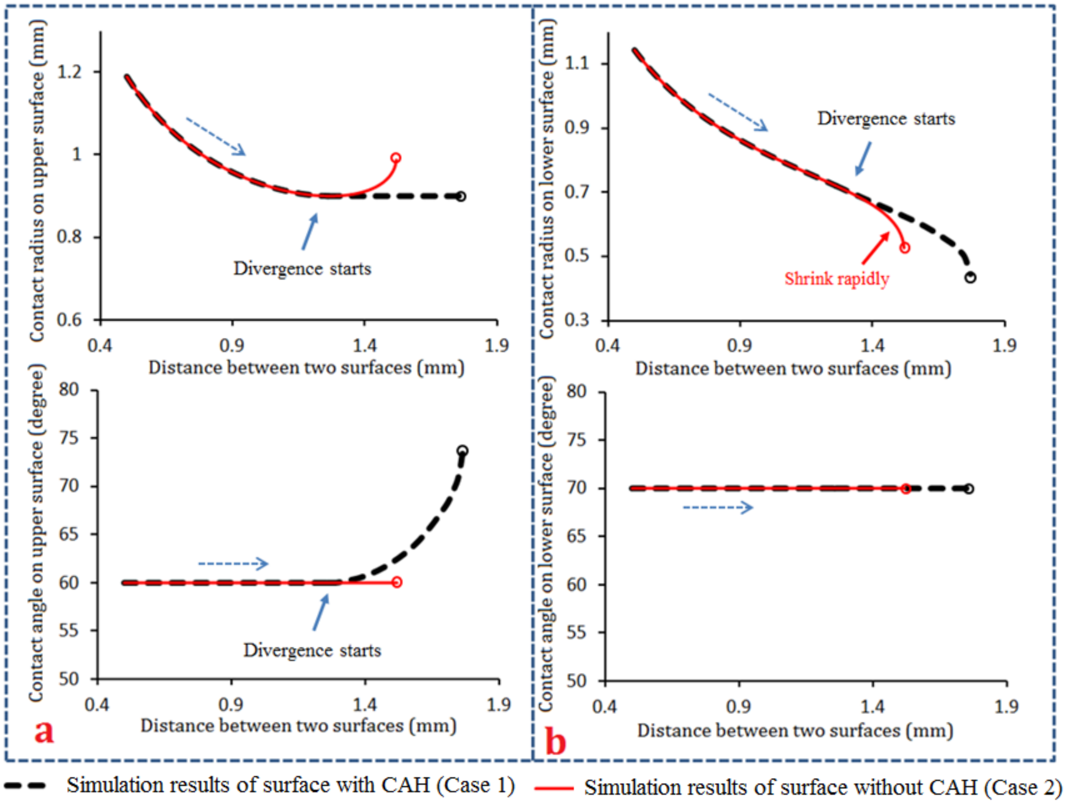

Figure 5.3: Evolution of contact radius and contact angle for Cases 1 and 2; (a) the upper surface; (b) the lower surface. Hollow circles denote the points at which the liquid bridge breaks.

The evolution of the contact radii and contact angles of the two cases are shown in Figure 5.3. It can be seen that in the early stage of the stretching process ($H < 1.27$ mm), because the contact angles of both cases are at the receding values, the curves of Cases 1 and 2 overlap. However, after H increases to 1.27 mm, the two contact radius curves diverge. Consider first the upper surface, shown in Figure 5.3(a). In Case 1 where *CAH* is present, instead of remaining at the receding value, the contact angle starts to increase, while the contact radius is pinned at 0.90 mm during the rest of the stretching stage. However, for Case 2 where *CAH* is absent, the contact angle stays constant while the contact line starts to expand after H reaches 1.27 mm. For the lower surface, shown in Figure 5.3(b), the contact angles on both surfaces stay at the receding value and no contact line pinning is observed. However, due to the distinct behavior of contact angle/contact line on the upper surface, the contact radius on the lower surface also behaves differently near the breaking point (where pull-off force is registered). For Case 2, since the volume of the liquid is constant, associated with the expansion of contact radius on the upper surface, the contact radius on the lower surface shrinks rapidly. On the contrary, the contact line pinning on the upper surface in Case 1 allows the contact radius on the lower surface to decrease at a slower rate. As a result, the liquid bridge in Case 1 breaks at a much larger H value than in Case 2. Specifically H_{max} = 1.77 mm in Case 1, a 16.4% increase compared with Case 2 where H_{max} = 1.52 mm.

To further confirm that *CAH* leads to larger H_{max}, two sets of simulations and one set of experiments were performed. Both simulation groups have the same set of lower surfaces with their receding contact angles varying from 20^o to 135^o. The difference between the two groups of simulations lies in the upper surface. In the first simulation group (Group I), the upper surface has *CAH* (θ_a: 80^o, θ_r: 60^o) and hence contact line pinning can occur on both upper and lower surfaces. In the second group (Group II), the contact angle of the upper surface is fixed at $60\ ^o$ (same as θ_r of upper surface in Group I) without *CAH*, and therefore contact line pinning can only occur on the lower surface. Experimental measurements (Group III) of liquid transfer from different lower surfaces to a fixed upper surface were also finished. The upper surface used in the experiment has $\theta_a = 72.6^o$ and $\theta_r = 60.3^o$, the latter almost the same as θ_r of the upper surface used in the simulations. Data on H_{max} versus θ_r of the lower surface obtained from all three groups are plotted in Figure 5.4 (a). It can be seen that due to the absence of *CAH* on the upper surface, the results from Group II are very different from those in Group I and Group III. The experimental data (Group III) fall nicely onto the curve generated from simulation Group I (with *CAH* on both surfaces) but deviate significantly from Group II, emphasizing the importance of considering CAH for any realistic system. At the same θ_r of the lower surface, the value of H_{max} in Group I is larger than those in Group II, confirming that the pinning of contact line at the end of stretching stage, in general, causes an increase in H_{max}.

The adhesion force between the liquid and surfaces is influenced by the geometry of the liquid bridge profile, so it can be affected by *CAH*. The evolution of the adhesion forces in the two cases simulated in Figure 5.3 are shown in Figure 5.4(b). It can be seen that the value of the adhesion force decreases with the increase of H. Because the liquid bridge in Case 1 breaks at larger H_{max}, compared with Case 2, Case 1 has a smaller value of F_{pf}. However, if we compare the adhesion force between the two cases at the same H, the adhesion force in Case 1 is the same as in Case 2 when H< 1.27 mm (before divergence starts), and slightly larger than in Case 2 when 1.27 mm< H< 1.52 mm (after divergence but before breakage in Case 2).

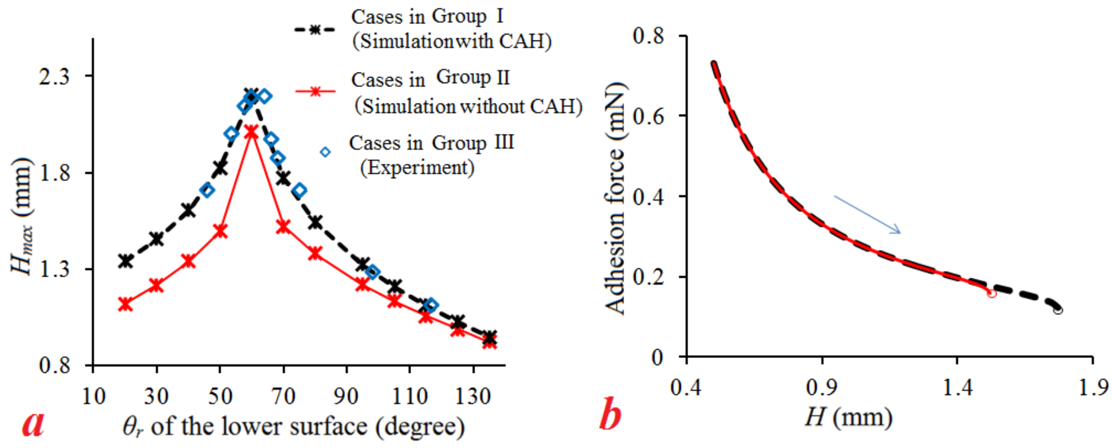

Figure 5.4: (a) Value of H_{max} versus θ_r for the lower surface in simulations (Groups I/II) and experiments (Group III). Lines are to guide the eyes. (b) Evolution of the adhesion force for Cases 1 and 2. Hollow circles mark the points at which the liquid bridge breaks.

Having understood the importance of *CAH* in the stretching of a liquid bridge, the following discussion is focused on how *CAH* and the pinning of contact line affect the value of F_{pf}. In [21], it was shown that depending on the receding contact angles of the two surfaces, the pinning of the contact line at the end of stretching stage can occur only on one surface when the receding angle of the two surfaces are very different, or on both surfaces, when the receding angle of the two surfaces are similar.

The pull-off force data from Group I (simulation) and Group III (experiment) are plotted in Figure 5.5(a) versus θ_r of the lower surface. Two observations can be made from the plot. First, when the lower surface has a large receding contact angle (> 70^o, for this group), F_{pf} clearly decreases with the increase of the receding contact angle. However, when the receding contact angle of the lower surface is small (< 70^o), no monotonic relation between F_{pf} and the receding contact angle can be found. In addition, there appears to be a local minimum in the F_{pf} curve, located about θ_r of the lower surface = 60^o, which is near the receding contact angle of the upper surface. For example, from Group I, F_{pf} at 60^o receding contact angle of lower surface (0.0835 mN) is significantly smaller than F_{pf} at both 70^o (0.1219 mN) and 50^o (0.1210 mN).

To further explore and understand the observations in Figure 5.5(a), we simulated six more groups of liquid transfer. In each group, the receding contact angle of upper surface is fixed (see Figure 5.5(b)) and different lower surfaces were used. The results for F_{pf} are shown in Figure 5.5(b) versus θ_r of the lower surface. Each curve in Figure 5.5(b) connects F_{pf} data associated with the same upper surface. Similar to Figure 5.5(a), for each curve, when θ_r of the lower surface is large (> 90^o for all the groups), F_{pf} decreases with an increasing value of θ_r on the lower surface. Furthermore, comparison among the different curves shows that F_{pf} also decreases with increasing θ_r on the upper surface. No monotonic relation between F_{pf} and θ_r of either surface can be found when θ_r of the lower surface becomes small (< 90^o). However, by examining θ_r of the two surfaces for the cases with significantly smaller F_{pf}, it was found that all of these cases have similar values of θ_r on the two surfaces. Furthermore, due to the similar θ_r values, contact line pinning takes place on both lower and upper surfaces at the end of the stretching stage (pointing to the importance of considering *CAH* when analyzing a liquid bridge).

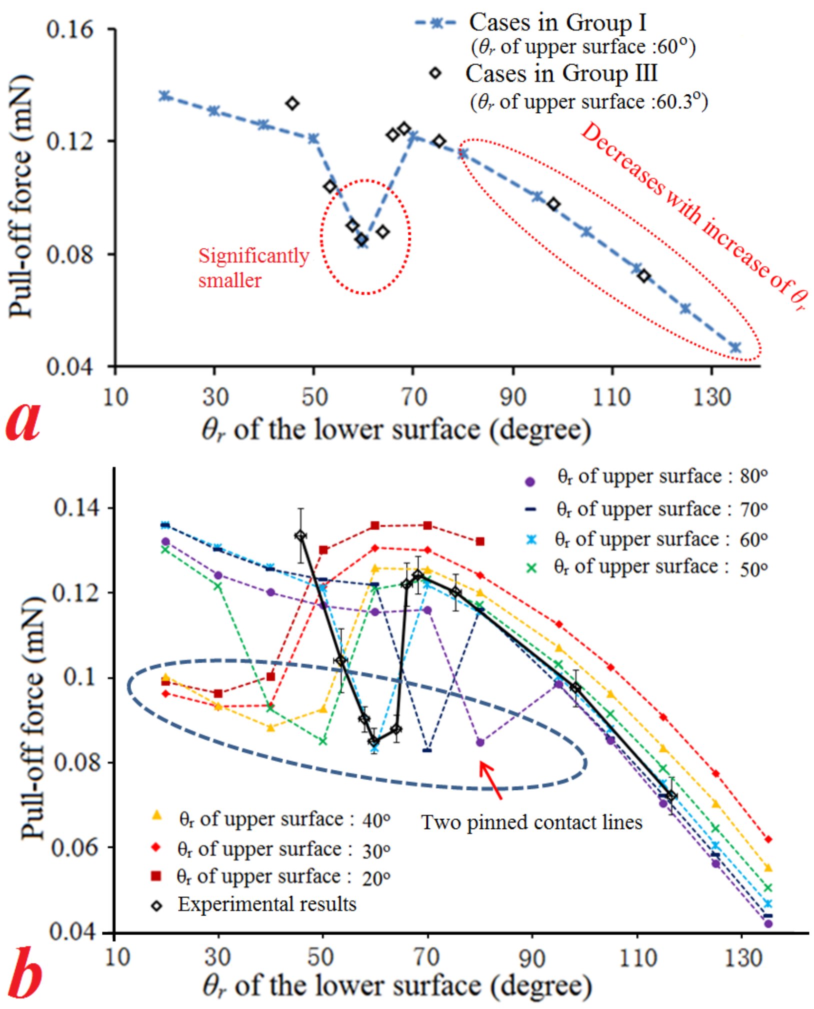

Figure 5.5: (a) Value of pull-off forces versus θ_r of the lower surface, data from simulations (Group I) and experiments (Group III). (b) Value of pull-off forces versus θ_r of the two surfaces of all the cases. Lines are to guide the eyes.

Since the adhesion force is influenced by the shape of the liquid bridge, the profiles of the liquid bridge near the breakage point for all the data shown in Figure 5.5 were examined to understand how the occurrence of contact line pinning affects F_{pf}. Figure 5.6 shows the profiles of three liquid bridges near pull-off obtained from the simulations. All three liquid bridges have the same θ_r on the upper surface (60°) but different θ_r on the lower surface (①: 50 °, ②: 60° and ③: 70°). The different value of θ_r on the lower surfaces results in completely different contact line pinning behaviors at the end of stretching stage (①: only on the lower surface; ②: on both surfaces; and

③: only on the upper surface). At the end of the stretching stage, the liquid has a tendency to stay near the surface which has a smaller contact angle, and hence contact line pinning on that surface can be observed. The more different the receding contact angles of the two surfaces, the stronger this tendency will be, and contact line pinning is more expected to occur only on one surface (with smaller θ_r). It can be seen that compared with the liquid bridges with only one pinned contact line, the one with two pinned contact lines has a more curved profile when it breaks. Due to the larger curvature, the value of $-\Delta P$ of bridge ② (-129.5 N/m^2) is much smaller than $-\Delta P$ of bridges ① (-98 N/m^2) and ③(−106.7 N/m^2). From the Eq. (5-4), the value of adhesion force is positively related to $-\Delta P$. Therefore, the adhesion force between the liquid and surface of the cases that have two pinning contact lines are smaller than the cases where only one contact line is pinned.

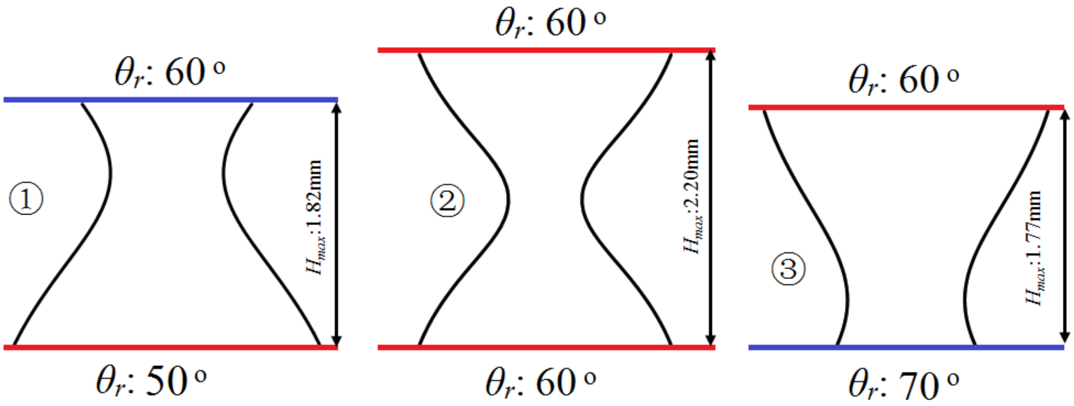

Figure 5.6: Profiles of liquid bridge before it breaks obtained from simulations; Red: surface with contact line pinning; Blue: surface without contact line pinning. The occurrences of contact line pinning are: ① only on lower surface; ② on both surfaces; ③ only on upper surface.

Another reason contributing to the smaller pull-off force associated with two pinned contact lines is the later breakage (larger H_{max}) of the liquid bridge. It has been observed in Figure 5.4(b) that compared with situations without *CAH*, contact line pinning delays breakage and reduces F_p. It can also be noticed from Figure 5.6 that liquid bridge ② has a larger H_{max}(②: H_{max}= 2.20 mm, ①:H_{max}= 1.82 mm and ③: H_{max}= 1.77 mm). Since F_{pf} is the adhesion force measured at H_{max}, it is of interest to compare the evolutions of the adhesion forces during stretching the three liquid bridges, which are shown in Figure 5.7. It is clear that the curve for liquid bridge ② extends to a much larger separation, leading to smaller value of F_{pf}. On the other hand, although bridge ② has the smallest F_{pf}, at the same H its adhesion force is not the smallest among these three bridges. When H is larger than 1.38mm, bridge ② in fact has the largest adhesion force compared with the other two. This is similar to observation in Figure 5.4(b) where the introduction of *CAH* does not cause reduction in the adhesion force at the same surface separation.

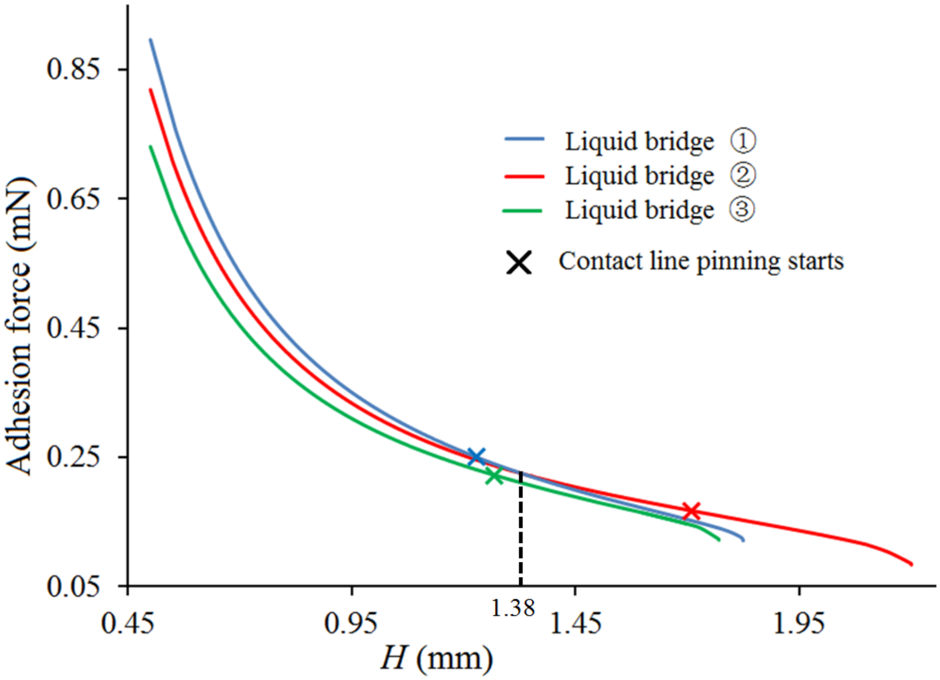

Figure 5.7: Evolution of adhesion force for the liquid bridge ①, ② and ③.

Summarized from the discussion, the contact lines of liquid bridge may become pinned when *CAH* is present during the process of stretching. Such phenomenon of contact line pinning alters significantly both the shape and stability of the liquid bridge. Due to the effect of *CAH*, it is shown that liquid bridges with free moving contact lines may behave as liquid bridge whose contact lines are forced (e.g. due to geometric constraints) to be pinned. For example, three of our experimental cases (water transfer from PMMA (3), Polystyrene & PMMA Blend (1), and

Polystyrene & PMMA Blend (2) to PMMA (1)) were found to have two pinned contact lines at the end of the stretching stage. We compared the these three cases with two previous studies [25, 26] which considered surfaces that had small areas and assumed that the liquid bridge had pinned contact lines on the edges of both surfaces. Good agreements were found (for detailed comparison, see Appendix D).

Results from this work can be useful to practical applications involving liquid bridges. The finding that in the presence of *CAH* liquid bridges break at a large separation distance, especially when both contact lines are pinned, can be useful in understanding wet adhesion systems. Compared with dry adhesion, wet adhesion usually can take effect at larger scales due to the existence of liquid bridges [24]. As shown in this study, the pinning of contact line due to *CAH*, especially on both surfaces, can significantly increases H_{max}, the effective interaction range, without causing great changes in the adhesion force at the same separation. Both features are desirable for wet adhesion systems, and can be achieved simultaneously by *CAH*-induced contact line pinning. The occurrence of contact line pinning can also be used to modulate the pull-off force. For instance, depending on the receding contact angles of the two surfaces, the value of F_{pf} can be decreased in two different ways. If one of the receding contact angles is very large ($>90^{o}$), a smaller F_{pf} can be obtained by increasing θ_r of either surface. If the θ_r values are smaller than 90^{o} for both surfaces, the way to decrease the pull-off force is to use two surfaces with similar values of θ_r. This will allow contact line pinning to occur on both surfaces in the end of the stretching stage, so as to achieve a smaller F_{pf}.

5.4 Conclusion

In this chapter, we clearly demonstrate that due to the pinning of the contact line at the end of the stretching stage, the contact angle between a liquid bridge and surfaces cannot be simply assumed to have a constant value. Contact line pinning can result in a larger H_{max}, and smaller F_{pf} for liquid transfer. A systematic study about the effect of *CAH* and the occurrence of contact line pinning on the value of F_{pf} and H_{max} was provided. It is found that when one of the surfaces has a receding contact angle larger than 90^o, F_{pf} decreases with the increase of the receding contact angle on either surface. For the cases where θ_r of both surfaces are smaller than 90^o, significantly smaller F_{pf} is seen when contact line pinning occurs on both surfaces, as compared to F_{pf} when contact line pinning occurs only on one of the surfaces. This smaller value of F_{pf} is caused by more curved profile and larger H_{max} of liquid bridge.

Bibliography

(5.1) P. G. de Gennes, *Rev. Mod. Phys.* **1985**, 57, 827.

(5.2) T. Young, *Philos. Trans. R. Soc. London* **1805**, 95, 65.

(5.3) C.N.C. Lam, R. Wu, D. Li, M. L. Hair, A.W. Neumann, *Adv. Colloid Interface Sci.* **2002**, 96, 169--191

(5.4) R. H. Dettre, R. E. Johnson Jr, *Adv. Chem. Ser.***1964***,* 43, 112.

(5.5) P. Roura, J. Fort, *Phy. Rev. E* **2001**, 64, 011601.

(5.6) E. Pierce, F.J. Carmona, A. Amirfazli, *Colloids Surfaces A* **2008**, 323, 73--82.

(5.7) W. Konrad, M. Ebner, C. Traiser, A. Roth-Nebelsick, *Pure Appl. Geophys*. **2012**, 169, 835.

(5.8) D. Qurere, *Annual Rev. Mater. Res.* **2008**, 38, 71.

(5.9) J. Wu, J. Xia, W. Lei, B. P. Wang, *Scientific Reports* **2013**, 3, 3268.

(5.10) L. W. Schwartz, *Langmuir* **1998**, 14, 3440.

(5.11) A. J. B. Milne, A. Amirfazli, *Langmuir* **2009**, 25(24), 14155--14164.

(5.12) A. V. Chadov, E. D. Yakhnin, *Kolloidn. Zh.* **1979**, 41, 817.

(5.13) S. Dodds, M. S. Carvalho, S. Kumar, Phy. Fluids **2009**, 21, 092103.

(5.14) H. W. Kang, H. J. Sung, T-M Lee, D-S Kim, C-J Kim, *J. Micromech. Microeng.* **2009**, 19, 015025.

(5.15) E. Cheung, M. Sitti, *J. Adhesion Sci. Tech.* **2008**, 22, 569--589.

(5.16) M. A. Fortes, *J. Colloid Interface Sci.* **1982**, 88, 338--352.

(5.17) H. Chen, A. Amirfazli, T. Tang, *Langmuir* **2013**, 29, 3310 --3319.

(5.18) E. J. De Souza, L. Gao, T. J. McCarthy, E. Arzt, A. J. Crosby, *Langmuir* **2008**, 24 (4), 1391--1396.

(5.19) S-J Hong, T-H Chou, S. H. Chan, Y-J Sheng, H-K Tsao, *Langmuir* **2012**, 28, 5606--5613.

(5.20) B. Samuel, H. Zhao, K-Y Law, *J. Phys. Chem. C* **2011**, 115, 14852--14861.

(5.21) H. Chen, T. Tang, A. Amirfazli, *Soft Matt.* 2014, **10**, 2503.

(5.22) H. Chen, T. Tang, A. Amirfazli, *Colloids Surface A* **2012**, 408, 17--21.

(5.23) J. Qian, H. Gao, *Acta Biomaterialia* **2006**, 2, 51--58.

(5.24) B. N. J. Persson, *J. Phys.: Condens. Matt.* **2007**, **19**, 376110.

(5.25) L. V. Slobozhanin, J. I. D. Alexander, *Phys. Fluids* **1998**, 10, 2473.

(5.26) J. M. Perales, J. Meseguer, *J. Crystal Growth* **1991**, 110, 855.

Chapter 6.

6. Understanding Quasi-static Liquid Transfer between Two Solid Surfaces

6.1 Introduction

Liquid bridge between two solid surfaces is relevant to a wide range of practical applications and has been studied for a long time. For example, in offset printing, ink transfer is achieved through stretching an ink bridge formed between donor and acceptor surfaces [1-4]. Depending on the surface and liquid properties, stretching speed and direction, the ink transfer ratio (volume of the liquid transferred onto acceptor surface over the total liquid volume) can be very different. The value of transfer ratio is important for the performance of printing, since small amount of ink remaining on the donor surface can result in image quality defects. Other examples include printing of micro-scale electrical circuits and semiconductors, electro-wetting-assisted drop deposition, printing of biological micro-arrays and packaging [5-8]. Wet adhesive systems, i.e., capillary adhesion due to the formation of liquid bridges between surfaces [9, 10], is another area where study of liquid bridge is important. Such wet adhesive systems are widely observed in nature. For instance, for animals like beetles, blowflies and ants, micro liquid bridges formed between their feet and surfaces can help them stick to the surfaces [11-13]. It is therefore important to investigate what factors can affect the adhesion force between liquid-bridged surfaces, and how the adhesion force depends on the deformation of the liquid bridge.

Within the context of liquid transfer, the liquid bridge being deformed and transferred can be subjected to many forces such as surfaces forces, viscous forces, and inertia forces. Literature shows that when the liquid bridge is compressed and stretched at a very low rate, viscous and inertial effects are negligible, and the transfer process is only governed by surfaces forces, which is influenced by surface wettability and liquid surface tension [14-15]. This is defined as the quasi-static liquid transfer and is the focus of the present work. A number of studies have been done to understand the behavior of liquid bridges as well as the associated adhesion force in quasi-static transfer [1-4, 8-20]. All of these studies showed that quasi-static liquid transfer can be affected by the surface contact angle. However, in practice, the contact angle between a solid and a liquid is not unique, but covers a range, the value of which is shown to be related to the molecular mobility, liquid penetration and surface swelling [21,22]. The upper bound of this range is called the advancing contact angle (θ_a) which is the contact angle when the contact line starts to expand. The lower bound is named the receding contact angle (θ_r) which is the value when the contact line starts to shrink/recede. Contact angle hysteresis (*CAH*) is the difference between θ_a and θ_r [23]. Several recent studies [24-27] found that during the process of quasi-static liquid transfer, the contact angles at the surfaces are not necessarily constant but can change between θ_a and θ_r, accompanied by the pinning of contact lines. Therefore, liquid transfer, even under quasi-static condition, is a complex process that could be affected by the advancing and/or receding contact angles, and *CAH*.

Two quantities are of particular importance to liquid transfer in practical applications: the transfer ratio (α), a measure of quantity of transfer; and the maximum adhesion force (F_{max}), which is the force required for the transfer to take place. An intuitive question is therefore: how are these quantities affected by *CAH*, present in all practical surfaces? To our knowledge, only two past works attempted to address this question. Samuel *et al.* [28] performed an experimental study of liquid transfer from different donor surfaces to a hydrophilic platinum ring with a fix diameter. The results of this study showed that a clear transfer with 100% transfer ratio could only be achieved with donor surfaces that had $\theta_r > 90^\circ$. In that study, by using a platinum ring as the acceptor surface, the contact radius on the acceptor surface was always fixed. In a recent work [29], we studied liquid transfer between two surfaces that can allow both the contact radii and contact angles to change. In contrary to the traditional belief that the transfer ratio depends on the pull-off force (adhesion force when liquid bridge breaks), the results showed that there was only a very weak correlation between transfer ratio and pull-off force. Instead, the transfer ratio had a strong dependence on $\Delta\theta_r$, the difference between the receding contact angles of donor and acceptor surfaces, which was attributed to the contact line pinning at the end of the transfer process. The concept that contact line pinning is the governing mechanism for quasi-static liquid transfer raised more questions: what is the quantitative connection between the occurrence of contact line pinning at the end of stretching stage and surface *CAH*? Is $\Delta\theta_r$ the only determining factor for quasi-static liquid transfer? What about receding contact angles of individual surfaces? What is the role of advancing contact angles? Do they affect either F_{max} or α during the transfer process? To answer these questions, a systematic study is necessary to understand the effect of *CAH* on quasi-static liquid transfer between two solid surfaces.

In this work, quasi-static liquid transfer between two surfaces was studied experimentally using a series of surfaces with different θ_a and θ_r. A theoretical model which can correctly predict the behavior of equilibrium liquid bridge between surfaces with *CAH* was used to aid in the explanation of results. Detailed discussions about how F_{max} and α are affected by contact angles and *CAH* of surfaces are provided based on both experimental and simulation results.

6.2 Methods

Water was used as the liquid in all of the experiments performed in this study. Twelve different surfaces (shown in Table 6.1) were used; they were fabricated from the following materials: silicon, Poly (ethyl methacrylate) (PEMA), Poly (methyl methacrylate) (PMMA), Polystyrene (PS), PMMA and PS mixture (“Blend”), self-assembled monolayer from octadecyltrichlorosilane (OTS), Teflon AF, and Polypropylene (PP). Several different techniques, such as spin coating and heat press, were used to fabricate surfaces that have similar θ_a but different θ_r, or similar θ_r but different θ_a. For example, the three types of PMMA surfaces (PMMA(1) to (3)) were all made using spinning coating. However, by using different spinning rate and solution concentration, they have similar θ_a but very different θ_r [30]. Detailed information on surface fabrication is provided in Table S1 of the Appendix E (Section E.1).

Table 6.1: Contact angle data of surfaces used in this study.

Surface Name	θ_a (degree)	θ_r (degree)
Silicon	55.1±0.67	45.7±1.23
PMMA(2)	71.9±0.70	52.7±1.54
PMMA(3)	72.8±0.93	57.9±0.86
Blend (1)	73.0±0.82	59.7±0.97
PMMA(1)	72.6±0.57	60.3±0.86
Blend (2)	79.4±0.73	63.9±0.94
PS (1)	88.6±1.43	66.0±1.27
PEMA	77.6±0.79	68.2±0.94
PS (2)	91.8±1.30	75.3±0.87
PP	101.4±1.30	91.9±1.60
OTS	111.1±1.33	98.2±0.89
Teflon AF	126.4±1.30	116.4±0.93

The experimental setup consists of a motion control system (ILS100CC Linear Stage and XPS-C6 motion controller/driver From Newport) which provided 0.005 mm/s movement during the whole process, a force cell with a resolution of 0.005 mN (F329 from Novatech), and two perpendicular cameras (DR1-D1312 (IE)-200-G2-8 from Photon Focus and A312f from Basler). The acceptor (upper) surface was connected to the motion control system, and the donor (lower) surface was placed on top of the force cell. Each liquid transfer test was conducted with the following steps to represent the process seen in many applications: A 2μL distilled water was placed on the donor surface (Figure 6.1(a)). The acceptor surface was then moved slowly towards the donor surface. A liquid bridge was formed (Figure 6.1(b)) when the donor surface touched the liquid drop. The separation between the two surfaces at this point is denoted as H_0 (initial separation). The movement was stopped when the surface separation decreased to H_{min} (Figure 6.1(c), H_{min} set to be 0.56 mm in all experiments). Then the liquid bridge was slowly stretched (Figure 6.1(d)). When the liquid bridge broke (Figure 6.1(e)), part of the liquid was transferred from the donor surface to the acceptor surface. The images of the liquid bridge during the transfer were recorded by the two perpendicular cameras. The vertical adhesion force between the liquid bridge and the surfaces was measured by the force cell. Twelve pairs of surfaces were used (numbered cases 1 to 12), experiment for each pair of surfaces was repeated 3 times, and average values of the transfer ratio and adhesion force were calculated. Detailed information of all experiments is shown in Table 6.2.

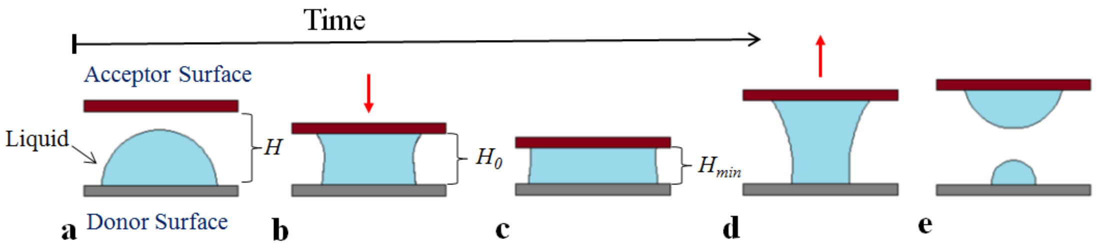

Figure 6.1: Process of quasi-static liquid transfer between two surfaces. (a) liquid drop is placed; (b) liquid bridge forms; (c) liquid bridge is compressed to minimum separation; (d) liquid bridge is stretched; (e) liquid bridge breaks.

Table 6.2: Surfaces used in each experiment, corresponding transfer ratio and occurrence of contact line pinning. $\Delta\theta_r$ is the receding contact angle of the donor surface minus that of the acceptor surface.

Case No.	Acceptor Surface	Donor Surface	$\Delta\theta_r$ (degree)	α (%)	Contact line pinning at the end of transfer occurs on
1	PMMA(1)	Silicon	-14.6	2.7±0.48	Donor surface
2		PMMA(2)	-7.6	12.9±2.98	Donor surface
3		PMMA(3)	-2.4	27.9±3.52	Both surfaces
4		Blend (1)	-0.6	38.5±1.63	Both surfaces
5		Blend (2)	3.6	62.7±1.83	Both surfaces
6		PS (1)	5.7	89.6±0.81	Acceptor surface
7		PEMA	7.9	95.1±0.55	Acceptor surface
8		PS (2)	15	99.4±0.13	Acceptor surface
9		OTS	37.9	100	Acceptor surface
10		Teflon AF	56.1	100	Acceptor surface
11	PP	OTS	6.3	100	Acceptor surface
12	OTS	Teflon AF	18.2	100	Acceptor surface

In all experiments, the ambient temperature was controlled at 19±0.9 ^{o}C. The evaporation ratio (volume of the water evaporated into the air over the total water volume) after the transfer was measured and calculated as 8.06±1.32%, which is considered to be negligible. In all the systems, the Bond Number $Bo = g\rho R^2/\gamma \sim O(10^{-2})$, Capillary Number $Ca = \mu U/\gamma \sim O(10^{-7})$ and Weber Number $We = \rho U^2 R/\gamma \sim O(10^{-9})$ were found to be small, therefore the liquid transfer was quasi-static and the effect of gravity can be neglected. Here g = 9.81 m/s^2 is the gravitational acceleration, U is velocity of the acceptor surface, R is the characteristic length of the liquid bridge, taken to be the contact radius on the donor surface when the liquid bridge forms, and γ, μ, ρ are, respectively, the surface tension (0.0729 N/m), viscosity (1.002 $\times 10^{-3}$ Pa·s), and density (0.9982 g/cm^3) of water.

To better understand the liquid transfer, a theoretical model was developed previously (see [24] for details) and employed in this study to complement experimental observations. As explained in [24], the model took into consideration *CAH* and was shown to accurately predict the behavior of a liquid bridge under quasi-static compression and stretching. Using the model, the evolution of liquid bridge geometry during the transfer process, shown schematically in Figure 6.1, can be obtained. Hence the contact angle and contact radius on both surfaces can be determined. can be obtained. In equilibrium, the adhesion force in the vertical direction (F) can be calculated using contact geometry at either the donor or the acceptor surface; here we used the donor surface:

$$F = 2\pi\gamma R_D \sin\theta_D - \pi R_D^2 \Delta P \qquad (6\text{-}1)$$

where R_D and θ_D are, respectively, the contact radius and angle on the donor surface. ΔP is the Laplace pressure, the pressure difference between inside and outside of the liquid bridge, which can be numerically found using the model. The first term on the right hand side of EQ. (1) arises from the surface tension force along the liquid-air interface, whereas the second term results from the Laplace pressure. The theoretical model is based on equilibrium and therefore can only work under quasi-static condition. When the liquid bridge breaks, it experiences a dynamic event; correspondingly, no convergence solutions can be found from the theoretical model when H exceeds a certain value (denoted as H_{max}).

6.3 Results and Discussion

6.3.1. Process of liquid transfer and contact line pinning

An example of a typical liquid transfer process is provided in Figure 6.2, where a 2 µl water drop was transferred from PMMA(2) to PMMA(1). Both experimental and simulation results are shown for the evolution of contact radius, contact angle and adhesion forces during the process. The liquid bridge was formed at point A, where the contact angles on both surfaces were between their θ_a and θ_r values. When the liquid bridge was compressed, the contact line on each surface first remained pinned while the contact angle increased to θ_a (at point B1 on the acceptor surface and B2 on the donor surface, see Figure 6.2). Further compression did not change the contact angles and the contact radii simply expanded until the end of compression stage (point C).

Next the acceptor surface started to retract and the liquid bridge was stretched. At the beginning of the stretching stage, due to *CAH*, the contact lines on both surfaces were pinned (see inserts 1 and 2 in Figure 6.2) as the contact angles decreased to θ_r (point D1 on the acceptor surface and D2 on the donor surface). As soon as the contact angle on one surface reached θ_r, the contact radius on that surface began to shrink, and the shrinkage continued for a certain distance. However, at the end of the stretching stage, instead of shrinking, the contact radii on both surfaces became pinned again (point E1 on the acceptor surface and E2 on the donor surface), and the contact angles started to increase, and the increase continued till pull-off (point F). Therefore, due to *CAH*, the contact angle can change between θ_a and θ_r, allowing the contact line to be pinned. Contact line pinning can occur multiple times during the transfer: at the beginning of the compression stage, in the early stretching stage, and in the late stretching stage before bridge breakage. The start and end points of the pinning period can be different on the two surfaces. For instance, points B1 and B2 (the ends of contact line pinning in early compression stage for the acceptor and donor surfaces) correspond to different separation distances, *H*. The same applies to points D1 and D2 (ends of contact line pinning in early stretching stage), as well as to points E1 and E2, which are the start points of contact line pinning in late stretching stage.

The adhesion force is completely determined by the shape of the liquid bridge according to EQ. (1). The contact line pinning observed above, which affects the geometry evolution of the liquid bridge, can therefore significantly influence the adhesion force. The evolution of the adhesion force *F* during the transfer process is shown in Figure 6.2(c). During the compression stage (from A to C), *F* continuously increased, although the increase was not smooth and there were two "kinks" in the curve (points B1 and B2, see the insert 3), which corresponds to the end of contact line pinning on the acceptor and donor surfaces, respectively. As stretching started, *F* first experienced a rapid increase, which was associated with contact line pinning in the early stretching stage. The peak value of *F*, i.e., F_{max}, corresponded to the end of contact line pinning on the acceptor surface (D1) for this particular case. As the liquid bridge was further stretched, *F* decreased continuously till the liquid bridge broke. Most previous studies on F_{max} have neglected the effect of contact line pining due to the absence of *CAH*. As seen in Figure 6.2(c), a rapid increase of *F* was observed during the period of contact line pinning (contact angle changing from θ_a or θ_r) in the early stretching stage. The period of contact line pining can become shorter or longer depending on the *CAH* of the surfaces, which in turn varies the period of rapid increase in F. Therefore, it is important and necessary to see how F_{max} is affected by the contact line pinning in the early stretching stage.

The pinning of contact line at the end of stretching stage, on the other hand, can play a crucial role in determining the transfer ratio, since the liquid tends to break at the neck of the bridge while the geometry of the liquid bridge is affected by contact line pinning. Although in the case shown in Figure 6.2, contact line pinning occurred on both surfaces, our results on other surfaces listed in Table 6.2 show that contact line pinning may occur only on the acceptor surface, or only on the donor surface. These different characteristics can lead to very different final transfer ratio. Below we provide a detailed discussion on how the contact line pinning at different stages of liquid transfer are affected by θ_a, θ_r and CAH, and their consequent effect on transfer ratio and maximum adhesion force.

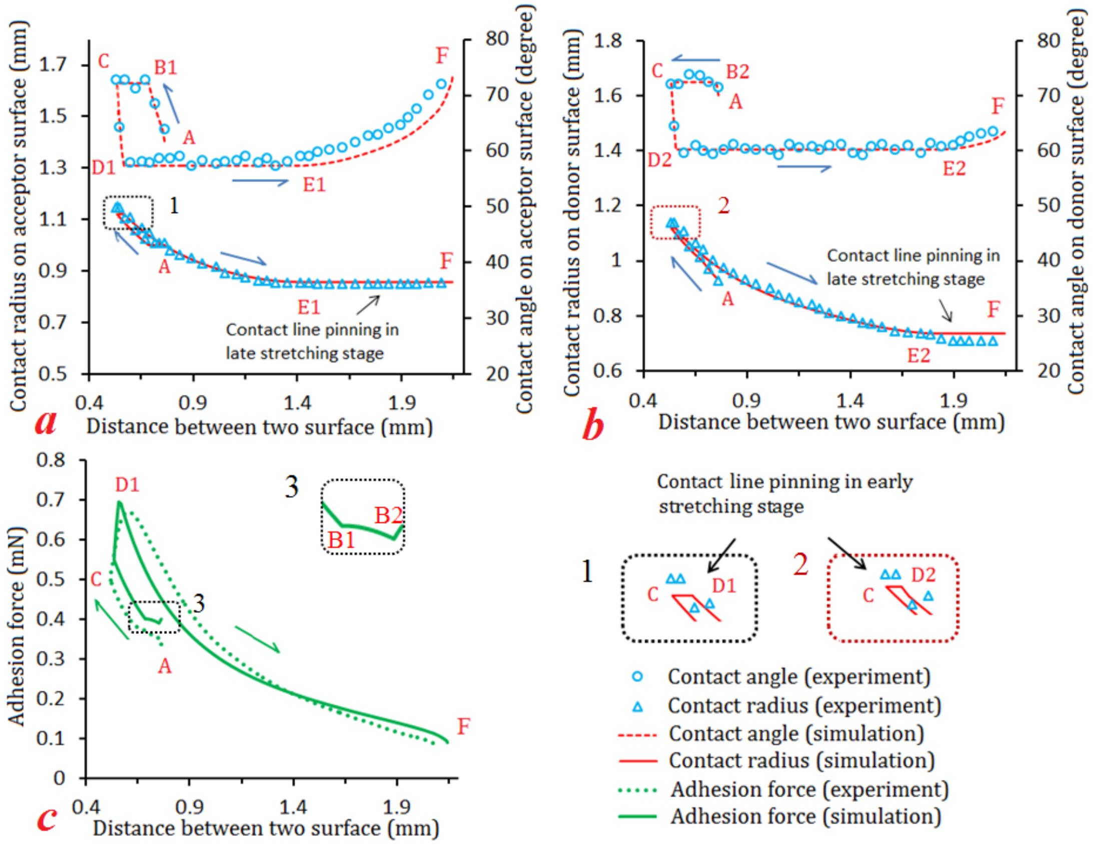

Figure 6.2: Liquid transfer from PMMA(2) to PMMA(1): (a) Evolution of contact angle and contact radius on the acceptor surface. (b) Evolution of contact angle and contact radius on the donor surface. (c) Evolution of the vertical adhesion force. Inserts 1 to 3 relate to (a) to (c), respectively.

6.3.2. Governing parameters for transfer ratio

Table 6.2 provides the transfer ratio, $\Delta\theta_r$, and the occurrence of the contact line pining in late stretching stage, found in experiments. A clear correlation between contact line pinning and $\Delta\theta_r$ of the two surfaces can be observed. Specifically, the characteristic of contact line pinning can be divided into three regimes: when $\Delta\theta_r$ is negative and smaller than ~−5°, contact line pinning can be observed only on the donor surface (Regime I); when $\Delta\theta_r$ is close to zero, contact line is pinned on both surfaces (Regime II); and when $\Delta\theta_r$ is positive and larger than ~+5°, contact line pining can be found only on the acceptor surfaces (Regime III). For Quasi-static liquid transfer, since the effects of the viscous and inertial forces are negligible, the shape of the liquid bridge before it breaks is critical to the value of transfer ratio. As expected, it can be seen that the transfer ratio is strongly correlated with contact line pinning: cases in Regime I have a small transfer ratio, those in Regime II have a medium transfer ratio while a large transfer ratio (close to 100%) can be found for cases in Regime III. The approximate boundaries between the three regimes in Table 6.2, in terms of $\Delta\theta_r$ (roughly -5^{o} and $+5^{o}$), are based only on the observation of the 12 experimental cases. To quantify the boundaries in a more rigorous manner, we used the theoretical model to conduct a series of simulations for a liquid bridge between surfaces with different receding contact angles. Specifically, for a given θ_r on the acceptor surface, θ_r on the donor surface was systematically varied from 0^{o} to 140^{o}. For each pair of surfaces, the liquid transfer process was tracked, and where contact line pinning occurred at the end of the stretching stage was identified. In addition, θ_r on the acceptor surface was also varied from 0^{o} to 140^{o} to allow a complete search. Over 200 pairs of surfaces were simulated, which allowed us to generate a map as shown in Figure 6.3. The map shows three distinct regimes, and they are symmetrical about the line $(\theta_r)_{\mathrm{acc}} = (\theta_r)_{\mathrm{don}}$, where $(\theta_r)_{\mathrm{acc}}$ and $(\theta_r)_{\mathrm{don}}$ denote the receding contact angles of the acceptor and donor surfaces, respectively. For example, if a pair of surfaces are located in Regime I (contact line pinning only on the acceptor surface), when the acceptor and donor surfaces are swapped, contact line pinning will be found only on the donor surface, i.e, in Regime III.

It can also be seen from Figure 6.3 that the occurrence of contact line pinning is not only affected by $\Delta\theta_r$, but also by the magnitude of $(\theta_r)_{\mathrm{acc}}$ and $(\theta_r)_{\mathrm{don}}$. In particular, when the acceptor surface has $(\theta_r)_{\mathrm{acc}} = 0^{o}$, the boundary between Regime II and III is at $(\theta_r)_{\mathrm{don}} = 30.7^{o}$. With the increase in $(\theta_r)_{\mathrm{acc}}$ and $(\theta_r)_{\mathrm{don}}$, the width of Regime II decreases. Regime II vanishes when one of the surfaces has a receding contact angle larger than 90^{o}. This implies that when either $(\theta_r)_{\mathrm{acc}}$ or $(\theta_r)_{\mathrm{don}}$ is larger than 90^{o}, contact line pinning on both surfaces can only be found when $(\theta_r)_{\mathrm{acc}}$ or $(\theta_r)_{\mathrm{don}}$ are identical. An example for this is demonstrated in the Appendix E (Section E.2), where we show that for liquid transfer between two identical surfaces with $(\theta_r)_{\mathrm{acc}} = (\theta_r)_{\mathrm{don}} = 95^{o}$, contact line pinning can be found on both surfaces. When we slightly increase $(\theta_r)_{\mathrm{don}}$ to 95.5^{o}, contact line pinning is found only on the acceptor surface. And if we decrease $(\theta_r)_{\mathrm{don}}$ to 94.5^{o}, contact line pinning can be found only on the donor surface.

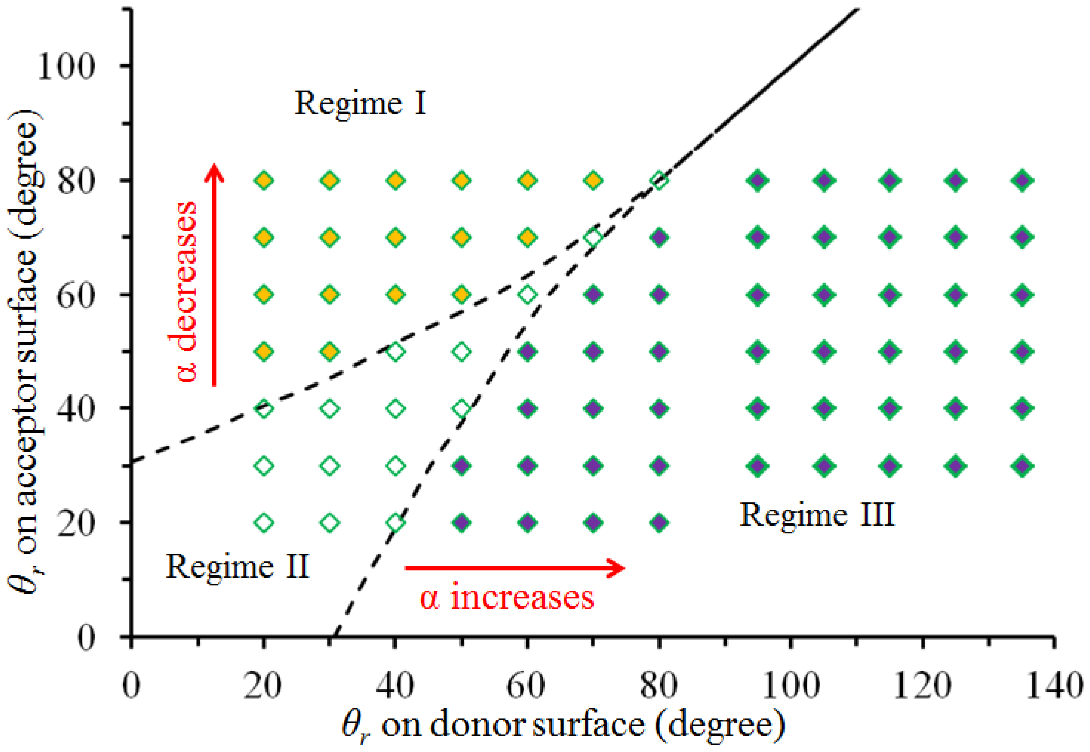

Figure 6.3: Map of three regimes for contact line pinning near the end of liquid transfer, in terms of the receding contact angles of the two surfaces. The map is generated by using the theoretical model developed in [24]. Regime I: contact line is pinned only on the donor surface. Regime II: contact lines are pinned on both acceptor and donor surfaces. Regime III: contact line is pinned only on the acceptor surface. The diamond points show $(\theta_r)_{\mathrm{don}}$ and $(\theta_r)_{\mathrm{acc}}$ of selected cases for the study of R_{min}.

Although the map shown in Figure 6.3 was obtained based on simulations of water with a particular surface tension of 72 mN/m, it can be shown that given the receding contact angles of the two surfaces the boundaries of the three regimes are insensitive to the changes in the liquid surface tension (see Appendix E Section E. 3). Hence this map is universal for all liquids, and can be used to predict the occurrence of contact line pinning as long as the receding contact angles between the liquid and surfaces are known. This certainly does not imply that the surface tension of liquid will not affect the liquid transfer process. For liquid transfer between two given surfaces, if the liquid surface tension changes, the contact angles will usually change as well, resulting in the liquid transfer being located in different places on the map.

Since the transfer ratio under quasi-static condition is mainly determined by the liquid bridge shape, the value of the pinned contact radius (hereafter denoted as R_{min}), which governs the breakage shape (the shape of the liquid bridge at H_{max}) of the liquid bridge is important to the final transfer ratio. While the occurrence of contact line pinning is categorized into 3 regimes in Figure 6.3, calculation of value of R_{min} each regime allows us to explore how its value depends on the receding contact angles. To do so, we took 79 cases from the 200 simulation cases (shown as diamonds in Figure 6.3), and calculated R_{min} for each case. Figure 6.4(a) shows the results for R_{min} on the acceptor surface, which only applies to cases in the regimes II and III; each curve corresponds to a particular $(\theta_r)_{\mathrm{acc}}$. Experimental data on the pinned contact radius are also shown on the same plot, which overlap with relevant simulation curves. From the plot, it can be seen that R_{min} on the acceptor surface increases as $(\theta_r)_{\mathrm{don}}$ increases or as $(\theta_r)_{\mathrm{acc}}$ decreases. This is because increasing $(\theta_r)_{\mathrm{don}}$ or decreasing $(\theta_r)_{\mathrm{acc}}$ both correspond to the situation where the liquid becomes more attracted by the acceptor surface. Therefore, more liquid tend to stay close to the acceptor surface, increasing R_{min} on the acceptor surface. A similar plot is generated in Figure 6.4(b), but for R_{min} on the donor surfaces, which only applies to cases in Regime I and II. Similar to Figure 6.4(a), R_{min} of the donor surfaces increase as the liquid becomes more attracted to the donor surface, i.e., when $(\theta_r)_{\mathrm{don}}$ decreases or when $(\theta_r)_{\mathrm{acc}}$ increases.

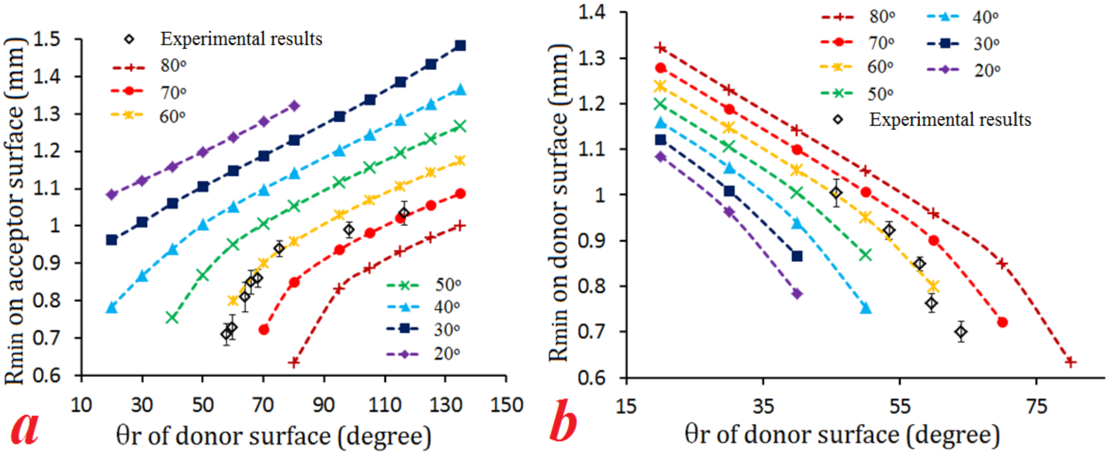

Figure 6.4: Value of R_{min}: (a) on the acceptor surface; (b) on the donor surface. In each graph, R_{min} is plotted against $(\theta_r)_{\mathrm{don}}$ and each curve corresponds to a particular $(\theta_r)_{\mathrm{acc}}$.

Associated with the change of R_{min} on the donor and/or acceptor surfaces, the neck i.e. the narrowest point of the liquid bridge also changes its location. Specifically, as $(\theta_r)_{\text{don}}$ increases or as $(\theta_r)_{\text{acc}}$ decreases, the liquid becomes more attracted to the acceptor surface, R_{min} on the acceptor surface increases and/or R_{min} on the donor surface decreases. Consequently, the neck of the liquid bridge is located closer to the donor surface. Figure 6.5(a) shows the experimental data for $H^* = H_N/H$ as a function of $(\theta_r)_{\text{don}}$, where H_N is the distance between the neck of the liquid bridge and the donor surface, when the bridge breaks. The corresponding transfer ratios are also shown in Figure 6.5(a). It can be seen that, as expected, the height of the neck decreases with the increase of $(\theta_r)_{\text{don}}$. Since the liquid bridge breaks at the neck, with the decrease in H^* the transfer ratio should increase. When $(\theta_r)_{\text{don}}$ is larger than 90°, H^* reduces to zero, the liquid bridge breaks at the donor surface and a complete transfer (α = 100%) can be observed.

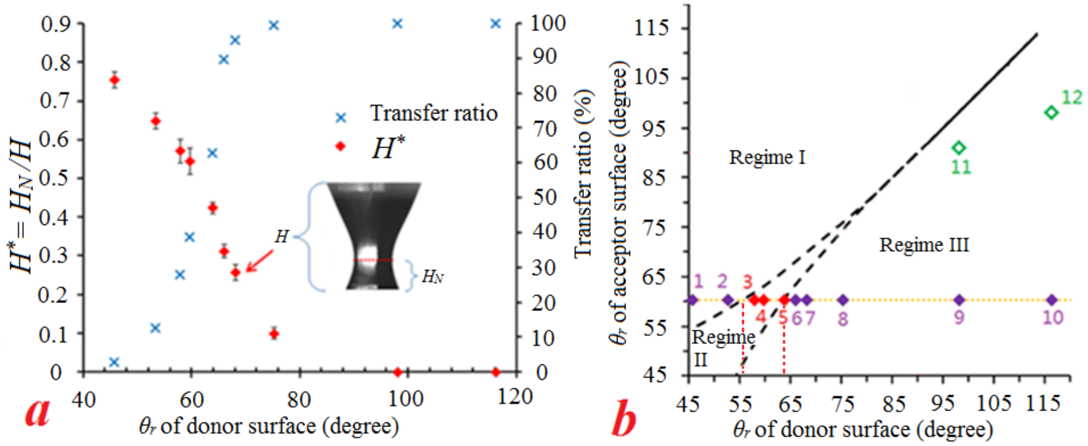

Figure 6.5: (a)$H^*$of experimental cases 1 to 10 as a function of $(\theta_r)_{\text{don}}$, and the corresponding transfer ratio. (b) Location of the 12 experimental cases in the regime map.

Based on the discussion above, the parameters that control the transfer ratios under quasi-static condition are identified to be the receding contact angles, and the transfer ratio of all the 12 experimental cases can be explained. Locations of all the experiment studies on the regime map are shown in Figure 6.5 (b). For cases 1 to 10, the acceptor surface ($(\theta_r)_{\text{acc}}$ = 60.3°) was fixed. The value of $(\theta_r)_{\text{don}}$ increases from cases 1 to 10. Therefore, R_{min} on the donor surface (for cases 1 to 5) decreases and R_{min} on the acceptor surface (for cases 3 to 10) increases. Associated with the change in R_{min}, H^* shows a decreasing trend from case 1 to 10, leading to an increase in transfer ratio. Also shown in Figure 6.5(b), for $(\theta_r)_{\text{acc}}$ = 60.3°, the width of Regime II is only approximate

8^{o} (from 56^{o} to 64^{o}, dashed line in Figure 6.5(b)). As a result, the transfer ratio changes rapidly from very small (in Regime I) to very large (in Regime III) values. Cases 9 to 12 all have a $(\theta_r)_{\mathrm{don}}$ larger than 90^{o}. In such situation, Regime II becomes a solid line, contact line pinning on both surfaces can only be observed when $(\theta_r)_{\mathrm{acc}} = (\theta_r)_{\mathrm{don}}$. As long as $(\theta_r)_{\mathrm{acc}} < (\theta_r)_{\mathrm{don}}$, the data will all be located in Regime III. This is why despite the large difference in $(\theta_r)_{\mathrm{acc}}$ for these cases, the liquid bridge all breaks on the donor surface ($H^{*}= 0$) and 100% transfer was achieved.

6.3.3. Transfer ratio prediction

Having understood how the transfer ratio is controlled by $(\theta_r)_{\mathrm{acc}}$ and $(\theta_r)_{\mathrm{don}}$, now one new question arises: is it possible to predict the transfer ratio based on the surface wettability? Given the general nature of the regime map in Figure 6.3 and the above discussion, a closed-form empirical equation for the transfer ratio should be obtainable in terms of $(\theta_r)_{\mathrm{acc}}$ and $(\theta_r)_{\mathrm{don}}$. An equation in the form of EQ. (2) is proposed, where $(\theta_r)_{\mathrm{acc}}$ and $(\theta_r)_{\mathrm{don}}$ are in radians, and m and n are positive and dimensionless constants. When $(\theta_r)_{\mathrm{don}} - (\theta_r)_{\mathrm{acc}}$ is very negative, the exponential in the denominator is very large, resulting in α being close to zero. For very large and positive $(\theta_r)_{\mathrm{don}} - (\theta_r)_{\mathrm{acc}}$, the exponential function is vanishingly small, and hence α converges to one. Because the width of Regime II decreases with the increases of $(\theta_r)_{\mathrm{acc}}$ and $(\theta_r)_{\mathrm{don}}$, the term $(\theta_r)_{\mathrm{don}} + (\theta_r)_{\mathrm{acc}}$ is added to describe how fast the transfer ratio changes from 0% to 100%. Therefore EQ. (2) captures the essential characteristics of transfer ratio observed earlier.

$$\alpha = \frac{1}{1+e^{-m((\theta r)acc+(\theta r)don)^{n} *((\theta r)don-(\theta r)acc)}} \quad (6\text{-}2)$$

To find the coefficients m and n, multiple regression analysis was conducted based on the experimental results shown in Table 6.2 as well as 9 additional experiments given in Section E.4 of the Appendix E where 3 other liquids than water were used. The value of m and n are found to be 3.142 and 2.528, respectively. Figure 6.6 shows the transfer ratio measured from the experiments versus the transfer ratio obtained with EQ(2). It can be seen that the empirical equation fit the experimental results well.

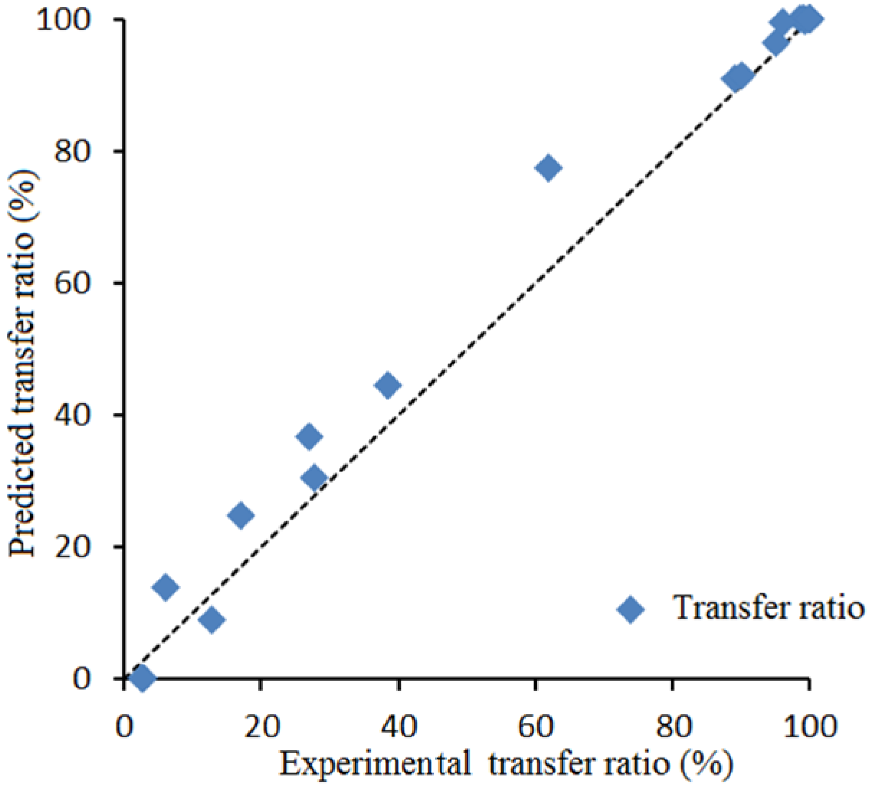

Figure 6.6: Transfer ratios measured from experiments versus those predicted from EQ. (2). Data fall on the dotted line when the experimental value is identical to the predicted value.

With the regime map and the empirical EQ (2), for any quasi-static liquid transfer, the occurrence of contact line pining as well as the transfer ratio can be estimated by only knowing θ_r of the two surfaces without performing any experiments. This provides a very useful predictive tool for selecting surfaces in many practical applications. Also according to the map, liquid transfer between two hydrophobic surfaces (θ_r larger than 90^o) is practically always in Regime I or III. This suggests that a very large transfer ratio can be achieved by even using two hydrophobic surfaces which have different receding contact angles.

6.3.4 Maximum adhesion force

During the process of liquid transfer, capillary forces (adhesion force) between liquid and the two surfaces are generated. Such capillary force provides another new strategy for the design of adhesion systems, i.e., wet adhesion. Recently, a number of studies were performed to design such wet adhesion system with liquid bridges between two surfaces. The value of F_{max} determines the adhesive strength of the wet adhesion system, and hence is of particular interest. Therefore, in this section, discussions on how the surface contact angles and *CAH* affect F_{max} are provided. F_{max} measured from experiments (cases 1 to 10) are shown in Figure 6.7. Since these experiments have the same acceptor surface, F_{max} is respectively plotted as a function of θ_a and θ_r of the donor surface in Figures 6.7 (a) and (b). Based on these two plots, F_{max} is seen to be affected by both θ_a and θ_r of the donor surface; i.e., F_{max} decreases as θ_a or θ_r increases. However, it is unclear from the results whether one of the contact angles may be more important in determining the value of F_{max}. For example, the donor surfaces in cases 5 (purple) and 6 (red) both have larger θ_a and smaller θ_r than the donor surface in case 7 (yellow). However, F_{max} in case 7 is larger than the maximum adhesion force in case 6 but smaller than that in case 5. To understand the roles of contact angles in determining F_{max}, a systematic study was performed using the theoretical model.

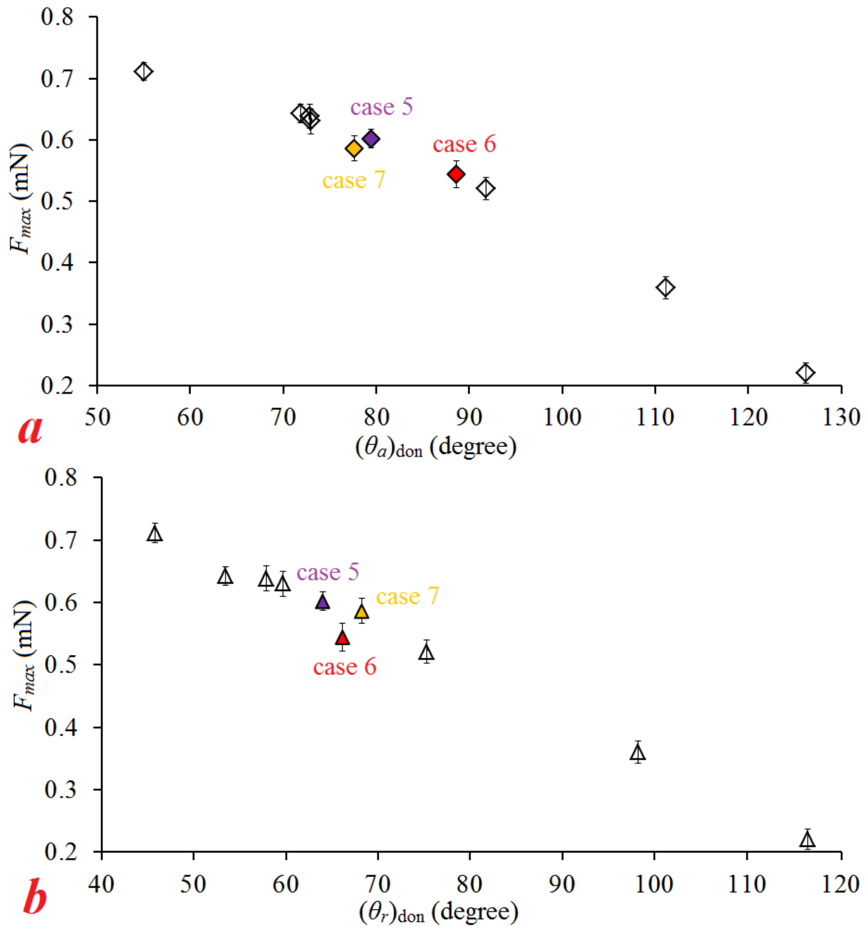

Figure 6.7: Maximum adhesion force as a function of (a): θ_a of donor surface, and (b): θ_r of donor surface.

6.3.4.1 Symmetric system

Simulations were first performed for a liquid bridge compressed and stretched between several pairs of identical surfaces ($(\theta_a)_{\text{acc}} = (\theta_a)_{\text{don}}$ and $(\theta_r)_{\text{acc}} = (\theta_r)_{\text{don}}$). In all simulations the initial (H_0) and minimum (H_{min}) separations were set as 0.8 mm and 0.6 mm, respectively. At the time when the liquid bridge is formed, the initial contact angle between the liquid bridge and the surfaces are set to be the average contact angle ($\theta_{ave}=(\theta_a+\theta_r)/2$). It was shown in [24] that as long as H_{min} is sufficiently small, this initial contact angle will not affect the process of liquid transfer or F_{max}.

Figure 6.8(a) shows F_{max} as a function of θ_r for five different θ_a values. When the surfaces have intermediate θ_r (between 55°-90°), similar to our experimental results, F_{max} shows a decreasing trend both with the increase in θ_r and in θ_a. However, for surfaces with a small value of θ_r (smaller than 55^o), the curves are paralleled with one another, indicating that F_{max} is only influenced by θ_a. For surfaces that have very large θ_r (larger than 90^o), all the curves collapse onto a single one and F_{max} is only affected by θ_r.

To understand the results shown in Figure 6.8(a), the evolutions of contact angle and adhesion force for a liquid bridge between three pairs of identical surfaces are provided in Figure 6.8(b), (c) and (d), respectively for surfaces with small receding contact angle (θ_a: 130^o θ_r: 45^o), intermediate receding contact angle (θ_a: 130^o θ_r: 85^o), and large receding contact angle (θ_a :130^o θ_r: 125^o).. In all the three cases, there is a period in the early stretching stage when the contact line is pinned and the contact angle reduces from θ_a to θ_r. The maximum adhesion force (circled with dashed lines) occurs at different locations in the three cases: during the contact line pinning in Figure 6.8(b), at the end of the contact line pinning in Figure 6.8(c), and well after the contact line pinning in Figure 6.8(d). First consider the situation in Figure 6.8(b). According to EQ (1), the magnitude of adhesion force F is controlled by R_D, θ_D and ΔP. When the contact angle is changing from θ_a to θ_r, R_D is a constant, which is the same as the contact radius at H_{min}. At H_{min}, the profile of liquid bridge is solved by applying θ_a and H_{min} as boundary conditions, so R_D is determined by θ_a and H_{min}. θ_D and ΔP during contact line pinning are obtained by applying the separation H and the contact radius on the two surfaces (R_D) as boundary conditions. Therefore, θ_D and ΔP are solely determined by H and R_D, while as explained above R_D is a function of θ_a and H_{min}. As a result, the profile of the liquid bridge when F_{max} occurs is determined by H_{min}, current H, and θ_a .This explains why when θ_r is small (< 55^o), F_{max} is influenced by θ_a but not θ_r.

When the surfaces have an intermediate receding contact angle (Figure 6.8(c)), F_{max} occurs when the contact angle just decreases to θ_r. As EQ (1) shows, the adhesion force at this point is determined by the instantaneous R_D (a function of θ_a and H_{min}), θ_D (= θ_r), and ΔP (determined by H and R_D). Therefore, for intermediate θ_r, F_{max} can be affected by both θ_a and θ_r. For surfaces with large θ_r (Figure 6.8(d)), F_{max} is found after the contact angles reduce to θ_r. In such situations, $\theta_D = \theta_r$, while the shape of the liquid bridge, including R_D and ΔP, are determined by H and θ_D. Hence it is expected that for these cases, F_{max} will only be affected by θ_r but not θ_a.

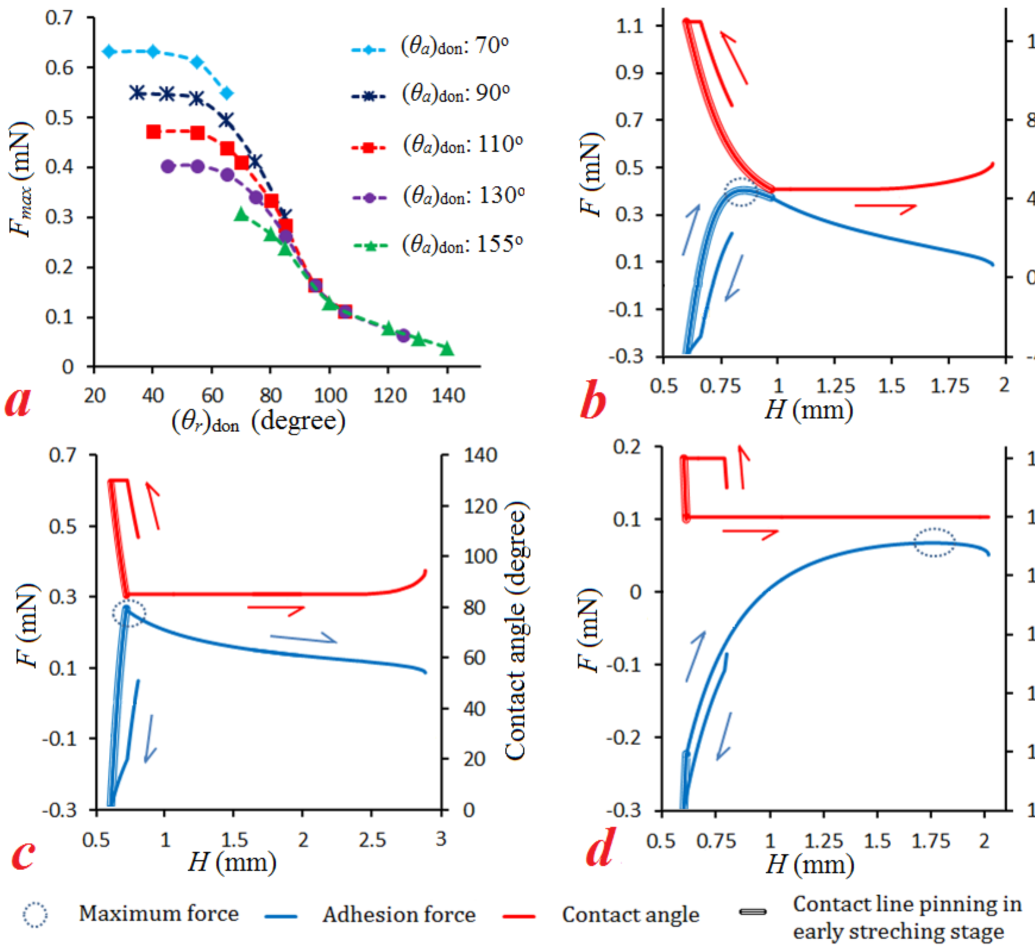

Figure 6.8: (a) Maximum adhesion force for a liquid bridge compressed and stretched between two identical surfaces. F_{max} is plotted as a function of θ_r of the surfaces for five different θ_a. (b)-(d) Evolution of contact angle and adhesion force during symmetric compressing and stretching of a water drop between two identical surfaces ((b): θ_a=130°, θ_r=45°; (c): θ_a=130°, θ_r=85°; (d): θ_a=130°, θ_r=125°).

6.3.4.2 Asymmetric System

Having understood how F_{max} of a symmetric liquid bridge (between two identical surfaces) is affected by θ_a and θ_r, we can now further study how F_{max} of an asymmetric liquid bridge (between two different surfaces) is influenced by surface wettability. To do so, liquid bridges compressed and stretched between a fixed acceptor surface (the same as the acceptor surface used in the experiments, with θ_a= 72.6° and θ_r= 60.3°) and different donor surfaces are simulated. In these simulations, H_0 and H_{min} were set as 0.8 mm and 0.56 mm (the same as in the experiments), respectively. Similar to the simulations in Figure 6.8(a), the initial contact angle was set to be θ_{ave} for each surface. The results are shown in Figure 6.9(a). Similar to the results shown in Figure 6.8(a), for each of the curves, when $(\theta_r)_{\mathrm{don}}$ is small, all the curves are leveled and only $(\theta_a)_{\mathrm{don}}$ influences F_{max}. When $(\theta_r)_{\mathrm{don}}$ becomes larger, the value of F_{max} decreases with the increase of $(\theta_r)_{\mathrm{don}}$. However, for the asymmetric liquid bridge, the curves do not overlap as in Figure 6.8(a), when $(\theta_r)_{\mathrm{don}}$ becomes large; hence $(\theta_r)_{\mathrm{don}}$ is not the only governing parameters for F_{max}. For example, for the symmetric liquid bridge, when the surfaces have the value of $\theta_r = 98^{\circ}$ (considered as large value of θ_r), the value of F_{max} of the transfer cases are always the same no matter the value of θ_a of surfaces. However, this observation becomes invalided for the asymmetric liquid bridge. It can be seen in Figure 6.9(a) that although cases A ($(\theta_a)_{\mathrm{don}}$: 100° and $(\theta_r)_{\mathrm{don}}$: 98°) and B ($(\theta_a)_{\mathrm{don}}$: 120° and $(\theta_r)_{\mathrm{don}}$: 98°) have the same value of $(\theta_r)_{\mathrm{don}} = 98^{\circ}$, the values of F_{max} of the cases A and B are different.

As demonstrated in the previous section of this chapter, for symmetric liquid bridge, governing parameters for F_{max} are determined by the status of contact line pinning in the early stretching stage when F_{max} occurs. That is, the governing parameters can be only θ_a, both θ_a and θ_r, or only θ_r, when F_{max} happens during, at the end of or after contact line pinning. However, for asymmetric liquid bridges, since the wettability of the two surfaces are different, when F_{max} occurs, the status of contact line pinning on the two surfaces can be very different. For instance, F_{max} can occur when the donor surface is at the end of contact line pinning but the contact angle on the acceptor surface has not reached θ_r yet. Figure 6.9 (b) and (c) show the evolutions of the contact angle on both surfaces in cases A and B. The evolutions of the adhesion force are also shown in the plots. It can be seen that, for case A, F_{max} happens within the period of contact line pinning on the acceptor surface, but after the contact line pinning on the donor surface. Therefore, based on the discussion in Section 6.3.4.1, the governing parameters for F_{max} in case A are $(\theta_a)_{\mathrm{acc}}$ and $(\theta_r)_{\mathrm{don}}$. However, for case B, which has a much larger $(\theta_a)_{\mathrm{don}}$, F_{max} happens at the end of the contact line pinning on the donor surface and after the contact line pinning on the acceptor surface; hence F_{max} in case B is governed by $(\theta_r)_{\mathrm{acc}}$, $(\theta_a)_{\mathrm{don}}$ and $(\theta_r)_{\mathrm{don}}$. The $(\theta_a)_{\mathrm{don}}$ of case B is different from that of case A. Therefore, the values of F_{max} of the cases A and B are different.

The different $(\theta_a)_{\text{don}}$ in cases A and B also lead to different F_{max} values. From Figure 6.9(b) and (c), it can be seen that in both cases the adhesion force experiences a rapidly increases during the period of contact line pinning on both surfaces ($a1$ to $a2$ in case A, $b1$ to $b2$ in case B). Due to the very small *CAH* (2°) of the donor surface in case A, the contact line pinning on the donor surface ($a1$ to $a2$ in Figure 6.9(b)) is much shorter compared to that of case B ($b1$ to $b2$ in Figure 6.9(c)). This has limited the increase in F_{max} and results in smaller F_{max} in case A compared with F_{max} in case B.

Since the length of the period of contact line pinning is controlled by the *CAH* of surfaces, it is of interest to see how F_{max} of all the cases shown in Figure 6.9(a) changes with the *CAH* of the donor surfaces, which is shown in Figure 6.9(d). Each of the curves is associated with a given $(\theta_a)_{\text{don}}$. It can be seen that F_{max} first increases with *CAH* of the donor surface when the *CAH* is small, but becomes insensitive to the *CAH* of the donor surface when it is large. To explain, we note that all the cases presented here share the same acceptor surface. Since the increase in adhesion force is limited by the termination of contact line pinning on both surfaces, the surface which has smaller *CAH* and hence shorter contact line pinning essentially controls the magnitude of F_{max}. When *CAH* of the donor surface is small, it controls the magnitude of F_{max}, which is why there is a positive relation between *CAH* of the donor surface and F_{max}. When *CAH* of the donor surface is large, *CAH* of the acceptor surface governs F_{max}. Therefore, all the curves in Figure 6.9(d) are leveled when *CAH* of the donor surface is large.

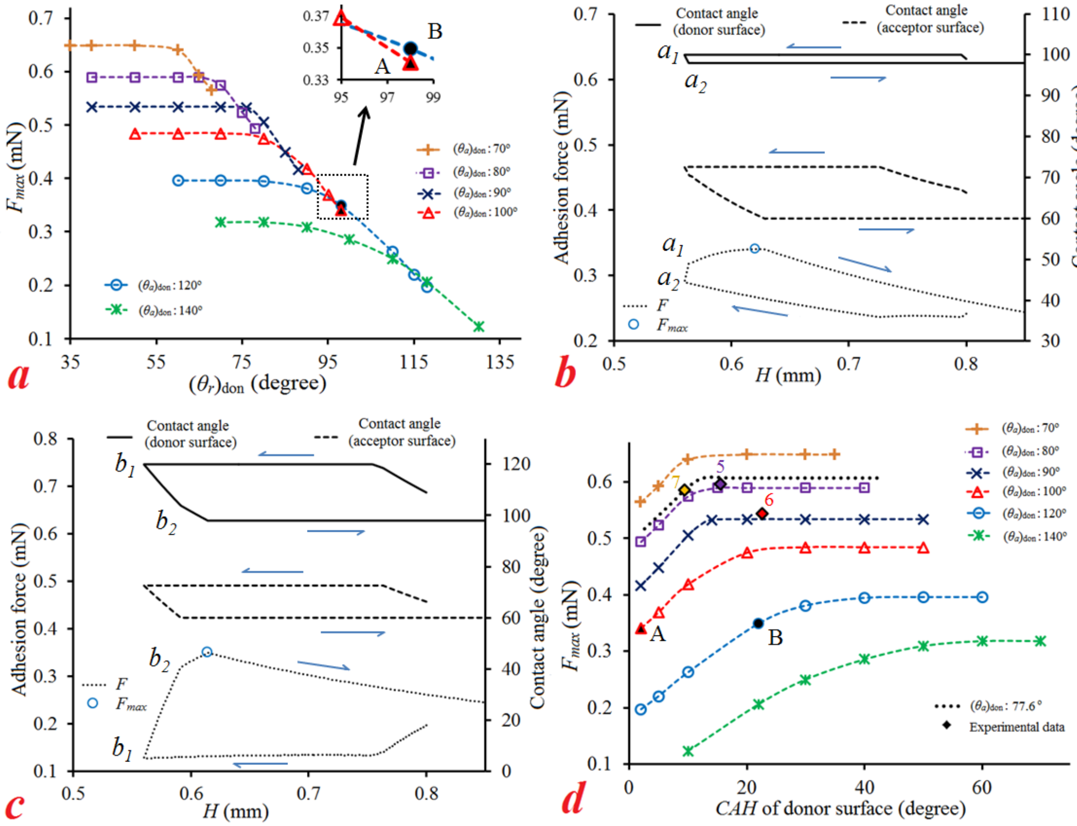

Figure 6.9: (a) Maximum adhesion force for a liquid bridge compressed and stretched between two different surfaces. The acceptor surface is fixed with θ_a: 72.6° and θ_r: 60.3°, while the donor surface is varied. (b) Evolutions of contact angle and adhesion force of cases A. (c) Evolutions of contact angle and adhesion force of cases B. (d) F_{max} versus CAH of the donor surface.

Summarized from the discussion above, for asymmetric liquid bridge, due to the different wettability of the two surfaces, the length of the contact line pinning on both surfaces are important to determine the value of F_{max}. A longer period of contact line pinning on both surfaces at the beginning of the stretching stage is desired for a larger value of F_{max}. With Figure 6.9(d), now we can answer the question why in the experimental results presented in Figure 6.7, F_{max} in case 7 is smaller than F_{max} in case 5 but larger than that in case 6. From Figure 6.9(d), it can be seen that the value of $(\theta_a)_{\text{don}}$ of case 6 (88.6 °) is much larger than $(\theta_a)_{\text{don}}$ of the other two cases(case 5: 79.4 °, and case 7: 77.6°). Therefore, case 6 has the smallest value of F_{max} among the three cases. Compared with case 5, the donor surfaces in case 7 has a relatively small CAH

(case 5:15.5 ^{o}, case 7: 9.4^{o}). The black dotted line in Figure 6.9(d) shows F_{max} as a function of *CAH* of the donor surface with $(\theta_a)_{\mathrm{don}} = 77.6^{o}$ (the same as in case 7). Based on this dotted line, it can be known that F_{max} of case 7 is not only controlled by $(\theta_a)_{\mathrm{don}}$, but also *CAH* of the donor surface. Therefore, although the case 7 has the smaller value of $(\theta_a)_{\mathrm{don}}$ than that of case 5, the F_{max} of case 7 is smaller than F_{max} in case 5 due to the small value of *CAH*.

6.4 Conclusions

This chapter provides systematic studies on the role of θ_a, θ_r and *CAH* in determining the transfer ratio and maximum adhesion force generated between the surfaces and liquid during the process of quasi-static liquid transfer. The transfer ratio was found to be governed by contact line pinning at the end of the transfer. A general transfer map based on θ_r of the donor and acceptor surfaces was generated to identify the three regimes where the contact line pinning occurs only on donor, only on acceptor or on both surface. Based on this map, an empirical equation is provided which is able to predict the transfer ratio by only knowing θ_r of the two surfaces. The maximum adhesion force F_{max} is strongly influenced by the contact line pinning in early stretching stage. For symmetric liquid bridge between two identical surfaces, F_{max} may be determined only by θ_a, only by θ_r, or by both θ_a and θ_r, depending on the magnitude of the contact angles. For asymmetric bridges, F_{max} is controlled by the lengths of contact line pinning periods on the two surfaces, which is affected by the *CAH* of the surfaces.

Bibliography

(6.1) A. A. Darhuber, S. M. Troian, *J. Appl. Phys.* **2001**, 90, 3602--3609.

(6.2) H. W. Kang, H. J. Sung, T-M Lee, D-S Kim, C-J Kim, *J. Micromech. Microeng.* **2009**, 19, 015025.

(6.3) J. A. Lee, J. P. Rothstein, M. Pasquali, *J. Non-Newtonian Fluid Mech.* **2013** 199, 1--11.

(6.4) W-X Huanga, S-H Leea, H. J. Sunga, T-M Leeb, D-S Kimb, *Inter. J. Heat Fluid Flow* **2008**, 29, 1436--1446.

(6.5) M. Pudas, J. Hagberg, S. Leppavuori, *J. Eur. Ceram. Soc.* **2004**, 24, 2943--2950.

(6.6) P. Kopola, T. Aernouts, S. Guillerez, H. Jin, M. Tuomikoski, A. Maaninen, J. Hast, *Solar Energy Mat. Solar Cells* **2010,** 94, 1673--1680.

(6.7) D. Bonn, J. Eggers, J. Indekeu, J. Meunier, E. Rolley, **2009**, 81, 739--805.

(6.8) B. Qian, K. S. Breuer, *J. Fluid Mech.* **2011**, 666, 554--572.

(6.9) J. Qian, H. Gao, *Acta Biomaterialia* **2006**, 2, 51--58.

(6.10) A. F. G. Dixon, P. C. Croghan, R. P. Gowing, *J. Expl. Biol.* **1990**, 152, 243--253.

(6.11) S. Gorb, *Proc. Roy. Soc. Lond. B* **1998**, 265, 747--52.

(6.12) T. Eisner, D. J. Aneshansley, *Proc. Natl. Acad. Sci.* **2000**, 97, 6568--6573.

(6.13) W. Federle, M. Riehle, A. S. G. Curtis, R. J. Full, *Integr. Comp. Biol.* **2002**, 42, 1100--1106.

(6.14) A. V. Chadov, E. D. Yakhnin, *Kolloidn. Zh.* **1979**, 41, 817.

(6.15) E. D. Yakhnin, A. V. Chadov, *Kolloidn. Zh.* **1983**, 45, 1183.

(6.16) E. Cheung, M. Sitti, *J. Adhesion Sci. Tech.* **2008**, 22, 569-589.

(6.17) B. Qian, M. Loureiro, D. Gagnon, A. Tripathi, and K. S. Breuer, *Phys. Rev. Lett.* **2009**, 102 (16), 164502.

(6.18) M. A. Fortes, *J. Colloid Interface Sci.* **1982**, 88, 338-352.

(6.19) G. Lian, C. Thornton, M. J. Adams *J. Colloid Interface Sci.* **1993**,161, 138--147.

(6.20) S. Dodds, M. Carvalho, S. Kumar *Phy. Fluids*, **2009**, 21, 092103.

(6.21) C. N. C. Lam, R. Wu, D. Li, M. L. Hair, A. W. Neumann, *Adv. Colloid Interface Sci.* **2002**, 96, 169--191.

(6.22) H. Tavana, in *Applied Surface Thermodynamics*, 2nd ed.; A.W. Neumann, R. David, Y. Zuo, Ed.; Surfactant Sci. Series; CRC: Boca Raton, USA, 2010; 151, 315--316.

(6.23) E. Pierce, F. J. Carmona, A. Amirfazli, *Colloids Surfaces A* **2008**, 323, 73--82.

(6.24) H. Chen, A. Amirfazli, T. Tang, *Langmuir* **2013**, 29, 3310--3319.

(6.25) E. J. De Souza, L. Gao , T. J. McCarthy, E. Arzt, A. J. Crosby, *Langmuir* **2008**, 24 (4), 1391--1396.

(6.26) E. J. De Souza, M. Brinkmann, C. Mohrdieck, E. Arzt, *Langmuir* **2008**, 24 (16), 8813--8820.

(6.27) S-J Hong, T-H Chou, S. H. Chan, Y-J Sheng, H-K Tsao, *Langmuir* **2012**, 28, 5606--5613.

(6.28) B. Samuel, H. Zhao, K-Y Law, *J. Phys. Chem. C* **2011**, 115, 14852--14861.

(6.29) H. Chen, T. Tang, A. Amirfazli, *Soft Matt.* **2014,** 10, 2503--2507.

(6.30) H. Chen, T. Tang, A. Amirfazli, *Colloids Surface A* **2012**, 408, 17--21.

Chapter 7

7. Effects of Surface Contact Angle on Fast Liquid Transfer

7.1 Introduction

The traditional roll to roll printing technique (i.e. offset printing) is one of the most common techniques used for high-volume printing of newspaper and books due to its good printing quality and operational convenience. Recently, a number of studies have been performed to print high resolution micro-scale electrical circuits, solar cells and semiconductors with such printing technique [1-3]. The key component of this printing technique is the liquid transfer from one surface (donor) to the target substrate (acceptor) by stretching and breaking a liquid bridge. Such liquid transfer process can not only be seen in printing, but also in other fields, e.g. packaging, drop deposition and micro-gripping [4-6]. The transfer ratio (α), which is defined as the liquid transferred to the acceptor surface over the total volume of the liquid, is always of interest due to its practical importance. For example, in the offset or electronic printing, a clean transfer ($\alpha = 1$) is desired to improve the printing quality (e.g. breaks in circuit) and minimize the quantity of wasted material.

The pioneering studies of liquid transfer were done by Chadov and Yakhnin [7, 8] where experiments of liquid transfer between different surfaces under different stretching speed were investigated. Based on the dominant forces, they defined, for the first time, three possible regimes for liquid transfer: Quasi-static Regime where surface forces dominate; Dynamic Regime where viscous/inertial forces dominate; and Transition Regime where both surface and viscous/inertial forces play important roles. Based on the dominant forces, different parameters were suggested to control the transfer ratio in different regimes. For example, in the Quasi-static Regime, the transfer ratio was proposed to be only controlled by the wettability of the surfaces, i.e., contact angles. When a very large stretching speed is used and thus the effects of viscous and inertial forces are large, the contact angles have negligible influence and the transfer ratio tends to converge to 0.5. While being pioneering in the fields, the works of Chadov and Yakhnin only focused describing of liquid transfer phenomenologically. They were neither rigorous nor comprehensive in discussing the underlying physics of the problem. For example, the three regimes were categorized in a qualitative manner; the exact boundaries between the regimes (i.e., stretching speeds at which the transfer transitions from one regime to another) were not investigated.

Following the works of Chadov and Yakhnin, a number of studies have attempted to advance the understanding of liquid transfer in those three regimes [9-25]. The liquid transfer in Quasi-static Regime is already understood well in [9-15] collectively. The most important finding is that in the Quasi-static Regime, the transfer ratio is governed by the contact line pinning at the end of the stretching process, which is caused by contact angle hysteresis (*CAH*), the difference between the values of the surface advancing contact angle (θ_a) and receding contact angle (θ_r). The transfer ratio is further shown to be only controlled by θ_r between the liquid and the two surfaces, and can be predicted with the following closed-form function [15]:

$$\alpha_0 = (1+exp\,[-3.142((\theta_r)_{\mathrm{acc}} + (\theta_r)_{\mathrm{don}})^{2.528}\times((\theta_r)_{\mathrm{don}} - (\theta_r)_{\mathrm{acc}})])^{-1} \quad (7\text{-}1)$$

where $(\theta_r)_{\mathrm{acc}}$ and $(\theta_r)_{\mathrm{don}}$, in radians, are respectively θ_r on the acceptor and donor surfaces. Based on EQ. (7-1), the value of α_0 (transfer ratio in Quasi-static Regime) is strongly affected by the difference between θ_r of the two surfaces. When $(\theta_r)_{\mathrm{acc}}$ is larger than $(\theta_r)_{\mathrm{don}}$ the transfer ratio is smaller than 0.5; when $(\theta_r)_{\mathrm{acc}}$ is smaller than $(\theta_r)_{\mathrm{don}}$ the transfer ratio is larger than 0.5. The value of α_0 can also be affected by the absolute values of $(\theta_r)_{\mathrm{acc}}$ and $(\theta_r)_{\mathrm{don}}$, which is reflected by the term of $((\theta_r)_{\mathrm{acc}} + (\theta_r)_{\mathrm{don}})^{2.528}$ in EQ.(7-1).

Compared with Quasi-static Regime, much less is understood about liquid transfer in the Transition and Dynamic Regimes, where the liquid is transferred quickly from the donor surface to the acceptor surface. Such fast liquid transfer is very important for many applications that require a high working efficiency. In most of the studies on the fast liquid transfer, the focus was put on the inertial and viscous effects during the entire process [16-26], whereas possible contributions from the surface contact angle were typically not considered. For example, in Zhang *et al.* [19], and Yildirim and Basaran [20], studies of liquid bridge with two pinned contact radii were performed. In these studies, the effects of viscous and inertial forces during the transfer were discussed based on either 1-D [19] or 2-D approximations [20]. However, due to the assumption of pinned contact lines, the surface contact angles were absent in these models. Although surface wettability can indeed be negligible in Dynamic Regime by its definition, its effect cannot be overlooked on the profile of the liquid bridge in Transition Regime; hence it can further affect the boundaries that separate the three regimes.

Several recent studies [22-26] noted the importance of the surface contact angles during fast liquid transfer. For example, with a finite element model, Dodds et al. [25] evaluated the effects of contact angles on the transfer ratio under three different capillary numbers (Ca, 0.01, 0.1 and 1), assuming the contact lines on both surfaces could move freely. By fixing the contact angle on one surface, it was found that for all three capillary numbers the amount of liquid transferred decreased as the contact angle on the other surface decreased. In this numerical study, the contact angles between the liquid and the surfaces were assumed to have constant values and the effect of *CAH* was neglected. Literature has shown that with a free moving contact line, the actual value of the contact angle can have a complex dependence on the motion of the contact line [27-29]. This suggests that the contact angle cannot be assumed to be a unique value, i.e. *CAH* should be considered. Furthermore, *CAH* effect can result in pinning of the contact line which is another factor to affect the final transfer ratio. Therefore, a study which properly considers the surface dynamic contact angle and *CAH* is needed to gain a first comprehensive view at the process of fast liquid transfer.

The present study aims at advancing the understanding of the liquid transfer in the Transition and Dynamic Regimes, with a focus on addressing: (1). the role of surface contact angles and *CAH* in determining the transfer ratio in the Transition Regime; and (2). how the boundaries between the three regimes are affected by the surface wettabilities.

A systematic experimental study of liquid transfer was performed with different liquids and different donor/acceptor surfaces. In most practical situations, e.g. printing, small volumes of viscous liquid are typically used, where the inertial forces are small compared with surface and viscous forces. Therefore, the experiments performed in this study all have a small Weber number ($We=\rho U^2\sqrt[3]{V}/\gamma$, where ρ is liquid density, U is the speed of the acceptor surface, V is the volume of liquid, and γ is liquid surface tension) and Reynolds number ($Re=\rho U\sqrt[3]{V}/\mu$; where μ is the liquid dynamic viscosity). Results from numerical simulation performed with Fluent were used to help understand the experimental findings. At the end, an analytical-empirical model is developed and verified by experimental results that can accurately predict the transfer ratio as a function of stretching speed.

7.2 Method

7.2.1 Experiment

Six different surfaces (silicon, Poly (methyl methacrylate) (PMMA), Polystyrene (PS), Poly (ethyl methacrylate) (PEMA), Teflon AF and Octadecyltrichlorosilane (OTS)) and three different liquids (silicone oil, glycerol and ethylene glycol) were used in the experiments. The properties of the liquids are shown in Table 7.1. The contact angles between surfaces and each of the liquid, measured by sessile drop method, are provided in Table 7.2. For all experiments, the PEMA surface served as the acceptor surface, and the other five surfaces were used as the donor surfaces. A typical process of liquid transfer is shown in Figure 7.1. First, a 2.0 μl liquid drop was placed on the donor surface (Figure 7.1(a)). The acceptor surface was then moved slowly towards the donor surface to form a liquid bridge between the two surfaces. The movement was stopped when the surface separation decreased to 0.45 mm (minimum separation, H_{min}, Figure 7.1(b)). Then the liquid bridge was stretched with a target stretching speed until it broke (Figure 7.1(c)). All the experiments were performed at the ambient temperature of ~20.5°C. When the liquid bridge broke, part of the liquid was transferred from the donor surface to the acceptor surface, and the volume of the transferred liquid was used to calculate the transfer ratio. Each of the experimental measurement was repeated 3 times, and the provided transfer ratio values are the average of the three measurements.

Table 7.1: Properties of the three liquid used in this work.

Liquid Name	Surface tension (mN/m)	Viscosity (Ns/m^2)
ethylene glycol	48.4	0.021
glycerol	63.4	1.350
silicone oil	21.2	0.967

Table 7. 2: Contact angle data of surfaces used in this work.

Surface Name	**between silicone oil (degree)**	**between glycerol (degree)**	**between ethylene glycol (degree)**
Silicon	*N/A*[1]	θ_a : 45.2±0.44 θ_r: 37.3±0.83	θ_a : 51.0±0.82 θ_r: 30.0±0.89
PMMA	*N/A*[1]	θ_a : 67.8±0.92 θ_r: 53.2±0.87	θ_a : 61.0±0.78 θ_r: 40.8±1.05
PEMA	*N/A*[1]	θ_a : 72.1±0.68 θ_r: 61.7±0.89	θ_a : 62.1±0.79 θ_r: 53.2±1.02
PS	*N/A*[1]	θ_a : 71.0±1.13 θ_r: 56.6±1.32	θ_a : 65.2±1.43 θ_r: 46.6±1.54
OTS	*N/A*[1]	θ_a : 97.5±0.72 θ_r: 83.9±0.87	θ_a : 76.9±0.92 θ_r: 59.5±1.32
Teflon AF	θ_a : 56.0±0.88 θ_r: 48.7±1.54	θ_a : 113.1±0.86 θ_r: 106.7±0.97	θ_a : 103.2±0.89 θ_r: 91.1±1.22

1. During the measurement of contact angle between silicone oil and Silicon, PMMA, PEMA, PS and OTS surfaces, the surfaces were wetted completely. Therefore, the contact angles between these five surfaces and silicone oil could not be measured. A value of 0° was used in the later discussions.

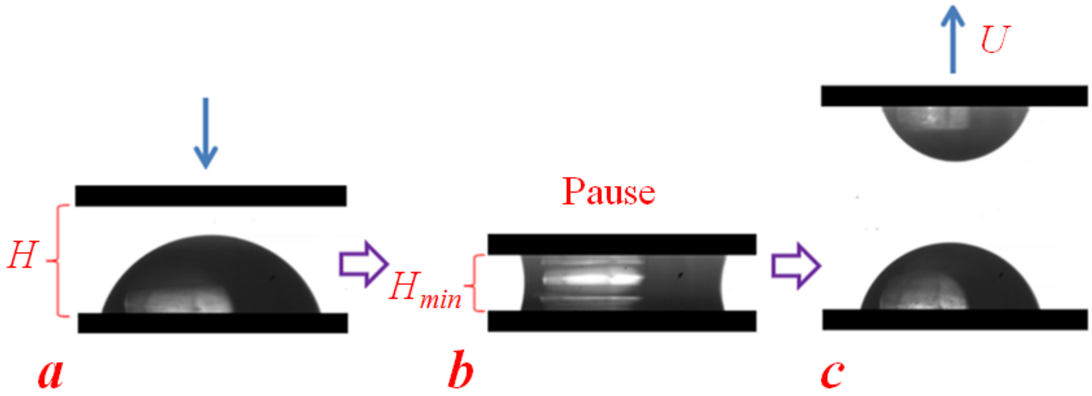

Figure 7.1: Process of liquid transfer between two surfaces. (a): liquid drop is placed on the donor surface; (b): liquid bridge is compressed to a minimum separation; (c): liquid bridge is stretched to breakage.

Two different experimental setups were used in this study, one for low speed tests and the other for high speed tests. The image of the low speed setup (target speed from 0.005 mm/s to 20 mm/s) is shown in Figure 7.2(a). The acceptor surface was connected to a Motion Controller (ILS100CC and XPS-C6 from Newport). During the stretching stage of each transfer, the acceptor surface was accelerated to a target speed with the acceleration of 400 mm/s^2 in a very short time, and stayed at this target speed until the liquid bridge broke. The details of the instantaneous speed of the acceptor surface during the stretching stage are provided in the Appendix F.

For the experiments with a large stretching speed (>20mm/s), a second experimental setup which consists of a spring system was used (Figure 7.2(b)). Two springs with stiffness of 0.22 N/mm were used to provide the movement of the acceptor surface, which was attached to a stage at the end of the two springs. A guide rail perpendicular to the surfaces was used to guide the motion of the stage. In the experiment, the springs were elongated to allow the separation between the two surfaces to reach H_{min}. The elastic restoring force generated by the springs could provide a very large acceleration, which allowed the acceptor surface to obtain a large speed during a short period of time. Details of how stretching of the springs can be used to manipulate the surface speed can be found in the Supplementary Material. Different from the speed provided by the low speed setup, the speed provided by the high speed setup is not constant during the transfer process. To be consistent, instead of using the target speed, the stretching speed *U* in the later discussion was defined as the average speed at the beginning of the stretching stage and the speed when the liquid bridge broke. Details of calculating the average stretching speed *U* can be found in the Supplementary Material. In both setups, Phantom Miro M310 camera (imaging speed of 10100 fps at the resolution of 640×480) was used to record the process of liquid transfer.

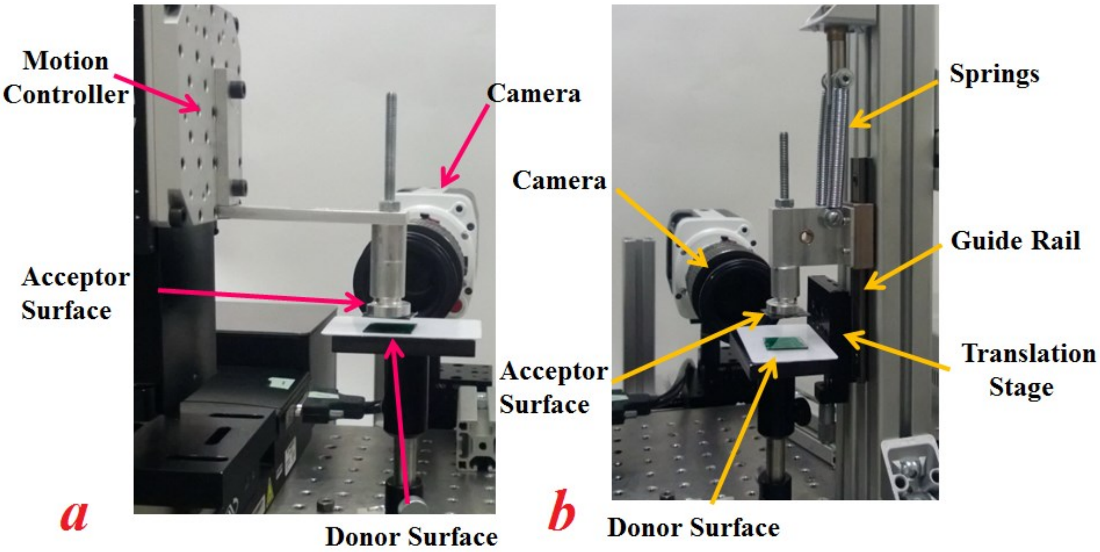

Figure 7.2: (a) Experimental setup for low speed tests. (b) Experiment setup for high speed tests.0.2

7.2.2 Simulation

A numerical model based on the Volume of Fluid (VOF) method was developed using the commercial CFD code Fluent. The VOF method is a well-known interface tracking method and is widely applied to capture the complex multiphase fluid flow and contact angle behaviour [28]. The liquid transfer is between two flat surfaces. Therefore, the liquid bridge possesses axisymmetry and was simulated in 2-D model. The movement of the acceptor surfaces was implemented by dynamic meshes defined by the User Defined Functions in Fluent.

To solve the liquid transfer process numerically, the contact angles between the liquid and the surfaces were needed as the boundary conditions. It is well-known that the dynamic contact angle (θ_d) has a complex dependence on the velocity of the contact line (v_{cl}), the relative velocity between the liquid and the solid surface [29-31]. In this study, the Kistler model [31] which is widely used to describe the dynamic contact angle was implemented to define dynamic contact angle for surfaces with *CAH* [32, 33]. With the Kistler model, the value of θ_d can be calculated as:

$$\theta_d = f_{Hoff}\left[\frac{\mu v_{cl}}{\gamma} + f_{Hoff}^{-1}(\theta_d)\right], \text{ in the advancing stage (7-2a)}$$

$$\theta_d = f_{Hoff}\left[\frac{\mu v_{cl}}{\gamma} + f_{Hoff}^{-1}(\theta_r)\right], \text{ in the receding stage (7-2b)}$$

$$f_{Hoff}(x) = arccos\left\{1\text{-}2tanh\left[5.16\left(\frac{x}{1+1.31x^{0.99}}\right)^{0.706}\right]\right\} \text{ (7-2c)}$$

According to EQ. 7-2, when the contact line advances, θ_d increases with the increase in the magnitude of v_{cl}. When the contact line recedes, θ_d decreases with the increase in the magnitude of v_{cl} (see Figure 7.3).

The Kistler model can be especially useful when contact line is moving decisively in either advancing or receding cases and when v_{cl} is fairly large. It should be noted however that Kistler model does not exactly represent the physical reality of contact line motion. When the contact line is pinned (i.e. v_{cl}=0), the contact angle varies through a range of values, but Kistler model can only have a single value for θ_d when v_{cl}=0 (usually the average value of θ_a and θ_r). As such Kistler model cannot correctly capture such a pinning phenomenon. This is not only the limitation of the Kistler model, but a common problem for other dynamic contact angle models [4, 34]. Due to the inaccessibility of the *CAH* phenomenon, the final transfer ratio obtained from the VOF model can be different from the experimental results, especially for the cases with relatively small *U* since the effect of *CAH* is more significant when *U* is small. Therefore, in this study, the transfer ratio obtained from the numerical simulation is not used for comparison or discussion. On the other hand, the numerical model can provide useful information which cannot be obtained from experiments, for example the distribution of the liquid velocity within the bridge during the process. Such information can be helpful in explaining observations made in the experiments.

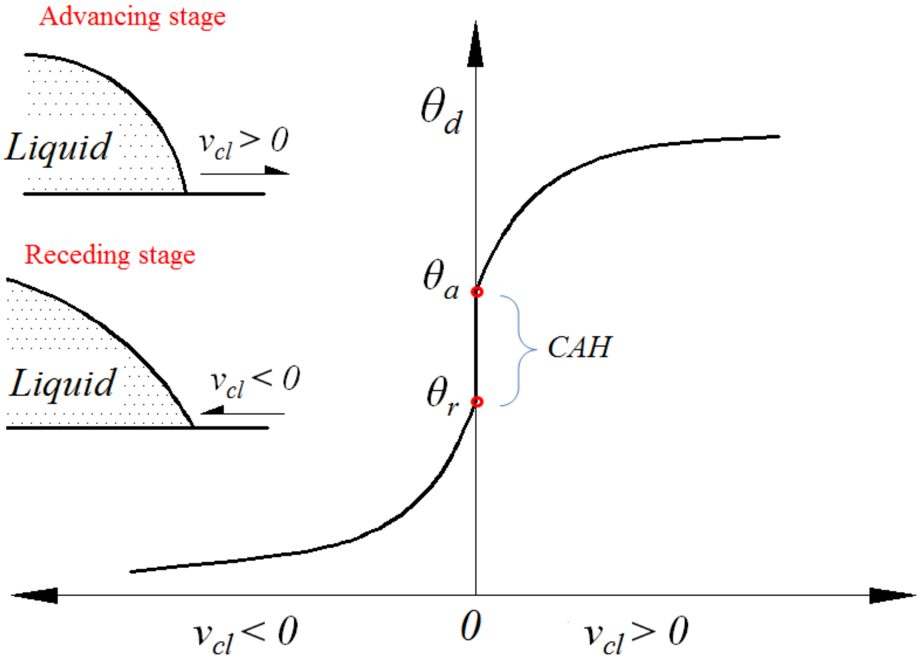

Figure 7.3: Sketch of the relation between the dynamic contact angle and the speed of the contact line based on the Kistler model [30]. When v_{cl}=0, average value of θ_a and θ_r is used.

7.3 Results and Discussion

7.3.1 Rate Dependence of Transfer Ratio

As a first example, Figure 7.4 shows the transfer ratio for a 2.0 μl glycerol drop transferred from OTS to PEMA under different average stretching speed U of the acceptor surface. Also shown are the shapes of the liquid bridge at breakup (hereafter referred to as the "breakage shape") for 9 selected cases. It can be seen that at small U, e.g. $U = 0.05$ mm/s, 0.1 mm/s and 0.2 mm/s, the surface separation when the liquid bridge breaks (H_{max}) and the breakage shapes are almost the same, and most of the liquid tends to stay on the acceptor surface. Consistently, when the speed is low ($U < 0.2$ mm/s), the transfer ratio remains constant and is close to one (0.986). As U increases, there is a clear increase in H_{max}, accompanied by more and more symmetric breakage shapes, i.e., the liquid is partitioned more evenly between the donor and acceptor surfaces, instead of staying mostly on the acceptor surface. A direct consequence of this is that the transfer ratio converges to 0.5 with the increases of the speed and remains 0.5 (drop equally split between the two surfaces) when U >16.5 mm/s.

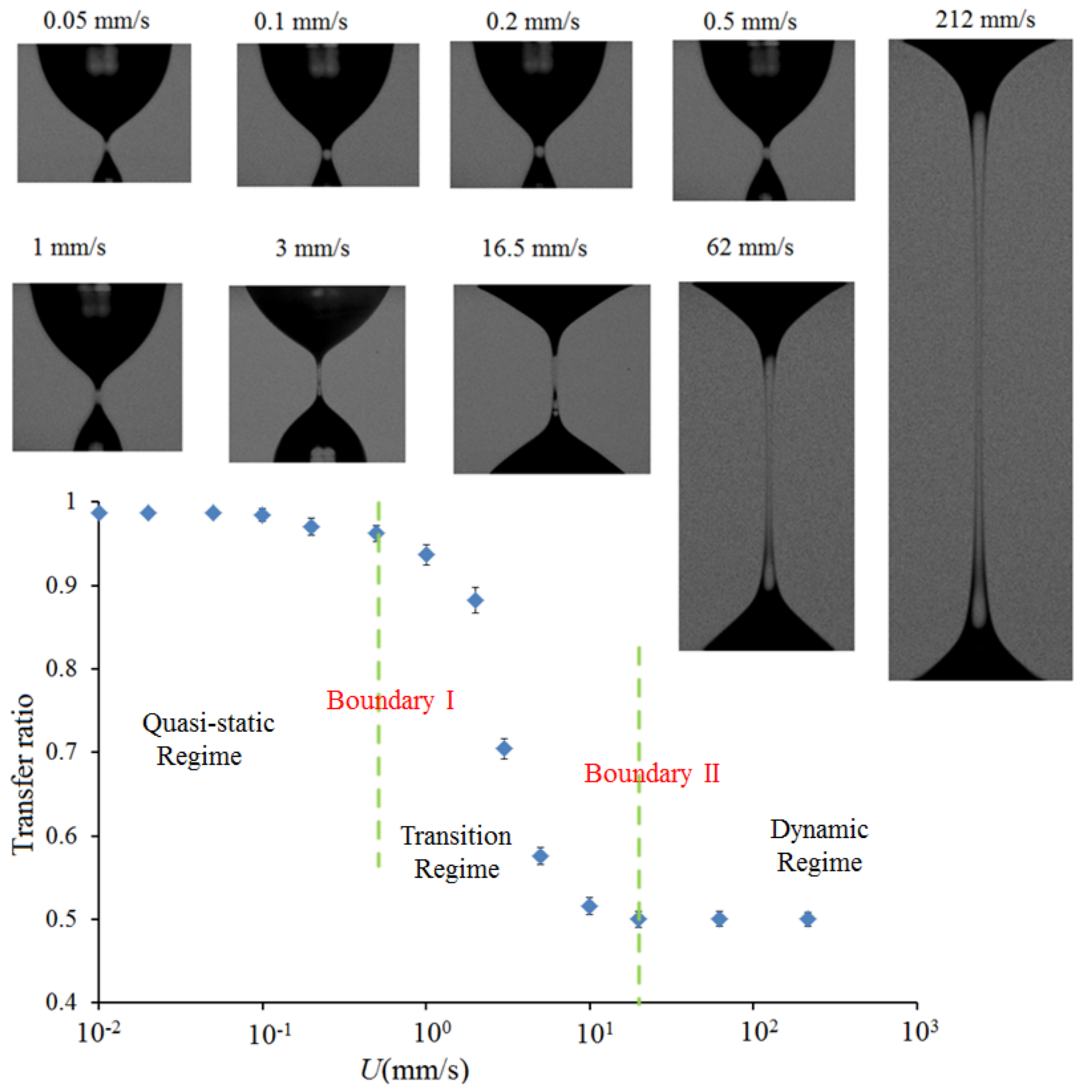

Figure 7.4: Relation between transfer ratio and U for glycerol transferred from OTS to PEMA surfaces. Shapes of the liquid bridge at breakup are also shown for 9 different stretching speeds. Boundary I and II are, respectively, the boundary speeds between Quasi-static and Transition Regimes, and between Transition and Dynamic Regimes.

To understand the results shown in Figure 7.4, the evolutions of contact radii on the OTS and PEMA surfaces, which show the behavior of the liquid bridge, are shown in Figures 7.5 and 7.6 respectively for different stretching speeds. First, let us examine the three curves at low speeds (U = 0.05 mm/s to 0.5 mm/s). It can be seen that on both plots the two curves almost overlap with one another, indicating that the transfer process is insensitive to the stretching speed, which is consistent with the observations in Figure 7.4 that the transfer ratio is a constant at low speed. In addition, Figures 7.5 and 6 show that for these three cases, after the surface separation reaches 1.42 mm, the contact radius on PEMA remains at approximately 0.89 mm (i.e., pinned contact line, see Figure 7.5) while the contact radius on OTS undergoes a rapid decrease (see Figure 7.6). As a result, near the end of the stretching process, most liquid stayed near PEMA (acceptor), and the transfer ratio is close to one (Figure 7.4). Next, for the stretching speed in the range of 2 mm/s to 16.5 mm/s, the evolutions of the contact radii start to change with the increase of the stretching speed. For U = 5 mm/s and 16.5 mm/s, contact line pinning (flat parts of the curves) is not only observed on PEMA, but also on the OTS surface (donor). That is, the tendency of the liquid to stay near the acceptor surface is not exclusive any longer; accordingly a reduction in the transfer ratio is seen in Figure 7.4. Finally, at even higher stretching speeds (62mm/s and 212mm/s), the contact line was pinned on both surfaces during almost the entire transfer process, leading to the liquid bridge being symmetrical and the transfer ratio being 0.5 as shown in Figure 7.4.

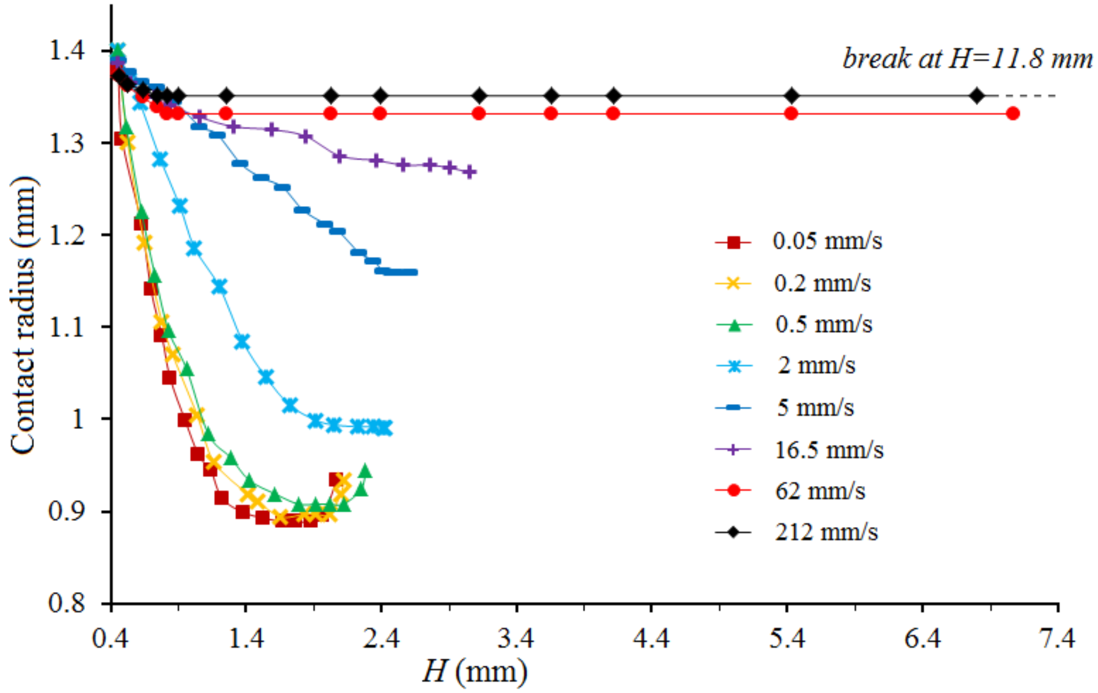

Figure 7.5: Evolution of contact radius on PEMA (acceptor surface) for glycerol transfer from OTS (donor surface). Flat parts of the curves indicate contact line pinning. Please note during the pining of contact line, the value of contact angle increases with the increase of *H*. For the cases with *U*= 0.05mm to *U*= 0.5, the contact angle on the PEMA increased to θ_a when *H* increased to approximately 2.1mm. Therefore, an increase of contact radius with further increase in *H* can be seen.

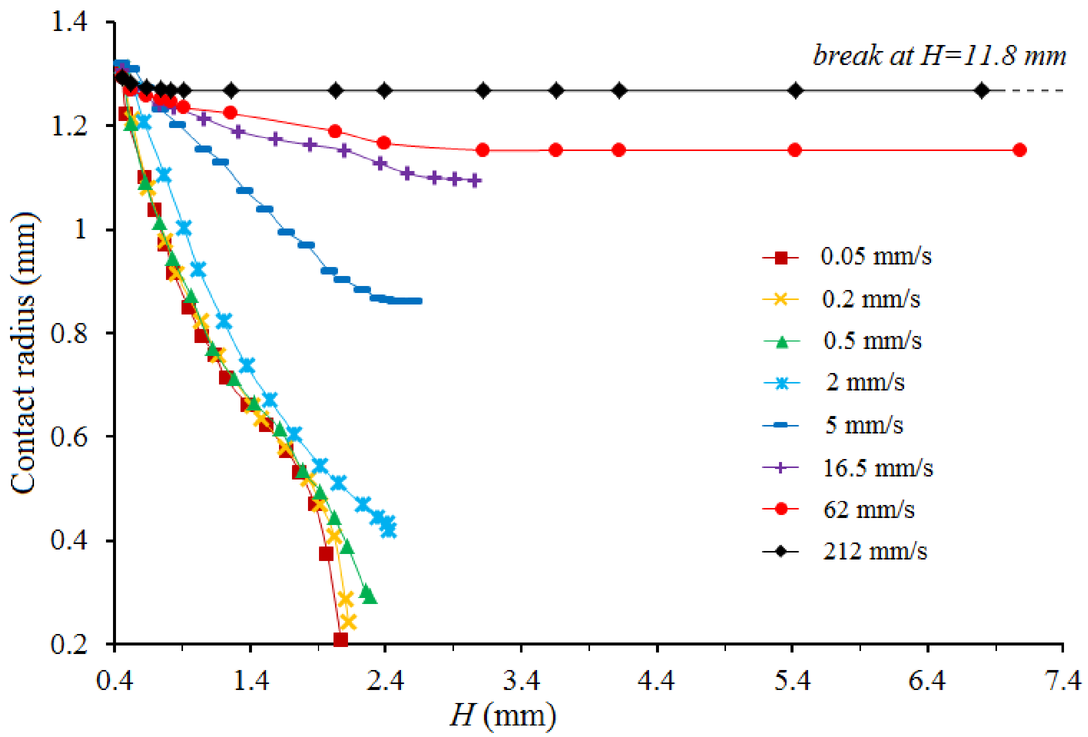

Figure 7.6: Evolution of contact radius on OTS (donor surface) for glycerol transfer to PEMA (acceptor surface). Flat parts of the curves indicate contact line pinning.

Clearly, the phenomenon that α is constant at low/high U and decreasing as U increases in the moderate range of U, is directly correlated with the distinct contact line pinning behaviors in different speed ranges. These distinct behaviors are caused by the competition between surface and viscous forces. For the system of 2μl glycerol transfer, the viscous/capillary time scale can be calculated as $t_v \sim \mu V^{1/3}/\gamma$ to be 0.0264s. At low speeds, the stretching of liquid bridge was completed in a relatively long time (e.g. 32s for the case of U=0.05mm/s), which is much larger than t_v. Therefore, the surface forces are the dominant force. Because the receding contact angle, θ_r, of the PEMA surface is much smaller than OTS, i.e., liquid is much more attracted to PEMA, contact radius pinning near the end of the transfer only occurs on the PEMA surface. As the stretching speed increases, the time of stretching process became closer to the value of t_v (e.g. 0.0725s for the case of U=62mm/s). Therefore, the viscous effects become more and more important with the increase of U; hence the difference in receding contact angles becomes less influential. In addition, the velocity gradient in vertical direction of this system also increases.

Therefore, the vertical momentum is spread downwards much more slowly from the liquid near the acceptor to that near the donor surface, and it is harder for the bottom half of the liquid bridge to catch up with the upper half. Consequently, contact line pinning on the donor surface begins to occur and the liquid bridge becomes more and more symmetrical. The results from simulation can be used to confirm this explanation. The distribution of the gradient of the vertical velocity inside glycerol liquid are shown in Figures 7(a) and (b), respectively, for the stretching speeds of 1 mm/s and 100 mm/s. It can be seen that for U = 1mm/s, the velocity gradient is very small and is nearly uniform throughout the liquid. However, for U = 100 mm/s, the velocity gradient is only small near the surfaces (almost 0 s^{-1}), but very large around the middle section of the liquid bridge (up to 500 s^{-1}). This large velocity gradient suggests the spread of momentum is slower at the middle section, compared with the section near the surfaces. Therefore, one can understand the observation that the liquid bridge can be stretched to a very large H_{max} with contact line pinning on both surfaces, and break with a very long and thin fiber-like geometry.

The results from simulation can be used to confirm this explanation. The distribution of the gradient of the vertical velocity inside glycerol liquid are shown in Figures 7.7 (a) and (b), respectively for the stretching speeds of 1 mm/s and 100 mm/s. It can be seen that for U = 1mm/s, the velocity gradient is very small and is nearly uniform throughout the liquid. However, for U = 100 mm/s, the velocity gradient is only small near the surfaces, but very large around the middle section of the liquid bridge. This large velocity gradient suggests the spread of momentum is slow at the middle section, explicitly the observation that the liquid bridge can be stretched to a very large H_{max} with contact line pinning on both surfaces, and break with a very long and thin fiber-like geometry. Although the snap shot of liquid bridges in Figures 7.7(a) and (b) both have the same H =1.60mm, due to the very different U, they happened at very different time (t) after the start of the stretching (t = 1.15s in Figure 7.7(a) and t = 0.0115s in Figure 7.7(b)). Given the slow spread of momentum and short t in Figure 7.7(b), even though the liquid was stretched under a much larger U, the contact lines slipped inwards much less than the case in Figure 7.7(a); hence the snap shot in Figure 7.7(b) has much larger contact radii than those in Figure 7.7(a). Therefore, in the experiment, when the liquid bridge was stretched with a large speed (e.g. U =212mm/s and 62mm/s in Figures 7.5 and 7.6) contact line pinning during the entire process can be seen.

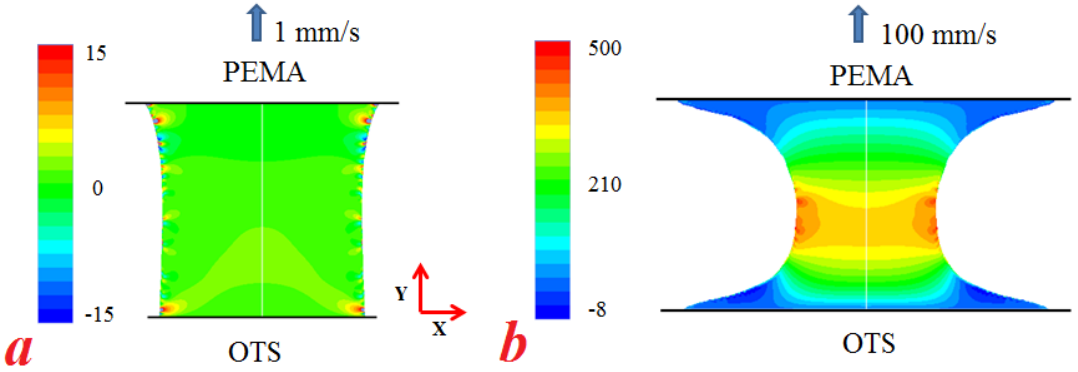

Figure 7.7: Gradient of the vertical velocity (with unit of s^{-1}) inside glycerol transferred from OTS to PEMA at H = 1.60mm. (a): U= 1 mm/s; (b): U= 100 mm/s. Note the scales of the velocity gradient in the two plots are different; if the scale of plot (b) was used for (a) only a single color indicating a uniform velocity gradient will be seen.

7.3.2 Separation of the Three Regimes

Since transfer ratio is of particular interest to many applications and its value shows distinct dependences on the stretching speed in different regimes, the transfer ratio is used as a criterion to separate these regimes. The separation can be made easily based on the experimental observation in Figure 7.4. When the stretching speed is very low, the transfer ratio does not change with the stretching speed; this will be identified as the Quasi-static Regime. When the speed is very large, the transfer ratio stays at 0.5, which will be categorized as the Dynamic Regime. And when a medium stretching speed is used, the transfer ratio converges from its low-speed plateau to 0.5 with the increase of speed; this will be called the Transition Regime. According to such definition, for glycerol transferred from OTS to PEMA, the boundary is ~0.5mm/s between Quasi-static and Transition regimes (Boundary I), and ~16.5mm/s between Transition and Dynamic regimes (Boundary II).

7.3.3 Effects of Surface Contact Angle on the Regime Boundaries

In order understand the effects of surface contact angle on the boundaries separating the three regimes, experiments of glycerol transfer and ethylene glycol transfer from different donor surfaces to PMEA surface were performed. Figure 7.8 shows the transfer ratio for a 2.0 μl glycerol drop transferred from five different donor surfaces (silicon, PMMA, PS, OTS, and Teflon AF) to PEMA. Figure 7.9 shows the experimental results of ethylene glycol transfer from three different donor surfaces (PS, OTS and Teflon AF) to PEMA. It can be seen that the data of all the cases exhibit similar characteristics: the transfer ratio is constant at very small U (Quasi-static Regime), changes with U at intermediate U (Transition Regime), and converges to 0.5 at very large U (Dynamic Regime). On the other hand, for each figure, two dissimilarities can be seen among the different groups of data. Firstly, the plateau values in the Quasi-static Regime are very different for different donor surfaces. For example, in Figure 7.8, α_0 equals to 1 for Teflon AF and 0.026 for silicon. Because the transfer ratio in the Quasi-static Regime can be greater or smaller than 0.5 (plateau value in Dynamic Regime), the behavior in the Transition Regime can also be very different, either increasing or decreasing with the increase of U. Secondly, the boundaries between the regimes are noticeably different. For example, in Figure 7.8, for OTS, the transfer ratio starts to deviate from its quasi-static plateau at approximately $U\sim$ 0.5 mm/s, while for PS the deviation starts at $U\sim$0.05 mm/s. For each figure, the transfer cases were performed using the liquid of the same volume. When the same U was applied, the value of Ca, Re, and We should be similar. Therefore, the differences observed above are caused by the different contact angle of the donor surfaces.

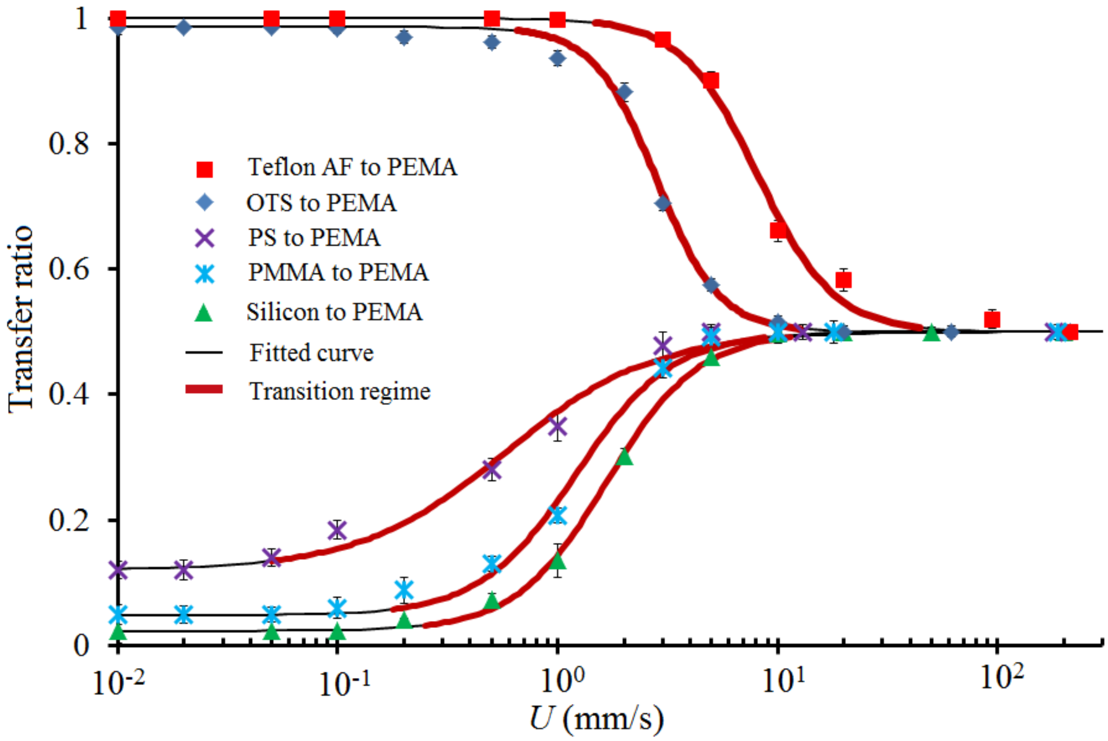

Figure 7.8: Relation between transfer ratio and U of glycerol transferred from 5 different donor surfaces to PEMA. The solid black lines are the fitting curves $\alpha=F(U)$ given by EQ. (7-3). For the glycerol transfer from Silicon, PMMA, PS, OTS and Teflon AF, the values of coefficient k are, respectively, 0.34, 0.68, 2.00, 4.32×10^{-2}, and 5.34×10^{-3}; and the values of coefficient n are, respectively, 2.09, 1.99, 1.31, 3.04, and 2.50. The thick solid red lines represent the Transition Regime of each group of data when 0.04 is chosen as the threshold value for the magnitude of the slope.

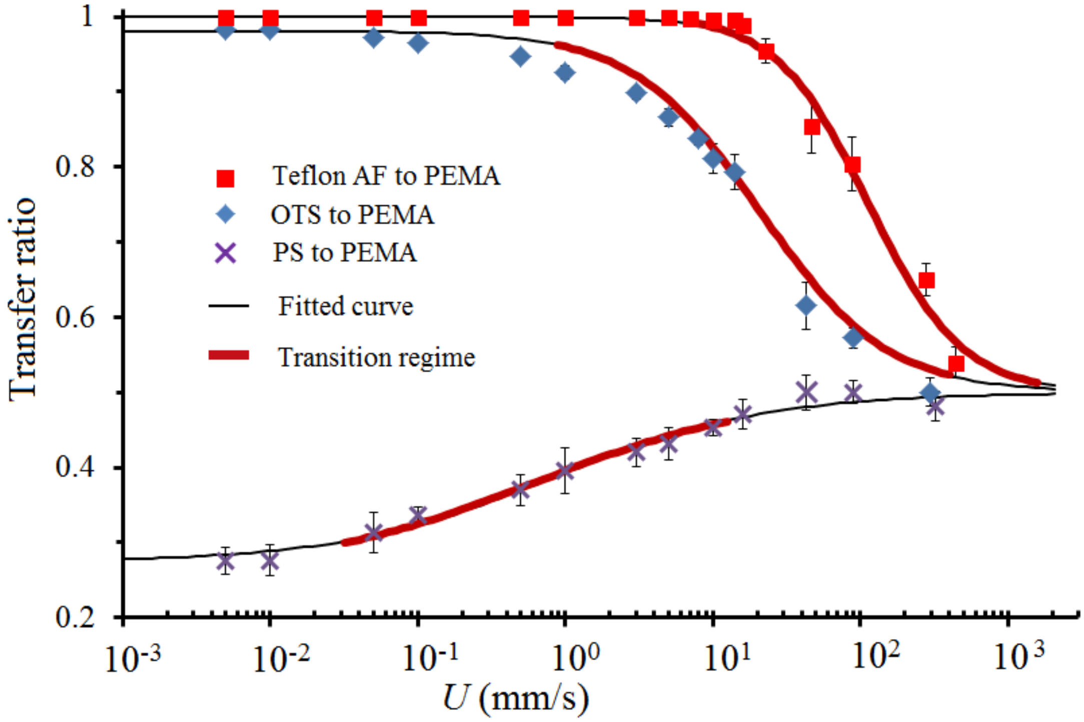

Figure 7.9: Relation between transfer ratio and *U* of ethylene glycol transferred from 3 different donor surfaces to PEMA. The solid black lines are the fitting curves $\alpha = F(U)$ given by EQ. (7-3). For the ethylene glycol transfer from PS, OTS and Teflon AF, the values of coefficient *k* are respectively 1.12, 4.55×10^{-2} and 1.38×10^{-3}; and the values of coefficient *n* are respectively 5.98×10^{-1}, 1.02 and 1.38. The thick solid red lines represent the Transition Regime of each group of data when 0.04 is chosen as the threshold value for the magnitude of the slope.

Shown in the previous section, the speed at which the momentum spreads from the acceptor surface to the donor surfaces is a key factor that determines the tendency of contact line pinning and hence the change of transfer ratio with the increase of *U*. The spread of momentum is not only influenced by the stretching speed but also by the shape of the liquid bridge. For liquid transfer in the Transition Regime, during the stretching stage, since the liquid profile on the surfaces needs to satisfy the boundary conditions on the contact angle, the shape of the liquid bridge is not only controlled by *U*, but also by the dynamic contact angle of the surfaces. The effect of the dynamic contact angle on the profile of the liquid bridge can further influence the spread of the momentum from the acceptor surface to the donor surface. This is confirmed by the simulation results from the VOF model. Simulations of glycerol transferred from Teflon AF and PS to PEMA with $U = 10$ mm/s were performed. Figures 7.10(a), (b) and (c) respectively show the gradient of the vertical velocity for the two cases at the beginning ($H = 0.66$mm), middle ($H = 1.42$mm), and end ($H = 2.03$mm) of the stretching stage. It can be seen that at the same stretching speed and the same H, the distribution of velocity gradient in these two cases are completely different. First of all, the transfer from PS to PEMA has a larger velocity gradient at the neck of the liquid bridge, especially at the end of the stretching stage (Figure 7.10(c)). This suggests that under the same stretching speed, the spread of momentum is slower for the transfer from PS. Secondly, not only the magnitude of the velocity gradient, but also the velocity gradient distribution is different between the two transfer cases. At the beginning of the stretching stage (Figure 7.10(a)), the velocity gradient distribution is almost symmetric for the PS case and the largest velocity gradient occurs near the neck of the liquid bridge. However, for the Teflon AF case, the distribution is not symmetric, and the largest velocity gradient occurs near the contact line on the bottom surface. The differences in velocity gradient distribution become more and more significant with the increase of H: the distribution remains symmetric for the PS case, while it becomes progressively asymmetric for the Teflon AF case. Due to differences in both the magnitude and distribution of the velocity gradient, these two transfer cases belong to different Regimes. From Figure 7.8, it can be seen that with $U = 10$ mm/s, the case of Teflon AF as donor surface belongs to the Transition Regime, while the case with PS as donor surface is already in the Dynamic Regime. Therefore, even with the same U, due to the different surface wettabilities, the transfer can be in different regimes.

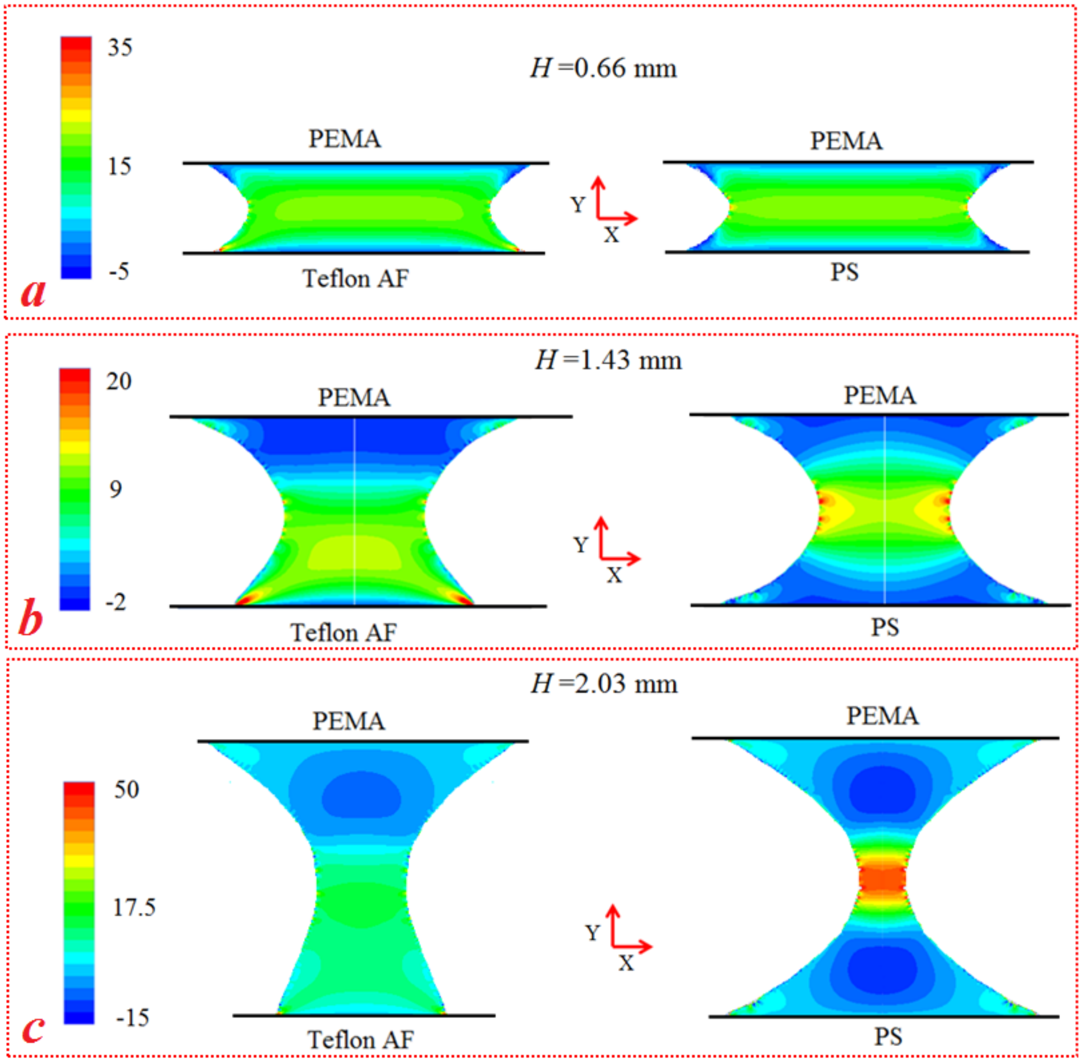

Figure 7.10: Vertical velocity gradient distribution (with unit of s^{-1}) for glycerol transferred from Teflon AF to PEMA (left) and PS to PEMA (right) with U = 10mm/s, snap shots at different H: (a) H= 0.66mm; (b) H= 1.43mm and (c) H= 2.03mm. Note the scale of the velocity gradient of (a), (b) and (c) are different.

To provide a quantitative measure of the regime boundaries, an empirical function $\alpha = F(U)$ is proposed below to relate the transfer ratio to the stretching speed:

$$\alpha = 0.5 + \frac{\alpha_0 - 0.5}{1 + kU^n} \quad (7\text{-}3)$$

where α_0 is the transfer ratio in Quasi-static Regime (EQ.(7-1)), and k and n are fitting parameters. EQ. (7-3) is proposed based on observations from the experimental results. Specifically, when U is very small, the term kU^n is almost zero, and hence α reduces to α_0. When U is very large, the term kU^n is large, making the second term on the right hand side of EQ. (7-3) negligible, resulting in the transfer ratio equal to 0.5. The values of k and n, which are dependent on the surface wettability and liquid properties (e.g. viscosity, surface tension), need to be obtained through data fitting with experiment results. The fitted curves for all transfer experiments are shown as solid black lines in Figures 7.8 and 7.9. Clearly EQ. (7-3) provides an excellent fit to all data with different types of liquid and different surfaces.

With the function $\alpha= F(U)$, the slope of each curve at any U can be obtained, which is close to zero for very small and large speeds. Therefore, by choosing a threshold value for the slope, the boundaries between the different regimes can be found. The thick (red) curves in Figure 7.8 show the Transition Regime for each group of data when 0.04 is chosen as the threshold value for the magnitude of the slope. Boundaries I and II for each group are the left and right ends of the thick (red) curves, respectively. Since the only difference among these five groups is the donor surface, the distinct values of Boundaries I and II are caused by the different wettability of the donor surfaces, which allows us to examine the role of surface contact angle in determining the regime boundaries.

Specifically, for liquid transfer in the Quasi-static regime, the breakage shape is completely governed by the surfaces' receding contact angles. The more different the receding contact angles of the two surfaces are, the more asymmetric the breakage shape will be. For liquid transfer in the Dynamic Regime, due to the very slow spread of momentum, the breakage is always symmetric ($\alpha = 0.5$) and independent of the surface contact angles. For liquid transfer in the Transition Regime, both the receding contact angles and U affect the transfer process. Given the same surface contact angles, Figure 7.4 shows that the breakage shape becomes more and more symmetric when U increases. Given the same stretching speed, Figure 7.11 (glycerol transfer from PS, PMMA, Silicon and OTS to PEMA at U = 1 mm/s) shows how the breakage shape is affected by the surface receding contact angles. From Figure 7.11, a clear correlation can be seen between the value of $|\alpha_0-0.5|$ and the breakage shape, which becomes more and more asymmetric when $|\alpha_0-0.5|$ increases. The quantitative dependence of α_0 on $(\theta_r)_{\mathrm{acc}}$ and $(\theta_r)_{\mathrm{don}}$ is given by EQ. (7-1), which predicts that $|\alpha_0-0.5|$ increases with the increase of $|(\theta_r)_{\mathrm{acc}} - (\theta_r)_{\mathrm{don}}|$ or $(\theta_r)_{\mathrm{acc}} + (\theta_r)_{\mathrm{don}}$; hence the breakage shape in the Quasi-Static regime becomes more asymmetric with the increases of $|(\theta_r)_{\mathrm{acc}} - (\theta_r)_{\mathrm{don}}|$ or $(\theta_r)_{\mathrm{acc}} + (\theta_r)_{\mathrm{don}}$. For example, among the four cases shown in Figure 7.11, the glycerol transfer from PS to PEMA has the smallest value of $|(\theta_r)_{\mathrm{acc}} - (\theta_r)_{\mathrm{don}}|$ and $(\theta_r)_{\mathrm{acc}} + (\theta_r)_{\mathrm{don}}$. Therefore, it has the smallest value of $|\alpha_0-0.5|$; hence an almost symmetric breakage shape can be seen.

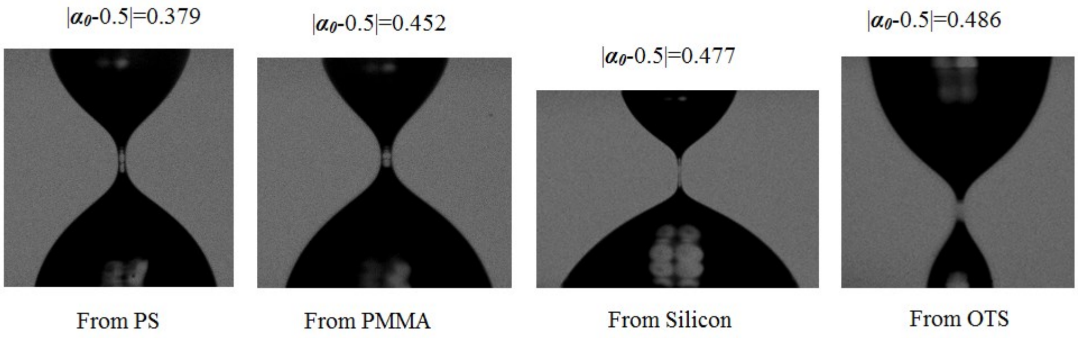

From PS From PMMA From Silicon From OTS

Figure 7.11: The breakage shape of glycerol transfer from PS, PMMA, Silicon and OTS surfaces to PEMA surface.

Based on the analysis above, the surface receding contact angles directly influence the value of $|\alpha_0-0.5|$, which in turn affects the speeds at the regime boundaries. This is confirmed by Figure 7-12 (a) and (b) which show the value of $|\alpha_0-0.5|$ and Boundary I/II for five groups of data in Figure 7.8, and three groups of data in Figure 7.9. It can be seen that the speeds at Boundary I/II both increases with the increase of $|\alpha_0-0.5|$. Another interesting observation can be made, if one compares Boundary I/II for the glycerol and ethylene glycol transfers from Teflon AF to PEMA (the rightmost data points in Figure 12 (a) and (b)). For both cases, $|\alpha_0-0.5|=0.5$, but one can see for the ethylene glycol case, the Boundary I/II are at a much higher velocities. During fast liquid transfer with small *Re*, surface and viscous forces are the two potential dominant forces.

Therefore, such difference can be understood by checking the value of t_v for the two types of liquid. For the 2µl liquid, t_v for glycerol and ethylene glycol are 0.0263s and 0.00055s, respectively. A smaller value of t_v for the ethylene glycol transfer suggests that a larger stretching speed (shorter time of the transfer process) is needed to allow the viscous forces to dominate and the transfer to reside in the Dynamic Regime.

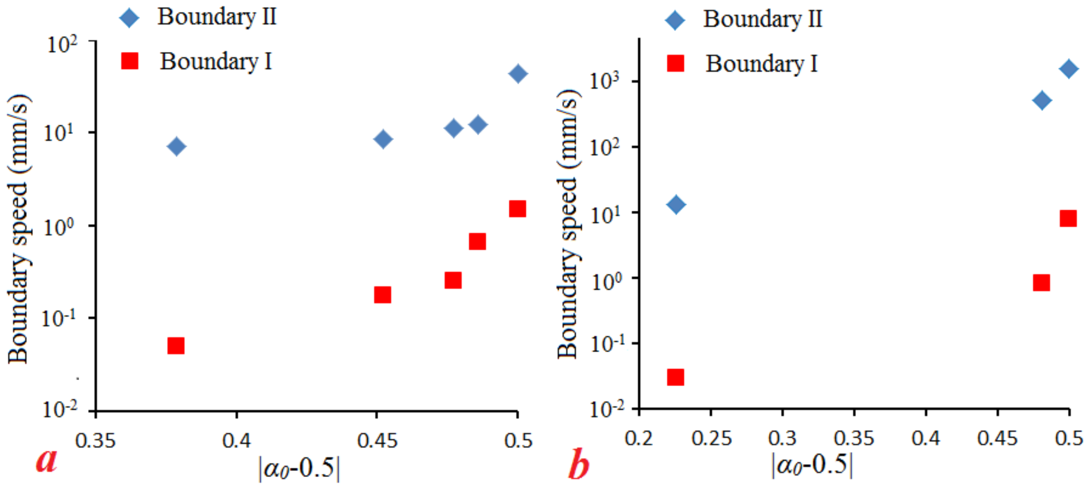

Figure 7.12: Speeds at Boundaries I and II vs. $|\alpha_0\text{-}0.5|$ for: (a) glycerol transfer from Silicon, PMMA, PS, OTS and Teflon AF to PEMA; (b). ethylene glycol transfer from PS, OTS and Teflon AF to PEMA.

7.3.4 Prediction of the Transfer Ratio

EQ. (7-3) not only provides excellent fitting to existing experimental data, but also can be used as a powerful tool to predict the transfer ratio at different U values. For a given liquid and pair of surfaces, only two coefficients (k and n) need to be determined to complete the relationship between α and U. Therefore, by knowing the transfer ratios at two different U values in the Transition Regime, the coefficients k and n can be obtained, and the general relation between α and U in all three regimes can be determined.

As an example, experiments of silicone oil transferred from Teflon AF to PEMA at 2 different U (0.05 mm/s and 0.1 mm/s) were performed and the transfer ratios are shown as the red solid points in Figure 7.13. The receding contact angles of silicone oil with Teflon AF and PEMA are 47.7^{o} and 0^{o}, respectively, which gives rise to a Quasi-static transfer ratio of $\alpha_0 = 0.851$ (using EQ.(7-1)). With the transfer ratios of the two additional data points in Figure 7.13, the coefficients k and n were found to be 82.80 and 1.68, respectively. Therefore, the transfer ratio of silicone oil from Teflon AF to PEMA can be described by:

$\alpha = 0.5+ 0.351/(1+82.8U^{1.68})$

In Figure 7.13, the predicted transfer ratio vs. U is shown as the solid black line. Additional experimental results (open symbols) are also presented, which show good agreement between the predicted results and experimental data.

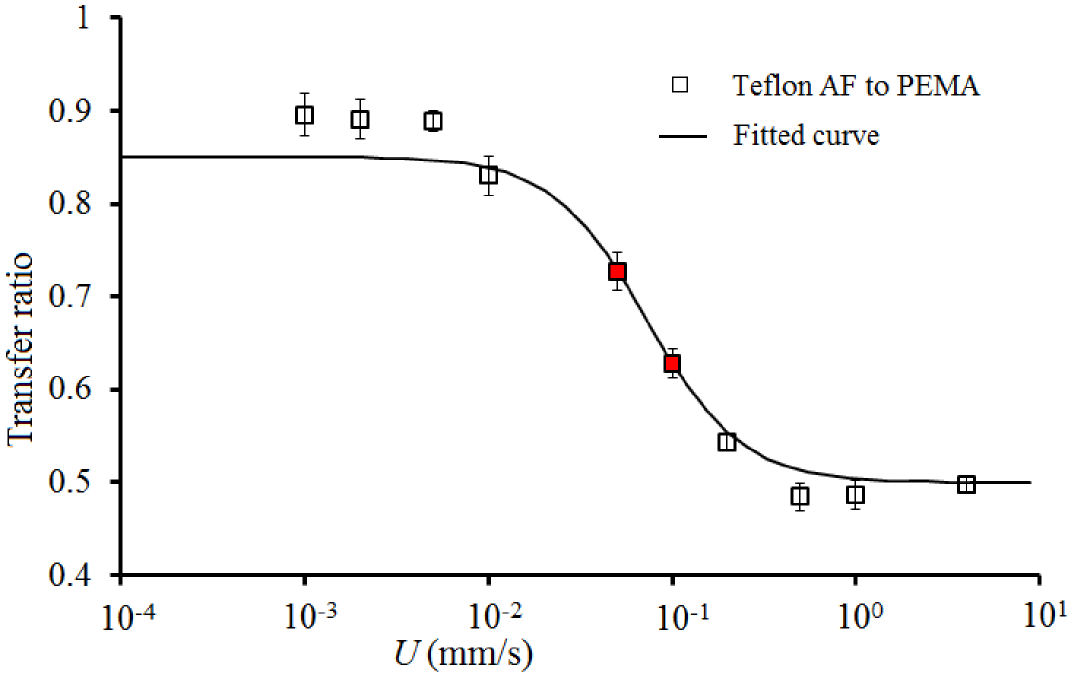

Figure 7.13: Relation between transfer ratio and U for silicone oil transferred from Teflon AF to PEMA. Note that the slight difference between the predicted results and experiments results at small U is caused by the error of calculating α_0 with the empirical model EQ.(7-1).

7.4 Conclusion

A systematic experimental study was performed to understand the role of the surface contact angle in determining the transfer ratio in fast liquid transfer. By examining the dependence of the transfer ratio on the stretching speed, the three regimes of transfer (Quasi-static, Transition and Dynamic) were identified. It was found that the wettability of the two surfaces can significantly affect the behaviour of liquid transfer in the Transition Regime, and hence can affect the boundaries separating the three regimes. Quantitatively, an empirical equation was provided to describe the transfer ratio as a function of stretching speed. The boundary speeds determined from this equation were found to increase with the increases of $|\alpha_0-0.5|$, which are completely determined by the receding contact angles of the two surfaces.

Bibliography

(7.1) M. Pudas, J. Hagberg, S. Leppavuori, *J. Eur. Ceram. Soc.* **2004**, 24, 2943--2950.

(7.2) C. M. Hong, S. Wagner, *IEEE Electron Device Lett.* **2000**, 21, 384--386.

(7.3) P. Kopola, T. Aernouts, S. Guillerez, H. Jin, M. Tuomikoski, A. Maaninen, A.; J. Hast, *Solar Energy Mat. Solar Cells* **2010,** 94, 1673--1680.

(7.4) D. Bonn, J. Eggers, J. Indekeu, J. Meunier, E. Rolley, *Rev. Mod. Phys.* **2009**, 81, 739--805.

(7.5) B. Qian, M. Loureiro, D. Gagnon, A. Tripathi, K. S. Breuer, *Phy. Rev. Lett.* **2009**, 102 (16), 164502

(7.6) I. Barbulovic-Nad, M. Lucente, Y. Sun, M. Zhang, A. R. Wheeler, M. Bussmann, *Crit. Rev. Biotechnol.* **2006**, 26, 237--259.

(7.7) A. V. Chadov, E. D. Yakhnin, *Kolloidn. Zh.* **1979**, 41, 817.

(7.8) E. D. Yakhnin, A. V. Chadov, *Kolloidn. Zh.* **1983**, 45, 1183.

(7.9) J. Qian, H. Gao, *Acta Biomaterialia* **2006**, 2, 51--58.

(7.10) H. Chen, A. Amirfazli, T. Tang, *Langmuir* **2013**, 29, 3310--3319.

(7.11) E. J. De Souza, L. Gao , T. J. McCarthy, E. Arzt, and A. J. Crosby, *Langmuir* **2008**, 24 (4), 1391--1396.

(7.12) S. J. Hong, T. H. Chou, S. H. Chan, Y. J. Sheng, H. K. Tsao, *Langmuir* **2012**, 28, 5606--5613.

(7.13) B. Samuel, H. Zhao, K. Y. Law, *J. Phys. Chem. C* **2011**, 115, 14852--14861.

(7.14) H. Chen, T. Tang, A. Amirfazli, *Soft Matt.* **2014,** 10, 2503--2507.

(7.15) H. Chen, T. Tang, A. Amirfazli, To be submitted.

(7.16) A. A. Darhuber, S. M. Troian, *J. Appl. Phys.* **2001**, 90, 3602--3609.

(7.17) P. Doshi, R. Suryo, O. E. Yildirim, G. H. McKinley, O. A. Basaran, *J. Non-Newtonian Fluid Mech.* **2003**, 113, 1--27.

(7.18) J. Meseguer, A. Sanz, *J. Fluid Mech.* **1985**, 153, 83--101.

(7.19) X. Zhang, R. S. Padgett, A. Basaran, *J. Fluid Mech.* **1996**, 329, 207--245.

(7.20) O. E. Yildirim,O. A. Basaran, *Chem. Eng. Sci*. **2001**, 56, 211--233.

(7.21) B. Qian, K. S. Breuer, *J. Fluid Mech.* **2011**, 666, 554--572.

(7.22) S. E. Bai, J. S. Shim, C. H. Lee, C. H. Bai, K. Y. Shin, *Jpn. J. Appl. Phy.* **2014**, 53, 05HC05.

(7.23) D. H. Ahmed, H. J. Sung, D. S. Kim, *Inter. J. Heat and Fluid Flow* **2011**, 32, 298--307

(7.24) H. W. Kang, H. J. Sung, T. M. Lee, D. S. Kim, C. J. Kim, *J. Micromech. Microeng.* **2009**, 19, 015025

(7.25) S. Dodds, M. Carvalho, S. Kumar S. *Phy. Fluids* **2009**, 21, 092103.

(7.26) S. Dodds, M. Carvalho, S. Kumar S. *Phy. Fluids* **2011**, 23, 092101

(7.27) H. S. Huynh, J. P. Guan, T. Vuong, T. W. Ng, *Langmuir* **2013**, 29 (37), 11615--11622.

(7.28) C. W. Hirt, B. D. Nichols, *J. Computational Phys.***1981**, 39,201-225.

(7.29) P. A.Thompson, M. O. Robbins, *Phy. Rev. Lett.* **1989**, 63 (7), 766--769.

(7.30) A. A. Saha, S. K. Mitra, *J. Colloid and Interface Sci.* **2009**, 339, 461--480.

(7.31) S. F. Kistler, Hydrodynamics of wetting. In: Berg, J.C.: Wettability, M. Dekker, USA, New York, 1993.

(7.32) I. V. Roisman, R. Rioboo, C. Tropea, *Proc. R. Soc. Lond. A* **2002**, 458, 1411--1430.

(7.33) M. Muradoglu, S. Tasoglu, Computers Fluids **2010**, 39, 615--625.

(7.34) L. H. Tanner, *J. Phys. D: Appl. Phys.***1979**, 12, 1473--1484.

Chapter 8

8. Fast Liquid Transfer between Surfaces: Breakup of Stretching Liquid Bridges

8.1 Introduction

Methods of transferring a liquid drop from one solid surface (donor surface) to another (acceptor surface) have been investigated for more than 100 years. One of the most widely seen transfer method is stretching liquid bridges formed between these two surfaces. When the liquid bridge is stretched to a certain height, the bridge breaks; hence part of the liquid can be transferred from one surface to the other. Such transfer process can be widely seen in plenty of industrial implications, e.g. in offset printing, drop deposition, packaging industry and electronic circuits printing [1-6] as well as in nature [7, 8]. The transfer ratio (α) which is defined as the volume that transferred to the acceptor surface over the total liquid volume is particularly important in determining the product quality and work efficiency in these applications. Therefore, understanding the governing parameters for the value of transfer ratio received considerable attention in the study of such liquid transfer process.

Chadov and Yakhnin [9, 10] for the first time, identified that the transfer process could be governed by three different forces, i.e. surface, inertia and viscous forces. In the literature, the three forces in the transfer systems are typically qualitatively described by several dimensionless numbers: Capillary number ($Ca = U\mu/\gamma$, ratio of viscous to surface forces, where U is the stretching speed, μ is liquid dynamic viscosity, and γ is liquid surface tension), Weber number ($We = \rho U^2 V^{1/3}/\gamma$, ratio of inertial to surface forces, where ρ and V are the liquid density and volume, respectively), and Reynolds number ($Re = \rho U V^{1/3}/\mu$, ratio of viscous force to the inertial forces). For example, when a transfer system has $Ca << 1$， the effects of the surfaces force are much more important than the viscous forces. The transfer ratio shows a very different dependence when the system is dominated by different forces. Specifically, when the liquid transfer process is performed with a very slow stretching speed, the value of Ca and We are very small ($<< 1$); hence the transfer is only governed by the surface forces. The value of transfer ratio is a constant value (denoted by α_0), and does not change with the change of stretching speed. When the liquid bridge is stretched at a very high speed, the effects of the surface forces become negligible. And transfer ratio also does not change with the change of stretching speed, but stays at 0.5. When a moderate stretching speed is applied, transfer ratio converges to 0.5 from α_0 with the increase of speed, and the process can be governed by all three forces.

A number of studies were performed on the liquid transfer under slow stretching speed (Ca and $We << 1$), and the receding contact angle (θ_r) of the two surfaces were found to be the governing parameters for the value of α_0 [11-15]. Compared with slow liquid transfer, the governing parameters for the transfer ratio during fast transfer are still not clear. In most applications, the liquid is transferred with a relatively fast stretching speed to provide a high working efficient; hence the effects of inertia and viscous forces are not negligible. Therefore, it is of interest to understand what parameters govern α during fast transfer. Based on the expression of the three dimensionless numbers, Ca, We, and Re, it can be see that, γ is related to the surface forces; U and μ are related to the viscous force; U, V and ρ are related to the inertia forces. Besides the five physical parameters involved in the three dimensionless numbers, the surface contact angle (*SCA*) which constraint the profile of liquid bridge close to the surface, and the minimum separation between two surfaces (H_{min}) which governs the initial shape of the liquid bridge can also affect the transfer process.

In most practical situations, e.g. offset printing, small volumes (on the order of 1 μm) of viscous liquid are normally used [16], which corresponds to small Re. Therefore, in the literature of the liquid transfer between two parallel surfaces, the inertia forces are typically neglected and only the surface and viscous forces are considered. By using the volume of fluid (VOF) method, Huang *et al.* [17] studied process of fast liquid transfer with small inertia affect (*Re* in the range of 0.0008-0.04). The results show the transfer ratio can be significantly different when γ, *U, SCA* and μ of the system are changed. On the other hand, how exactly these parameters affect the surface or viscous forces were not thoroughly discussed. A study performed by Dodds *et al.* [18] investigated the effects of the viscous and surface forces during the fast transfer, again neglecting inertia forces. *Ca* was used to characterize the liquid transfer process. It was found that the transfer ratio converges to 0.5 when *Ca* becomes sufficient large, which agreed with the observations made in [9, 10]. In the above two studies, the contact angle was assumed to be constant on both surfaces during the entire process.

As demonstrated by Bai *el al.*[19], the values of the contact angle during the process of fast transfer can have a complex dependence on the stretching speed, which can in turn affect the transfer ratio. A series of experiments and simulations were performed in our group to study the effect of *SCA* and *U* on fast liquid transfer [20]. It was shown that the transfer ratio as function of *U* ($\alpha=F(U)$) converged from one plateau value (α_0) to 0.5 with the increase of *U*, and that the value of α_0 was only dependent on the *SCA*. The critical speeds at which the converging of transfer ratio from α_0 to 0.5 with increase of *U* starts and ends, are also significantly affected by *SCA*.

Many studies so far have focused on liquid transfer with negligible inertia effect (*Re* <<1). Liquid transfer with considerable inertia effects does exist in some situations. For example, when cats lap, water adheres to the tongue tip forming a water bridge. By retreating its tongue, the water can be drawn into the cat's mouth. Shown in [7], such retreat speed can be up to ~ 720mm/s. Given the small viscosity of water, with such fast speed, the *Re* of the system could be quite large (>500). Therefore, it is of interest to understand the transfer behavior under inertia effects. To understand the inertia effects, Dodds *et al.* [21] performed a numerical study of liquid transfer from one surface (*SCA*: 70^o) to another (*SCA*: 90^o) with the same *Ca* (0.1) but five different *Re* (0, 0.1, 1, 10 and 100). It is shown that when *Re* > 1, formation of satellite drops at the bridge breakage can be observed. And the transfer ratio was found to increase from 0.08 to approximate 0.5 when *Re* increase from 0.1 to 100. In Park *et al.* [22], water transfer from a donor surface with *SCA* of 60° to an acceptor surface with *SCA* of 70° at different *U* (10 mm/s to 250 mm/s) were simulated with VOF method. Their results showed that the transfer ratio increased from 0.07 to 0.36 with the increase of *U* from 10 mm/s to 200 mm/s. However, when *U* was further increased to 250 mm/s (*Re* =277), instead of staying at 0.5, the transfer ratio decreased to 0.33. Therefore the observations made at small *Re* that transfer ratio always converges to 0.5 at high speed may not be valid when the inertia effects become important.

In this work, an experimental study is performed on fast liquid transfer at both small and large *Re* numbers. When the value of *Re* of the transfer system is small, the effects of inertia forces are negligible; hence the process is governed by *SCA*, *U*, μ, γ and H_{min}. *S*ince the effects of *SCA*, and *U* were well discussed in [20], the effects of μ, γ and H_{min} are the focus of this chapter. Experiments of the fast liquid transfer system with large *Re* are also performed to understand the inertial effects and investigate if the transfer ratio still converges to 0.5 with increase of *U* under strong inertial effects.

8.2 Method

The experimental procedure is shown in Figure 8.1. A liquid drop is first placed on a donor surface. The acceptor surface was brought towards the drop so that a liquid bridge can form between the two surfaces. The compression stage was stopped when the separation between the two surfaces reached a certain distance (defined as H_{min}). After a short pause, the liquid bridge is stretched with a certain speed (*U*), until the liquid bridge breaks. After this transfer process, part of the liquid is transferred from the donor surface to the acceptor surface. All the experiments were performed at the ambient temperature of approximate 20.5°C, and 2.0 µl volume of liquid was used. Phantom Miro M310 which can provide imaging speed of 5000 fps with the resolution of 896 × 720 was used to record the process.

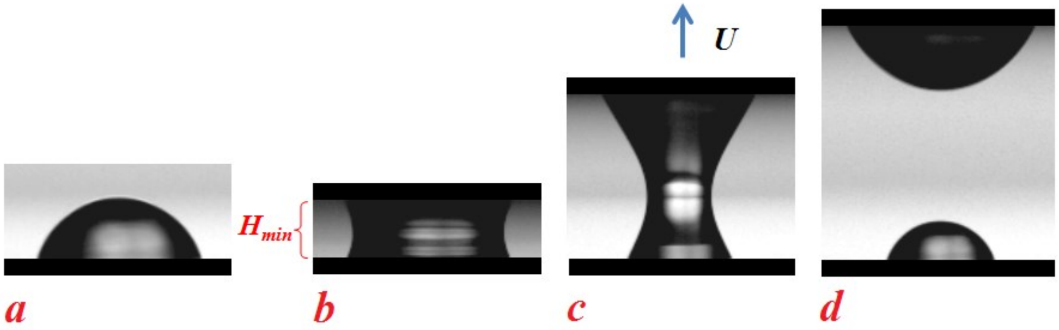

Figure 8.1: Process of fast liquid transfer (a). Liquid drop is placed on the donor surface. (b). liquid bridge between two surfaces before transfer. (c). liquid bridge is stretched by applying a velocity *U* on the acceptor surface. (d). liquid bridge breaks.

Two different experimental setups were used. For the experiments with relatively small stretching speed ($U < 20$ mm/s), the motion of the acceptor surface is provided by a Motion Controller system (ILS100CC and XPS-C6 from Newport) (shown in Figure 8.2a). With this setup, the acceptor surface can be accelerated to a target velocity (< 20mm/s) in a very short time. Therefore, for the experiments performed with this setup, the stretching speed can be treated as a constant during the whole process. Due to the limitation of the maximum acceleration of this motion controller system (400mm/s^2), for a 2.0 μl liquid transfer, the liquid bridge usually breaks at a short separation distance where the stretching speed is still low. Therefore, another setup which consists of a spring system (shown in Figure 8.2b) was used to provide the motion for the liquid transfer with a large stretching speed. In this setup, the acceptor surface is attached with a platform connected to the two springs. The springs were stretched to attach the platform to a translation stage underneath. Based on the Hook's Law, an elastic force can be generated. When the springs are released, this elastic force can provide a sufficiently large acceleration to the acceptor surface. By adjusting the distance between the platform and the translation stage, the value of the elastic force can be varied, hence changing the stretching velocity. The details of the velocity measurements and calibration are provided in the Appendix G. Since the velocity provided in the second setup is not a constant during the transfer process, the speed averaged from the beginning of the stretching stage to the breakage of the liquid bridge is used as *U* for the second experimental setup in the later discussion.

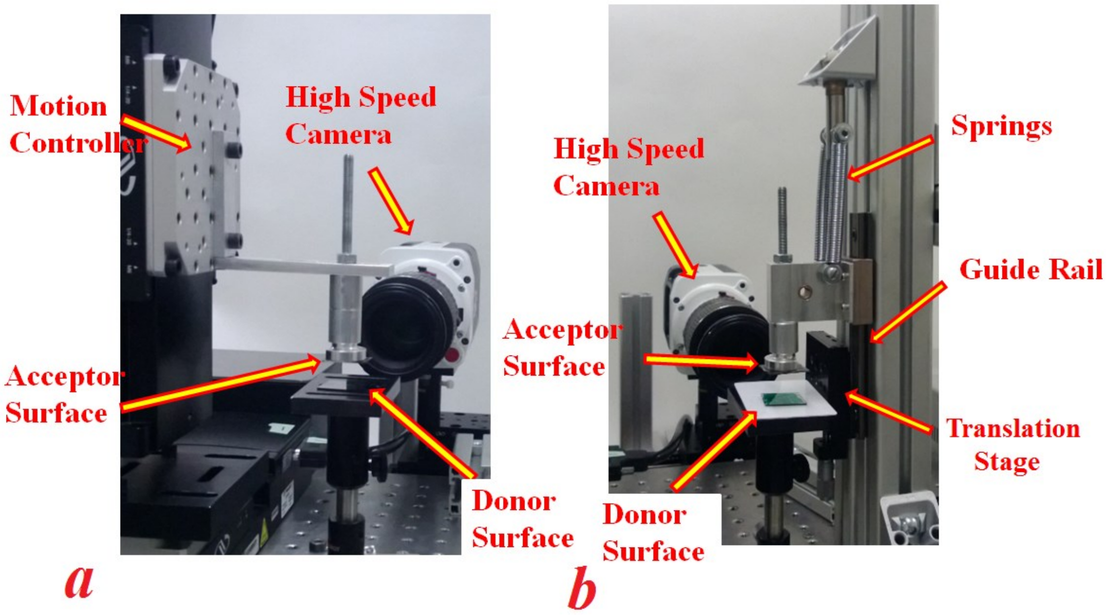

Figure 8.2: (a). Experimental setup for low speed tests. (b). Experiment setup for high speed tests.

Seven different liquid, i.e. distilled water, ethylene glycol, glycerol and four different types of silicone oil were used in this study, and the properties of these liquids are shown in Table 8.1. The surfaces used in this study were fabricated with different material, i.e. Poly (methyl methacrylate) (PMMA), Polystyrene (PS), Poly (ethyl methacrylate) (PEMA), Teflon AF, Octadecyltrichlorosilane (OTS) and glass, and by applying different fabrication method, i.e. spin coating and heat press. The contact angle between the surfaces and liquids were measured with sessile drop method. The details of surface fabrication are shown in the Appendix G.

Table 8.1: Surface tension, viscosity, and density of the liquids.

Liquid Name	γ **(mN/m)**	μ **(Ns/m^2)**	ρ **(kg/m^3)**
Silicone oil 1	20.6	0.019	950
Silicone oil 2	20.9	0.096	966
Silicone oil 3	21.2	0.967	971
Silicone oil 4	21.5	9.719	974
Ethylene glycol	48.4	0.021	1115
Glycerol	63.4	1.350	1264
Distilled water	72.8	0.001	998

H_{min} was varied when its influence was studied, but otherwise was fixed at 0.45 mm. For the investigation of the liquid viscosity, experiments were performed with four silicone oils (shown in Table 8.1) which have similar surface tension but different viscosity (transfer was from Teflon AF to PEMA). Due to the similar surface tension, the values of *SCA* between the four silicone oils and surfaces are also similar; hence the viscosity can be decoupled from H_{min}, γ and *SCA*. In the study of the surface tension, results of ethylene glycol transfer from PS to glass surfaces were used to compare with the silicone oil results. Shown in Supporting Information, *SCA* between silicone oil and Teflon AF/PEMA are similar to the values of *SCA* between ethylene glycol and PS/glass surfaces. Therefore, the effects of *SCA* can be minimized. For the study of H_{min}, experiments of glycerol transfer from Teflon AF to OTS were performed under the same U but with different H_{min}. Due to the large contact angle between glycerol and OTS/Teflon AF, a wide range of H_{min} (from 0.38mm to 0.98mm) can be covered.

8.3 Results and Discussion

The values of *Ca* and *We* for all 89 experimental cases are shown in Figure 8.3. Each dash line represents a particular value of *Re*. It can be seen that except for the majority of water transfer cases, all the other transfer cases (the hollow symbols in Figure 8.3) have small *Re* (< 1) and hence small inertia effects. Therefore, these are the experiments used to investigate the effect of μ, γ and H_{min} when the inertia effects are negligible. Results for these experiments will be presented in section 8.3.1. Due to the small viscosity of water, the cases of water transfer (solid circles) can have significantly larger Re. Therefore, the results of the water transfer can help us understand the behavior of liquid transfer with large inertia effects; these results will be presented in section 8.3.2.

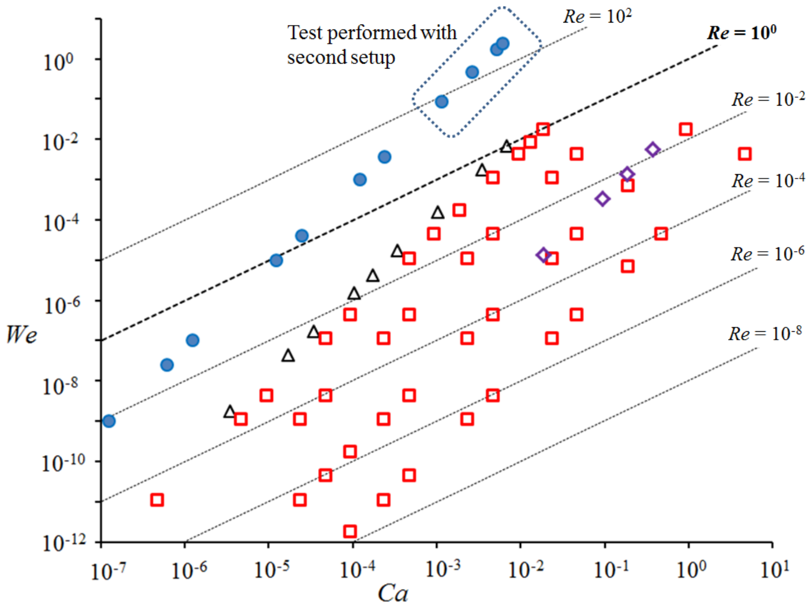

Figure 8.3: Values of *Ca, We* and *Re* for all of the 89 experimental transfer cases (Δ: ethylene glycol transfer from PS to Glass, □: Four types of silicone oil transfer from Teflon AF to PEMA. ●: Water transfer from PS to PEMA, ◇: Glycerol transfer from Teflon AF to OTS).

8.3.1 Liquid transfer with negligible inertia effects

8.3.1.1 Effects of viscosity

Four types of silicone oil which have similar surface tension but very different viscosity (see Table 8.1) were used in the experiments to study the effect of viscosity. Teflon AF surface and PEMA surface were served as donor and acceptor surfaces, respectively. Due to the very similar surface tension, the contact angle of the four types of silicone oil on Teflon AF (θ_a~57°, θ_r ~48°) and PEMA surfaces (the surface was wetted completely, the contact angle is treated as 0°) are also very similar. Figure 8.4 shows the transfer ratio as a function of U for the four different types of silicone oil (symbols). Shown in [20], the relation between transfer ratio and U can be described by:

$$\alpha = 0.5 + \frac{\alpha_0 - 0.5}{1 + kU^n} \quad (8\text{-}1)$$

where k and n are fitting coefficients that can possibly depend on SCA, μ, γ and H_{min}. The solid lines in Figure 8.4 are the curve $\alpha=F(U)$ fitted using EQ. (8-1) to the experimental data. It is clear that all of the curves start from approximately 0.9 (α_0). This is because the value of α_0 is only governed by θ_r of the two surfaces [15]. All four type of silicone oil have similar θ_r with the two surfaces, and hence similar α_0. Also similar for the four silicone oils is that the transfer ratio converges to 0.5 for very large values of U. More interestingly, the four curves have almost the same shape but are shifted to the left with the increase of liquid viscosity. This seems to suggest that the viscosity μ serves as a velocity shift in affecting the transfer ratio. Since μ and U are combined in the capillary number $Ca=U\mu/\gamma$, it is of interest to examine the dependence of the transfer ratio on Ca.

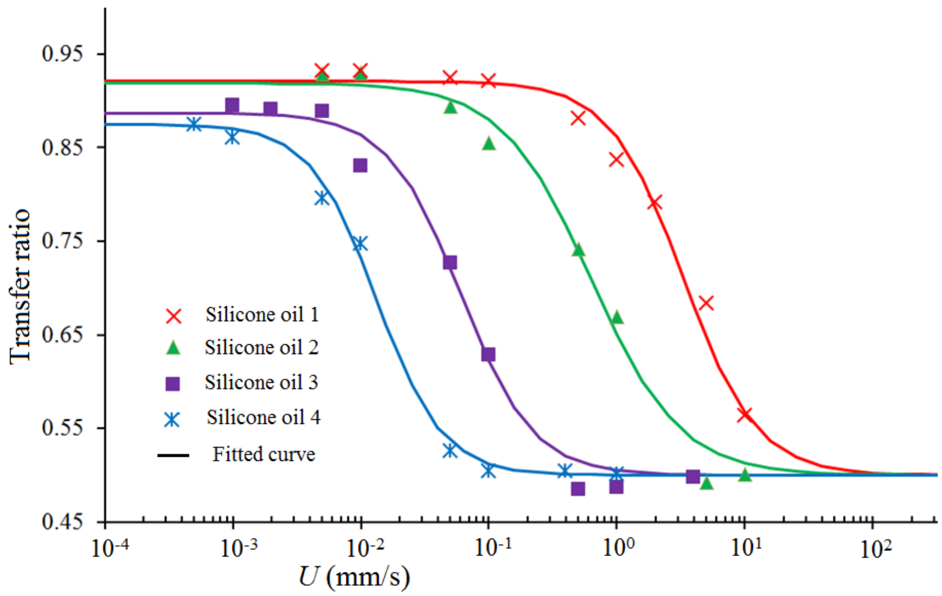

Figure 8.4: Transfer ratio as a function of U for the four different types of silicone oil. The solid curves are the curve $\alpha=F(U)$ fitted using EQ. (1) to the experimental data.

In Figure 8.5, the value of transfer ratio is plotted against Ca for the four types of silicone oil. It can be seen that all the data collapse onto a single master curve. The shapes of the liquid bridge at the breakage were also checked for all the cases, which were observed to be very similar at the same Ca. For example, the insert pictures on the left side of Figure 8.5 show the shape of the liquid bridge at the breakage (breakage shape) of three cases with a small value of Ca (4.6×10^{-4}), and the insert pictures on the right side show the breakage shape of three cases with a relatively large Ca (0.46). Despite the different viscosities, the shapes are very close to one another at the same Ca. This confirms that viscosity μ serves as a velocity shift, and indicates that α depends on U through Ca, i.e., $\alpha = G(Ca)$.

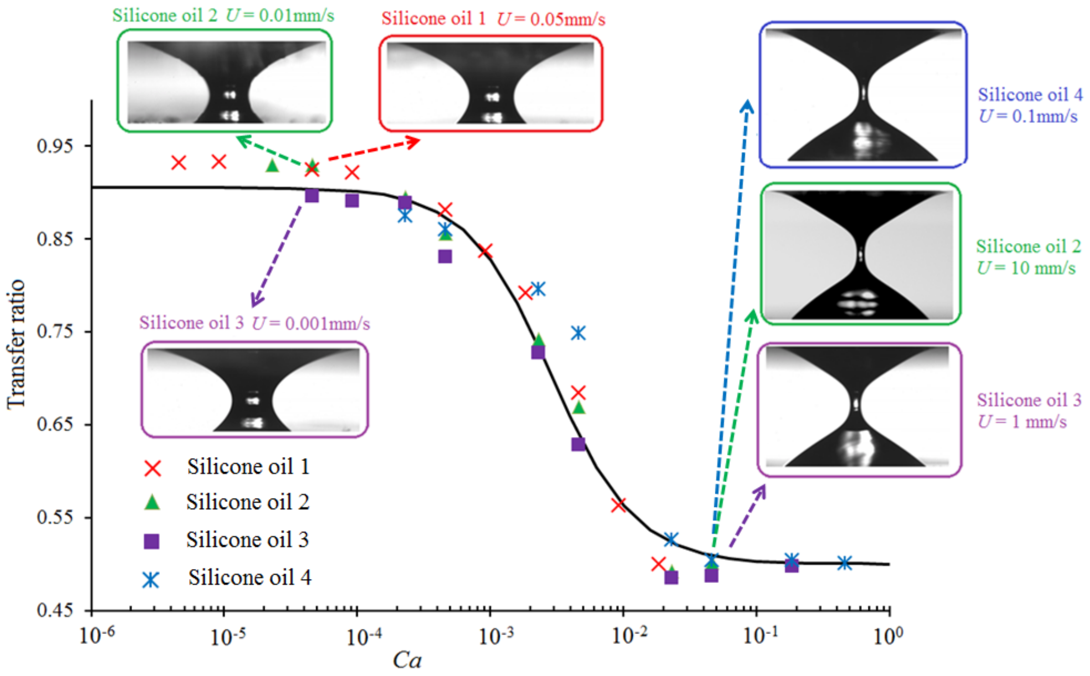

Figure 8.5: α as a function of Ca for the four silicone oils. The insert pictures are the shapes of the liquid bridge at the breakage. The solid line is the curve $\alpha=G\ (Ca)$ fitted using EQ. (2) with the experimental data. The value of p and q for this specific case are 5408.72 and 1.52, respectively.

8.3.1.2 Effects of surface tension

To explore the effect of surface tension, ethylene glycol transfer from PS (contact angle between ethylen glycol and PS: θ_a=61.0±1.6^{o}, θ_r= 47.5±1.9^{o}) to glass surfaces (the surfaces were wetted completely, the contact angle is treated as 0^{o}) were performed with different stretching speeds. Ethylene glycol, PS and glass were chosen as the liquid and sufaces beacuse the *SCA* between ethylene glycol and PS/glass are similar to those in the silicone oil transfer systems (section 8.3.1.1 and Figure 8.5). The surface tension of ethylene glycol (47.7mN/m), however, is more than twice of the surface tenion of the silicone oil (~21mN/m). Knowing that the effect of viscosity is embedded with *Ca*, studying the dependence of transfer ratio on *Ca* for the ethylene glycol transfer and comparison with Figure 8.5 will alow us to examine the effect of surface tension. Transfer ratio as a funcion of *Ca* for the ethylene glycol transfer is shown in Figure 8.6. The data of silicone oil transfer are also shown in Figure 8.6 for comparison. From Figure 8.6, it can be seen that for the ethylene glycol transfer cases, α as function of Ca starts from $\alpha \sim 0.9$ at small Ca ($<10^{-4}$), and convergers to 0.5 when a large Ca ($\sim 10^{-2}$) is applied. More interestly, the function of $\alpha = G(Ca)$ of the ethlylene glycol case has very similar shape with $\alpha = G(Ca)$ of the silicone oil cases. When Ca is small, the value of the ethlylene glycol case transfer ratio is almost the same as it of the silicone oil cases. This is because when Ca is small, only surface force dominate the transfer process. Shown in [15], in such situation, *SCA* of the two surfaces are the only governing parameters for the transfer ratio. The *SCA*s of the ethylene glycol system are quite similar to the *SCA*s of the silicone oil system. Therefore, the value of transfer ratio of ethylene glycol system is similar to it of silicone oil systems with small Ca. When Ca becomes larger, $\alpha = G(Ca)$ for the ethylene glycol transfer system also converges to 0.5. Since $\alpha = G(Ca)$ for the ethylene glycol cases has the same starting and ending value (0.9 and 0.5, respectively) as the silicone oil cases, a similar behavior of $\alpha = G(Ca)$ can be seen at the meddle range of Ca. Therefore, it can be seen that even the surface tension of ethlylene glycol is more than twice of it of silicone oils, the shape of $\alpha = G(Ca)$ of the ethlylene glycol system is similar to it of silicone oil transfer systerm. Hence, we could know that similar to the liquid viscosity, liquid surface tension also does not strongly affect the function of $\alpha = G(Ca)$.

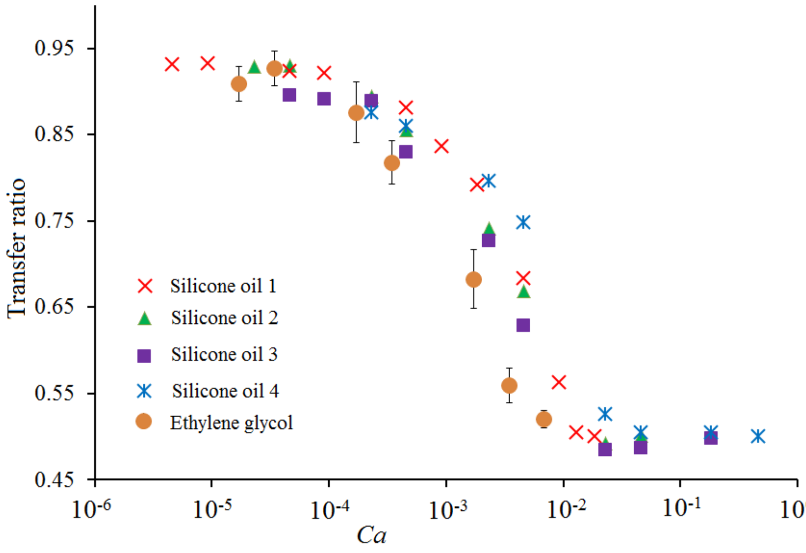

Figure 8.6: α as a function of Ca for four types of silicone oil (transferred from Teflon AF to PEMA surface) and ethylene glycol (transferred from glass to PS surface).

8.3.1.3 Emperical function *α =G(Ca)*

From both Figures 8.5 and 8.6, it has been demonstrated that when the effects of the inertia forces are neglegible (as shown in Figure 3, these cases have very small *Re*), as long as the *SCA* and H_{min} are fixed, *Ca* is the only parameter that controls the transfer ratio. Therefore, the expression of EQ.(8-1) can be revised to

$$\alpha = 0.5 + \frac{\alpha_0 - 0.5}{1 + pCa^q} \quad (8\text{-}2)$$

where *p* and *q* are two fitting coeffcients. Different from the coeffcients *k* and *n* in EQ.(8-1), *p* and *q* in EQ.(8-2) are not influnced by *μ* or *γ* of the liquid. Since α_0 is only controlled by *SCA* [15]. Therefore, for any liquid transfer system, as long as the *SCA* and H_{min} are fixed, the function *α =G(Ca)* can be uniquely determined.

EQ. (8-2) is useful in the following two aspects. Firstly, for a given liquid transfer system (with liquid and surfaces specified), EQ.(8-2) involves only two unknown coefficients (*p* and *q*). Therefore, if the transfer ratio under two different *Ca* can be measured, the values of *p* and *q* can be calculated, allowing the prediction of the transfer ratio at any other *Ca*. Secondly, the effect of liquid viscosity is embedded in *Ca* in EQ.(8-2). As such, transfer ratios for liquids with the same *SCA* and H_{min} are predicted by the same relation *α* = *G*(*Ca*). For example, in offset printing, it is possible for different types of ink to have similar *SCA*, but different viscosity. The transfer ratios for these inks can be obtained by knowning the funcion *α* = *G*(*Ca*) from the measurement of one ink.

8.3.1.4 Effects of H_{min}

During the process of fast liquid transfer, in the liquid, the momentum is spread from the acceptor to the donor surface. Therefore, the speed of the spread of momentum is important in determining the transfer ratio, which can be affected not only by the stretching speed and liquid properties, but also by the shape of the liquid bridge. Therefore, one more parameter, H_{min}, which to date has been typically missing in the study of the liquid transfer with free moving contact line, should be considered.

To study the effects of H_{min}, glycerol transfer from OTS to Teflon AF with seven different H_{min} (from 0.38 mm to 0.98 mm) were performed (all these experimental cases have a small *Re* as shown in Figure 8.3). For each H_{min}, 4 different stretching speeds (1 mm/s, 5 mm/s, 10 mm/s, and 20 mm/s) were used. The corresponding *Ca* values are 0.0197, 0.0984, 0.1969 and 0.3937, respectively. Figure 8.7 shows the transfer ratio as a function of *Ca* for the 7 groups of data. It can be seen that when *Ca* is very small (*Ca* = 0.0197), the transfer ratio is identical (= 0) for the 7 different H_{min}. This is because when *Ca* is small, viscous force is negligible and the transfer process is mainly governed by the surface force. Given the identical liquid and donor/acceptor surfaces used in these 7 experiments, the transfer ratio is expected to be the same. When *Ca* becomes larger, the effects of viscous force become more and more important, and the deviation of transfer ratios in the 7 experiments becomes evident. Such difference increases with the increases of *Ca*, and when *Ca* is increased to 0.3937 (*U* =20 mm/s), the transfer ratio is significantly different. For example, for the case of H_{min} = 0.38 mm, the transfer ratio is 0.43, while for the case of H_{min} = 0.98mm, the transfer ratio is only 0.2.

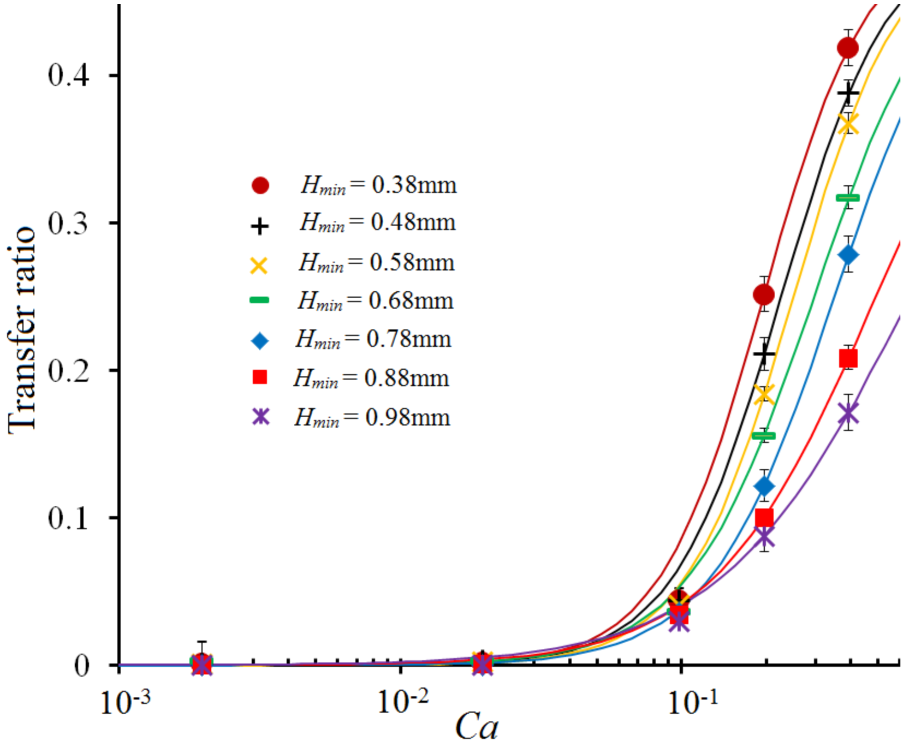

Figure 8.7: Transfer ratio as a function of *Ca* for glycerol transfer from OTS to Teflon AF with different H_{min}. The advancing and receding contact angles between glycerol and OTS, and between glycerol and Teflon AF are respectively: θ_a : 97.5°, θ_r: 83.9 °, and θ_a : 113.1 °, θ_r: 106.7 °. The solid lines are the curve of function $\alpha = G(Ca)$ for each group of data. The coefficients p and q in $G(Ca)$ were calculated based on the two transfer ratios at $Ca = 0.1969$ and $Ca = 0.3937$.

When the liquid bridge is stretched, based on the non-slip boundary condition, the liquid on the acceptor surface should have the same vertical velocity as the acceptor surface, and the liquid on the donor surface has zero vertical velocity. Therefore, with the same U, the transfer cases with smaller H_{min} can have a larger vertical velocity gradient, and hence slower momentum transfer from the acceptor surface to donor surface. Shown in literature [20, 21], the slower spread of momentum can help the liquid bridge split more equally between the two surfaces. As a result, we can see from Figure 8.7 that as H_{min} is decreased from 0.98 mm to 0.38 mm, the transfer ratio increases from 0.088 to 0.251 (becoming closer to 0.5). The shapes of the liquid bridges at both H_{min} and breakage of all the seven groups of experiments are examined to further help understand the results. The cases with U = 10 mm/s (Ca = 0.1969) are chosen as examples, and shown in Figure 8.8. First consider the shapes of the liquid bridge at H_{min}.It can be seen that with the increase of H_{min} the difference between the contact radii on the two surfaces increases. For example, with H_{min} = 0.38mm, the contact radius on the acceptor surface was 0.626mm, 96.1% of that on the donor surface (0.652mm). When H_{min} was increased to 0.98mm, the contact radius on the acceptor surface (0.343mm) became only 82.6% of that on the donor surfaces (0.416mm). This suggests that when H_{min} becomes smaller, a larger portion of the liquid can have a vertical velocity close to that of the acceptor surface at the beginning of the stretching stage, which helps more liquid to be transferred from the donor to the acceptor. As a result, if the breakage shapes are examined, with the decrease of H_{min}, a significant increase of the contact radius on the acceptor surface can be seen. The different breakage shapes then lead to the different transfer ratio for different H_{min}.

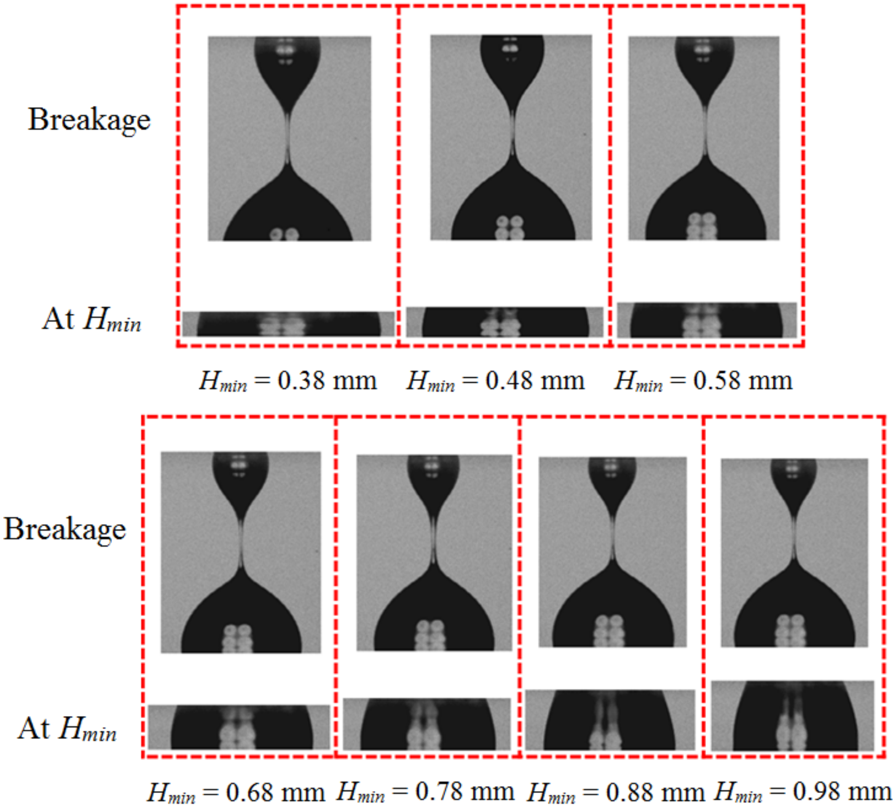

Figure 8.8: The shapes of the liquid bridge for glycerol transfer from OTS to Teflon AF surface at both H_{min} and breakage with different H_{min}. The stretching speed for all cases is U = 10 mm/s.

8.3.2 Liquid transfer with the effect of inertia forces

In order to achieved a large *Re*, distilled water with a small viscosity was used. Experiments of 2µl water transfer from PEMA (θ_a: 77.1°, θ_r: 66.9°) to PMMA surface (θ_a: 73.1°, θ_r: 58.3°) under different stretching speed were performed (from 0.01mm/s to 494mm/s). Transfer ratio as a function of *Ca* is shown in Figure 8.9, along with the values of *Re* (blue color, underneath the data point) and *We* (red color, above the data point) for each case. It can be seen that, similar to Figure 8.7, when *Ca* is small, the transfer ratio is also a constant in Figure 8.9. However, the transfer ratio does not converge to 0.5 at large *Ca* as seen in Figure 8.7, but shows a trend of continuous decrease with the increase of *Ca*. Furthermore, for the transfer cases with *Re*= 328.9 and *Re* = 386.8, the transfer ratio become smaller than 0.5.

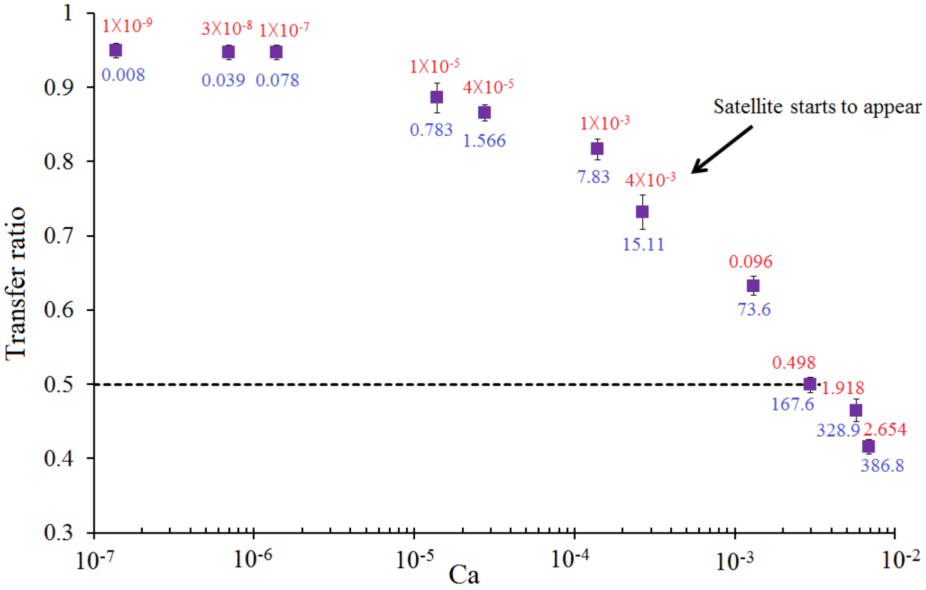

Figure 8.9. Transfer ratio as a function of *Ca* for water transfer from PEMA to PMMA. The values of *Re* and *We* for each case are labeled with dark (blue) and light (red) color text, respectively.

Figure 10a-d show the shape of the water bridge just before the breakage and just after the breakage, obtained with different stretching speed. Two observations can be made from these images. Firstly, similar to the observations made in [21], satellite droplets can be seen for the transfer cases with a large value of *Re* (starting from *Re*=15.11). And the volume of the satellite droplet increases with the increases of *Re*. Secondly, the shape of the liquid bridge just before the breakage becomes more and more symmetric when the *Re* increases from 0.078 to 167.6 (from Figure 8.10a to 10c). At *Re* = 167.6, the breakage shape becomes almost symmetric, which results in approximate 0.5 for the transfer ratio. However, when *Re* continues to increase, instead of having the symmetric breakage shape, an asymmetric breakage shape can be observed (Figure 10d). The asymmetric shape of the liquid bridge just before the breakage and the presence of the satellite droplet just after the breakage eventually result in the transfer ratio being smaller than 0.5 when *Re* becomes sufficient large (*Re* = 328.9 and 369.8 in Figure 8.9). It should be pointed out that the two critical values of *Re* (*Re*=15.11 at which the satellite droplets start appearing and *Re* = 167.6 after which the transfer ratio become smaller than 0.5) are only applicable to this particular system tested. If the system is changed, e.g. V, μ, γ, *SCA* and H_{min} are changed, the critical values can be different. However, based on the observations made in Figure 8.9 and 8.10, we can confidently conclude that the transfer ratio does not converge to 0.5 at large *Ca* when the inertia effects are significant.

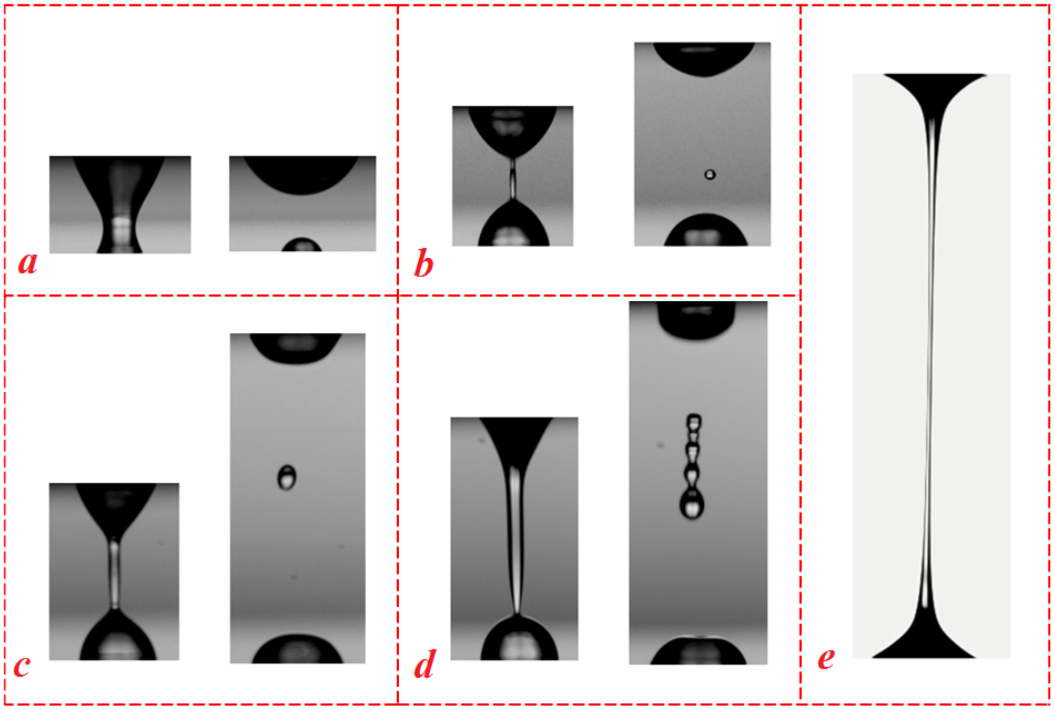

Figure 8.10. The shape of the liquid bridge just before breakage and just after the breakage, for water transfer from PEMA to PMMA surfaces: (a).U = 0.1mm/s, Re = 0.078, $We = 1\times10^{-7}$, and $Ca = 1.39\times10^{-6}$; (b). U = 94mm/s, Re = 73.6, We = 0.096, and $Ca = 1.31\times10^{-3}$; (c). U = 214 mm/s, Re = 167.6, We = 0.498, and $Ca = 2.97\times10^{-3}$; (d). U = 420mm/s, Re = 328.9, We = 2.654, and $Ca = 5.83\times10^{-3}$ (e). Breakage shape of glycerol transfer from PS to PEMA, U = 403mm/s, We = 3.86, Re = 0.45, and Ca = 7.53.

To have a clearer understanding of the inertia effects, Figure 8.10e shows the breakage shape of glycerol transfer from PS to PEMA under 403mm/s which is similar to the stretching speed applied in Figure 8.10d. If we further compare the value of Re, We, and Ca of the transfer cases shown in Figures 8.10d (Water) and 10e (Glycerol), these two cases have similar We, but the Water case has a significantly smaller Ca and larger Re due to its much smaller μ. Due to the significantly smaller viscosity of water, the shear stress within the water is much smaller than it in glycerol cases. The larger value of Re in the Water case suggests that compared with the Glycerol case, the spread of the momentum from the acceptor surface to the donor surface is much slower in the water transfer. The part of water which is close to the donor surface could not catch up the movement of the acceptor surface. Therefore, the asymmetric breakage shape can be observed. The different behaviors of the water and glycerol transfer under fast stretching speed can also be understood by calculating the viscous/capillary time scale ($t_v \sim \mu V^{1/3}/\gamma$) and inertial/capillary time scale ($t_i \sim (\rho V/\gamma)^{1/2}$) of the two systems. With 2μl volume, the value of the t_v and t_i are 1.4×10^{-5}s and 5.2×10^{-3}s for water, and 2.64×10^{-2}s and 6.26×10^{-3}s for glycerol. The experiments of water and glycerol cases were finished in approximately 8.1×10^{-3}s and 2.5×10^{-2}s (is calculated from the start of stretching stage to the time that the radius of neck of the liquid bridge decreased to 10% of the average of the contact radii on the two surfaces). It can be seen that for glycerol case, the time to complete the experiment is in the order of magnitude of $t_{v,}$ while for the water case, the time to complete the experiment is in the order of the magnitude of t_i. Therefore, it can be known that the glycerol transfer case is governed by the viscous forces, while the water case is governed by the inertial forces; hence different breakage shape of the two cases can be seen.

8.4 Conclusion

In this chapter, a systematic experimental study was performed to understand fast liquid transfer process between two surfaces. For transfer with negligible inertia effects, the transfer ratio was shown to be given by a monotonic function of the capillary number $\alpha = G(Ca)$.This function involves only two unknown coefficients which are affected by *SCA* and H_{min}, but not by the liquid viscosity or surface tension. Knowing the transfer ratios at two different *Ca* values, the function can be completely determined and the transfer ratio under any other *Ca* can be estimated, providing a very useful way of predicting transfer ratio in practical applications. For transfer with strong inertia effects (large *Re*), satellite drops can be observed at the breakage of the liquid bridge. In addition, due to the slow spread of momentum, an asymmetric breakage shape can be observed at large stretching speeds. These two phenomena result in an observation not made in small *Re* transfer, namely that the transfer ratio does not converge to 0.5 with the increase of the stretching speed when $Re > 1$.

Bibliography

(8.1) H. W. Kang, H. J. Sung, T. M. Lee, D. S. Kim, C. J. Kim, *J. Micromech. Microeng.* **2009**, 19, 015025.

(8.2) S. Deladi, N. R. Tas, J. W. Berenschot, G. J. M. Krijnen, M. J. de Boer, J. H. de Boer, M. Peter, M. C. Elwenspoek, *Appl. Phys. Lett*. 85, 5361--5363.

(8.3) S. Kumar, *Annu. Rev. Fluid Mech.* **2015**, 47, 67--94.

(8.4) P. Lambert, A. Chau, A. Delchambre, S. Regnier, *Langmuir*, **2008**, 24 (7), 3157--3163.

(8.5) M. Pudas, J. Hagberg, S. Leppavuori, *J. Eur. Ceram. Soc.* **2004**, 24, 2943--2950.

(8.6) P. Kopola, T. Aernouts, S. Guillerez, H. Jin, M. Tuomikoski, A. Maaninen, A.; J. Hast, *Solar Energy Mat. Solar Cells* **2010,** 94, 1673--1680.

(8.7) P. M. Reis, S. Jung, J. M. Aristoff, R. Stocker, *Science*, **2010**, 330, 1231.

(8.8) S. Gorb, S. *Proc. Roy. Soc. Lond. B* **1998**, 265, 747--52.

(8.9) A. V. Chadov, E. D. Yakhnin, *Kolloidn. Zh.* **1979**, 41, 817.

(8.10) E. D. Yakhnin, A. V. Chadov, *Kolloidn. Zh.* **1983**, 45, 1183.

(8.11) A. A. Darhuber, S. M. Troian, *J. Appl. Phys.* **2001**, 90, 3602--3609.

(8.12) J. Qian, H. Gao, *Acta Biomaterialia* **2006**, 2, 51--58.

(8.13) B. Qian, K. S. Breuer, *J. Fluid Mech.* **2011**, 666, 554--572.

(8.14) H. Chen, T. Tang, A. Amirfazli, *Soft Matt.* **2014,** 10, 2503--2507.

(8.15) H. Chen, T. Tang, A. Amirfazli, Understanding Quasi-static Liquid Transfer between two Solid Surfaces. To be submitted.

(8.16) H. W. Kang, H. J. Sung, T. M. Lee, D. S. Kim, C. J. Kim, *J. Micromech. Microeng.* **2009**, 19, 015025

(8.17) W. X. Huang, S. H. Lee, H. J. Sung, T. M. Lee, D. S. Kim, *Int. J. Heat Fluid Flow* **2008**, 29, 1436--1446

(8.18) S. Dodds, M. Carvalho, S. Kumar S. *Phy. Fluids* **2009**, 21, 092103.

(8.19) Bai, S-E; Shim, J-S; Lee, C-H; Bai, C-H; Shin, K-Y Dynamic effect of surface contact angle on liquid transfer in a low speed printing process. *Jpn. J. Appl. Phy.* **2014**, 53, 05HC05.

(8.20) H. Chen, T. Tang, A. Amirfazli, Effects of Surface Contact Angle on Fast Liquid

Transfer, to be submitted

(8.21) S. Dodds, M. Carvalho, S. Kumar S. *Phy. Fluids* **2011**, 23, 092101

(8.22) S. S. Park, Y. Jeon, M. Cho, C. Bai, D. Lee, J. Shim, *Microsyst Technol* **2012**, 18, 2027--2034.

Chapter 9.

9. Conclusions and Remarks

9.1 Implication

In this thesis, the processes of the liquid transfer in all the three different regimes were studied. The results in this thesis can significantly help the design of both the liquid transfer system and wet adhesion system. For the liquid transfer system, the governing parameters for the transfer ratio in all the three regimes were clearly demonstrated. For most of liquid transfer implications, a total transfer (α=1) is always desired. As shown in this thesis, the function of $\alpha=G(Ca)$ converges from one plateau value (α_0, in the Quasi-static Regime) to 0.5 with the increase of *Ca*. This suggests that a total transfer can only happen when the transfer system fulfills the following two requirements. Frist, the transfer system has α_0 =1 (i.e. should locate in the Domain III in Figure 6.3, and the donor surface should have θ_r >90°). Second, the system needs to be in the Quasi-static Regime. Besides the transfer ratio, the speed of acceptor surface is also important. Usually, a quick stretching speed is desired to improve the working efficiency under the precondition of total transfer. As shown in Chapter 7, this maximal speed is actually the speed boundary between the Quasi-static and Transition Regimes, which can be obtained from the function of $\alpha=G(Ca)$.

For the wet adhesion system with two same surfaces, F_{max} is determined only by θ_a, only by θ_r or by both θ_a, and θ_r when the value of surfaces θ_r are small, large or medium, respectively. Such understanding can be used to guide the design of wet adhesion system. For example, for the system with small θ_r, in order to improve the strength of the system, one should only work on reducing θ_a of surfaces (since θ_a is the only governing parameter). For wet adhesion system consists of asymmetric bridges, F_{max} is found to be affected by the length of the contact line pinning period on the two surfaces at the start of stretching. Therefore, in order to achieve a large F_{max}, it is important to use two surfaces which can allow a long period of the contact line pinning.

9.2 Conclusions

In this dissertation, study of both slow liquid transfer (transfer in Quasi-static Regime) and fast transfer (transfer in the Transition, and Dynamic Regimes) from one solid surface to the other are performed. The effects of each of the physical parameters, i.e. μ, γ, H_{min}, U, θ_r θ_a, and CAH, on the transfer process are discussed. This thesis is the first study of the liquid transfer which systematically considers the effects of surface CAH.

In order to systematically study the effects of the CAH on the liquid transfer process, surfaces which have similar contact angle but different CAH are needed. Therefore, this thesis starts with investigating the methods to fabricate such type of surfaces. Given the facts that surface roughness and heterogeneity are the two main factors causing surface CAH, two different strategies are used. For a polymer surface made of one polymer, surface roughness, which can be manipulated by using different surface fabrication methods and specifications, was utilized to affect the surface CAH. For a surface made of more than one polymer (e.g. PMMA and PS mixture), the chemical heterogeneity is other way that can be used to affect surface CAH. By changing the ratio of the polymer mixture, pattern and size of the heterogeneous domains on the surface can be significantly different, which can further results a different value of CAH.

For slow liquid transfer, both experiments and analytical simulations of liquid transfer between two solid surfaces with CAH are performed. An analytical model which is able to capture the effects of CAH during the compression and stretching the liquid bridge is built. It is found that due to the exiting of CAH, the shape of the liquid bridge during the transfer process is dependent on the history of the movement; hence the profile of the liquid bridge in the compression and stretching stage can be difference at the same H. The different shapes of the liquid bridge can further cause the adhesion force between the liquid bridge and surfaces become very different between the compression and stretching stages. Systematic studies on the role of θ_a, θ_r and CAH in determining the transfer ratio, F_{max} and F_{pf} are performed. The transfer ratio was found to be governed by contact line pinning at the end of the transfer caused by CAH of surfaces. The occurrence of the contact line pining is controlled by the value of θ_r of the two surfaces; hence the transfer ratio is decided by θ_r of the two surfaces. A map based on θ_r of the two surfaces was generated to identify the three Domains for liquid transfer: (I) contact line pinning occurs only on donor surface, (II) contact line pinning occurs on both surfaces, and (III) contact line pinning occurs only on acceptor surface. With this map, an empirical equation is provided which is able to predict the transfer ratio by only knowing θ_r of the two surfaces.

The value of F_{max} is found to be strongly influenced by the contact line pinning in early stretching stage. For symmetric liquid bridge between two identical surfaces, F_{max} is only determined by θ_a, when the surface has a small magnitude of contact angle. F_{max} is only determined by θ_r, when the surface has a large magnitude of contact angle. And when the surface has a medium magnitude of contact angle, F_{max} is governed by both θ_a and θ_r. For asymmetric bridges, F_{max} is found to be affected by the length of the contact line pinning period on the two surfaces. For the pull-off force, it is found that when one of the surfaces has a θ_r larger than 90^o, F_{pf} decreases with the increase of θ_r on either surface. For the cases where θ_r of both surfaces are smaller than 90^o, significantly smaller F_{pf} is seen when contact line pinning occurs on both surfaces, as compared to F_{pf} when contact line pinning occurs only on one of the surfaces.

For the fast liquid transfer, a numerical model based on Volume of Fluid method was used to help understand the experimental observations. It is found that besides the three dominate forces (surface, viscous and inertia forces), the speed of the momentum spread from the acceptor surface to the donor surface which can be affected by H_{min} and *SCA,* is also important determining the transfer ratio. According to the value of Reynolds number (*Re*), the fast transfer is further divided into two different scenarios, liquid transfer with negligible inertia effects ($Re<<1$) and liquid transfer with significant inertia effects ($Re>1$).

For the liquid transfer with negligible inertia effects, the transfer process is mainly governed by H_{min}, *SCA* and *Ca* of the system. For the transfer ratio as function of *Ca*, it was found that the transfer ratio converges from one plateau value to 0.5 with the increasing of *Ca*. The first plateau value is actually the transfer ratio in the Quasi-static Regime which is governed by θ_r of both surfaces. The 0.5 transfer ratio is caused by the symmetric breakage shape of liquid bridge at large value of *Ca*. By examining the dependent of the transfer ratio and *Ca*, the Quasi-static, Transition and Dynamic Regimes can be identified. Based on the observations, an empirical function $\alpha=F(Ca)$ was proposed and validated with experimental results. With this equation, by only knowing transfer ratio at two different stretching speeds in the Transition Regime, the transfer ratio under any value of stretching speed can be estimated. When the inertia forces effects become important (system with large *Re*), satellite drops appear when the liquid bridge breaks. Different from the transfer cases with negligible inertia effects, asymmetric shape of liquid bridge at the breakage is observed. Due to both the satellite drop and asymmetric breakage shape, when inertia effects are important, the transfer ratio does not converge to 0.5 with the increase of the stretching speed.

9.3 Future Prospects

In closing, some recommendations for the future study on this topic are provided. First of all, all of the discussions in this thesis are based on the facts that the two surfaces are parallel, the liquid is Newtonian fluid, the stretching speed is normal to the surfaces. However, in practice, these assumptions may not always valid. For example, in most types of ink used in printing industry are non-Newtonian liquid. When one or more of these assumptions becomes violated, the liquid transfer process in those situations can become more complex than the one discussed in this dissertation.

The empirical function $\alpha=G(Ca)$ is based on the assumption of negligible inertia effects. When the inertia effects become important, it is shown in the Chapter 8 that, $\alpha=G(Ca)$ does not converge to 0.5; hence this empirical function cannot work for the cases with inertia effects. Due to the limitation of the experimental setup, we can only perform the transfer cases with *Re* smaller than 400. Therefore, it is of interest to see the behaviour of the liquid transfer with a very large $Re>400$ in the future and advance the empirical function $\alpha=G(Ca)$ to cover the range of liquid transfer with inertia effects.

Bibliography

(1.1) J. A. Lee, J. P. Rothstein, M. Pasquali, J. Non-Newtonian Fluid Mech. 199, 1-11(2013).

(1.2) W. X. Huang, S. H. Lee, H. J. Sung, T. M. Lee, D. S. Kim, Int. J. Heat Fluid Flow 29, 1436-1446 (2008).

(1.3) A. A. Darhuber, S. M. Troian, J. Appl. Phys. 90, 3602-3609 (2001).

(1.4) H. W. Kang, H. J. Sung, T.M. Lee, D.S. Kim, C.J. Kim, J. Micromech. Microeng. 19, 015025 (2009).

(1.5) S. Deladi, N. R. Tas, J. W. Berenschot, G. J. M. Krijnen, M. J. de Boer, J. H. de Boer, M. Peter, M. C. Elwenspoek, Appl. Phys. Lett. 85, 5361–5363(2004).

(1.6) S. Kumar, Annu. Rev. Fluid Mech. 47, 67-94 (2015).

(1.7) P. Lambert, A. Chau, A. Delchambre, S. Regnier, Langmuir, 24 (7), 3157-3163 (2008).

(1.8) M. Pudas, J. Hagberg, S. Leppavuori, J. Eur. Ceram. Soc. 24, 2943-2950 (2004).

(1.9) P. Kopola, T. Aernouts, S. Guillerez, H. Jin, M. Tuomikoski, A. Maaninen, J. Hast, Solar Energy Mat. Solar Cells 94, 1673-1680 (2010).

(1.10) M. Prakash, D. Quere, J. W. M. Bush, Science 320, 931-934 (2008).

(1.11) P. M. Reis, S. Jung, J. M. Aristoff, R. Stocker, Science, 330, 1231 (2010).

(1.12) S. Gorb, Proc. Roy. Soc. Lond. B 265, 747–52 (1998).

(1.13) B. N. J. Persson, J. Phys.: Condens. Matter 19, 376110 (2007).

(1.14) T. Eisner, D. J. Aneshansley, Proc. Natl. Acad. Sci. 97, 6568–6573 (2000).

(1.15) A. F. G. Dixon, P. C. Croghan, R. P. Gowing, J. Expl. Biol. 152, 243–253 (1990).

(1.16) W. Federle, M. Riehle, A. S. G. Curtis, R. J. Full, Integr. Comp. Biol. 42, 1100–1106 (2002).

(1.17) A. V. Chadov, E. D. Yakhnin, Kolloidn. Zh. 41, 817 (1979).

(1.18) E. D. Yakhnin, A. V. Chadov, Kolloidn. Zh. 45, 1183 (1983).

(1.19) M. A. Fortes, J. Colloid Interface Sci. 88, 338-352 (1982).

(1.20) A. A. Darhuber, S. M. Troian, J. Appl. Phys. 90, 3602-3609 (2001).

(1.21) S. J. Hong, T. H. Chou, S. H. Chan, Y. J. Sheng, H. K. Tsao, Langmuir 28, 5606−5613 (2012).

(1.22) J. Qian, H. Gao, Acta Biomaterialia 2, 51–58 (2006).

(1.23) E. Cheung, M. Sitti, J. Adhesion Sci. Tech. 22, 569-589 (2008).

(1.24) B. N. J. Persson, J. Phys.: Condens. Matter. 19, 376110 (2007).

(1.25) B. Qian, K. S. Breuer, J. Fluid Mech. 666, 554-572 (2011).

(1.26) G. Lian, C. Thornton, M. J. Adams J. Colloid Interface Sci.161, 138-147 (1993).

(1.27) S. Gorb, Proc. Roy. Soc. Lond. B 265, 747-52 (1998).

(1.28) B. Qian, M. Loureiro, D. Gagnon, A. Tripathi, K. S. Breuer, Phys. Rev. Lett. 102 (16), 164502 (2009).

(1.29) T. Young, Philos. Trans. R. Soc. London 95, 65−87 (1805).

(1.30) Adamson AW. Physical chemistry of surfaces. New York, NY: John Wiley & Sons Inc; 1976

(1.31) C. N. C. Lam, R. Wu, D. Li, M. L. Hair, A. W. Neumann, Adv. Colloid Interface Sci., 96, 169-191(2002).

(1.32) H. Tavana, in Applied Surface Thermodynamics, 2nd ed.; A.W. Neumann, R. David, Y. Zuo, Ed.; Surfactant Sci. Series; CRC: Boca Raton, USA, 2010; vol. 151, 315-316.

(1.33) E. J. D. Souza, L. Gao , T. J. McCarthy, E. Arzt, A. J. Crosby, Langmuir, 24 (4), 1391-1396 (2008).

(1.34) E. J. De Souza, M. Brinkmann, C. Mohrdieck, E. Arzt, Langmuir 24 (16), 8813-8820 (2008).

(1.35) B. Samuel, H. Zhao, K-Y Law, J. Phys. Chem. C 115, 14852-14861(2011).

(1.36) X. Zhang, R. S. Padgett, A. Basaran, J. Fluid Mech. 329, 207-245(1996).

(1.37) O. E. Yildirim, O. A. Basaran, Chem. Eng. Sci. 56, 211–233 (2001).

(1.38) J. Meseguer, A. Sanz, J. Fluid Mech. 153, 83-101 (1985).

(1.39) P. Doshi, R. Suryo, O. E. Yildirim, G. H. McKinley, O. A. Basaran, J. Non-Newtonian Fluid Mech. 113, 1–27 (2003).

(1.40) H. S. Huynh, J. P. Guan, T. Vuong, T. W. Ng, Langmuir 29 (37), 11615–11622 (2013).

(1.41) Y. C. Liao, E. I. Franses, O. A. Basaran, Phys. Fluids 18, 022101 (2006).

(1.42) W.X. Huang, S.H. Lee, H.J. Sung, T. M. Lee, D. S. Kim, Int. J. Heat Fluid Flow 29, 1436–1446 (2008)

(1.43) S. Dodds, M. Carvalho, S. Kumar, Phy. Fluids 21, 092103 (2009).

(1.44) S. E. Bai, J. S. Shim, C. H. Lee, C. H. Bai, K. Y. Shin, Jpn. J. Appl. Phy. 53, 05HC05 (2014).

(1.45) S. Dodds, M. Carvalho, S. Kumar, Phy. Fluids 23, 092101 (2011).

(1.46) Park, S-S; Jeon, Y.; Cho, M.; Bai, C.; Lee, D.; Shim, J.; The FEM based liquid transfer model in gravure offset printing using phase field method. Microsyst Technol 2012, 18, 2027–2034.

(2.1) C.N.C. Lam, R. Wu, D. Li, M.L. Hair, A.W. Neumann, Adv. Colloid Interface Sci. 2002, 96, 169-191.

(2.2) S. Semenov, V.M. Starov, R.G. Rubio, H. Agogo, M.G. Velarde, Colloids Surface. A 2011, 391, 135-144.

(2.3) M. Sakai, J. Song, N. Yoshida, S. Suzuki, Y. Kameshima, A. Nakajima, M. Sakai, Surface Sci. 2006, 600, 204-208.

(2.4) M.A. Nilsson and J.P. Rothstein, J. Colloid Interface Sci. 2011, 363, 646-654.

(2.5) J.D. Le Roux and D.R. Paul, J. Membrane Sci. 1992, 74, 233-252.

(2.6) P.C. Sukanek, Dependence of film thickness on speed in spin coating. J. Electrochem Soc. 1991, 138, 1712-1719.

(2.7) D.W. Schubert and T. Dunkel, Mat. Res. Innovat. 2003, 7, 314-321.

(2.8) D. Barona, A. Amirfazli, Lab Chip, 2011, 11, 936-940.

(2.9) G. Perfetti, T. Alphazan, P. van Hee, W.J. Wildeboer, G.M.H. Meesters, Eur. J. Pharm. Sci. 2011, 43, 262-272.

(2.10) H. Tavana, Contact Angle Measurements: General Procedures and Approaches, in: A.W. Neumann, D. Y. Kwok, R. David, Y. Zuo (Eds.), Applied Surface Thermodynamics, 2nd, CRC, Boca Raton, USA, 2010, PP. 315-316.

(2.11) G. Zografi, B. A. Johnson, Int. J. Pharm. 1984, 22, 159-176.

(2.12) R. H. Dettre, R. E. Johnson Jr, Adv. Chem. Ser. 1964, 43, 112-144.

(2.13) W. Li, A. Amirfazli, Adv. Colloid Interface Sci. 2007, 132, 51-68.

(2.14) S. Walheim, M. Böltau, J. Mlynek, G. Krausch, U. Steiner, Marcromolecules 1997, 30, 4995-5003.

(2.15) S. Y. Heriot, R. A. L. Jone, Nat. Mater. 2005, 4, 782-786.

(2.16) R. P. Kusy, M. J. Katz, J. Mater. Sci. 1976, 11, 1475-1486.

(2.17) A.D. Nikolov, D.T. Wasan, A. Chengara, K. Koczo, G.A. Policello, I. Kolossvary, Adv. Colloid Interface Sci. 2002, 96, 325-338.

(2.18) B. S. Dunn, E. J. A. Pope, H. K. Schmidt, M. Yamane, Proc. SPIE 2000, 3943, 280-284.

(3.1) B. Qian, K. S. Breuer, J. Fluid Mech. 2011, 666, 554--572.

(3.2) A. A. Darhuber, S. M. Troian, J. Appl. Phys. 2001, 90, 3602--3609.

(3.3) H. W. Kang, H. J. Sung, T. M. Lee, D. S. Kim, C. J. Kim, J. Micromech. Microeng. 2009, 19, 015025.

(3.4) D. Bonn, J. Eggers, J. Indekeu, J. Meunier, E. Rolley, Rev. Mod. Phys. 2009, 81, 739--805.

(3.5) M. Prakash, D. Quere, J. W. M. Bush, Science 2008, 320, 931--934.

(3.6) S. Gorb, Proc. Roy. Soc. Lond. B 1998, 265, 747--52.

(3.7) T. Eisner, D. J. Aneshansley, Proc. Natl. Acad. Sci. 2000, 97, 6568--6573.

(3.8) A. F. G. Dixon, P. C. Croghan, R. P. Gowing, J. Expl. Biol. 1990, 152, 243--253.

(3.9) W. Federle, M. Riehle, A.S.G. Curtis, R.J. Full, Integr. Comp. Biol. 2002, 42, 1100--1106.

(3.10) A. V. Chadov, E. D. Yakhnin, Kolloidn. Zh. 1979, 41, 817.

(3.11) E. D. Yakhnin, A. V. Chadov, Kolloidn. Zh. 1983, 45, 1183.

(3.12) M. A. Fortes, J. Colloid Interface Sci. 1982, 88, 338--352.

(3.13) J. Qian, H. Gao, Acta Biomaterialia 2006, 2, 51--58.

(3.14) E. Cheung, M. Sitti, J. Adhesion Sci. Tech. 2008, 22, 569--589.

(3.15) S. J. Hong, T. H. Chou, S. H. Chan, Y. J. Sheng, H. K. Tsao, Langmuir 2012, 28, 5606--5613.

(3.16) C. N. C. Lam, R. Wu, D. Li, M. L. Hair, A. W. Neumann, Adv. Colloid Interface Sci. 2002, 96, 169--191.

(3.17) H. Tavana in Applied Surface Thermodynamics, 2nd ed.; A.W. Neumann, R. David, Y. Zuo, Ed.; Surfactant Sci. Series; CRC: Boca Raton, USA, 2010; 151, pp 315--316.

(3.18) E. Pierce, F. J. Carmona, A. Amirfazli, Colloids Surfaces A 2008, 323, 73--82.

(3.19) E. L. Decker, B. Frank, Y. Suo, S. Garoff, S. Colloids and Surfaces A 1999, 156, 177--189.

(3.20) T. H. Chou, S. J. Hong, S. H. Chan, Y. J. Sheng, H. K. Tsao, Langmuir 2012, 28, 5158--5166.

(3.21) S. M. I. Saad, Z. Policova, A. W. Neumann, Colloids Surfaces A 2011, 384, 442--452.

(3.22) V. S. Ajaev, G. M. Homsy, Annu. Rev. Fluid Mech. 2006, 38, 277--307.

(3.23) A. W. Adamson, Physical chemistry of surfaces; Wiley: New York, 1997; pp 6--8.

(3.24) H. Chen, T. Tang, A. Amirfazli, Colloids Surfaces A 2012, 408, 17--21.

(3.25) B. N. J. Persson, J. Phys.: Condens. Matter. 2007, 19, 376110.

(4.1) A. F. G. Dixon, P. C. Croghan, R. P. Gowing, J. Expl. Biol. 1990, 152, 243--253.

(4.2) S. Gorb, Proc. Roy. Soc. Lond. B 1998, 265, 747--752.

(4.3) T. Eisner, D. J. Aneshansley, Proc. Natl. Acad. Sci. 2000, 97, 6568--6573.

(4.4) W. Federle, M. Riehle, A. S. G. Curtis, Integr. Comp. Biol. 2002, 42, 1100--1106.

(4.5) D. Bonn, J. Eggers, J. Indekeu, J. Meunier, E. Rolley, Rev. Mod. Phys. 2009, 81, 739--805.

(4.6) B. Qian, M. Loureiro, D. Gagnon, A. Tripathi, and K. S. Breuer, Phy. Rev. Lett. 2009, 102 (16), 164502.

(4.7) H. W. Kang, H. J. Sung, T. M. Lee, D. S. Kim, C. J. Kim, J. Micromech. Microeng. 2009, 19, 015025.

(4.8) W. X. Huang, S.H. Lee, H. J. Sung, T.M. Lee, D. S. Kim, Int. J. Heat Fluid Flow, 2008, 29, 1436--1446.

(4.9) M. R. Pedro, J. Sunghwan, M. A. Jeffrey, S. Roman, Science, 2010, 330, 1231--1234.

(4.10) A. V. Chadov, E. D Yakhnin, Kolloidn. Zh. 1979, 41, 817.

(4.11) E. D. Yakhnin, A. V. Chadov, Kolloidn. Zh. 1983, 45, 1183.

(4.12) A. A. Darhuber, S. M. Troian, J. Appl. Phys. 2001, 90, 3602--3609.

(4.13) C. N. C. Lam, R. Wu, D. Li M. L. Hair, A. W. Neumann, Adv. Colloid Interface Sci. 2002, 96, 169--191.

(4.14) S. Benedict, Z. Hong, K. Y. Law, J. Phys. Chem. C 2011, 115, 14852--14861.

(4.15) H. Chen, T. Tang and A. Amirfazli, Colloid Surface A, 2012, 408, 17--21.

(4.16) J. Qian, H. Gao, Acta Biomaterialia 2006, 2, 51--58.

(4.17) H. Chen, A. Amirfazli and T. Tang, Langmuir, 2013, 29, 3310--3319.

(4.18) B. Qian, K. S. Breuer, J. Fluid Mech. 2011, 666, 554--572.

(5.1) P. G. de Gennes, Rev. Mod. Phys. 1985, 57, 827.

(5.2) T. Young, Philos. Trans. R. Soc. London 1805, 95, 65.

(5.3) C.N.C. Lam, R. Wu, D. Li, M. L. Hair, A.W. Neumann, Adv. Colloid Interface Sci. 2002, 96, 169--191

(5.4) R. H. Dettre, R. E. Johnson Jr, Adv. Chem. Ser.1964, 43, 112.

(5.5) P. Roura, J. Fort, Phy. Rev. E 2001, 64, 011601.

(5.6) E. Pierce, F.J. Carmona, A. Amirfazli, Colloids Surfaces A 2008, 323, 73--82.

(5.7) W. Konrad, M. Ebner, C. Traiser, A. Roth-Nebelsick, Pure Appl. Geophys. 2012, 169, 835.

(5.8) D. Qurere, Annual Rev. Mater. Res. 2008, 38, 71.

(5.9) J. Wu, J. Xia, W. Lei, B. P. Wang, Scientific Reports 2013, 3, 3268.

(5.10) L. W. Schwartz, Langmuir 1998, 14, 3440.

(5.11) A. J. B. Milne, A. Amirfazli, Langmuir 2009, 25(24), 14155--14164.

(5.12) A. V. Chadov, E. D. Yakhnin, Kolloidn. Zh. 1979, 41, 817.

(5.13) S. Dodds, M. S. Carvalho, S. Kumar, Phy. Fluids 2009, 21, 092103.

(5.14) H. W. Kang, H. J. Sung, T-M Lee, D-S Kim, C-J Kim, J. Micromech. Microeng. 2009, 19, 015025.

(5.15) E. Cheung, M. Sitti, J. Adhesion Sci. Tech. 2008, 22, 569--589.

(5.16) M. A. Fortes, J. Colloid Interface Sci. 1982, 88, 338--352.

(5.17) H. Chen, A. Amirfazli, T. Tang, Langmuir 2013, 29, 3310 --3319.

(5.18) E. J. De Souza, L. Gao, T. J. McCarthy, E. Arzt, A. J. Crosby, Langmuir 2008, 24 (4), 1391--1396.

(5.19) S-J Hong, T-H Chou, S. H. Chan, Y-J Sheng, H-K Tsao, Langmuir 2012, 28, 5606--5613.

(5.20) B. Samuel, H. Zhao, K-Y Law, J. Phys. Chem. C 2011, 115, 14852--14861.

(5.21) H. Chen, T. Tang, A. Amirfazli, Soft Matt. 2014, 10, 2503.

(5.22) H. Chen, T. Tang, A. Amirfazli, Colloids Surface A 2012, 408, 17--21.

(5.23) J. Qian, H. Gao, Acta Biomaterialia 2006, 2, 51--58.

(5.24) B. N. J. Persson, J. Phys.: Condens. Matt. 2007, 19, 376110.

(5.25) L. V. Slobozhanin, J. I. D. Alexander, Phys. Fluids 1998, 10, 2473.

(5.26) J. M. Perales, J. Meseguer, J. Crystal Growth 1991, 110, 855.

(6.1) A. A. Darhuber, S. M. Troian, J. Appl. Phys. 2001, 90, 3602--3609.

(6.2) H. W. Kang, H. J. Sung, T-M Lee, D-S Kim, C-J Kim, J. Micromech. Microeng. 2009, 19, 015025.

(6.3) J. A. Lee, J. P. Rothstein, M. Pasquali, J. Non-Newtonian Fluid Mech. 2013 199, 1--11.

(6.4) W-X Huanga, S-H Leea, H. J. Sunga, T-M Leeb, D-S Kimb, Inter. J. Heat Fluid Flow 2008, 29, 1436--1446.

(6.5) M. Pudas, J. Hagberg, S. Leppavuori, J. Eur. Ceram. Soc. 2004, 24, 2943--2950.

(6.6) P. Kopola, T. Aernouts, S. Guillerez, H. Jin, M. Tuomikoski, A. Maaninen, J. Hast, Solar Energy Mat. Solar Cells 2010, 94, 1673--1680.

(6.7) D. Bonn, J. Eggers, J. Indekeu, J. Meunier, E. Rolley, 2009, 81, 739--805.

(6.8) B. Qian, K. S. Breuer, J. Fluid Mech. 2011, 666, 554--572.

(6.9) J. Qian, H. Gao, Acta Biomaterialia 2006, 2, 51--58.

(6.10) A. F. G. Dixon, P. C. Croghan, R. P. Gowing, J. Expl. Biol. 1990, 152, 243--253.

(6.11) S. Gorb, Proc. Roy. Soc. Lond. B 1998, 265, 747--52.

(6.12) T. Eisner, D. J. Aneshansley, Proc. Natl. Acad. Sci. 2000, 97, 6568--6573.

(6.13) W. Federle, M. Riehle, A. S. G. Curtis, R. J. Full, Integr. Comp. Biol. 2002, 42, 1100--1106.

(6.14) A. V. Chadov, E. D. Yakhnin, Kolloidn. Zh. 1979, 41, 817.

(6.15) E. D. Yakhnin, A. V. Chadov, Kolloidn. Zh. 1983, 45, 1183.

(6.16) E. Cheung, M. Sitti, J. Adhesion Sci. Tech. 2008, 22, 569-589.

(6.17) B. Qian, M. Loureiro, D. Gagnon, A. Tripathi, and K. S. Breuer, Phys. Rev. Lett. 2009, 102 (16), 164502.

(6.18) M. A. Fortes, J. Colloid Interface Sci. 1982, 88, 338-352.

(6.19) G. Lian, C. Thornton, M. J. Adams J. Colloid Interface Sci. 1993,161, 138--147.

(6.20) S. Dodds, M. Carvalho, S. Kumar Phy. Fluids, 2009, 21, 092103.

(6.21) C. N. C. Lam, R. Wu, D. Li, M. L. Hair, A. W. Neumann, Adv. Colloid Interface Sci. 2002, 96, 169--191.

(6.22) H. Tavana, in Applied Surface Thermodynamics, 2nd ed.; A.W. Neumann, R. David, Y. Zuo, Ed.; Surfactant Sci. Series; CRC: Boca Raton, USA, 2010; 151, 315--316.

(6.23) E. Pierce, F. J. Carmona, A. Amirfazli, Colloids Surfaces A 2008, 323, 73--82.

(6.24) H. Chen, A. Amirfazli, T. Tang, Langmuir 2013, 29, 3310--3319.

(6.25) E. J. De Souza, L. Gao , T. J. McCarthy, E. Arzt, A. J. Crosby, Langmuir 2008, 24 (4), 1391--1396.

(6.26) E. J. De Souza, M. Brinkmann, C. Mohrdieck, E. Arzt, Langmuir 2008, 24 (16), 8813--8820.

(6.27) S-J Hong, T-H Chou, S. H. Chan, Y-J Sheng, H-K Tsao, Langmuir 2012, 28, 5606--5613.

(6.28) B. Samuel, H. Zhao, K-Y Law, J. Phys. Chem. C 2011, 115, 14852--14861.

(6.29) H. Chen, T. Tang, A. Amirfazli, Soft Matt. 2014, 10, 2503--2507.

(6.30) H. Chen, T. Tang, A. Amirfazli, Colloids Surface A 2012, 408, 17--21.

(7.1) M. Pudas, J. Hagberg, S. Leppavuori, J. Eur. Ceram. Soc. 2004, 24, 2943--2950.

(7.2) C. M. Hong, S. Wagner, IEEE Electron Device Lett. 2000, 21, 384--386.

(7.3) P. Kopola, T. Aernouts, S. Guillerez, H. Jin, M. Tuomikoski, A. Maaninen, A.; J. Hast, Solar Energy Mat. Solar Cells 2010, 94, 1673--1680.

(7.4) D. Bonn, J. Eggers, J. Indekeu, J. Meunier, E. Rolley, Rev. Mod. Phys. 2009, 81, 739--805.

(7.5) B. Qian, M. Loureiro, D. Gagnon, A. Tripathi, K. S. Breuer, Phy. Rev. Lett. 2009, 102 (16), 164502

(7.6) I. Barbulovic-Nad, M. Lucente, Y. Sun, M. Zhang, A. R. Wheeler, M. Bussmann, Crit. Rev. Biotechnol. 2006, 26, 237--259.

(7.7) A. V. Chadov, E. D. Yakhnin, Kolloidn. Zh. 1979, 41, 817.

(7.8) E. D. Yakhnin, A. V. Chadov, Kolloidn. Zh. 1983, 45, 1183.

(7.9) J. Qian, H. Gao, Acta Biomaterialia 2006, 2, 51--58.

(7.10) H. Chen, A. Amirfazli, T. Tang, Langmuir 2013, 29, 3310--3319.

(7.11) E. J. De Souza, L. Gao , T. J. McCarthy, E. Arzt, and A. J. Crosby, Langmuir 2008, 24 (4), 1391--1396.

(7.12) S. J. Hong, T. H. Chou, S. H. Chan, Y. J. Sheng, H. K. Tsao, Langmuir 2012, 28, 5606--5613.

(7.13) B. Samuel, H. Zhao, K. Y. Law, J. Phys. Chem. C 2011, 115, 14852--14861.

(7.14) H. Chen, T. Tang, A. Amirfazli, Soft Matt. 2014, 10, 2503--2507.

(7.15) H. Chen, T. Tang, A. Amirfazli, To be submitted.

(7.16) A. A. Darhuber, S. M. Troian, J. Appl. Phys. 2001, 90, 3602--3609.

(7.17) P. Doshi, R. Suryo, O. E. Yildirim, G. H. McKinley, O. A. Basaran, J. Non-Newtonian Fluid Mech. 2003, 113, 1--27.

(7.18) J. Meseguer, A. Sanz, J. Fluid Mech. 1985, 153, 83--101.

(7.19) X. Zhang, R. S. Padgett, A. Basaran, J. Fluid Mech. 1996, 329, 207--245.

(7.20) O. E. Yildirim,O. A. Basaran, Chem. Eng. Sci. 2001, 56, 211--233.

(7.21) B. Qian, K. S. Breuer, J. Fluid Mech. 2011, 666, 554--572.

(7.22) S. E. Bai, J. S. Shim, C. H. Lee, C. H. Bai, K. Y. Shin, Jpn. J. Appl. Phy. 2014, 53, 05HC05.

(7.23) D. H. Ahmed, H. J. Sung, D. S. Kim, Inter. J. Heat and Fluid Flow 2011, 32, 298--307

(7.24) H. W. Kang, H. J. Sung, T. M. Lee, D. S. Kim, C. J. Kim, J. Micromech. Microeng. 2009, 19, 015025

(7.25) S. Dodds, M. Carvalho, S. Kumar S. Phy. Fluids 2009, 21, 092103.

(7.26) S. Dodds, M. Carvalho, S. Kumar S. Phy. Fluids 2011, 23, 092101

(7.27) H. S. Huynh, J. P. Guan, T. Vuong, T. W. Ng, Langmuir 2013, 29 (37), 11615--11622.

(7.28) C. W. Hirt, B. D. Nichols, J. Computational Phys.1981, 39,201-225.

(7.29) P. A.Thompson, M. O. Robbins, Phy. Rev. Lett. 1989, 63 (7), 766--769.

(7.30) A. A. Saha, S. K. Mitra, J. Colloid and Interface Sci. 2009, 339, 461--480.

(7.31) S. F. Kistler, Hydrodynamics of wetting. In: Berg, J.C.: Wettability, M. Dekker, USA, New York, 1993.

(7.32) I. V. Roisman, R. Rioboo, C. Tropea, Proc. R. Soc. Lond. A 2002, 458, 1411--1430.

(7.33) M. Muradoglu, S. Tasoglu, Computers Fluids 2010, 39, 615--625.

(7.34) L. H. Tanner, J. Phys. D: Appl. Phys.1979, 12, 1473--1484.

(8.1) H. W. Kang, H. J. Sung, T. M. Lee, D. S. Kim, C. J. Kim, J. Micromech. Microeng. 2009, 19, 015025.

(8.2) S. Deladi, N. R. Tas, J. W. Berenschot, G. J. M. Krijnen, M. J. de Boer, J. H. de Boer, M. Peter, M. C. Elwenspoek, Appl. Phys. Lett. 85, 5361--5363.

(8.3) S. Kumar, Annu. Rev. Fluid Mech. 2015, 47, 67--94.

(8.4) P. Lambert, A. Chau, A. Delchambre, S. Regnier, Langmuir, 2008, 24 (7), 3157--3163.

(8.5) M. Pudas, J. Hagberg, S. Leppavuori, J. Eur. Ceram. Soc. 2004, 24, 2943--2950.

(8.6) P. Kopola, T. Aernouts, S. Guillerez, H. Jin, M. Tuomikoski, A. Maaninen, A.; J. Hast, Solar Energy Mat. Solar Cells 2010, 94, 1673--1680.

(8.7) P. M. Reis, S. Jung, J. M. Aristoff, R. Stocker, Science, 2010, 330, 1231.

(8.8) S. Gorb, S. Proc. Roy. Soc. Lond. B 1998, 265, 747--52.

(8.9) A. V. Chadov, E. D. Yakhnin, Kolloidn. Zh. 1979, 41, 817.

(8.10) E. D. Yakhnin, A. V. Chadov, Kolloidn. Zh. 1983, 45, 1183.

(8.11) A. A. Darhuber, S. M. Troian, J. Appl. Phys. 2001, 90, 3602--3609.

(8.12) J. Qian, H. Gao, Acta Biomaterialia 2006, 2, 51--58.

(8.13) B. Qian, K. S. Breuer, J. Fluid Mech. 2011, 666, 554--572.

(8.14) H. Chen, T. Tang, A. Amirfazli, Soft Matt. 2014, 10, 2503--2507.

(8.15) H. Chen, T. Tang, A. Amirfazli, Understanding Quasi-static Liquid Transfer between two Solid Surfaces. To be submitted.

(8.16) H. W. Kang, H. J. Sung, T. M. Lee, D. S. Kim, C. J. Kim, J. Micromech. Microeng. 2009, 19, 015025

(8.17) W. X. Huang, S. H. Lee, H. J. Sung, T. M. Lee, D. S. Kim, Int. J. Heat Fluid Flow 2008, 29, 1436--1446

(8.18) S. Dodds, M. Carvalho, S. Kumar S. Phy. Fluids 2009, 21, 092103.

(8.19) Bai, S-E; Shim, J-S; Lee, C-H; Bai, C-H; Shin, K-Y Dynamic effect of surface contact angle on liquid transfer in a low speed printing process. Jpn. J. Appl. Phy. 2014, 53, 05HC05.

(8.20) H. Chen, T. Tang, A. Amirfazli, Effects of Surface Contact Angle on Fast Liquid Transfer, to be submitted

(8.21) S. Dodds, M. Carvalho, S. Kumar S. Phy. Fluids 2011, 23, 092101

(8.22) S. S. Park, Y. Jeon, M. Cho, C. Bai, D. Lee, J. Shim, Microsyst Technol 2012, 18, 2027--2034.

Appendix A

A. Supporting Information for Chapter 2

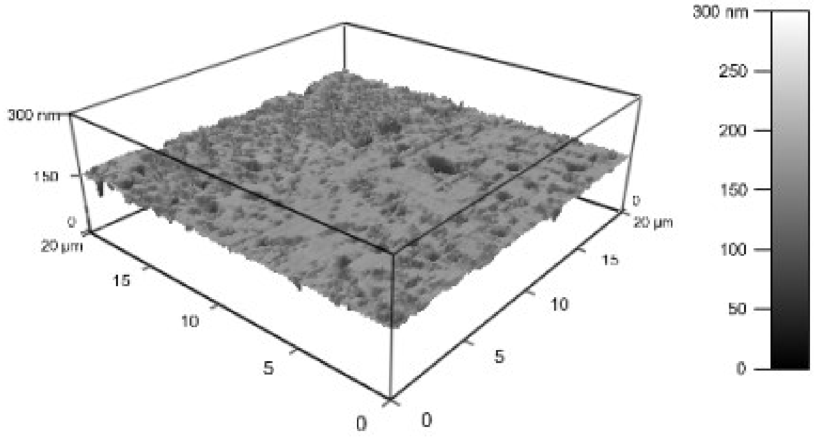

Figure A.1: AFM image of heat pressed polystyrene.

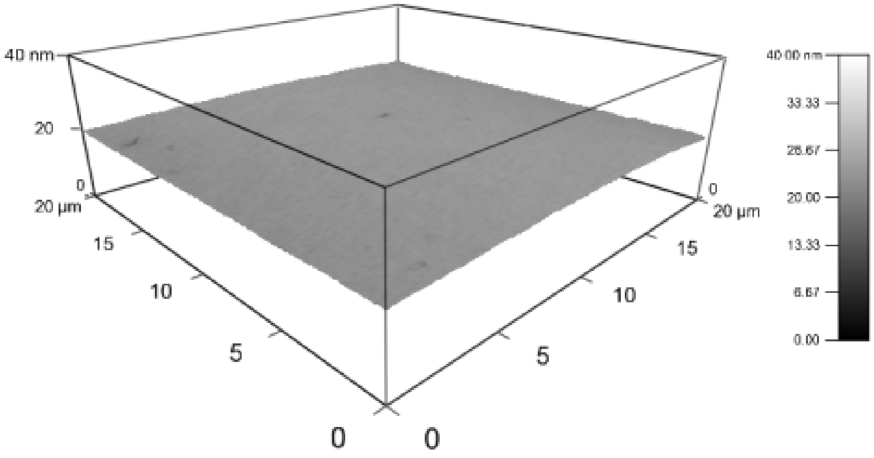

Figure A.2: AFM image of spin coated polystyrene.

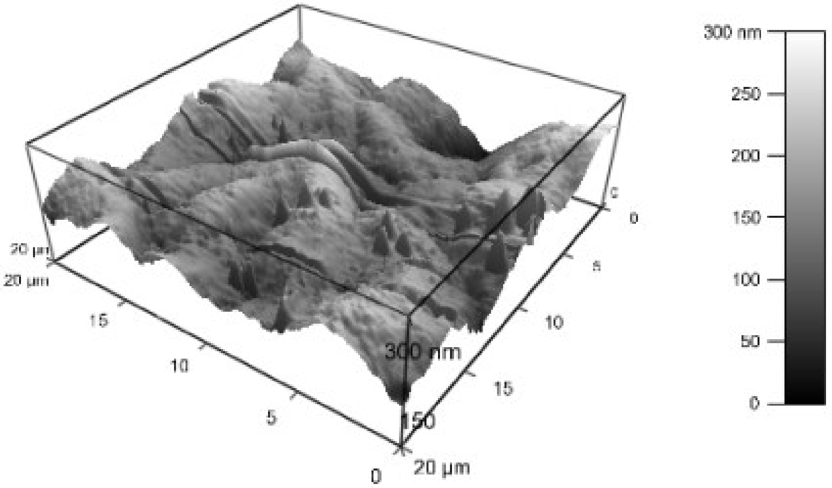

Figure A.3: AFM image of spray coated Teflon AF.

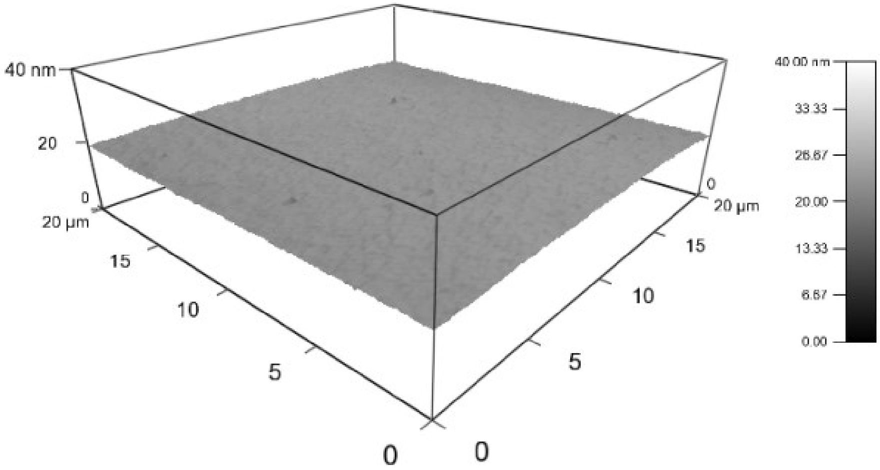

Figure A.4: AFM image of spin coated Teflon AF.

Appendix B

B. Supporting Information for Chapter 3

B.1 Effect of liquid volume

To see the effect of liquid volume, we introduce the following normalization:

$$\widehat{X} = \frac{X}{\sqrt[3]{V}}, \widehat{Z} = \frac{Z}{\sqrt[3]{V}}, \widehat{S} = \frac{S}{\sqrt[3]{V}}, \widehat{R} = \frac{R}{\sqrt[3]{V}}, \widehat{H} = \frac{H}{\sqrt[3]{V}}, \triangle \widehat{P} = \frac{\sqrt[3]{V}\triangle P}{\gamma}. \quad \text{(B-1)}$$

With this normalization, the governing equations become

$$\frac{d\widehat{X}}{d\widehat{S}} = \cos\theta \quad \text{(B-2)}$$

$$\frac{d\widehat{Z}}{d\widehat{S}} = \sin\theta \quad \text{(B-3)}$$

$$\frac{d\theta}{d\widehat{S}} = \triangle \widehat{P} - \frac{\sin\theta}{\widehat{X}} \quad \text{(B-4)}$$

The common boundary conditions for the four cases are, after the normalization

$$\widehat{Z}(0) = 0 \quad \text{(B-5)}$$

$$\widehat{Z}(\widehat{S}_{BA}) = \widehat{H} \quad \text{(B-6)}$$

$$\int_0^{\widehat{H}} \pi\widehat{X}^2 d\widehat{Z} = 1 \quad \text{(B-7)}$$

One additional normalized boundary condition on the lower surface is given by

$$\text{either} \quad \widehat{R}(0) = \widehat{R}_2 \quad \text{or} \quad \theta(0) = \theta_2 \quad \text{(B-8)}$$

One additional normalized boundary condition on the upper surface is given by

$$\text{either} \quad \widehat{R}(\widehat{S}_{BA}) = \widehat{R}1 \quad \text{or} \quad \theta(\widehat{S}_{BA}) = \theta 1 \quad \text{(B-9)}$$

Since $\triangle \hat{P}$ and $\hat{S}_{BA}$ are part of the solution, it is clear from above that the normalized liquid profile depends on $\hat{H}$ as well as $\hat{R}1$, $\hat{R}2$, $\theta 1$, and $\theta 2$ at the beginning of the process. If these dimensionless parameters are the same, then all the lengths that describe the profile of the liquid bridge will simply scale with $\sqrt[3]{V}$.This is confirmed in Figure B.1, which shows the values of $\hat{R}$ and contact angle versus $\hat{H}$ for three different liquid volumes, and all three curves coincide in each figure.

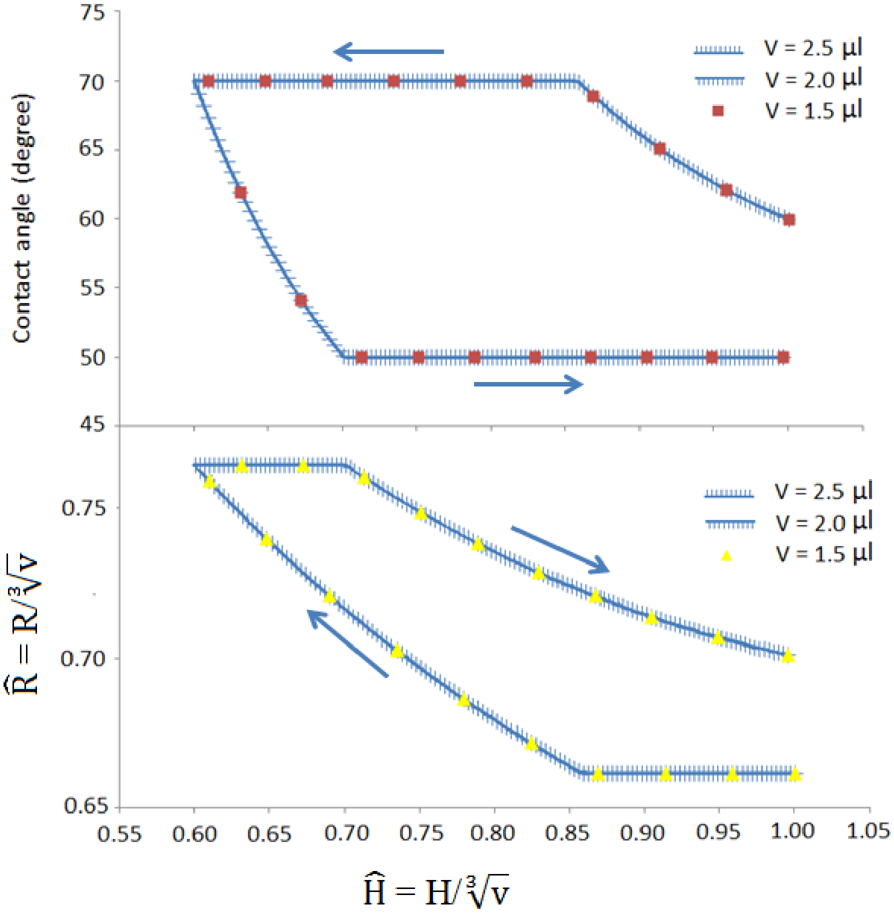

Figure B.1: $\hat{R}$ - $\hat{H}$ and contact angle - $\hat{H}$ curves for a liquid bridge between two identical surfaces (θ_r=50°, θ_a=70°, *CAH*=20°) with water volume of 2.5µl, 2.0µl and 1.5µl.

The total vertical adhesion force is given by

$$F = \pi\gamma\sqrt[3]{V}[2\hat{R}_1\sin(\theta_1) - \triangle \hat{P}\, \hat{R}_1^{\,2}] \qquad \text{(B-10)}$$

which also scales with $\sqrt[3]{V}$. During the loading process, the work done by the vertical adhesion force F is hence

$$W=\pi\gamma\sqrt[3]{V^2}\int[2\hat{R}_1\sin(\theta_1)\ -\triangle\hat{P}\,\hat{R}_1^2]d\hat{H} \qquad \text{(B-11)}$$

which scales with $\sqrt[3]{V^2}$.

B.2 Additional validation for the model

As an important part of model verification, we regenerated two figures from the work of Qian and Breuer [1]. In their study, the liquid bridges were formed between a fibril with a given radius (pinned contact radius) and a substrate (fixed contact angle). In order to regenerate their results, in our model, the contact angle of the surface with pinned contact radius is set as $\theta_a = 180^{\circ}$ and $\theta_r = 0^{\circ}$, and *CAH* of the other surface was set as 0.01°. Figure B.2 shows the normalized free moving contact radius ($\check{R}$) on the substrate as a function of the normalized bridge height (Λ) obtained from our model. $\bar{R}$ here is the contact radius of the fibril, r(0) is the contact radius on the substrate, and H is the separation between the two surfaces. The solid lines are shown for different θ_{avg} on the substrate. The dotted lines show the theoretically possible and stable but practically unfeasible contact line locations. The results in Figure S2 match the data (symbols) from the analytical solution of Qian and Breuer [1] well. (only data of $\theta_{avg} = 65^{\circ}$ from their work are shown in the Figure B.2; see Figure 6 in their work for others). Clearly, the model developed in this work reduces to the model of Qian and Breuer when the limiting conditions (negligible *CAH* or extremely large *CAH*) are considered on the two solid surfaces.

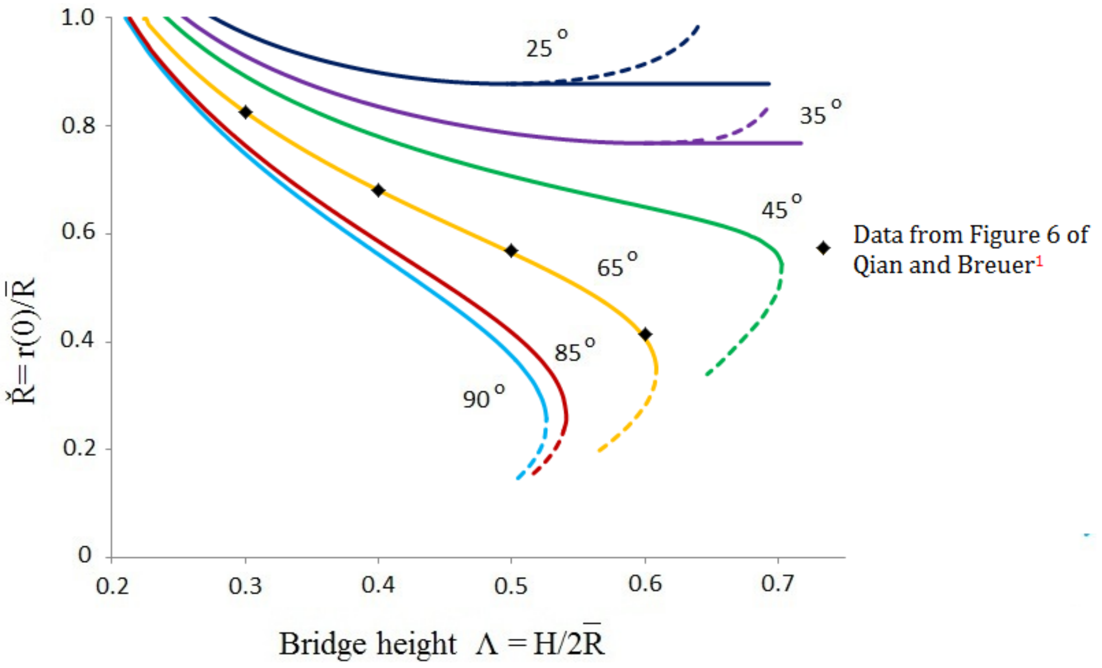

Figure B.2: Normalized free moving contact radius (Ř) on the substrate as a function of the normalized bridge height (Λ). The dotted lines show the theoretically possible and stable but practically unfeasible contact line locations.

The contour plot below (Figure B.3) presents contact angles as a function of the normalized bridge height Λ and volume v generated by setting both the two surfaces with $\theta_a = 180^\circ$ and $\theta_r = 0^\circ$, which results in two pinned contact radii as boundary conditions. At a given liquid volume (reading the contours along a horizontal line), as the separation between the two surfaces increases, the contact angle at the two surfaces first decreases, reaching a minimum, and then increases. However, the bridge cannot be stretched indefinitely. The solid curve on Figure B.3 represents the boundary at which a statically stable bridge can no longer exist. Beyond this boundary, no solution can be obtained from our model. The results in Figure B.2 match the data (symbols) from the analytical solution of Qian and Breuer [1] well. (only data corresponding to contact angle = 70° from their work are shown in the Figure B.2; see Figure 5 in their work for others).

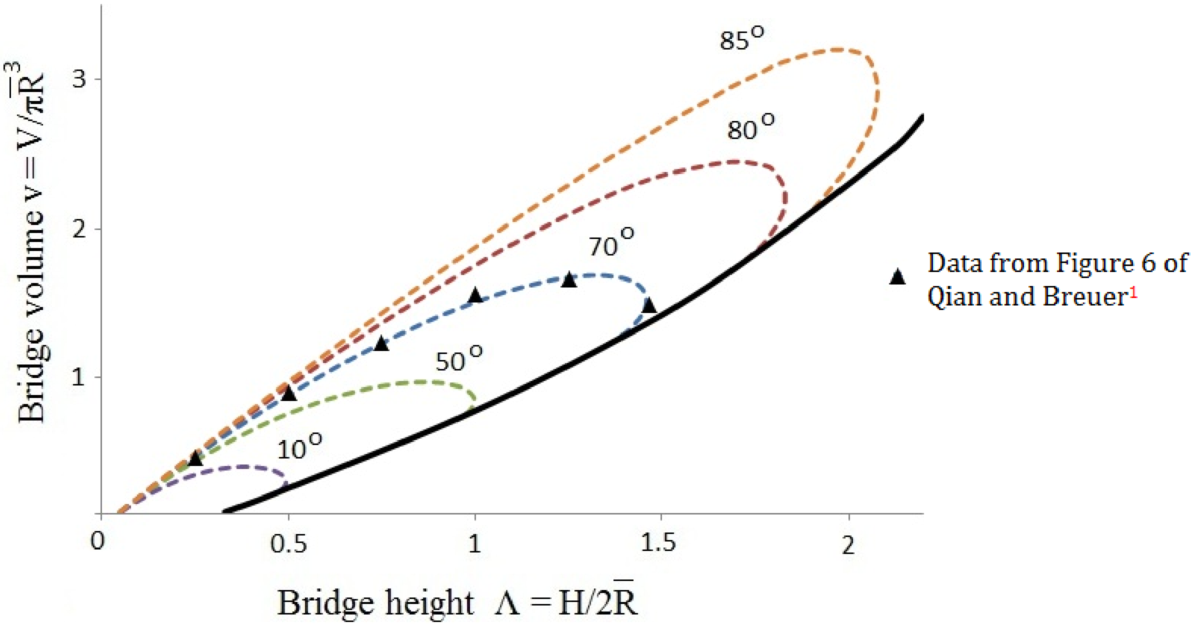

Figure B.3: Contact angles as a function of the normalized bridge height Λ and volume v. This example is for fixed contact line positions on both surfaces, $\breve{R} = r(0)/R = 1$.

B.3 Additional information for liquid compressing and stretching between PMMA surface and Teflon AF surface

Figure B.4 shows the values of the contact angle and contact radius on the Teflon AF surface during the process. Since compared with PMMA surface, θ_{avg} of Teflon AF is much larger, no R_{min} is observed on the Teflon AF surface.

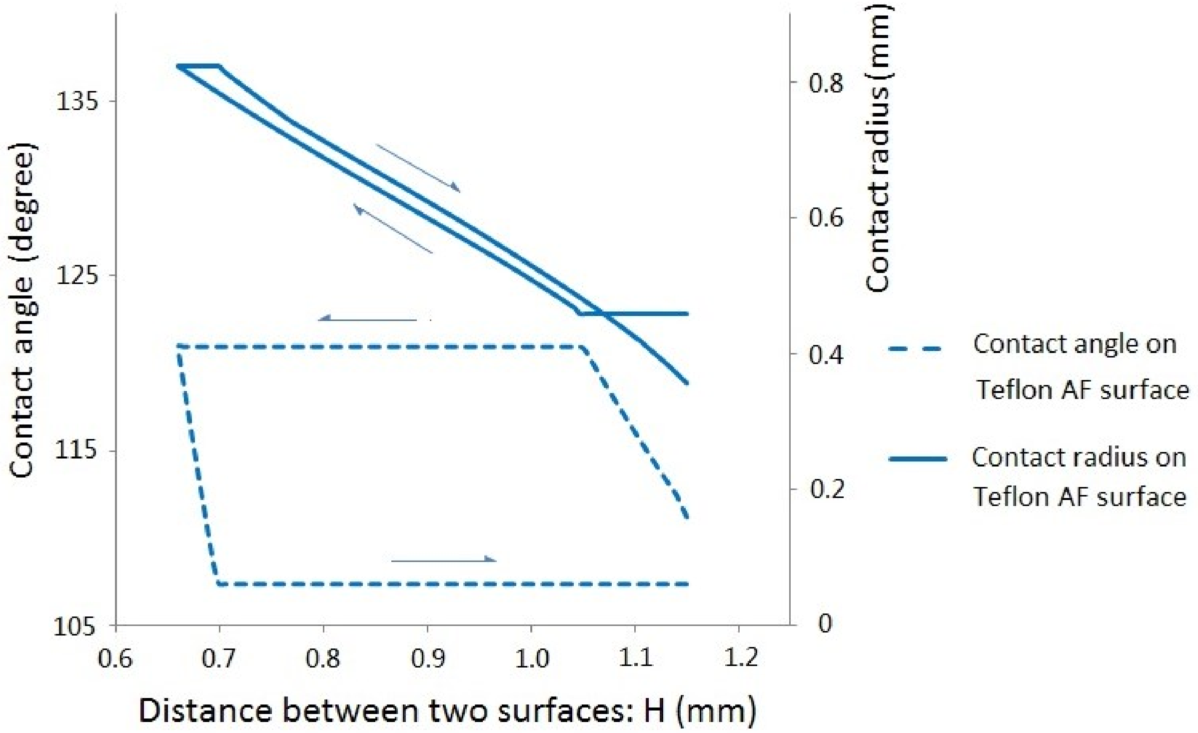

Figure B.4: Values of contact angle and contact radius on Teflon AF surfaces with different *H*.

Appendix C

C. Supporting Information for Chapter 4

C.1 Details of surfaces fabrication and contact angle measurements

Table C.1 shows the details of the selected material, fabrication methods, and the parameters chosen for each of the fabrication methods. Sessile drop method was used to measure the dynamic contact angle between distilled water and the fabricated surfaces. On each surface, measurements for contact angle were conducted at three different locations. Each of the advancing contact angles and receding contact angle in Table 1 of the letter are the average value of the 3 measurements.

Table C.1. Technical details of fabricating each surface used in this study. Except Silicon and OTS surfaces, all the other surfaces were fabricated with the techniques similar to one found in Ref.15.

Surface Name	Method	Material and fabrication details
Silicon	N/A	100 mm -orientation silicon wafers (Silicon Valley Microelectronics, Inc.)
PMMA(1)	Spin coat	Solution: 2wt% solution of PMMA (Aldrich Mw~120000) in toluene Spin coater speed: 1000 RPM Spin time: 60s
PMMA(2)	Spin coat	Solution: 0.2wt% solution of PMMA (Aldrich Mw~120000) in toluene Spin coater speed: 2000 RPM Spin time: 60s
PMMA(3)	Spin coat	Solution: 1wt% solution of PMMA (Aldrich Mw~120000) in toluene Spin coater speed: 2000 RPM Spin time: 60s
Blend (1)	Spin coat	Solution: 1wt% PMMA (Aldrich Mw~120,000) and Polystyrene (Aldrich Mw~35,000) mixed in toluene solution , ratio of PMMA: Polystyrene = 15:1 Spin coater speed: 1500 RPM Spin time: 60s
Blend (2)	Spin coat	Solution: 1wt% PMMA (Aldrich Mw~120,000) and Polystyrene (Aldrich Mw~35,000) mixed in toluene solution , ratio of PMMA: Polystyrene = 6:1 Spin coater speed: 1500 RPM Spin time: 60s
PS (1)	Heat press	Material: Polystyrene (Aldrich Mw~35,000) Plate: Two slices of spin coated Teflon AF surface Temperature: 185°C Time: 2 mins. Pressure: 645 Pa After heat press, surface was placed into 20 °C distilled water immediately. Cleaned by FC-75 again, after detached from the plate.
PEMA	Spin coat	Solution: 1wt% solution of Poly (ethyl methacrylate), (Aldrich Mw~515,000) in toluene Spin coater speed: 2000 RPM Spin time: 60s
PS (2)	Spin coat	Solution: 1wt% solution of Polystyrene, (Aldrich Mw~35,000) in toluene Spin coater speed: 2000 RPM Spin time: 60s
OTS	N/A	Microscope slides wafers were soaked in 95% OTS Solution for 30 mins.
Teflon AF	Spin coat	Solution: Teflon AF (DuPont Teflon AF 601s2-100-6) diluted with FC-75 (3M) in the ratio of 1:5 Spin coater speed: 1500 RPM Spin time: 60s

C.2 Evolutions of total adhesion force during liquid transfer

The evolutions of total adhesion force with surface separation are shown in Figure C.1 for cases 1 and 8 in Chapter 4. From this plot, it can be seen that due to the different wettability of the donor surface (Case 1: θ_a =55.1°, θ_r = 45.7°; Case 8: θ_a = 91.8°, θ_r = 75.3°), the evolutions of the total adhesion force are very different for the two cases. Specifically, because the donor surface is more hydrophilic in case 1 than in case 8, at the same separation, the adhesion force is larger in case 1 than in case 8. However, after contact line pinning starts, the geometry of the liquid bridge near the donor surface of case 1 approaches that near the acceptor surface of case 8; as well the geometry of the liquid bridge near the acceptor surface of case 1 approaches that near the donor surface of case 8. The difference in adhesion force becomes smaller and the values of F_{pf} are almost identical.

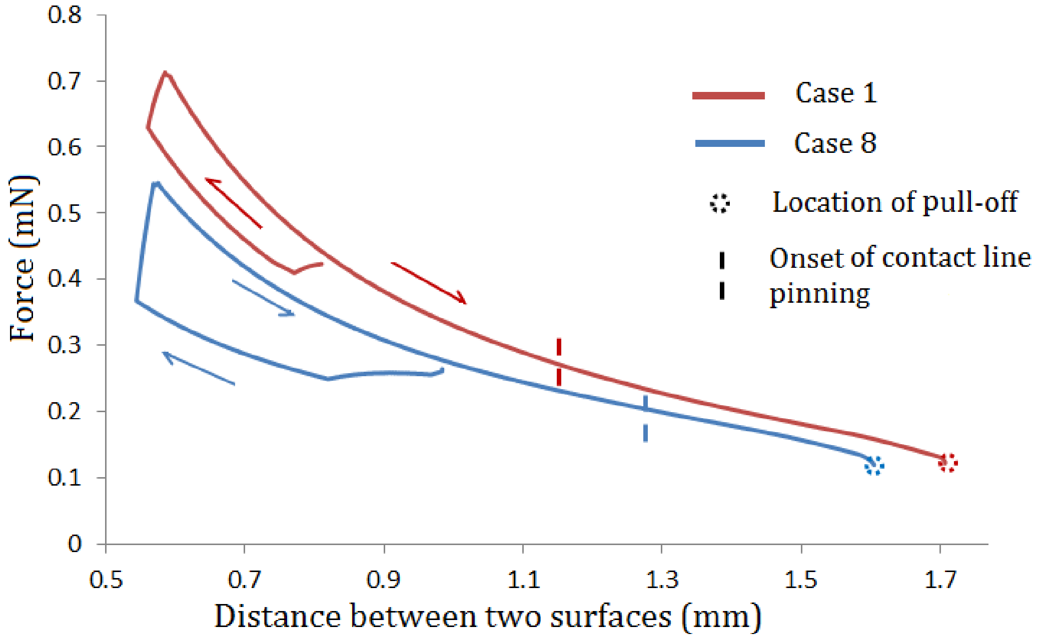

Figure C.1: Evolution of total adhesion force with surface separation in cases 1 and 8.

Appendix D

D. Supporting Information for Chapter 5

Ref. [25] in Chapter 5 cited in the main texts studied the stability of a liquid bridge between surfaces that had small areas and assumed that the liquid bridge had pinned contact lines on the edges of both surfaces. Four dimensionless parameters were introduced to describe the stability of the liquid bridge: K (ratio of smaller contact radius over the larger contact radius), V ($v/2\pi R^2 H_{max}$, where v is the actual volume of liquid, H_{max} is the separation where the liquid bridge becomes unstable, and R is the average of the contact radii on the acceptor and donor surfaces), Λ ($H_{max}/2R$) and B (Bond Number, positive if the gravity is directed toward the smaller surface, and negative if the gravity is directed toward the larger surface). The values of these four dimensionless numbers of three experimental cases in our study (water transfer from PMMA (3), Polystyrene & PMMA Blend (1), and Polystyrene & PMMA Blend (2) to PMMA (1)) where two pinned contact lines are present due to CAH are shown in Table D.1. All of the three cases have similar values for the four dimensionless numbers: B is close to zero, K is near 0.9, Λ is around 1.4 and V is around 1.46. Consulting with Figure 2(a) in Ref. [25] where K= 0.9 (shown as Figure D.1 here) and consider the curve that corresponds to B=0, it can be seen that the values of Λ and V from our experiments fall on the curve. This confirms that a liquid bridge without constrained contact lines can behave like a liquid bridge whose contact lines are constrained by finite surfaces, due to contact line pinning caused by *CAH*.

Table D.1: Value of K, V, Λ and B of the three experimental cases results.

Name of donor surface	K	V	Λ	B
PMMA (3)	0.858	0.467	1.345	-0.0860
Polystyrene & PMMA Blend (1)	0.930	0.458	1.374	-0.0859
Polystyrene & PMMA Blend (2)	0.871	0.477	1.408	0.0826

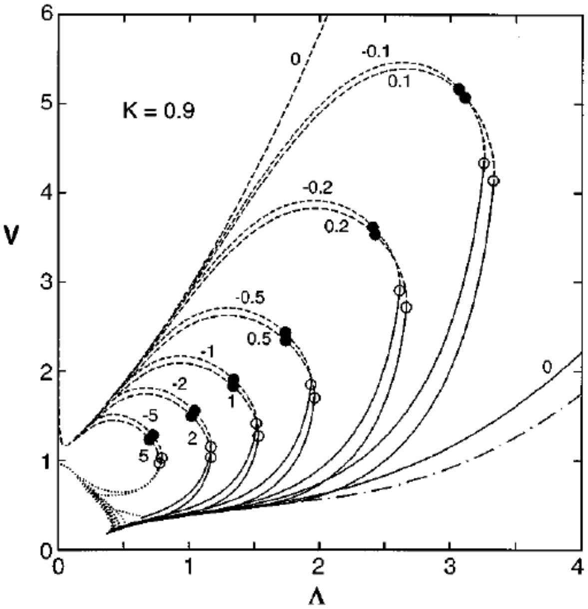

Figure D.1: Influence of positive and negative Bond number on the stability limits with K=0.9. Numbers on curves denote values of B. Solid (dashed) lines correspond to states critical to axisymmetric (nonaxisymmetric) perturbations. Dotted lines represent states with limiting surfaces, and the dot–dash line is the minimum volume stability limit for zero-gravity bridges between equal disks (K=1, B=0).

Appendix E

E. Supporting Information for Chapter 6

E.1 Details of surface fabrication

Table E.1: Technical details on the fabrication of surfaces used in this study. Except Silicon and OTS, all surfaces were fabricated with the techniques similar to one described in Ref.30 of Chapter 6.

Surface Name	Method	Material and fabrication details
Silicon	N/A	100 mm -orientation silicon wafers (Silicon Valley Microelectronics, Inc.)
PMMA(1)	Spin coat	Solution: 2wt% of PMMA (Aldrich Mw~120000) in toluene Spin coater speed: 1000 RPM Spin time: 60s
PMMA(2)	Spin coat	Solution: 0.2wt% of PMMA (Aldrich Mw~120000) in toluene Spin coater speed: 2000 RPM Spin time: 60s
PMMA(3)	Spin coat	Solution: 1wt% of PMMA (Aldrich Mw~120000) in toluene Spin coater speed: 2000 RPM Spin time: 60s
Blend (1)	Spin coat	Solution: 1wt% PMMA (Aldrich Mw~120,000) and Polystyrene (Aldrich Mw~35,000) mixed in toluene solution , ratio of PMMA: PS= 15:1. Spin coater speed: 1500 RPM Spin time: 60s
Blend (2)	Spin coat	Solution: 1wt% PMMA (Aldrich Mw~120,000) and Polystyrene (Aldrich Mw~35,000) mixed in toluene solution , ratio of PMMA: PS = 6:1. Spin coater speed: 1500 RPM Spin time: 60s
PS (1)	Heat press	Material: Polystyrene (Aldrich Mw~35,000) Plate: Two slices of spin coated Teflon AF surface Temperature: 185°C Time: 2 mins. Pressure: 645 Pa After heat press, surface was placed into 20 °C distilled water immediately. Cleaned by FC-75 again, after detached from the plate.

PEMA	Spin coat	Solution: 1wt% solution of Poly (ethyl methacrylate), (Aldrich Mw~515,000) in toluene Spin coater speed: 2000 RPM Spin time: 60s
PS (2)	Spin coat	Solution: 1wt% solution of Polystyrene, (Aldrich Mw~35,000) in toluene. Spin coater speed: 2000 RPM Spin time: 60s
OTS	N/A	Microscope slides wafers were soaked in 95% OTS solution (30 mins) and cleaned with ethanol
Teflon AF	Spin coat	Solution: Teflon AF (DuPont Teflon AF 601s2-100-6) diluted with FC-75 (3M) in the ratio of 1:5 Spin coater speed: 1500 RPM Spin time: 60s
PP	Heat press	Material: Polypropylene (Aldrich Mw~12,000) Plate: Two slices of spin coated Teflon AF surface Temperature: 200°C Time: 2 mins. Pressure: 645 Pa

E.2 Examples for regime II vanishing when one of the surfaces has $\theta_r > 90^o$

Here, we show the process of 2μl water transfer from surface ① to surface ② (Case SA) and from surface ③ to surface ② (Case SB), simulated using the theoretical model. The receding contact angle of surface ①, ② and ③ are 95.5^o, 95^o and 94.5^o, respectively. The evolutions of contact radius and contact angle are shown in Figures E.1 and E.2, respectively. For Case SA, the pinning of contact line is found on the acceptor surface. For case SB, the receding contact angle of donor surfaces is only decreased very slightly, from 95.5^o to 94.5^o, but the contact line pinning is observed only on the donor surface. Therefore, Case SB is in Regime I, and Case SA is in Regime III (Figure E.3), which is evidence for the vanishing width of Regime II when the receding angles exceed 90^o.

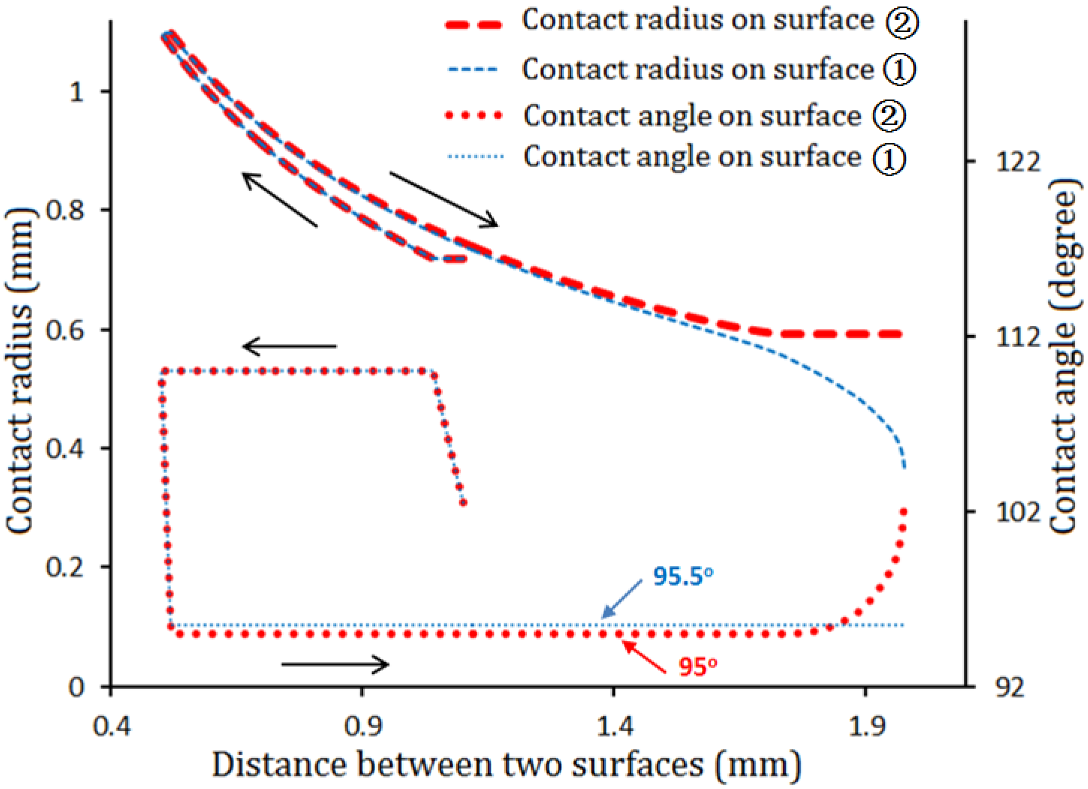

Figure E.1: Evolution of contact radius and contact angle of the liquid transfer from surface ① to surface ②.

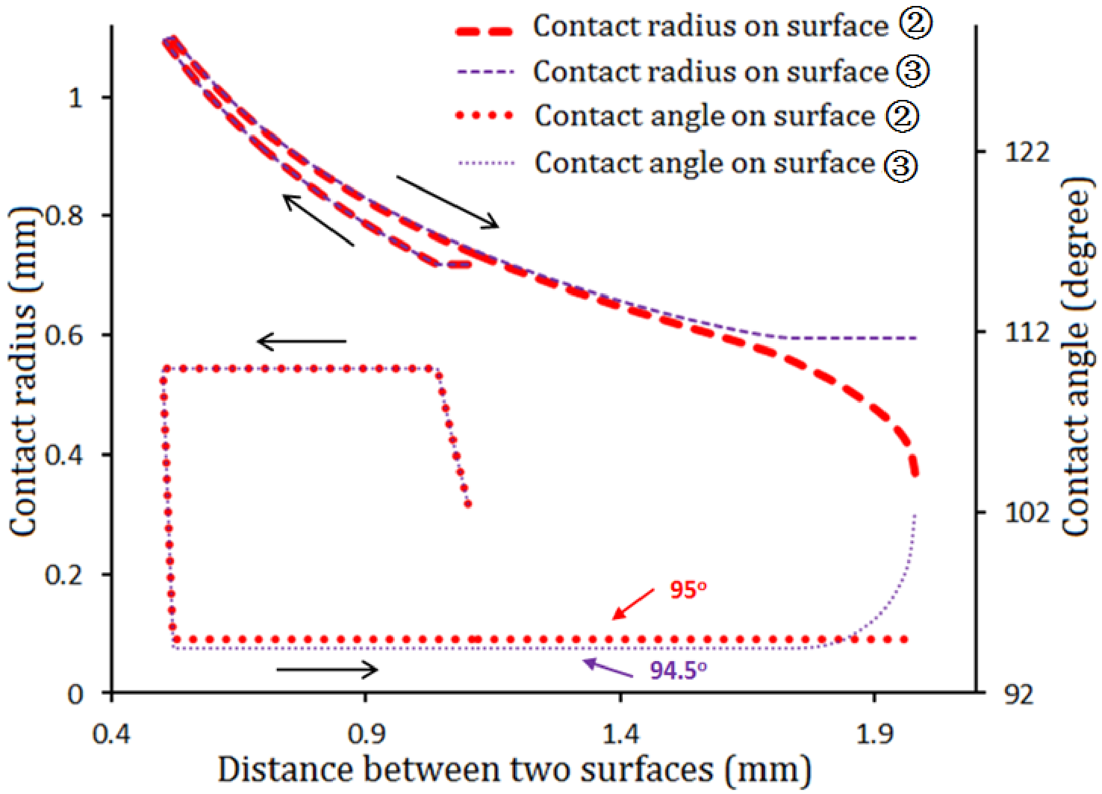

Figure E.2: Evolution of contact radius and contact angle of the liquid transfer from surface ③ to surface ②.

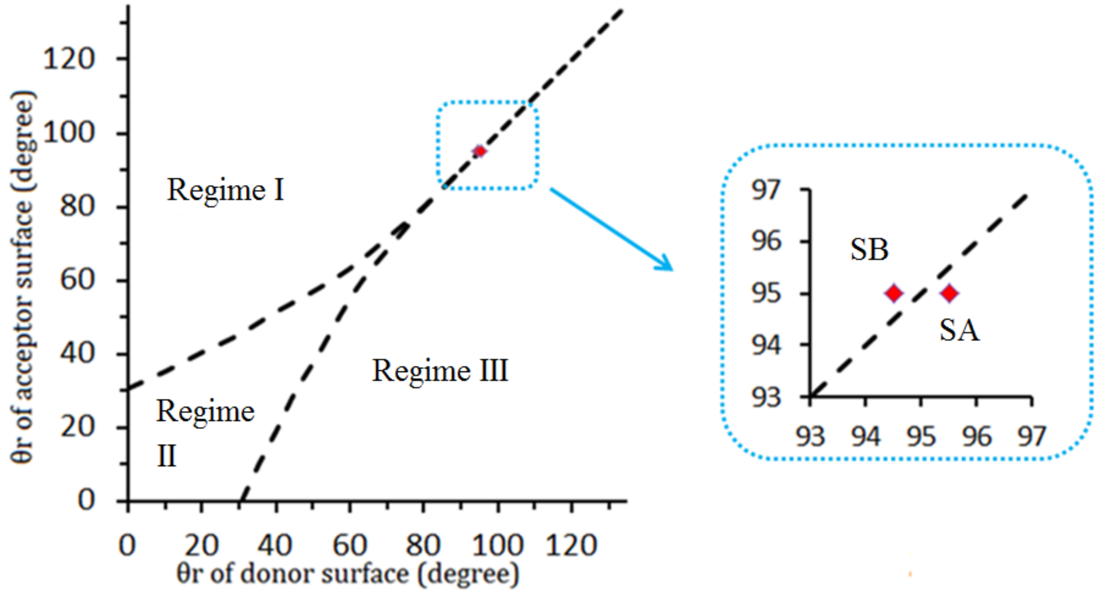

Figure E.3: Locations of Cases SA and SB in the transfer regime Map.

E.3 Effect of surface tension

Two liquid bridges which have the same H (distance between two surfaces: 0.8 mm), volume (2μl) and contact angle (lower: 60^o Upper: 100^o), but different surface tensions (72mN/m and 63mN/m) are simulated. Their profiles are shown in Figure E.4a. It can be seen that the shape of the two bridges are exactly the same despite their different surface tensions. The only difference between the two bridges is the value of ΔP (Laplace pressure difference), which is found to be 43.1N/m^2 for the liquid with surface tension of 72 mN/m, but 37.7N/m^2 for the liquid with surface tension of 63 mN/m.

The observation can be understood by examining the equations (EQ(E-1) – (E-3)) that are used to solve the profile of liquid bridge:

$$\frac{dX}{dS} = cos\theta \qquad \text{(E-1)}$$

$$\frac{dZ}{dS} = sin\theta \qquad \text{(E-2)}$$

$$\frac{d\theta}{dS} = \frac{\Delta P}{\gamma} - \frac{sin\theta}{X} \qquad \text{(E-3)}$$

where X and Z are the horizontal and vertical coordinates of the axisymmetric liquid bridge, S is the arc length measured from the contact point of the liquid with the lower surface, and θ is the angle between the local tangent of the liquid surface and the horizontal axis; γ is the surface tension of the liquid. These equations are solved with boundary conditions on the two solid surfaces, either presented as contact radius or as contact angle. The Laplace pressure ΔP is not unknown a priori and is part of the solution. It can be seen that the surface tension γ only appears in the EQ (E-3) together with ΔP. Therefore, if one defines a normalized Laplace pressure $\Delta P' = \frac{\Delta P}{\gamma}$, then EQ (E-3) can be re-written as

$$\frac{d\theta}{dS} = \Delta P' - \frac{sin\theta}{X} \qquad \text{(E-4)}$$

EQs (E-1), (E-2) and (E-4), together with boundary conditions on the surfaces, completely determine the liquid profile and the value of $\Delta P'$, while the surface tension does not play a role in the solution. In other words, ΔP accommodates the change of surface tension. Therefore, the transfer regime Map of quasi-static liquid transfer (Figure 6.3 in the main text) is not affected by the surface tension of the liquid. We also simulated two more liquid bridges, which have the same contact radius as the boundary conditions (upper: 1.2 mm, lower: 1.0 mm), but different surfaces tension (72mN/m and 63mN/m). Again the profiles of the two liquid bridges are identical, as shown in Figure E.4b.

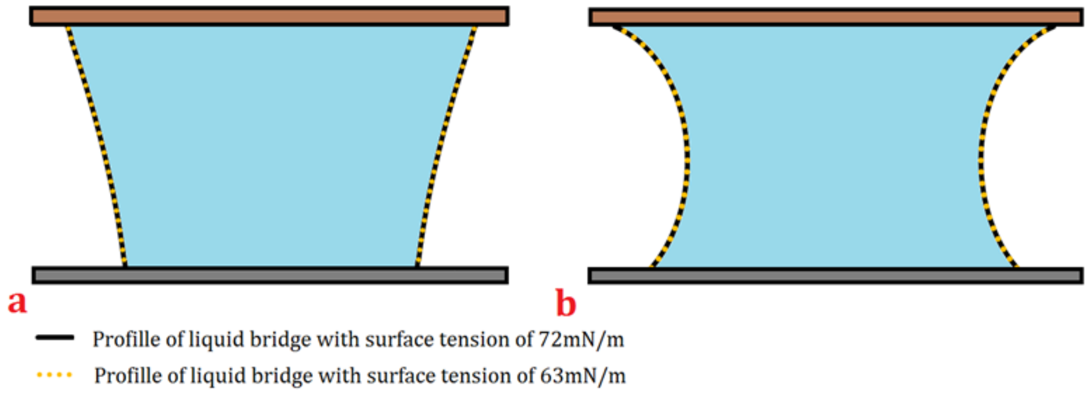

Figure E.4: (a) Profiles of liquid bridges have the same H, volume, lower and upper contact angles but different surface tension. (b) Profiles of liquid bridges have the same H, volume, lower and upper contact radius but different surface tension.

E.4 Details of the nine more experiments to find *m* and *n* used in the regression analysis

Table E.2: Details of the nine more experimental results used in the regression analysis to find *m* and *n* coefficients in EQ.(2). All experiments follow the same procedures as described in the main text.

Liquid	Name of acceptor surface and its θ_r	Name of donor surface and its θ_r	Transfer ratio (%)
Glycerol	PEMA, θ_r:63.1°	Silicon, θ_r:34.5°	2.5
Glycerol	PEMA, θ_r:63.1°	PMMA(1), θ_r:58.1°	6
Glycerol	PEMA, θ_r:63.1°	PS(1), θ_r:61.2°	17
Glycerol	PEMA, θ_r:63.1°	OTS, θ_r:85.9°	98.5
Glycerol	PEMA, θ_r:63.1°	Teflon AF, θ_r: 107.3°	100
Ethylene glycol	PEMA, θ_r:53.1°	PS(1), θ_r: 51.1°	96
Ethylene glycol	PEMA, θ_r:53.1°	OTS, θ_r: 68.1°	96
Ethylene glycol	PEMA, θ_r:53.1°	Teflon AF, θ_r: 96.2°	99.9
Silicon oil	PEMA, θ_r: ∼4°	Teflon AF, θ_r: 50.2°	89

Appendix F

F. Supporting Information for Chapter 7

With the first experimental setup, the acceptor surface was accelerated from rest to a target speed (v_{tg}) with the acceleration (a) of 400 mm/s^2 (the maximum acceleration allowed by this setup), and stayed at this target speed until the liquid bridge broke. Under this condition, the instantaneous speed v can be evaluated as a function of time (t, $t = 0$ when the stretching starts) as:

$v = a \times t$ ($t < v_{tg} / a$),

$v = v_{tg}$ ($t \geq v_{tg} / a$).

In addition, v can also be written as a function of the displacement of the acceptor surface (ΔH, $\Delta H = 0$ at H_{min}) as:

$v = \sqrt{2a\Delta H}$ ($\Delta H < v_{tg}^2/2a$),

$v = v_{tg}$ ($\Delta H \geq v_{tg}^2/2a$).

Figures F.1a and b respectively show v vs. t and ΔH when the target speed was 1mm/s. It can be seen that the acceptor surface was stretched at the target speed (1mm/s) during almost the entire stretching stage. The instantaneous speed as functions of t and ΔH with the target speed of 20mm/s (the largest speed used with the first setup) are shown in Figures F.2 a and b, respectively. Even with v_{tg} =20mm/s, the acceptor surface was stretched with the target speed during most of the process.

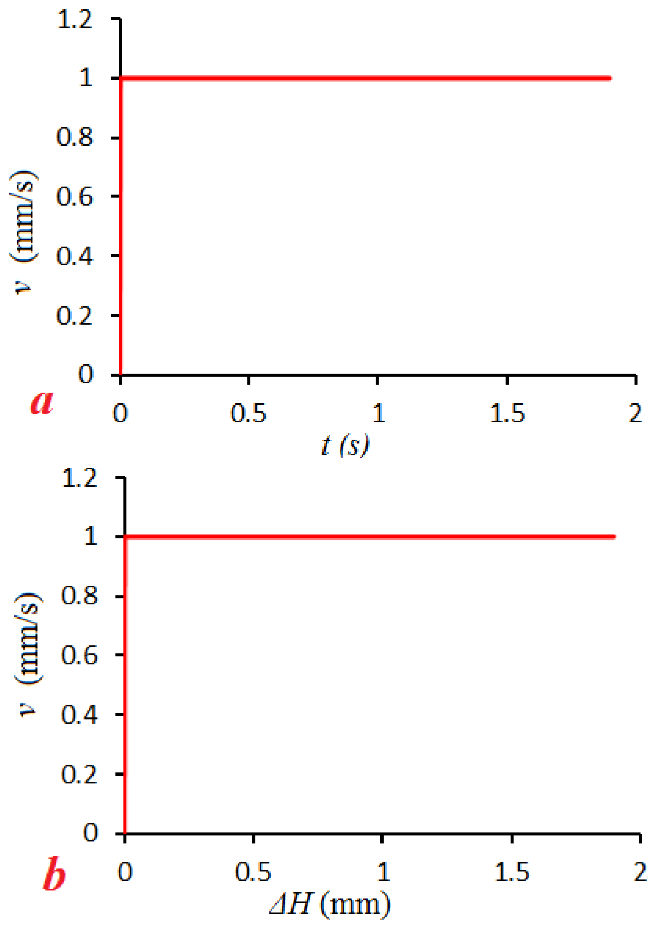

Figure F.1(a): Instantaneous speed as a function of the time with the target speed of 1mm/s. (b). Instantaneous speed as a function of the displacement of the acceptor surface with the target speed of 1mm/s. Liquid bridge broke at $\Delta H \sim 2$ mm.

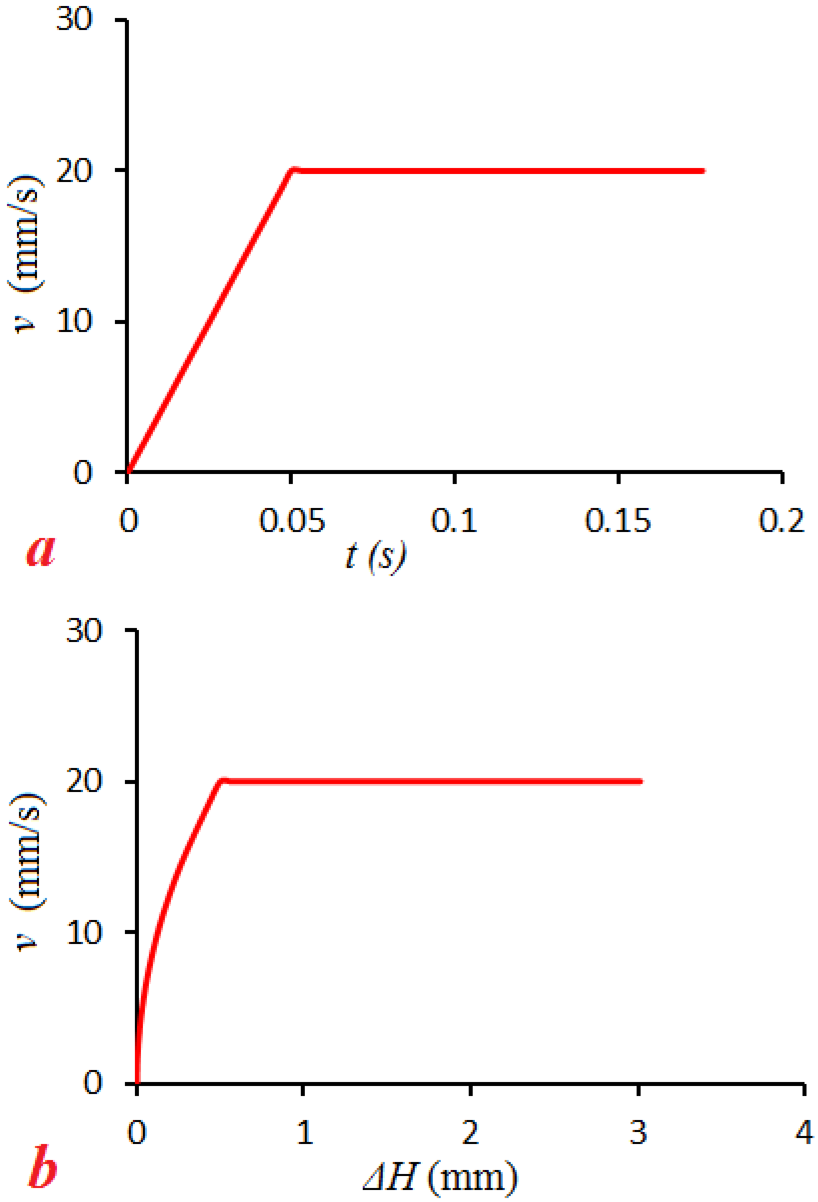

Figure F2: (a). Instantaneous speed as a function of time with the target speed of 20mm/s. (b). Instantaneous speed as a function of the displacement of the acceptor surface with the target speed of 20mm/s. Liquid bridge broke at $\Delta H \sim$3mm.

The second experimental setup included two springs with stiffness (K) of 0.22 N/mm. According to the Hook’s law, when a stretch (X) is applied to the spring, the force generated by the spring is

$F = -KX$. Therefore, by applying different X, different force in the springs can be generated, allowing for different acceleration of the acceptor surface and hence different speed before the liquid bridge breaks.

Ideally, the instantaneous speed v as functions of t and ΔH could be roughly estimated knowing the stretch of the spring and the weight of the stage to which the acceptor surface is attached. However, in the experiment, friction between the stage and the guide rail can significantly affect the speed of the acceptor surface. Therefore, v in the experiments was calculated based on the images obtained from the high speed camera. Knowing the size of each pixel in the images and the speed of the camera that was used to take the images, v as functions of t and ΔH was obtained through image analysis. Figure F.3a and b show v as functions of t and ΔH respectively for a transfer where U = 212mm/s. The average stretching speed U was then calculated as $\frac{\int_o^T v dt}{T}$, where T is the time at which the liquid bridge broke.

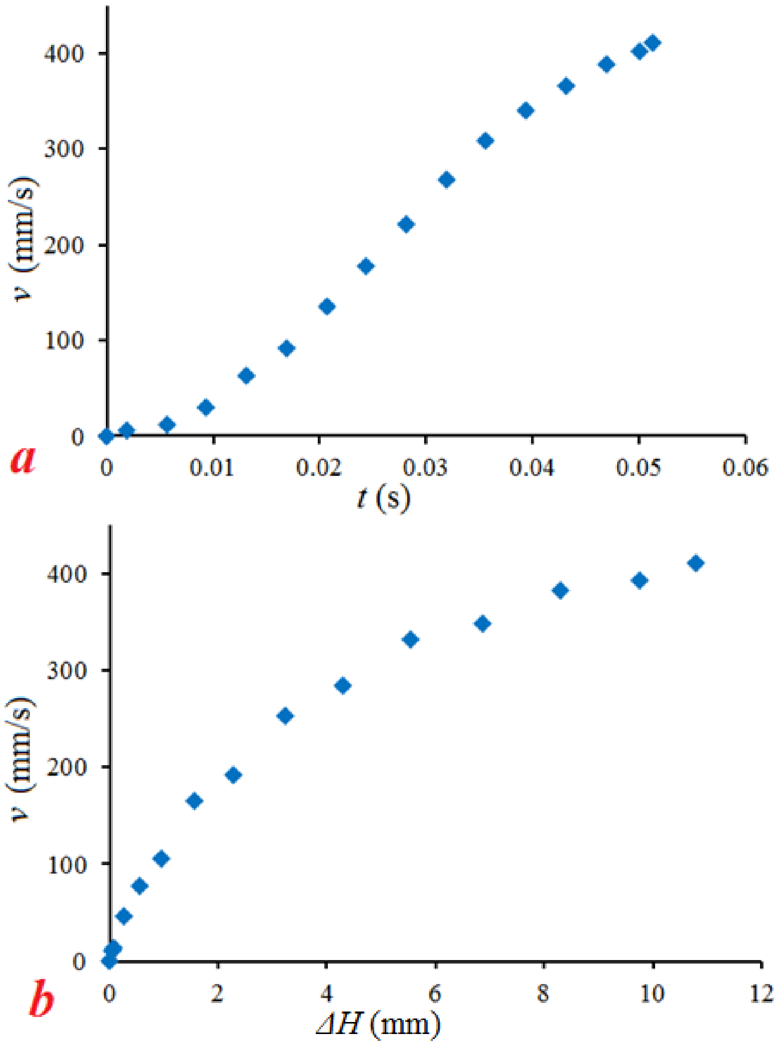

Figure F.3: (a). Instantaneous speed as a function of the time for glycerol transfer from OTS to PEMA with $U = 212$mm/s. (b). Instantaneous speed as a function of the displacement of the acceptor surface for glycerol transfer from OTS to PEMA with $U = 212$mm/s.

Appendix G

G. Supporting Information for Chapter 8

G.1 Details of surface fabrication

Table G.1:Technical details on the fabrication of surfaces used in this study. Except Silicon and OTS, all surfaces were fabricated with the techniques similar to one described in Ref.32.

Surface Name	Method	Material and fabrication details
PMMA	Spin coat	Solution: 1wt% of PMMA (Aldrich Mw~120000) in toluene Spin coater speed: 2000 RPM Spin time: 60s
PS	Heat press	Material: Polystyrene (Aldrich Mw~35,000) Plate: Two slices of spin coated Teflon AF surface Temperature: 185°C Time: 2 mins. Pressure: 645 Pa After heat press, surface was placed into 20 °C distilled water immediately. Cleaned by FC-75 again, after detached from the plate.
PEMA	Spin coat	Solution: 1wt% solution of Poly (ethyl methacrylate), (Aldrich Mw~515,000) in toluene Spin coater speed: 2000 RPM Spin time: 60s
OTS	N/A	Microscope slides wafers were soaked in 95% OTS solution (30 mins) and cleaned with ethanol
Teflon AF	Spin coat	Solution: Teflon AF (DuPont Teflon AF 601s2-100-6) diluted with FC-75 (3M) in the ratio of 1:5 Spin coater speed: 1500 RPM Spin time: 60s

G.2 Details of surface contact angle used in this study

Table G.2: Contact angle between surfaces and liquid used in this study.

Liquid Name	Name of acceptor surface and its SCA (degree)	Name of donor surface and its SCA (degree)
Silicone oil 1	PEMA, 0[1]	Teflon AF, θ_a=57.1±1.3, θ_r=47.1±1.5
Silicone oil 2	PEMA, 0[1]	Teflon AF, θ_a=57.4±1.1, θ_r=48.1±1.3
Silicone oil 3	PEMA, 0[1]	Teflon AF, θ_a=56.9±1.7, θ_r=48.7±1.8
Silicone oil 4	PEMA, 0[1]	Teflon AF, θ_a=58.2±1.2, θ_r=48.2±1.5
Ethylene glycol	Glass: 0[1]	PS, θ_a=61.1°±1.6, θ_r= 47.5° ±1.9
Water	PMMA, θ_a: 73.1°±0.9, θ_r: 58.3°±1.1	PEMA, θ_a: 77.1°±1.2, θ_r: 66.9°±1.3
Glycerol	OTS, θ_a : 97.5°±1.1, θ_r: 83.9 °±1.8	Teflon AF, θ_a : 113.1°±1.2, θ_r: 106.7°±1.4

1. During the measurement of contact angle between silicone oil and PEMA surface, the surfaces were wetted completely. Therefore, the contact angles between PEMA surface and silicone oil could not be measured. A value of 0° was used.

G. 3 Velocity measurements and calibration

With the first experimental setup, the acceptor surface was accelerated from static to a target velocity in a short time with the acceleration of 400 mm/s^2 (the maximum acceleration allowed by this setup). Once the target velocity is researched, the velocity of the acceptor surface will stay this target velocity until the liquid bridge broke. Figure S1 shows an example of instantaneous velocity (v) as function of stretched distance (ΔH). It can be seen that the velocity of acceptor surface stay in the target velocity in most of the stretching stage.

The velocity of the acceptor surface of the second experimental setup is provided by two springs with stiffness (K) of 0.22 N/mm. With applying a stretch (X) to the spring, an elastic force can be generated by the spring. Ideally, the magnitude of the force, $\mathrm{F} = -\mathrm{KX}$ (according to the Hook's law). Therefore, the velocity of the acceptor surface can be manipulated by using different X. However, in the experiment, the magnitude of F can also be affected by other factors, e.g. friction between the stage and the guide rail. Therefore, images obtained from the camera were used to calculate the value of v in the experiments. Knowing the size of each pixel in the images and the imaging speed of the camera, v as functions of t (stretching time, t =0s at the start of stretching) can be obtained.

Figure S2 shows one example of the instantaneous velocity as function of t obtained from image analysis of the second system. The whole transfer process was finished in 0.0515 s. It can be seen that v as function of t fits with the function of $v = t$ *8000 (mm/s^2) well. Therefore, the stretching speed in the second system can be treated as uniformly accelerated motion with a constant acceleration.Since the velocity provided in the second system is not a constant during the transfer process, the speed averaged from the beginning of the stretching stage to the breakage of the liquid bridge is used as U for the second experimental setup in the later discussion. The average stretching speed U was then calculated as $\frac{\int_o^T vdt}{T}$, where T is the time at which the liquid bridge broke. The average velocity, U of the example shown in Figure S2 is 212mm/s.

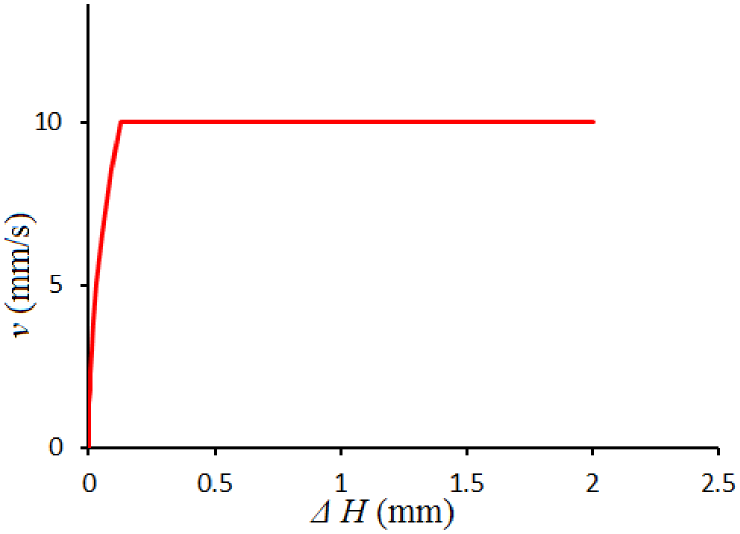

Figure G.1: Instantaneous speed as a function of ΔH with the target speed of 10mm/s provided by the first experimental setup.

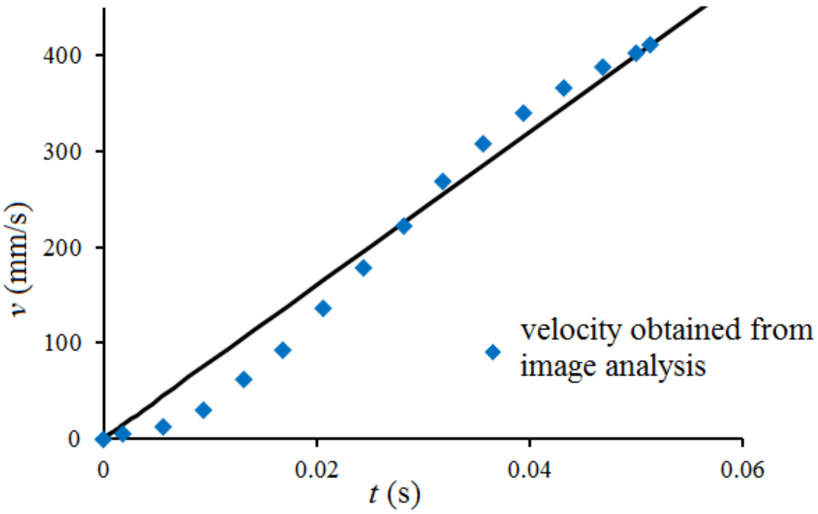

Figure G.2: Instantaneous speed as a function of *t* with *U* = 212mm/s provided by the second experimental setup. The solid line is the function of v = t *8000 (mm/s^2).